LASER COULOMB EXPLOSION IMAGING OF MOLECULAR DYNAMICS

by

IRINA A BOCHAROVA

B. Sc., Voronezh State University, Russia, 2000
M. Sc., Voronezh State University, Russia, 2002

AN ABSTRACT OF A DISSERTATION

submitted in partial fulfillment of the requirements for the degree

DOCTOR OF PHILOSOPHY

Department of Physics
College of Arts and Sciences

KANSAS STATE UNIVERSITY
Manhattan, Kansas

2009

Abstract

The goal of this dissertation project was to study the dynamics of nuclear motion in diatomic (H_2, N_2, O_2, CO) and triatomic (CO_2) molecules initiated by the ionization and/or excitation of these molecules with near-IR few-cycle laser pulses. This dynamics includes vibrational and rotational motion on the electronic potential surfaces of the molecules and their molecular ions. The experimental techniques used included the pump-probe approach, laser Coulomb explosion imaging and the COLTRIMS technique.

The results are presented in four chapters. A study of rotational and vibrational nuclear dynamics in H_2 and D_2 molecules and ions initiated by 8 fs near-IR pulses is presented in Chapter 4. Transient alignment of the neutral molecules was observed and simulated; rotational frequency components contributing to the rotational wavepacket dynamics were recovered. Chapter 5 is dedicated to revealing the contribution of excited dissociative states of D_2^+ ions to the process of fragmentation by electron recollision. It was shown that it is possible to isolate the process of resonant excitation and estimate the individual contributions of the $^2\Sigma_u^+$ and $^2\Pi_u$ states. In Chapter 6 the subject of investigation is the nuclear dynamics of N_2, O_2 and CO molecules initiated by ionization of a neutral molecule by a short intense laser pulse. It was shown that the kinetic energy release of the Coulomb explosion fragments, measured as a function of the delay time between pump and probe pulses, reveals the behavior of nuclear wave packet evolution on electronic states of the molecular ions. It was shown that information on the dissociation and excitation pathways can be extracted from the experimental spectra and the relative contributions of particular electronic states can be estimated. Chapter 7 is focused on studying the fragmentation of CO_2 following the interaction of this molecule with the laser field. The most important result of this study was that it presented direct experimental evidence of charge-resonant enhanced ionization (CREI), a phenomenon well-studied for diatomic molecules and predicted theoretically for triatomic molecules. The critical internuclear distance, the relevant ionic charge state and a pair of charge-resonant states responsible for the CREI were also found.

LASER COULOMB EXPLOSION IMAGING OF MOLECULAR DYNAMICS

by

IRINA A BOCHAROVA

B. Sc., Voronezh State University, Russia, 2000
M. Sc., Voronezh State University, Russia, 2002

A DISSERTATION

submitted in partial fulfillment of the requirements for the degree

DOCTOR OF PHILOSOPHY

Department of Physics
College of Arts and Sciences

KANSAS STATE UNIVERSITY
Manhattan, Kansas

2009

Approved by:

Major Professor
I.V. Litvinyuk

Abstract

The goal of this dissertation project was to study the dynamics of nuclear motion in diatomic (H_2, N_2, O_2, CO) and triatomic (CO_2) molecules initiated by the ionization and/or excitation of these molecules with near-IR few-cycle laser pulses. This dynamics includes vibrational and rotational motion on the electronic potential surfaces of the molecules and their molecular ions. The experimental techniques used included the pump-probe approach, laser Coulomb explosion imaging and the COLTRIMS technique.

The results are presented in four chapters. A study of rotational and vibrational nuclear dynamics in H_2 and D_2 molecules and ions initiated by 8 fs near-IR pulses is presented in Chapter 4. Transient alignment of the neutral molecules was observed and simulated; rotational frequency components contributing to the rotational wavepacket dynamics were recovered. Chapter 5 is dedicated to revealing the contribution of excited dissociative states of D_2^+ ions to the process of fragmentation by electron recollision. It was shown that it is possible to isolate the process of resonant excitation and estimate the individual contributions of the $^2\Sigma_u^+$ and $^2\Pi_u$ states. In Chapter 6 the subject of investigation is the nuclear dynamics of N_2, O_2 and CO molecules initiated by ionization of a neutral molecule by a short intense laser pulse. It was shown that the kinetic energy release of the Coulomb explosion fragments, measured as a function of the delay time between pump and probe pulses, reveals the behavior of nuclear wave packet evolution on electronic states of the molecular ions. It was shown that information on the dissociation and excitation pathways can be extracted from the experimental spectra and the relative contributions of particular electronic states can be estimated. Chapter 7 is focused on studying the fragmentation of CO_2 following the interaction of this molecule with the laser field. The most important result of this study was that it presented direct experimental evidence of charge-resonant enhanced ionization (CREI), a phenomenon well-studied for diatomic molecules and predicted theoretically for triatomic molecules. The critical internuclear distance, the relevant ionic charge state and a pair of charge-resonant states responsible for the CREI were also found.

Table of Contents

List of Figures

Acknowledgments

To make my dissertation complete I would like to dedicate several pages of this manuscript to express my gratitude and acknowledge the contributions of many people who helped, supported and guided me through the graduate school years.

First of all, I would like to thank my adviser Prof. Igor Litvinyuk for his guidance and all the things he had taught me, for his willingness to become my adviser when I decided to enter the unfamiliar field of atomic and molecular physics. He was always available for questions and discussions, very patient with me and ready to explain ideas again and again until there were perfectly clear. He was not only the generator of ideas but active leader in any activity in the laboratory whether it was regular experiment or troubleshooting. Also I am grateful for his friendly attitude in daily life; he and his family were always there for me ready to help in any situation.

I am grateful to Prof. Lewis Cocke for letting me join the group. He is a great scientist, leader and mentor, very passionate, and the real heart of our group. I have learned many useful lessons from him, and not only in physics, but in life. Prof. Cocke is also one of the people who represents the spirit of the AMO community, makes you feel welcomed and the part of the AMO family.

Present and former members of our group whom I have met during these five years were the great people to work with. They are Dipanwita Ray, Chakra Maharjan, Predrag Ranitovic, Ali Alnaser, Sankar De, Maia Magrakvelidze, Ben Gramkow and Wei Cao. We had supported and helped each other, were interested and sometimes involved in each other's experiments, no matter how different our projects were, transfer our knowledge and skills, we had fun together, and it was a pleasure to be a part of this group. Dr. Ali Alnaser, who was a postdoctoral assistant at KSU at the time I joined the group, dedicated a lot of time introducing to me the basics of the experiments and analysis; and also I appreciate very much his help on the reviewing and editing this manuscript. I am also grateful to Dr. Timur Osipov, who is the former student of Prof. Cocke and now is the research staff scientist in Lawrence Berkeley National Lab. He was the precious source of information on the experimental techniques and analysis for me.

I want to say thank you to Prof. Zenghu Chang and all present and former members of his group who were helping me in my every experiment through these years. They were not only maintaining laser system in a working condition but also always “on call” twenty four hours a day, seven days a week – ready to troubleshoot, optimize, align, teach and help. Special thanks to Chengquan Li, Hiroki Mashiko, Steven Gilbertson and He Wang.

For many fruitful discussions and guidance in my modeling efforts, and also for being outstanding teachers I thank Prof. Brett Esry and Prof. Uwe Thumm. Thomas Niederghausen, the former student of Prof. Thumm, was extremely helpful and provided me with his computer software I have used as a starting point in my data analysis. Fatima Anis, the former student of Prof. Esry actively collaborated with us and kindly consulted me on FORTRAN coding.

I cannot forget to express my appreciation of the great experience of working with Prof. François Légaré from INRS-EMT (National Institute of Scientific Research – Energy, Materials and Telecommunications) Quebec, Canada. Very productive work and an opportunity to participate in experiments in the great modern facility (Advanced Laser Light Source) are the two of many advantages of the collaboration with Prof. Légaré. A great deal of my experimental work included in this thesis was done thanks to our mutual efforts. I am also grateful for his support and readiness to help.

I thank Prof. Lew Cocke, Prof. Kristan Corwin, Prof. Larry Weaver and Prof. Viktor Chikan for agreeing to be the members of my committee and closely following my progress. Special thanks to Prof. Corwin and Prof. Weaver for helpful discussions on different subjects.

I greatly appreciate the job of machine-shop personnel and lab stuff: Al Rankin, Scott Chainey, Bob Krause, Mike Wells, Russ Reynolds and others. Kevin Carnes and Vince Needham were of a great help with any computer issues. There are very nice people on the department like Peggy Matthews, Deanna Selby, Jane Peterson, Lindsay Thompson and Lisa Mc Neil who made my life as a member of the Physics department go smoothly and organized.

I am thankful to the whole AMO team. There is not a single person in this community who was not friendly to me, was not ready to help, who I have not felt

support from and have not heard a warm word or advice during my work in KSU. These people created together a wonderful friendly environment for knowledge, skills and experience exchange.

I would like to say several words about my friends, fellow graduate students and postdoctoral assistants. Dipanwita Ray became a very special friend to me through all the years of working next to each other. Her support, help, hand, advice and humor were with me every day for five years and made my grad school days much easier and merrier. Chris Nakamura and his wife Sarah, Hiroki Mashiko, Chengquan Li and Ioannis Chatzakis are my very good friends without whom it would be many more grey days in my life as a graduate student.

And finally, I want to thank my close friends and family outside the university walls, who always encourage me, bear my busyness and talks about job, support me and cheer for me in my every endeavor. They are my mom, my grandmother, Sergiy, Yurii, Olga and Dan, Olena, Svetlana.

CHAPTER 1 – Introduction

Practical applications of lasers involve the interactions of laser field with matter [**1**]. Matter is made of atoms and molecules, and their behavior in laser field defines the laser-matter interaction in many aspects. It makes sense to start an investigation of the complex phenomena with studying the effects of intense laser fields on atoms and molecules. Beside that, the practical interest of studying molecules in the laser field lies in the possibility of learning how to control molecular transformations in various physical, chemical and biological reactions using laser as a tool.

On the microscopic scale "intense field" means that the field is strong enough to affect the bound states of electron in the atom/molecule including the ground state; couple and modify field-free electronic states noticeably at the peak of the pulse. For that the laser field magnitude should be comparable to the internal field strength in atoms. For instance, the field binding an electron in hydrogen atom is 5×10^9 V/cm. This field corresponds to laser peak intensity on the order of 10^{16} W/cm^2.

At these and even lower intensities variety of phenomena takes place in atoms and molecules that have been studied as the effects of strong laser field – atom/molecule interactions. Among these phenomena studied in atoms are ionization, above threshold ionization (ATI), and high harmonic generation (HHG). Single ionization of atoms is well studied and is usually separated into three regimes according to the characteristic Keldysh parameter: tunneling, multiphoton and over-the-barrier ionization (see Section **3.2**). Tunneling ionization rate is given by the Amosov-Delane-Krainov (ADK) theory [**2**] and agrees well with the experiment [**3**]. But trying to extend this theory to double ionization one runs into the effect of non-sequential double ionization (NSDI), the mechanisms of which have been actively under discussion [**4**-**6**].

Molecules offer more challenges, exhibiting all the phenomena observed in atoms, and also presenting a wide range of new physics, resulting from increasing number of degrees of freedom. For diatomic molecules, two spatially separated nuclei bring nuclear rotational and vibrational motion into play, causing, for instance, ionization rate dependence on internuclear distance and molecule's axis orientation relative to the laser polarization [**7**, **8**]. The shape of molecular orbitals also was found to have an effect

on the ionization rate [**9**]. The dissociation process is closely related to the ionization of molecules. With a rising number of electrons in a diatomic molecule the number of possible fragmentation channels and intermediate charged states characterized by unique electronic structure increases. Dynamics of this process is rich and complex and it is associated with many interesting physical phenomena, which are going to be discussed in this study. Understanding the dynamics of molecular dissociation gives the possibility in the future to manipulate the excitations pathways, energy levels repopulation and the resulting yields with lasers.

The goal of this project is to study the dynamics of nuclear vibrational and rotational motion in molecules following an interaction with a laser field. To understand how a system evolves from the initial to the final state it is necessary to take several snap shots of the nuclear wave packet as it progresses in time. For this kind of time-resolved measurements pump-probe technique has been widely employed. Pump and probe are two short intense laser pulses impacting the target molecule with a certain time delay between them. The pump pulse interacts with the target initiating some process and the second pulse probes the reaction of the molecule to the first pulse. By probing the structure at different times after the molecule was hit by the pump one can create a kind of "molecular movie". The dynamics in molecules is an ultrafast process and the molecular bond length is of the order of a few angstroms. To achieve high temporal resolution it is crucial to use laser pulses shorter than the characteristic time of the observed process. To map molecular geometry with high spatial resolution the Coulomb Explosion Imaging technique is combined with a pump-probe experiment. Its basic principle is in the fast ionization of a molecule with a probe pulse to produce highly charged ions which dissociate very quickly due to the Coulomb repulsion between the nuclei [**10**]. By measuring the final momenta of the fragments one can reconstruct the initial geometry of the molecule at the very moment of explosion. COLTRIMS (cold target recoil ion momentum spectroscopy) is a powerful technique for measuring momentum distribution of ion products in laser-matter interaction experiments. This technique offers high momentum resolution in all directions and full 4π fragments detection solid angle [**11**]. With a cold and dilute target gas one can study individual atoms or molecules. COLTRIMS is also often called the "reaction microscope" to

emphasize the microscopic resolution for dynamic processes occurring in atoms and molecules.

The hydrogen molecule and its molecular ion are the simplest targets for the experimental and theoretical studies of laser-molecule interactions. H_2 (a homonuclear diatomic molecule with just two electrons) exhibits a wide range of phenomena, observed also in more complex molecules. Bond softening [**12**], vibrational trapping [**13**], charge resonant enhanced ionization CREI [**14**], above threshold ionization [**15**], and high-order harmonic generation [**16**] have been observed and studied in hydrogen and deuterium molecules and ions over recent years. As a result, we now have a good qualitative understanding of these phenomena. However the agreement between experiment and theory is still far from being quantitative. On the other hand, the smallest molecule offers a unique challenge in studying its vibrational and rotational nuclear dynamics. Being the lightest molecule it is characterized by the shortest vibrational and rotational periods for the nuclear motion on excited states. It requires employing very short pulses for time-resolved CEI of the molecule [**17**]. The hydrogen molecule also has a very low polarizability and widely-separated rotation states, which make the observation of such phenomena as dynamical alignment and ionization rate angular dependence a non-trivial task. Electron rescattering and the mechanisms of related to it non-sequential double ionization and recollision excitation phenomena are still under debate [**18**, **19**]. The part of this project is dedicated to studying rotational nuclear dynamics, angular-dependent ionization and inelastic rescattering processes in hydrogen molecule.

Nitrogen and oxygen are also diatomic homonuclear molecules like hydrogen but the increasing number of electrons puts us on the next level of complexity in the nuclear dynamics. Multiple ionization and fragmentation in many possible dissociation channels are causing nuclear vibrational dynamics which reflects different possible pathways of these processes and electronic structure of intermediate states accessible at certain experimental conditions. As part of this project we take the challenge to use time-resolved CEI to picture nuclear wave packet evolution following the interaction of oxygen and nitrogen molecule with intense laser pulse and use it as a method of extracting detailed information on the dissociation pathways for any diatomic molecule. Carbon monoxide molecule (CO) is chosen next as an example of the heteronuclear

diatomic molecule. The next logical step is to see if the lack of inversion symmetry in a molecule would bring any special features in dynamics compared to a homonuclear one; and if the method worked out for the former ones can be generalized to study any kind of diatomic molecule.

A triatomic linear molecule like CO_2 brings new nuclear degrees of freedom into play. Except for rotation of the molecule as a whole and vibration of nuclei with symmetric and asymmetric C-O bonds stretching, it also can bend, which certainly brings new challenges and complexity into studying molecular dynamics. The question is: can we generalize the techniques and models developed for diatomics and whether the same phenomena (i.e. CREI) define their behavior. In the final part of this study we applied the CEI technique to successfully reconstruct molecular geometries and to demonstrate the CREI in triatomic molecules.

The structure of this thesis is as follows. After the first introductory Chapter, Chapter 2 presents the description of the experimental setup as well as all the techniques used and the important elements of data acquisition and analysis. Chapter 3 presents some background information on physics, which is necessary for better understanding of the phenomena investigated in this dissertation project. Chapters 4, 5, 6, 7 contain all the experimental results, discussion and summary for each part of the project. The chapters are followed by several appendices with supplementary materials like programming code and details of numerical calculations.

CHAPTER 2 – Experimental Setup and Techniques; Data Acquisition and Analysis

The whole experimental setup is presented schematically in Fig**. 2.1**. In the following I will explain it step by step and also describe the techniques we employed in the experiment and discuss some important aspects of data acquisition and analysis.

Figure 2.1 Schematic of the experimental setup

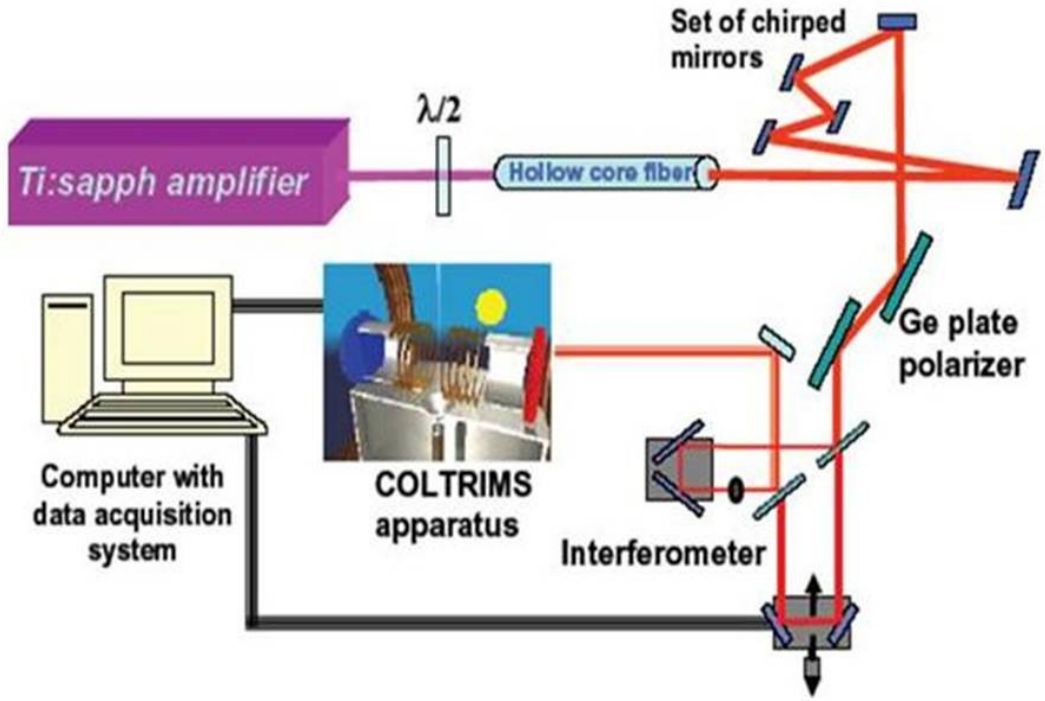

2.1 Laser Pulses

The experiments were conducted at the J. R. Macdonald Laboratory in Kansas State University. A one kilohertz 1 mJ Ti:Sapphire amplifier was used to produce ~ 35 fs long 800 nm pulses. It is seeded by the pulse which originates from a Ti:Sapphire oscillator that is pumped by a CW laser. The wave bouncing in the cavity of the oscillator creates standing waves which form a discrete set of frequencies (longitudinal and axial modes). The axial modes are separated by $\Delta\nu = c/2L$, where c is the speed of light and L is the cavity length. To obtain an output in a form of a pulse the oscillator needs to be "mode-locked". It means that each mode does not oscillate randomly, but with phase fixed relative to the other modes. Therefore, the modes interfere constructively producing intense bursts of light separated by the time of round-trip in the cavity. In practice, a number of modes are locked, not all of them, because of the dispersion in a media. The mode-locking of the oscillator is achieved by so-called self-mode-locking. Due to the non-linear effects in the Ti:Sapphire crystal the effective refractive index varies with the laser intensity.

$$n(t)=n_0+n_2 I(t) \qquad \textbf{(2.1)}$$

The beam intensity has a certain profile (Gaussian shape see eq. **(2.1)**, τ is the pulse length) and the refractive index changes across the profile.

$$I(t)=I_0\, exp(-4\ln t^2/\tau^2), \qquad \textbf{(2.2)}$$

Thus, the effect of the lens action is created in the crystal (Kerr lens effect). The higher the beam intensity rises the stronger the lens effect is. The oscillator is constructed in such a way that it is unstable (lossy, does not generate) when there is no lens effect. Due to Kerr effect the refraction index is varying with *I(t)* creating a periodic loss modulation in time. If the amplified modes have their phases synchronized and their maximum amplitudes coincide with the minimum of losses then these modes interfere constructively to give a short pulse of high energy. If the peak of some amplified mode does not exactly coincide with the dip in losses then the maximum of the amplified peak is reduced due to the loss and the new maximum is shifted towards the minimum loss.

Eventually, the amplified modes phases are self-synchronized because the minimizing of losses brings the oscillator to the most stable regime. [**20**]

The pulse duration is defined by the number of modes oscillating in phase. Ti:Sapphire material is characterized by the largest gain bandwidth (235 nm) of all laser media in use [**21**]. Such a broad bandwidth gives an opportunity of having the shortest possible pulse on the exit of the oscillator of 10 femtoseconds. If N modes altogether are locked and Δn is the frequency separation, then $N\Delta n$ is the total mode-locked bandwidth. However, the pulse duration is not only defined by this product, but also by the pulse temporal shape. For the Gaussian shaped pulse the minimum pulse duration that can be achieved is $\Delta t = 0.44/N\Delta n$, where 0.44 is so-called time-bandwidth product.

The pulse energy on the stage of exiting the oscillator is of the order of a nanojoule, which is too low for the most laser applications, and needs to be amplified using the principle of chirped pulse amplification. To avoid damaging the crystal in the amplifier the seed pulse is stretched to 100 picoseconds by a pair of gratings. In order to amplify the pulse up to a millijoule it has to pass Ti:Sapphire crystal several times. The crystal is pumped by a Nd:Yag laser. After amplification another pair of gratings is used to compress the pulse to 30 fs (for the detailed information on the laser source in JRM Laboratory see the website [**22**]).

To compress a laser pulse to sub-10 fs duration a rare-gas filled hollow core fiber and a set of chirped mirrors (7 Femtolaser and 4 Layertec) were placed after the amplifier. A half wave plate before the fiber controls the polarization of the laser pulse (Fig. **2.1**). The pulse compression technique relies on spectral broadening due to nonlinear effects in a waveguide filled with a rare gas (Ar or Ne) and controlling a group velocity dispersion with chirped dielectric mirrors.

The hollow core fiber is a fused silica capillary with inner diameter of 400 μm and 90 cm long, enclosed in an aluminum tube filled with gas at pressure of ~10 psi (depending on gas). Inside the waveguide light energy is confined in a very small mode area for a long interaction region so that strong self-phase modulation and dispersion effects accumulate at energies well below those that produce optical damage. Very strong nonlinear propagation effects are achieved, such as pulse self-chirping. In eq. **(2.1)** n_2 is the nonlinear diffraction index, which is responsible for appearance of new frequency

components and acquiring chirp. The pulse length in time domain becomes shorter as a result of frequency spectrum broadening. Chirp is caused by separation of frequency components in time while pulse is traveling through a dispersive media. In other words, the refractive index of gas in the fiber is different for each frequency component of the spectrum. Therefore the velocity of traveling through the media is also different for each component. As a result, the group velocity dispersion (GVD) occurs: high frequency components are delayed in comparison with low frequency components (positive chirp). For GVD compensation, mirrors with a special coating are used: this is a multilayered coating with each layer of different thickness reflecting a certain wavelength.

The intensity profile of the laser beam we use is described by Gaussian form:

$$I(x,y,z)=\frac{2P}{\pi w(z)^2}\exp\left(-2\frac{x^2+y^2}{w(z)^2}\right). \qquad \textbf{(2.3)}$$

In this equation z is the propagation direction, P is the power.

The propagation of the beam in space is described by the following formula:

$$E(x,y,z)=E_0\left(\frac{w_0}{w}\right)\exp\left(-\frac{x^2+y^2}{w(z)^2}\right)\times$$
$$\times\exp\left(ik\left(z+\frac{x^2+y^2}{2R(z)}-ct\right)-\arctan\left(\frac{z}{z_R}\right)\right) \qquad \textbf{(2.4)}$$

Starting with flat wave front, the beam propagates, and the wave front acquires curvature. Thus, at any point the radius of the wave front is:

$$R(z)=z\left(1+\left(\frac{\pi w_0^2}{\lambda z}\right)^2\right), \qquad \textbf{(2.5)}$$

here λ is the wavelength,

$$w(z)=w_0\left(1+\left(\frac{\lambda z}{\pi w_0^2}\right)^2\right)^{1/2} \qquad \textbf{(2.6)}$$

is the radius of $1/e^2$ contour (meaning that the intensity drops by $1/e^2$ factor (13.5%) from its maximum value, see Fig. **2.2**) and w_0 is the waist radius of the beam. z = 0 marks the location of the waist w_0, where the wave front is flat and *R* is infinity (Fig. **2.3**).

Figure 2.2 Gaussian beam intensity profile. The figure is from reference [23]

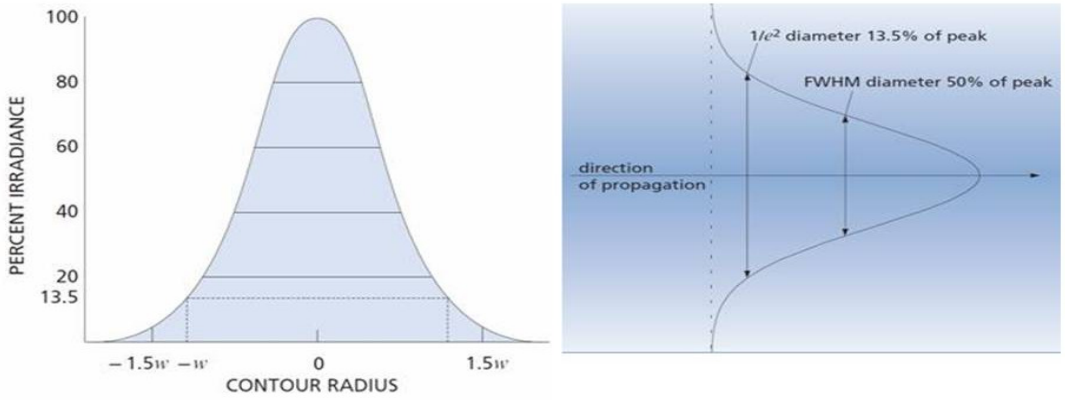

Figure 2.3 Gaussian beam wave front evolution. The figure is from reference [23]

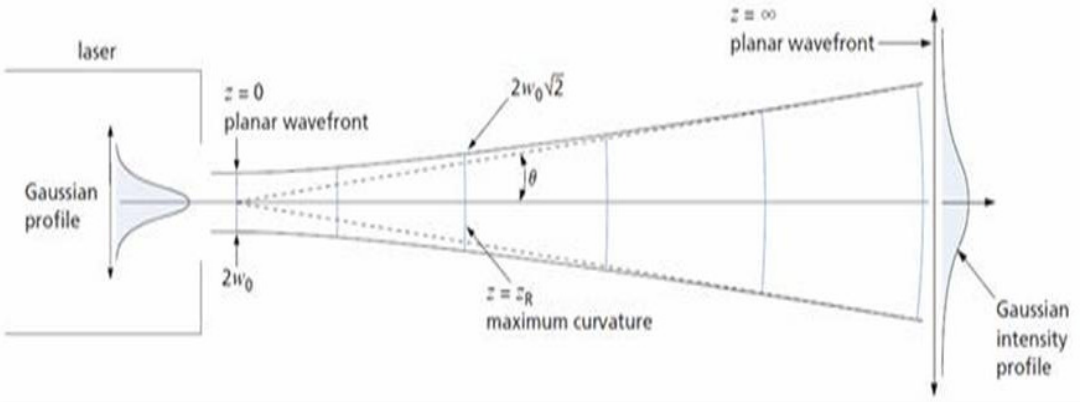

From eq. **(2.5)** one can see, that as *z* increases *R* also increases to some maximum value, then begins to decrease, but as z goes to infinity, *R,* again, increases and asymptotically approaches the value of *z*. As z becomes much larger than $\pi w_0/\lambda$, $1/e^2$ beam radius (eq. **(2.6)**) can be written as:

$$w(z) = \frac{\lambda z}{\pi w_0}. \qquad \textbf{(2.7)}$$

This is a far-field angular radius of the beam. Near the waist the divergence of the beam is small. When we want to characterize the distance on which beam is well collimated we use the Raleigh range parameter:

$$z_R = \frac{\pi w_0^2}{\lambda} \tag{2.8}$$

It is defined as a distance over which the radius spreads by a factor of $\sqrt{2}$ (see Fig. **2.3**). If the beam is tightly focused, as in our experiment, the Raleigh range can reduce to a few micrometers. Using this definition and eq. **(2.6)** we can relate the beam radius and z_R:

$$w(z) = w_0\left(1+\left(\frac{z}{z_R^2}\right)^2\right)^{1/2} \tag{2.6a}$$

and use eq. (**2.6a**) to balance the spot size and Raleigh range length. If the pulse is collimated initially and then is focused by a mirror or lens with a focal length *f*, then the collimated beam radius can be related to the focal length:

$$w = \frac{\lambda f}{\pi w_0} \tag{2.9}$$

In the experiment, knowing the wavelength, focal length and regulating the beam size, we can vary the waist width and make sure that the interaction between the target and laser pulse takes place inside the Raleigh range (Fig. **2.4**). [**24**]

Figure 2.4 Focal region of Gaussian beam

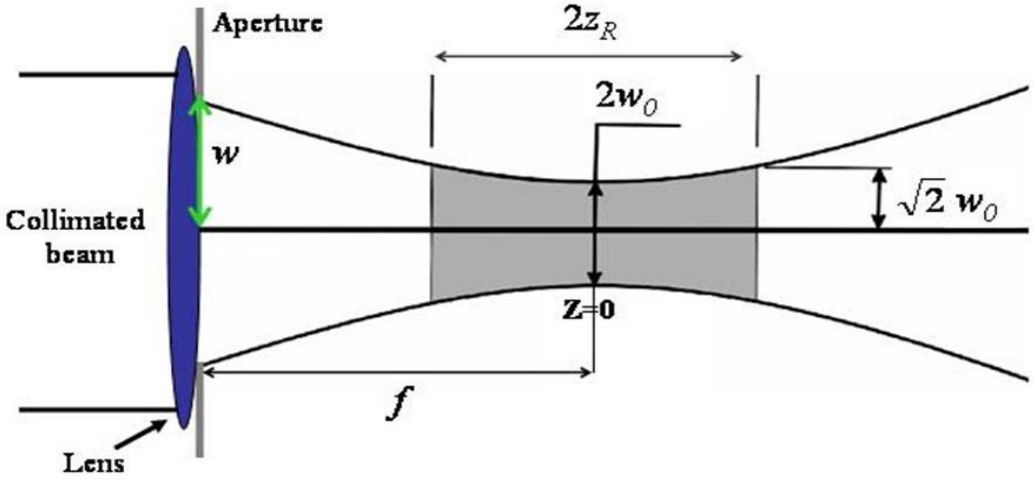

Pulse duration was confirmed with FROG (frequency-resolved optical gating) technique [**25**], as well as by autocorrelation measuring the ion yield inside the chamber, and checked during the experiment using the known proton kinetic energy release spectra from D_2 target [**19**]. The pulse duration of sub-ten femtosecond pulse is extremely sensitive to the chirp compensation. This sensitivity affects kinetic energy spectra of the fragments of Coulomb explosion produced by the pulse. After the pulse passes the chirped mirrors, a positive chirp can be slightly overcompensated and the pulse becomes negatively chirped. It is useful to have some negative chirp because on its way from the fiber to the target the laser beam passes through the air, necessary optics (beam splitters) and fused silica chamber window, all chirping pulse positively. To optimize the compensation of positive and negative chirp in our experiment we used the set of fused silica glass windows of different thickness (from 0.2 mm to 4 mm). Online monitoring of the change in deuteron kinetic energy release spectrum along with varying the total thickness of the fused silica glass in the laser beam path allows for fine-tuning of the chirp. The highest Coulomb explosion energy peak in kinetic energy release spectrum corresponds to the shortest pulse duration.

Two Germanium plates fixed at the Brewster angle (reflective polarizer) were used for controlling the total pulse energy by rotating polarization before the fiber.

In the experimental study COLTRIMS (see section **2.4**) technique in combination with pump-probe approach (section **2.2**) and Coulomb Explosion Imaging (section **2.3**) were employed.

2.2 Pump-probe technique

A pump-probe technique is a commonly used method for investigation of an ultrafast dynamics in molecular systems triggered by interaction with laser field. It is a way of recording a “movie” of the process under investigation by taking “snapshots” with a small time step. Two laser pulses are separated by some time delay. The first pulse, the “pump”, initiates some process in a system (molecule). Then the second pulse - the “probe” - monitors the property under investigation. Depending on the property that one wants to study and origin of the pulse, probe can excite, ionize, Coulomb explode the

molecule or diffract on the sample structure. In fluorescence life-time imaging the probe is employed to stimulate a fluorescent emission in a sample stimulated with the pump [**26**]. Absorption pump-probe spectroscopy monitors, for instance, relaxation dynamics of transient (short-lived) exited states in relevant molecules, which are accessible through absorption of photons of the probe pulse field [**27**]. Time-resolved photoelectron spectroscopy can be applied for measuring of the relaxation dynamics of the electronic states excited in large molecules and clusters by UV light. The probe pulse is used to ionize excited molecules and produce electrons and ionic fragments in the excited state which are collected afterward [**28**]. X-ray or electron bunch probes are applied in time-resolved diffraction experiments on the dynamics of phase transitions, functioning of biological cell etc. on the atomic time and length scale [**29**]. In our experiments pump and probe pulses are of the same duration and wavelength, but the pump pulse is usually weaker in intensity, so that it only excites a neutral molecule (for instance, in the experiment on rotational wave packet of a neutral hydrogen molecule) or removes one or two electrons by the field ionization. Probe pulse is strong enough to strip molecular ion of several more electrons leading to its immediate dissociation (Coulomb explosion) (Fig**. 2.5**).

The delay between the pump and the probe can be varied causing the evolving molecular ion to be exploded at different times after the dynamics was initiated. The resulting fragments can be detected and analyzed using, for instance, Coulomb Explosion Imaging technique, like in the experiments presented in this dissertation project. Coulomb Explosion Imaging technique is discussed in the following section.

Figure 2.5 Schematic drawing of the pump-probe approach. The pump and probe pulses are separated in time. Pump pulse initiate dynamics of a molecule or molecular ion. The probe pulse Coulomb explodes it after some time. Molecular charged fragments are carried to a detector by the uniform electric field

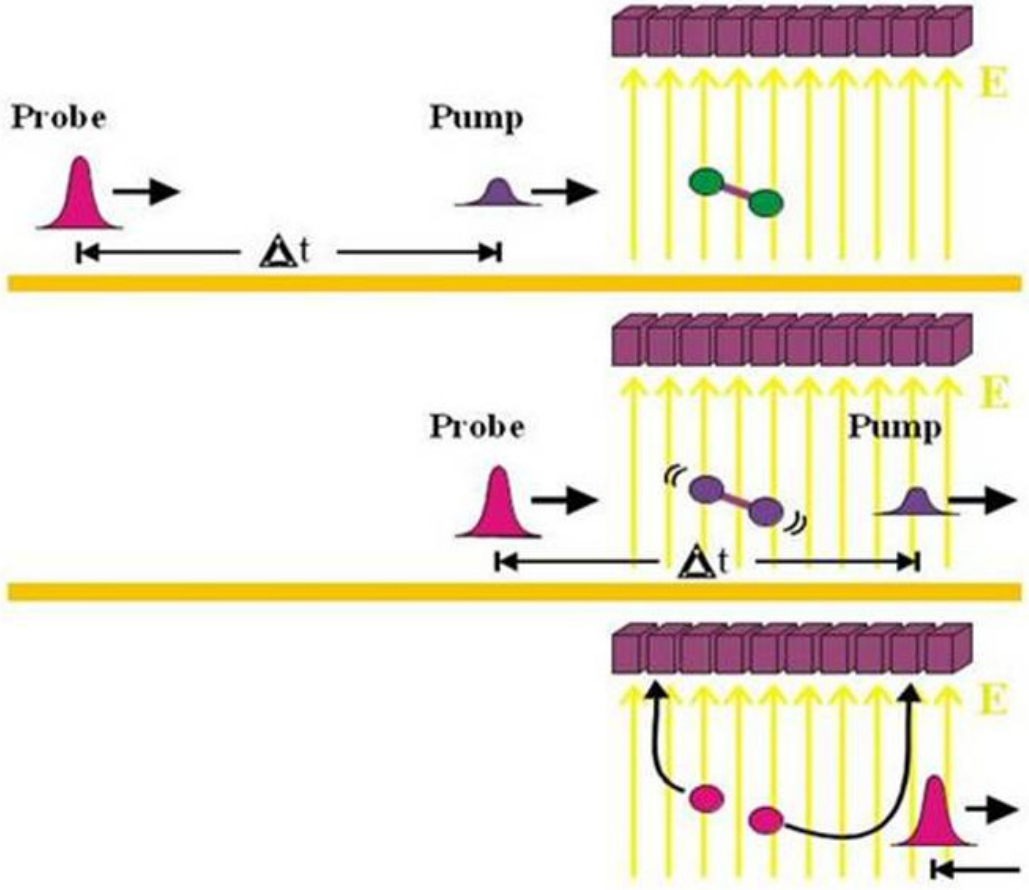

In our pump-probe setup we employ a Mach-Zehnder interferometer with a pair of broadband beam splitters (Femtolaser) to split one laser pulse into the pump and probe arms (Fig**. 2.6**). It is situated after the germanium plates and before the COLTRIMS apparatus (Fig**. 2.1**). An iris is placed in the pump arm of the interferometer to control the diameter and intensity of the pump beam. Reducing the diameter of the pump beam makes it weaker than the probe and also makes focal volume of the pump pulse larger than that of the probe pulse: it assures that only the "pumped" molecules are probed (Fig**. 2.7**). The pump arm of the interferometer includes a computer controlled piezo delay stage, therefore, we can scan over a wide range of delays with a time step as small as 1 fs. Zero delay corresponds to a situation when the pump and probe overlap in time. The target gas consists of neutral molecules. Initially, the electronic population distribution on

vibrational and rotational levels of the molecule depends on the temperature of the target gas jet (see section **2.4** and Appendix **A**). The pump pulse reaches the molecule first initiating the process one wishes to investigate. If the goal is to study vibrational or rotational nuclear dynamics in a neutral molecule the pump pulse intensity is adjusted to redistribute the population on rotational levels of the ground vibrational state or excite the molecule to higher vibrational states. In the studies of the nuclear dynamics of a particular molecular ion or the process of dissociation of highly charged states, the pump is employed to ionized molecule to the desired state. It initiates nuclear vibrational and rotational dynamics by transferring and redistributing the electronic population on the variety of energy surfaces of intermediate and final charge states. To map the evolution of the system using Coulomb explosion imaging one needs to make the probe pulse strong enough to ionize the molecule further to the highly charged states to produce Coulomb explosion (this requirement is discussed in section **2.3**).

Detecting charged fragments of the break up, we analyze them to recover the molecular structure and orientation at the moment immediately before the explosion.

Figure 2.6 Mach-Zehnder interferometer

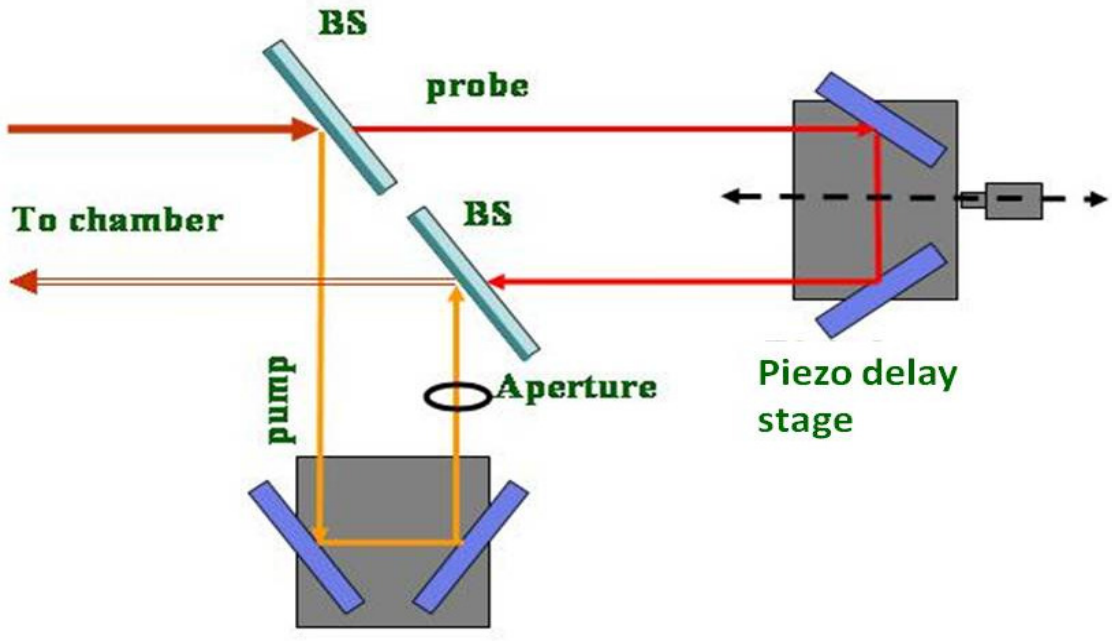

Figure 2.7 Schematic drawing of the pump and probe focusing

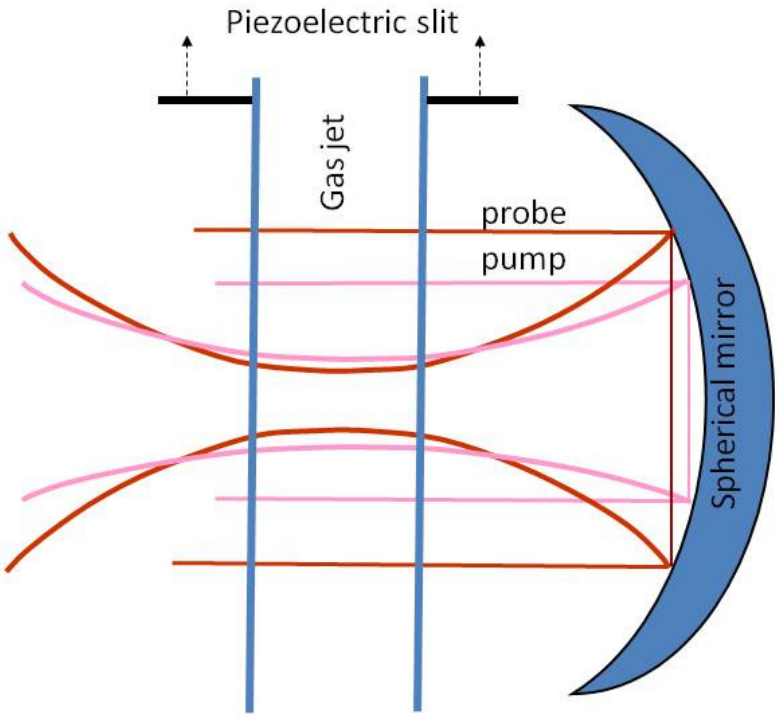

2.3 Coulomb Explosion Imaging

Most studies of molecular geometry are based on indirect observations by spectroscopic methods. We measure properties that reflect peculiarities of molecular structure, recording mass or energy spectra. The Coulomb explosion imaging (CEI) technique is an alternative to spectroscopy. It was developed (Kanter 1979) for direct studies of molecular structure. This method is based on the fact that when a molecule is stripped rapidly of several valence electrons, Coulomb repulsion of the nuclei triggers very fast dissociation (Coulomb explosion). By measuring final velocities of the fragments one can reconstruct the initial molecular geometry and orientation.

Originally the technique was developed for experiments on collisions of molecular beams with thin aluminum foil [**30**]. In the first CEI experiments molecular ion beam of MeV energy passed through a thin foil (~10 A). The projectile electrons are scattered to the large angles along with the electrons in the target solid film and separated from the projectile molecules. In Fig**. 2.8** the molecular ion beam consists of CH_4^+ ions. The process of stripping is faster (~ 10^{-16} s) than any characteristic motion of the nuclei, like vibration or rotation [**31**]. Starting from this moment, as time zero molecular ions dissociate fast: remaining positive ions repel each other. At this time the relative positions of nuclei for each ion in the beam will be different due to nuclear motion (vibration and rotation). Therefore, all information about this motion is contained in geometrical structures at time zero. All the explosion fragments can be captured and analyzed by an appropriate detector. The time evolution on a repulsive Coulomb potential can be easily traced. It means that measuring velocities in the center-of-mass system and relative velocities of all the ions provides us with all the information we need to reconstruct the 3D structure of a molecule.

Figure 2.8 A schematic view of a Coulomb explosion experiment. The figure is from Z. Vager et al. Science 244, 426 (1989) [30]. Fragments of exploded molecule are collected by a detector; time, x and y coordinates are measured and converted later into original molecular structure CH_4^+

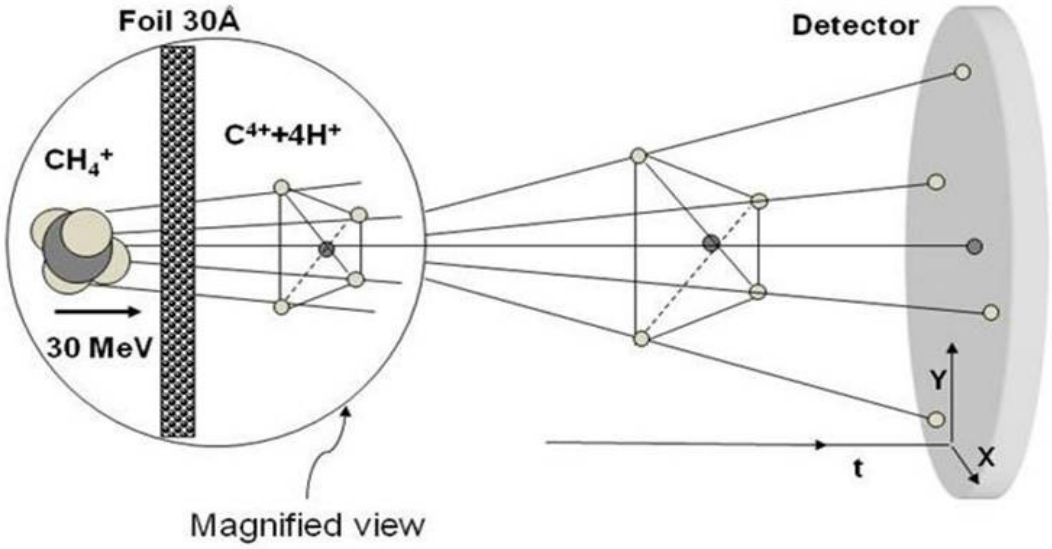

Center-of-mass kinetic energy before the explosion is usually negligible in comparison with Coulomb energy, and after the explosion all the Coulomb energy is transferred into the kinetic energy defined by final velocities:

$$\frac{4e^2}{\left|\mathbf{r}_c - \mathbf{r}_n\right|} = \frac{\mu\left|\mathbf{V}_c - \mathbf{V}_n\right|^2}{2} \qquad \textbf{(2.10)}$$

$\mathbf{V}_C$ and $\mathbf{r}_c$, $\mathbf{V}_n$ and $\mathbf{r}_n$ – are final velocities and position vectors of carbon and *n*th proton correspondingly. Interaction between protons is neglected. In such a way we can measure the vector $\mathbf{R}(i) = \{\mathbf{r}_C(i),\mathbf{r}_1(i),\mathbf{r}_2(i),\mathbf{r}_3(i)\}$ representing geometry of the *i*th molecule in the beam and thus obtain an image of the molecule. Measuring N such vectors we acquire statistics for calculating observables depending on structure.

As an alternative to the experiment of shooting a molecular ion beam through a foil, bombardment of molecules with highly charged ions to remove electrons had been used [**31**]. In these methods the electrons are removed in less than 1 fs, before heavy nuclei change their positions, as required to obtain an accurate image.

The CEI technique with the collision ionization described above, allow for measuring the equilibrium structure of small molecules, but it is difficult to adapt it to the

dynamic imaging. The advantage of the laser Coulomb Explosion technique is that it can be combined with the femtosecond laser pump-probe approach for time-resolved studies of molecular dynamics.

Nowadays scientists use intense laser pulses to Coulomb explode neutral molecules and ions. In order to apply the method correctly one should take into account several requirements.

1) The ionizing pulse must be short enough to freeze the positions of the nuclei at the explosion time. For such a light molecule as D_2 one vibration of nuclei on the $X^2\Sigma_g^+$ potential of molecular ion D_2^+ takes only about 20 fs. In [**32**] F. Legare et al chose to study a nuclear motion in two molecules D_2 and SO_2 to demonstrate the capability and advantages of the time-resolved CEI technique. The deuterium molecule is challenging because of its extremely fast dynamics. SO_2 was chosen to demonstrate the ability of the technique to image multiple dissociation channels, including imaging of intermediate unstable ions which are hard to measure using any other available technique. The structure of the D_2 molecule was studied with 8 and 40 fs pulses. The authors demonstrate that to map the equilibrium D_2 geometry measuring kinetic energy release fragments of deuterons resulting from CE 8 fs or shorter pulses are needed.

2) The reconstruction of geometry relies on the fact that a known Coulomb potential describes the interaction of the charged particles during the explosion. For it to be a good approximation, we must ionize molecules to highly charged states. There are several studies dedicated to investigation of an effect of non-Coulombic states of highly charged ions on dissociation of molecules. [**33-35**]. The model suggested by Hill et all [**33**] shows that true Coulomb explosions will only occur for AB^{Z+} for $Z \geq 4$ and only for intense pulses with rise times short enough to reach these highly charged states before the molecule completely dissociates on the non-Coulombic curves. Even if Coulombic states are accessed before the fragmentation occurs, the dissociation energy is reduced when the time between ionizations is long enough to let the molecule expand on a non-Coulombic curve. The requirements on pulse duration depend on the specific molecule. C. P. Safvan and D. Mathur [**34**] calculated center-of-mass kinetic energy release KER_{calc} for dissociation of various N_2^{q+} ($q = 2 \div 12$) ions using LCAO-MO method (see section **3.1.1**). Comparison was made with KE_{Coul} – energy values expected in case of

dissociation on purely Coulombic curves. For q = 3 the deviation of KER_{calc} from KER_{Coul} is 36.5% and it does not show clear tendency of going down with higher charged state, but rather stays in the interval form 15 to 37 % up to q = 8. The authors conclude that only for q ≥10 the deviation of real potential from Coulombic drops below 10%. Theoretical work of Bandrauk et al [**35**] is dedicated to studies of low-lying potential energy curves of the triply charged nitrogen molecular cation. All states were found to be repulsive and pure Coulombic for internuclear distance larger than 5 atomic units.

3) The interaction between the laser field and the molecule must not affect the measurement process: only Coulomb repulsion accelerates the nuclei [**36**]. In this way electronic potentials of molecules and atoms under investigation are the same as the field free ones.

4) All the fragments of explosions occurred in the region of laser and target gas interaction are collected by detectors and the pairs of ions (in case of two-fragment break up) are sorted in the true and false coincidence. The procedure of determination which two fragments originated from the same molecule is based on momentum conservation law (see section **2.5**). To improve the ratio of true to random coincidences it is crucial to reduce the number of explosions per pulse to one or less. This requirement puts restrictions on the laser focus size and molecular jet density: tight focus and diluted target must be provided in order to explode not more than one molecule per laser pulse.

Comparing to classical spectroscopic methods, which give detailed information on equilibrium structure of neutral molecules, Coulomb explosion imaging has a great advantage of being compatible with femtosecond pump-probe technology. This combination of the two techniques allows for imaging of excited states and structural changes during molecular ultra-fast dynamics.

In [**32**, **10**, **37**] it was demonstrated that it is possible to use the pump-probe technique and CEI to study the time-dependent structure of diatomic and triatomic molecules undergoing dynamics with a sub-bond length resolution. Only the Coulomb explosion imaging allows a complete molecular structure and orientation to be obtained from each fully detected explosion. This imaging capability can be used to follow complex molecular processes, including molecular rotations, symmetric and asymmetric dissociation, isomerization, excitation, bond breaking and formation and so on.

2.4 COLTRIMS technique and apparatus

Recoil Ion Momentum Spectroscopy (RIMS) techniques for investigation of any kind of atomic or molecular reactions (e.g. interaction with electron, ions or photons) in which target charged fragments emerge, has been developing since early 1990s. The first goal was to measure multiple ionization and capture cross section for fast (1.4-5.6 MeV) heavy ion-atom collisions in projectile scattering angle [**38**]. The deflection of the projectile was very insignificant (a few μm over 10 m), therefore, the intention was to extracts the transverse momentum transferred to the projectile during collision by measuring the momentum of the recoil. The known spectroscopic methods were suffering from lack of resolution and low count rates which restricted studies to certain kinematical conditions like measuring particles emerging in one plane or a very narrow solid angle. The possibility of kinematically complete measurements is crucial for studying of many reactions. Kinematically complete means that the momenta (energies and angles) of all involved particles can be measured in coincidence, only spin is not determined. This kind of measurements gives unique information on the dynamics of reactions [**38**].

At first, the idea of recoil ion momentum measurements in collision reactions ran into a problem of immeasurably small relative momentum change during reaction. In target gases at room temperature atom has such a large initial momentum spread that it exceeds the momenta gained after collision. For fast charged particles collisions and photoionization the product energies can be of the order of meV and even lower. Before the first RIMS spectrometer only charged states distribution was possible to measure for such low energy ions, using time-of-flight spectrometer or magnetic deflection. The first spectrometer for momenta and angles measurements of slow recoil ions combined the time-of-flight and magnetic deflection techniques. Ulrich et al [**39**] in 1987 succeeded in measuring of transverse recoil ion momenta with a solid angle of a few percent in collision of 340 MeV U^{32+} on Ne. They used a static room temperature gas target. The next improvement was a cooled to 30 K gas cell, which allowed for coincident measurements of a recoil ion and projectile transverse momenta; and warm effusive jet in combination with the extraction electric field for measuring first recoil ion longitudinal momentum distribution in 4π solid angle (references in review paper [**38**]). In 1991 the first spectrometer based on supersonic gas jet targets was built [**11**]. The temperature of

such jet can go lower than 1K and resolution of momentum measurement is limited not by the thermal distribution but by the extension of the target in the spectrometer. The new spectroscopy technique was later generalized for electrons as well.

As a result of many improvements, nowadays we have the COLTRIMS (COLd Target Recoil Ion Molecular Spectroscopy) technique, which is often referred to as the "reaction microscope". The COLTRIMS technique combines advantages of a supersonic cold jet of target gas, well localized reaction zone, position imaging, coincident measurement technique, large area detectors and multi-hit detection of charged reaction fragments. Using internally cold supersonic jet, focusing geometry and electrostatic extracting field the measuring of complete momenta of reaction products emitted into full 4π solid angle with a resolution of a few per cent of an atomic unit became possible [**11**].

The COLTRIMS apparatus is the next element of the experimental setup on Fig. **2.1**. The interaction between laser beam and target molecule takes place inside the vacuum chamber. The chamber is equipped with the COLTRIMS spectrometer and a supersonic molecular jet.

The whole vacuum system includes a source chamber, two intermediate chambers, main (interaction) chamber and a catcher (Fig. **2.9**). In order to obtain a supersonic jet, target gas is expanded into the lower pressure chamber through a 30 μm nozzle (to reach a supersonic speed the ratio of pressures on the two sides of the nozzle must be larger than 2 [**38**]). The gas jet is geometrically cooled by expansion into the next chamber through a skimmer 0.5 mm wide. The next two intermediate chambers are separated by a 2 mm aperture. Each of the two stages is differentially pumped to reduce the background. The gas enters the interaction chamber through the externally controlled piezoelectric slit. The transverse diameter of the jet (in the direction perpendicular to the spectrometer axis) can be manipulated with this voltage controlled slit in the range from 1.5 mm to 40 μm. Ability to produce a thin jet is important because in this case the interaction volume can be made very small. It means that we can confine the interaction to the high intensity region in the laser pulse with the Gaussian waist w_0 of 5-10 μm and also control the number of molecular fragments produced by a single laser shot.

Figure 2.9 Schematic of the experimental setup vacuum system. The figure is from C. Maharjan. PhD dissertation. Kansas State University (2007)

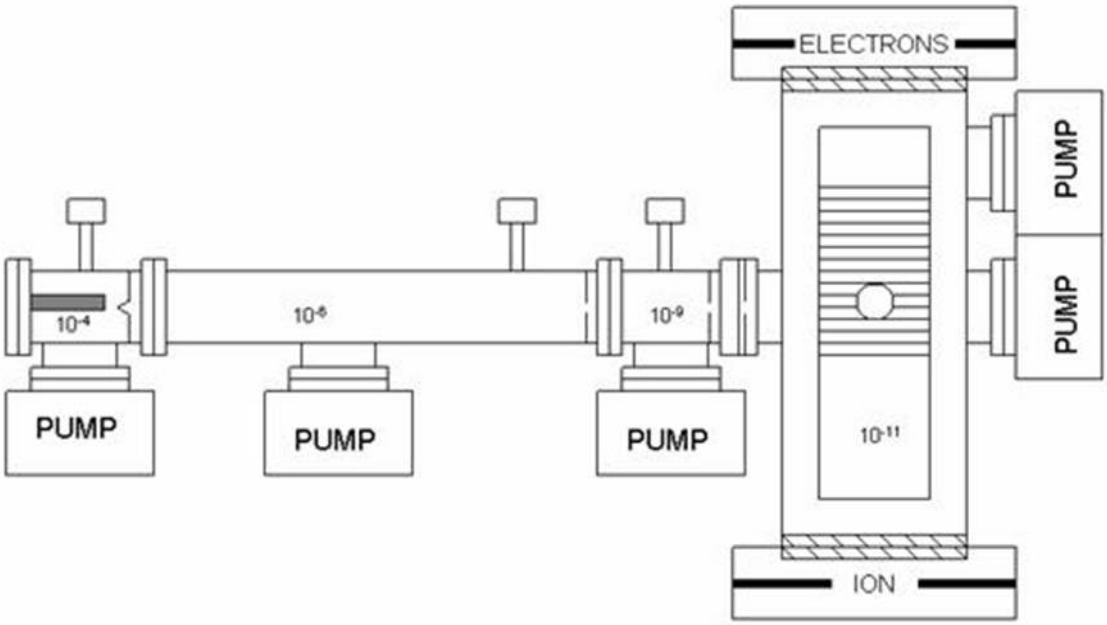

After passing through the main chamber, gas is collected by the catcher and evacuated by another turbo-pump to prevent its spreading inside the main chamber and increasing the background pressure. As a result, the background pressure in the main chamber is maintained below 10^{-10} Torr. With the jet present, it typically rises up to $2x10^{-10}$ Torr. The pressure in the jet is typically of the order of 10^{-7} Torr in the interaction region. After passing through the system of the nozzle, skimmer and two slits, the gas jet is internally cold and collimated. A part of the thermal energy is converted to a kinetic energy of the directional gas flow and various degrees of freedom are cooled to different extent. Cooling of the internal degrees of freedom is important to reduce complexity of vibrational and rotational spectra in the targeted molecule. The translational temperature of the jet defines the momentum resolution in the experiment because in the data analysis we assume that the target had zero momentum before the explosion. The translational temperature was estimated in our chamber by measuring a velocity distribution for molecular ions and fitting Maxwell-Boltzmann distribution to it (see Appendix **A**). The special property of the supersonic flow is that it increases velocity with the distance and collisions which occur during this process make the speed of a molecule directed along

the gas flow: the transverse momentum is converted into longitudinal due to the expansion [**40**].

To reach intensities as high as 10^{13}-10^{16} W/cm^2 needed for our experiments, laser energy has to be concentrated in a small region. For that purpose the laser beam is tightly focused by spherical mirror (25 mm diameter, 75 mm focal length) located inside the spectrometer just behind the interaction region. The holder is mounted on a 3D translational stage with an external manual control. It provides the possibility for the best adjustment of the overlap between the jet and the laser focus. We determined the laser peak intensity by first calibrating it using the method described in [**41**]. It is based on measuring momentum distributions of ions produced by a circularly polarized light.

Figure 2.10 COLTRIMS spectrometer picture. The figure is from C. Maharjan. PhD dissertation. Kansas State University (2007)

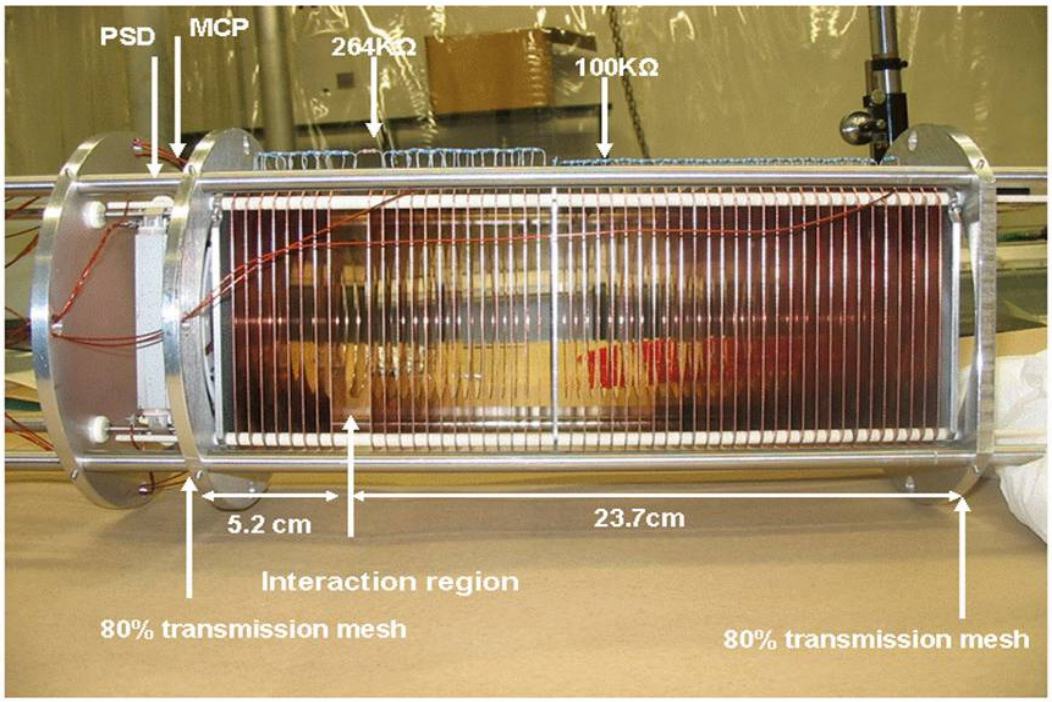

The COLTRIMS spectrometer is a standard parallel-plate spectrometer: it consists of a series of copper plates, with holes in the middle, connected by resistors and separated by a narrow gap to provide an isotropic constant electric field, with a wider gap in the interaction region. The spectrometer is terminated by the 80% transmittance grids used to minimize electrostatic lens effect (Fig. **2.10**). Electric field separates and accelerates positively and negatively charged fragments to corresponding detectors on the left and

right sides of the spectrometer. For positive fragments (ions) the voltage applied across the spectrometer is adjusted so that it is high enough to drive fragments with all possible energies over the flight distance of 5 cm to the detector; collect fragments in 4π solid angle; the ions do not spread outside the detection area; and low enough to provide good peak resolution on the time-of-flight spectra.

The spectrometer is positioned so that its extraction direction is perpendicular to both the direction of laser beam propagation and the gas jet.

Figure 2.11 Schematic view of the COLTRIMS spectrometer with a detector on the ion side. The figure is from S. Voss et al. J. Phys. B 37, 4239 (2004) [42]

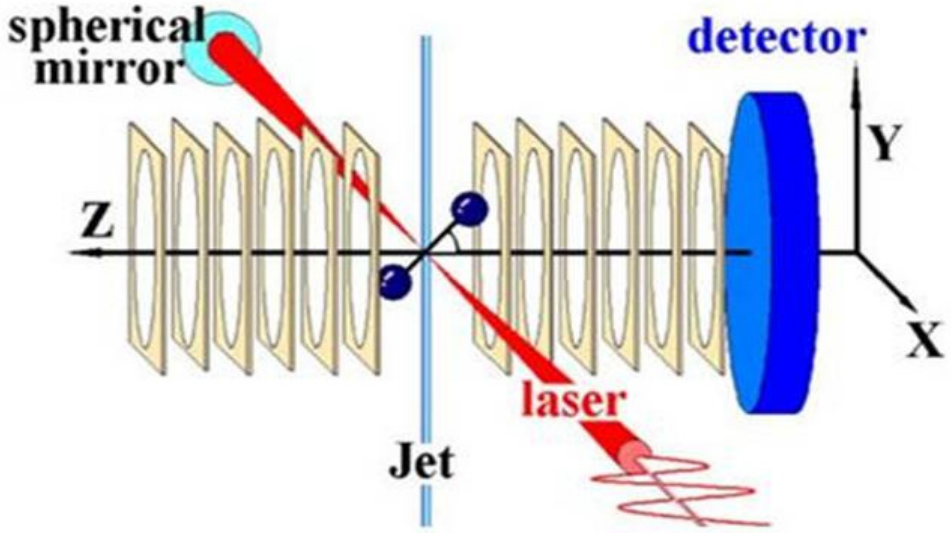

2.5 Data acquisition

Figure 2.12 Drawing of position and time sensitive detector: delay anode line and micro channel plates. The figure is from T. Osipov. PhD Dissertation. Kansas State University (2003) [43]

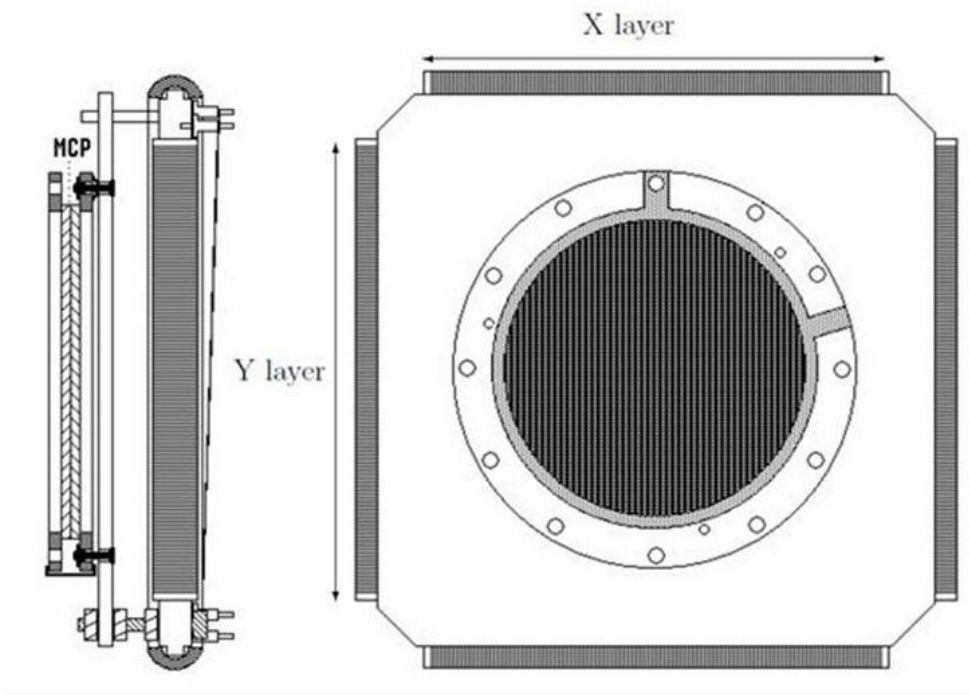

The detectors we use to collect charged fragments are time and position sensitive detectors consisting of micro channel plates (MCPs) and 80 mm square RoentDek delay-line detectors (PSD – position-sensitive detector) (Fig. **2.12**). On the short side, used for ion detection, MCPs and PSD are located approximately 5 cm away from the interaction region. The front side of the MCP double stack is biased with 2.1 kV negative potential and the back side is grounded. The extracting voltage across the spectrometer is varied, depending on the type of fragments one wants to collect and their kinetic energy, between 10 and 4000 V. The potential applied to the transmission grid on the short side is negative and the grid on the other side of the spectrometer is grounded. Thus, a positive ion, emerging from the spectrometer, undergoes a very brief acceleration before hitting the MCP. Each fragment reaching the multichannel plates sets off an avalanche of electrons amplifying the charge of the impacting particle to the level that can be registered by

available electronics. At the same time this current is used to measure arrival time of the particle (stop time) to the detector.

A position-sensitive delay-line anode detector is capable of detecting 2D positions of ions, which are energetic enough to induce the electron avalanche in MCP. Position resolution can be less than 0.1 mm with proper electronics. It has a multi-hit capability with a pulse pair resolution of less than 10 ns. The delay lines are double wires wound in X and Y directions around a ceramic frame. One wire is a "signal" wire and the other is a "reference" wire. Positive voltage (~250 V) is applied to the signal wire, which is about 50 V higher than voltage applied to the reference wire. Thus, only the signal wire gets the electron signal and the two wires are close enough to pick up the same electric noise. The signals from both wires are subtracted in the differential amplifier eliminating the electric noise. The principle of extracting 2D positions from delay-line signals is based on time delay of signals traveling in wires (Fig. **2.13**).

Figure 2.13 Principle of the positions detection. The figure is from T. Osipov. PhD Dissertation. Kansas State University (2003) [43]

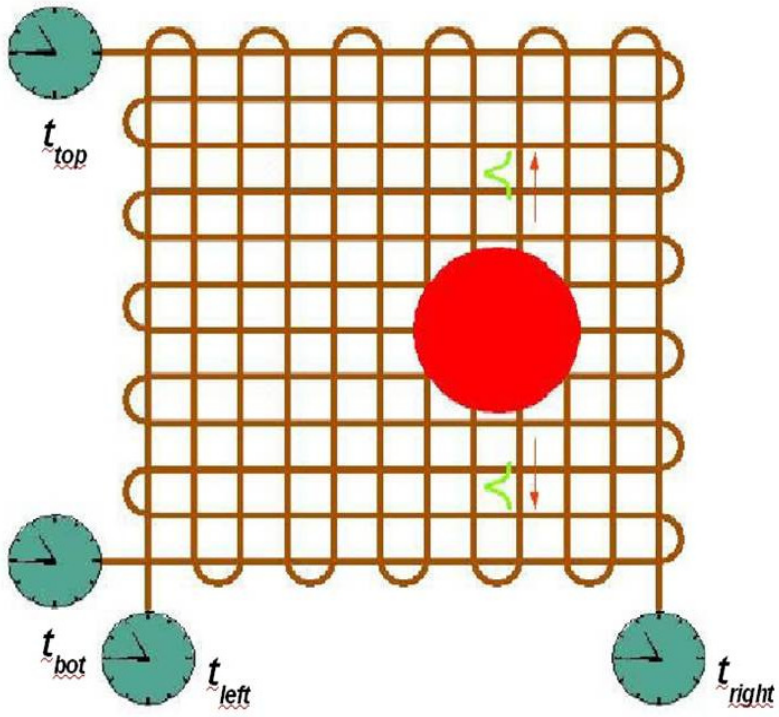

The electron avalanche produced in the MCP hits the wires and creates a charge traveling in X and Y wires to the both ends of each wire. The X or Y coordinate of the hit

is proportional to the time it takes for signal to travel to the end of the wire. The signals from both ends of one wire are used to determine the position:

$$X = k\,(t_r - t_l);\ Y = k(t_t - t_b) \qquad \textbf{(2.11)}$$

where t_r, t_l, t_t, t_b are the times of arrival for signals from right, left, top and bottom ends of X and Y wires; k is the conversion constant in mm/ns determined by the detector calibration.

It is also important to make sure that X and Y signals of the hit, which determine the position, are put into correspondence with correct time signal from the MCP, which determines the time-of-flight. For that purpose the value of time-sum is used. If t_{mcp} is the MCP time of hit then $(t_r - t_{mcp})$ is the time it takes for signals to get from the hit position to one edge of the detector. Then X and Y time-sums are defined as

$$ts_X = (t_r - t_{mcp}) + (t_l - t_{mcp}) = t_r + t_l - 2t_{mcp}\ ; \qquad \textbf{(2.12a)}$$

$$ts_Y = t_t + t_b - 2t_{mcp} \qquad \textbf{(2.12b)}$$

These are the times it takes for signals to travel across the whole detector wire. This value is constant and can be calculated as length of the corresponding wire divided by the speed of light. If for each hit we check that this condition is true for the collected signals then we can filter out signals due to noise.

All the raw signals go through the constant fraction discriminator (CFD) unit before being fed to the digitizing electronics. CFD produces NIM pulses – standard negative logic signals of ~10 ns width. This unit is serving the purpose of producing accurate timing information from analog signals of varying heights but the same rise time. The incoming signal is split in two, one of which is attenuated, inverted and delayed. Then both signals are added together and the effect is that the timing of the zero level crossing point is independent of the initial signal height. The NIM signal is triggered at this crossing point which always corresponds to a constant fraction of the input amplitude (usually set at 20%).

To digitize all multi-hit signals coming from MCP and PSD the following electronics setup was used. A 32-channel Multi-Hit Time-to-Digital-Converter (LeCroy 3377 TDC) capable of registering up to 16 hits per channel is an important component. It

has 0.5 ns timing resolution and 8 to 32 μs time range per event. Thus, position resolution, time-of-flight resolution, as well as the time-of-flight range, are defined by the TDC. The pulse-pair resolution for each TDC channel is determined by the width of raw signals from the detectors. In our experiment pulse-pair resolution is 10 ns meaning that if two ions hit the detector within 10 ns then only one is registered and the position information is not quite reliable. The TDC can collect up to 16 hits per event from one detector separated by more than ten nanoseconds. The time range can be set according to the time-of-flight of the slowest ion in events up to 32 μs.

The data acquisition system is initialized with a start laser signal from photodiode located right outside the COLTRIMS chamber. This signal serves as a bunch marker for TDC – start point for converting an MCP signal into the time-of-flight; it sets the time window for TDC depending on mass and charge of the particle to be detected; it triggers the process of data transfer to the computer. Once triggered, the TDC records all the hits in a set time window of up to 32 μs.

2.6 Data analysis

LabVIEW software by National Instruments was used for the computer/CAMAC-crate communication, data collection and online data analysis. Further off-line analysis was performed using FORTRAN programs written by Timur Osipov [**43**] and PAW software by CERN.

The FORTRAN code we use to analyze the data, performs calculations and creates files with final results to be presented in form of plots and diagrams in PAW. This code contains a subroutine, which is called by the main program for each event. An event is a block of data from a single discharge of the TDC, meaning that it is the information on all hits recorded in a 32 μs interval following each laser pulse. We define our experimental parameters, like the spectrometer field, masses and charges of the fragments and so on in this subroutine. It also contains all the equations for calculating the experimental values we plan on extracting form our data. This particular part of the program is presented in Appendix **B**.

Figure 2.14 Momentum conservation for the ions, resulting from Coulomb explosion of a single molecule. Velocity of the center-of-mass of the ions in Z direction considered to be negligibly small compared to the fragments velocities

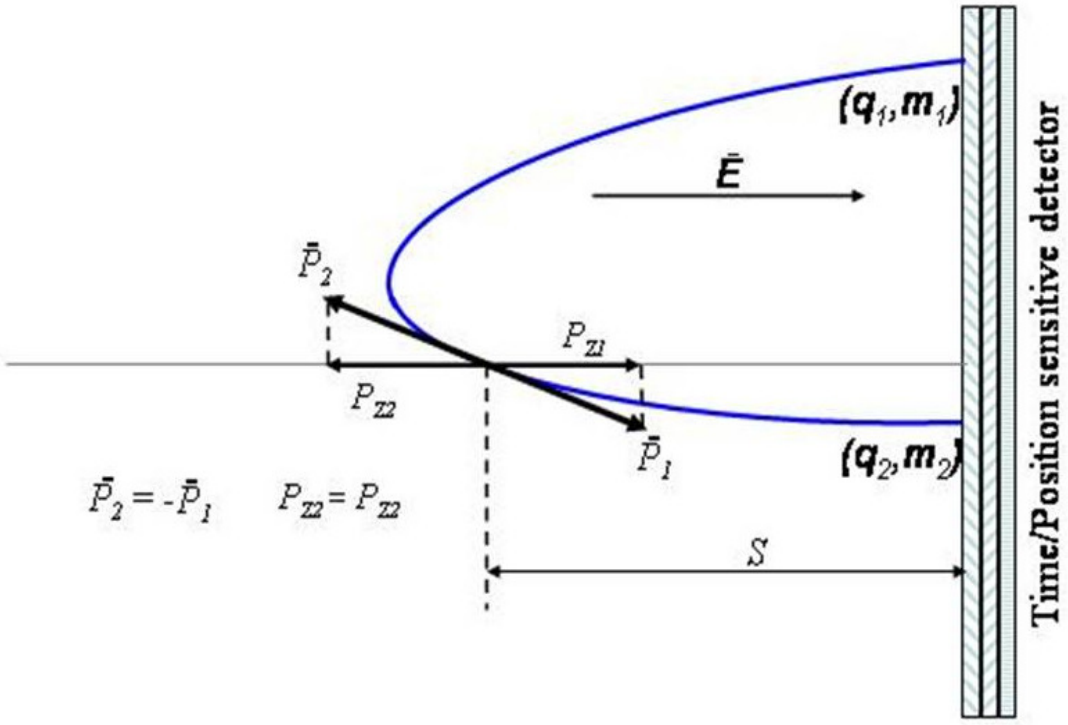

The important step in the analysis is the reconstruction of three-dimensional momenta of the ions in coincidence. Having the timing (TOF) and position (X,Y) information and the experimental parameters like the spectrometer electric field *E*, distance from the interaction volume to the detector *S*, particle charge *q* and its mass *m* we can use classical equations for accelerated motion to find the momentum vector components:

$$P_Z = \frac{mS}{t} - \frac{Eqt}{2} \qquad \textbf{(2.13)}$$

$$P_X = \frac{mX}{t} \qquad \textbf{(2.14)}$$

$$P_Y = \frac{mY}{t} \qquad \textbf{(2.15)}$$

Here electric field is parallel to the Z-axis (spectrometer axis, time-of-flight axis). Time in these equations is actually the difference between TOF (which is the STOP signal from

the MCP) and photodiode signal (START) with a small correction on signal travel time in the cables. Positions are found relative to the detector image center. A typical detector image for D^+ fragments and its projections for finding the exact center are presented in Fig. **2.15**. This way of presenting data is called an intensity map or density plot. This is a three-dimensional plot in which the color scale serves as the third dimension. For instance, on the particular map, Y coordinate is plotted on the vertical axis, X coordinate is on the horizontal axis and the number of ions (ion yield) having each particular (X,Y) pair of coordinates is reflected by color of the point on the XY plane. Color scale is shown on the side of the plot. The scale can be linear or logarithmic. Value of the magnitude goes up with the color from blue to bright yellow.

If we wish to perform the analysis for the fragments in coincidence, in other words, analyze ions originated from the same molecule, we use gating on the total momentum versus kinetic energy release intensity map (Fig. **2.16**). Kinetic energy release KER is the sum of kinetic energies of the explosion fragments. The atomic ions originating from the Coulomb explosion of the same molecule are subject to the momentum conservation. In Fig. **2.16** only fragments forming the "blob" inside the white rectangle are the real coincidences because their momenta add up to near zero. The reason why the momenta do not sum exactly to zero is that the molecular ions acquire a small momentum of the order of an atomic unit from accelerating laser field following each ionization, which is not accounted for in the momentum conservation law for the atomic fragments. Therefore, the higher the charged state of the exploding molecular ion is, the greater momentum it acquires from the laser, and the further the "blob" is from the vertical axis. The width of the laser-induced momentum distribution in combination with the momentum distribution of the center-of-mass of exploding molecule also defines how wide the "blob" is in a horizontal direction.

Figure 2.15 Detector image for D^+ ions. Projections on X and Y axes are taken to find exact image center

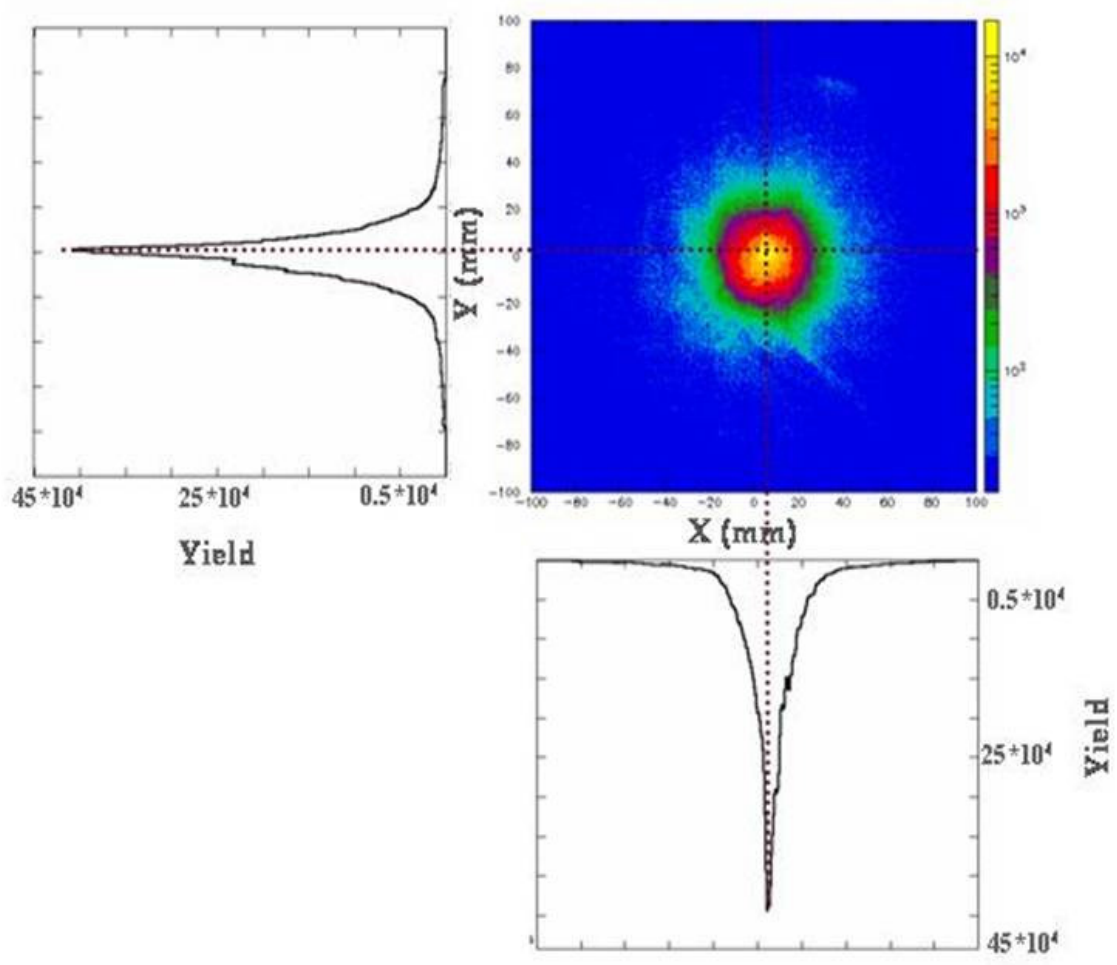

Figure 2.16 Kinetic energy release versus total momentum for the fragments of hydrogen molecule Coulomb explosion

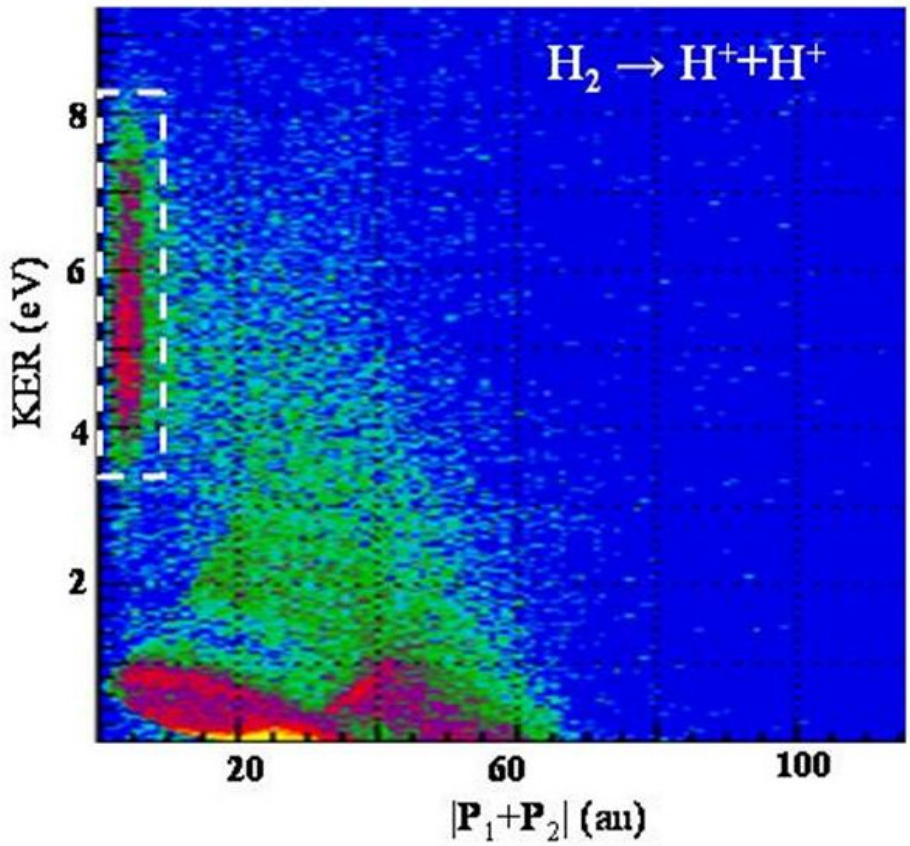

All possible two-body molecular fragmentation channels in the Coulomb explosion experiment can be identified on the Photoion-Photoion-Coincidence (PIPICO) spectrum. PIPICO spectrum is an intensity map plot with the time-of-flight for each of the two ions plotted on horizontal and vertical axis. The times-of-flight (TOF) are defined by initial velocities of the ions in the lab frame, not center-of-mass frame. Typical TOF spectrum for D_2 CE experiment is shown in Fig. **2.17**. The quality of our cold jet allows us to assume that before the fragmentation the center-of-mass momentum in transverse direction is negligibly small compared to the momenta achieved by the fragments. The width of the coincidence features (stripes) is defined by the same factors that the real coincidence feature in Fig. **2.16**. In addition to the sharp bright stripes in Fig.**2. 18 (a**), one can also see a rich false coincidence background. The majority of the points on the picture are random coincidences. As we can see, the background of random coincidences makes the real features of the plots look much less clear. To "clean" the experimental

spectra we added "background subtraction" as a part of the main code (Appendix **B**). The idea was to create an array of random coincidences and to subtract it from the array containing both false and true coincidences. This idea was implemented by "saving the memory" of the previous event to be able to use it when analyzing the next one (Appendix **B**, lines **279-284**). If we create an array, consisting of pairs of hits coming from two consecutive events it will be the array of false coincidences, because no two ions from the same molecule can arrive in two different events (Appendix **B**, lines **137**, **142**, **143**). As a result of subtracting this array from the one containing all the coincidences from the current event we obtain a clean spectrum with sharp features which is presented in Fig. **2.18 (b)** with all dissociation channels labeled.

Figure 2.17 Time-of-flight spectrum for D_2 molecule, Coulomb explosion experiment. Narrow peak represents D_2^+ molecular ion

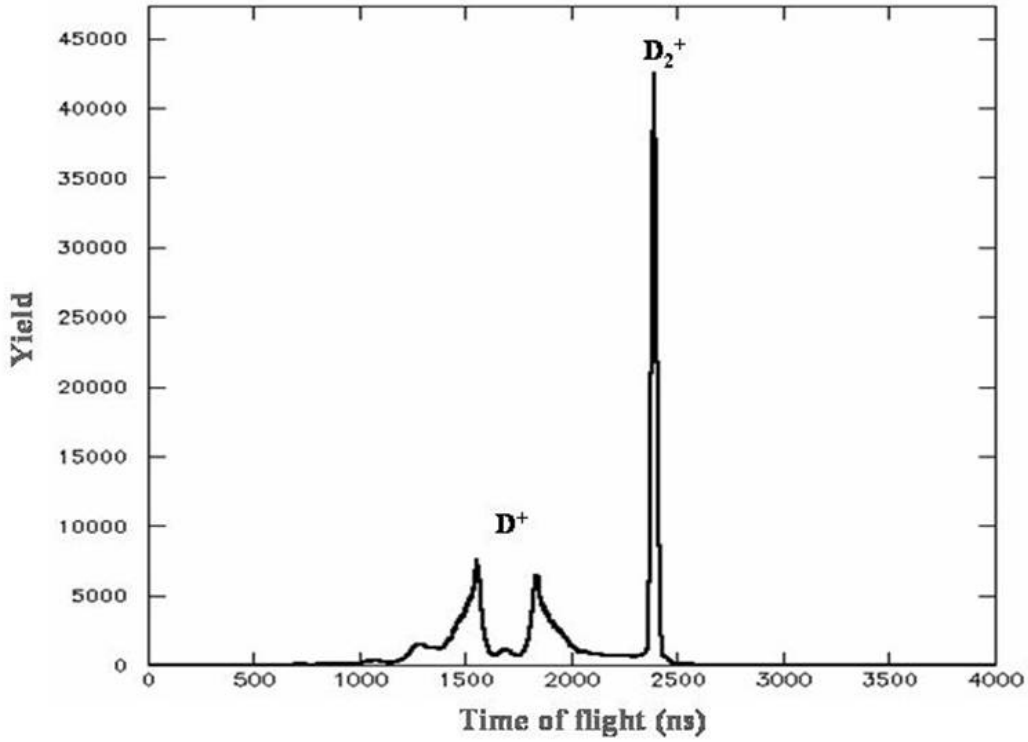

Figure 2.18 Photoion-Photoion-Coincidence spectra for the Coulomb explosion of N_2 experiment: vertical and horizontal axes are time of flight of the first and second ion from each pair of registered ions. (a) Bright traces are the real coincidences and background is random pairs of ions, originated from different molecules; (b) background reduced by subtracting an array of random coincidences. This array is created from pairs of ions from two different events.

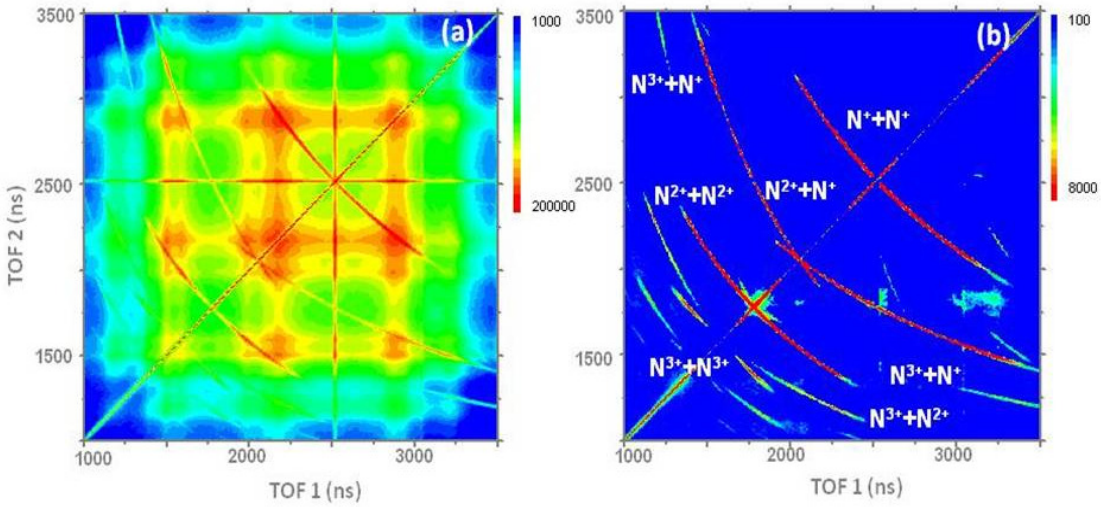

In the course of analyzing the data we plot the results as two-dimensional histograms or density maps and set axes binning in a certain convenient way. Every parameter changes stepwise and axes binning cannot be perfectly matched with the measurement discretization due to the discrete TDC digitizing. This slight mismatch accumulates through several binning steps shifting the measurement point to the border of a bin. It finally brings us to the case when two measurements for two consecutive steps correspond to one bin and the next bin is missing a measurement. As a result we may have regular gaps in our plots like those shown in Fig. **2.19(a)**. To overcome this problem in the code we added a small random number to each of five signals coming from the TDC (Appendix **B**, lines **82**, **86**, **90**, **94**, **98**) and it assures that the mismatch is not constant anymore and does not accumulate in one direction (see Fig. **2.19(b)**).

Figure 2.19 Detector image (a) before and (b) after eliminating of the measurement discretization and binning mismatch

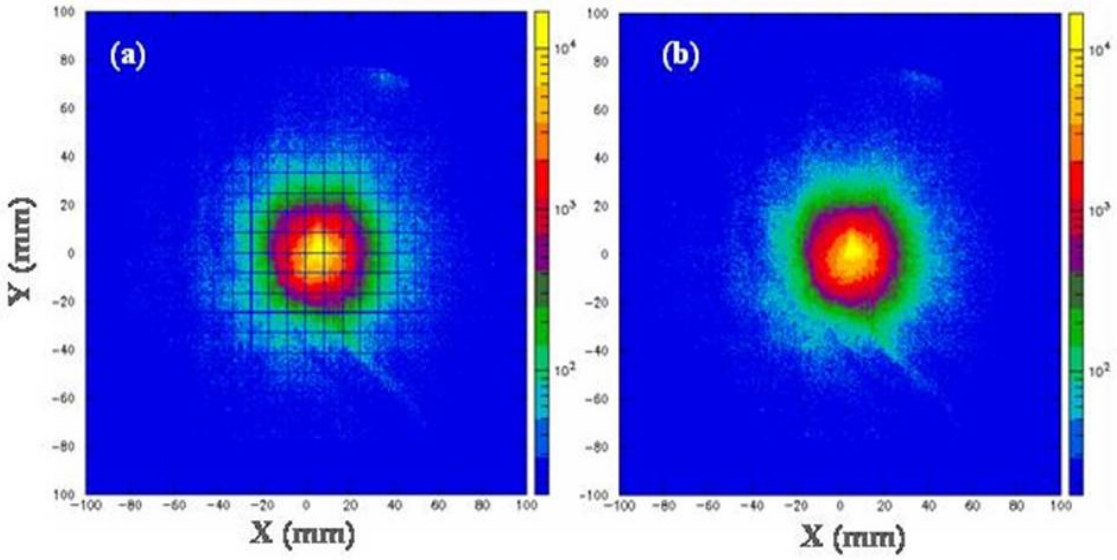

As we analyze the results of a pump-probe experiment we plot some observables as a function of the delay between pump and probe pulses. For instance, we create KER versus delay density maps. At the time of recording data files, during the experiment, the delay translation stage does not go from one delay to another after a certain time interval. It is rather moved to the next step after a certain amount of data is collected. It means that a number of laser pulses can be different for different delays (see Fig. **2.20**). On diagrams like KER vs delay Fig. **2.21(a)**, this effect superposes with density variation reflecting real physical phenomena by adding color scale variation depending on number of laser shots per delay step. Therefore, the diagram needs to be normalized to the number of laser pulses. Each laser pulse triggers the photodiode, therefore the number of pulses can be counted in the code by counting photodiode signals. To plot the histogram presented in Fig. **2.20** at each delay a unit is added to previous count of laser pulses for every photodiode signal (Appendix **B**, line **75**). Normalization is done by the means of PAW++ software. The KER vs delay density plot, is divided by the diagram in Fig. **2.20**, which simply means that each value on z-axis, representing ion yield at a certain delay, is divided by the number of laser pulses at this delay. The normalized KER vs delay plot is shown in Fig. **2.21 (b)**.

I have described the main features of the experimental setup, the techniques that we employ in the experiments and the most important aspects of data acquisition and analysis. The next chapter presents the background of the conducted experiments.

Figure 2.20 Number of laser pulses as a function of delay between pump and probe. Data is not collected for an equal amount of time for each delay step

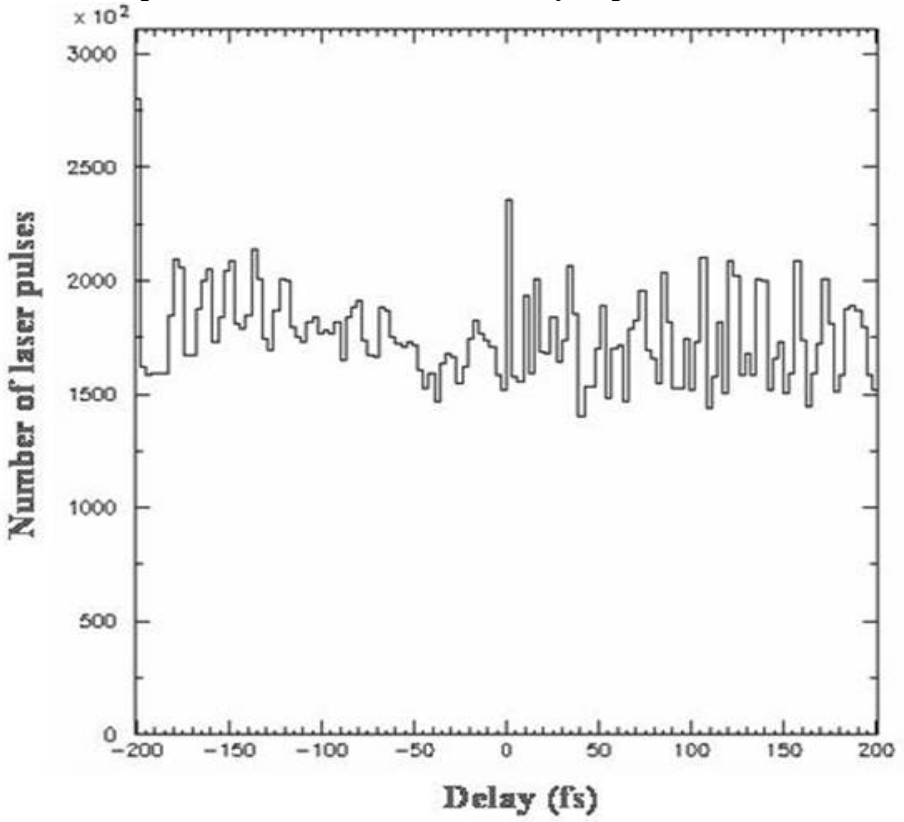

Figure 2.21 Kinetic energy release as a function of time: (a) spectrum is not normalized to the number of laser pulses per delay; (b) normalized spectrum

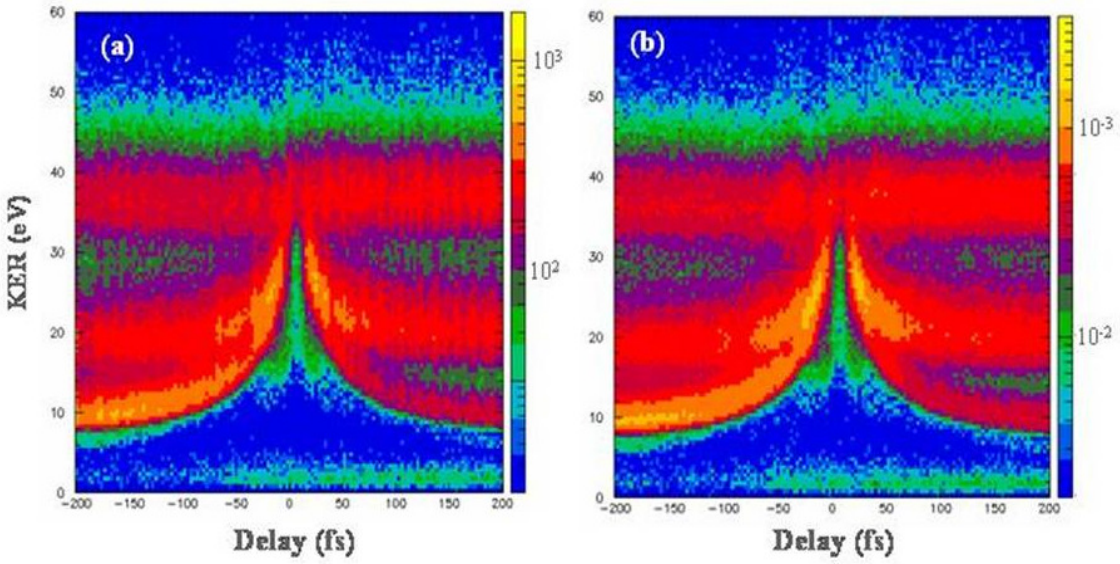

CHAPTER 3 – Background

In this chapter some basics of molecular physics and the physics of laser-molecule interactions will be presented. Outlined fundamentals will provide physical insights and lay the foundation towards the understanding of the phenomena presented in subsequent chapters of this dissertation.

3.1 Molecular structure

A molecule is a combination of two or more atoms bonded together. The distribution of the inner shell electrons in a molecule is similar to that in an isolated atom. The overlapping of the outer (valence) electron clouds and their redistribution around the molecule provide the binding force, and determine the structure and the chemical behavior of the molecule.

An analytical description of the molecular structure is much more complicated than that of atoms due to the increased number of degrees of freedom. Fortunately, electrons are much smaller and lighter than nuclei: electron is 2000 times lighter than protons and neutrons that constitute the nucleus. Therefore, the motion of the nuclei is much slower than the electron motion. When one attempts to describe electron motion within the molecule, nuclei are often considered stationary. This approximation is called *Born-Oppenheimer (or adiabatic) approximation* [**44**]. In the frame of this approximation nuclear motion and the behavior of electrons in the nuclear potential can be treated separately.

Proposed by Born and Oppenheimer [**44**] this approximation allows for solving Schrödinger equation for nuclear and electronic coordinates separately. Such an elegant approach leads to the significant simplification of the quantum mechanical treatment of the molecular systems. For a diatomic molecular system with nuclei A and B containing N electrons, the time independent Schrodinger equation for the entire system can be written as:

$$\hat{\mathbf{H}}\Psi(Q_A, Q_B; q_1, ..q_N) = E\Psi(Q_A, Q_B; q_1, ..q_N) \qquad \textbf{(3.1)}$$

where $\hat{\mathbf{H}} = \hat{\mathbf{T}}_\mathbf{e} + \hat{\mathbf{T}}_\mathbf{n} + \hat{\mathbf{V}}$ is the Hamiltonian operator for the molecule. It consists of kinetic energy operators for electrons and nuclei, and potential energy operator for Coulomb interaction between A and B, electrons and nuclei, and between electrons themselves. Q_A and Q_B is the full set of space $\{\mathbf{R}\}$ and spin coordinates for A and B; $\{q_N\}$ are space $\{\mathbf{r_N}\}$ and spin coordinates for all N electrons. E represents energy levels and Ψ is the total wave function of the system, which must obey the Pauli Exclusion Principle. Therefore, Ψ must be antisymmetric with respect to the interchange of coordinates of any pair of electrons. If the molecule is homonuclear then Ψ also must be symmetric (if nuclei are bosons) or antisymmetric (if nuclei are fermions) under interchange of nuclear coordinates.

In polar coordinates one can introduce the set of *coupled equations* equivalent to eq.(**3.1**):

$$\sum_i \left\langle \Phi_s \left| -\frac{\hbar^2}{2\mu}\frac{1}{R^2}\frac{\partial}{\partial R}\left(R^2\frac{\partial}{\partial R}\right) + \frac{\hat{\mathbf{N}}^2}{2\mu R^2} \right| \Phi_i \right\rangle F_i(\mathbf{R}) + [E_s(R) - E]F_s(\mathbf{R}) = 0 \qquad \textbf{(3.2)}$$

$s = 1,2....$

where $\mathbf{R}$, internuclear distance, is treated as a parameter. Spin coordinates are not displayed. $\Phi_i(\mathbf{R};\mathbf{r_1},\mathbf{....r_N})$ wave functions for each electronic state i are calculated at fixed $\mathbf{R}$. $\mathbf{N}$ is the nuclear total orbital angular momentum. $F_i(\mathbf{R})$ are the wave functions representing the nuclear motion, both vibration and rotation. $\mu = \frac{M_A M_B}{M_A + M_B}$ is the reduced mass of A and B. $E_s(R)$ are the electron energy levels, which are the eigenvalues of the electronic Hamiltonian.

For the electron motion in the field of nuclei, fixed at their positions eq. **(3.1)** reduces to the *electronic wave equation* [**45**]:

$$(\hat{\mathbf{T}}_\mathbf{e} + \hat{\mathbf{V}})\Phi_i(\mathbf{R}, \mathbf{r}_1, ..\mathbf{r}_N) = E_i(\mathbf{R})\Phi_i(\mathbf{R}, \mathbf{r}_1, ..\mathbf{r}_N) \qquad \textbf{(3.3)}$$

Eigenfunctions Φ and eigenvalues E in this equation depend parametrically on R which is fixed during the calculations.

Figure 3.1 A general form of the electronic energy for a bound state of a diatomic molecule. The quantity D_e is the dissociation energy of the molecule in the state s; R_0 is the equilibrium internuclear distance, the minimum of the potential

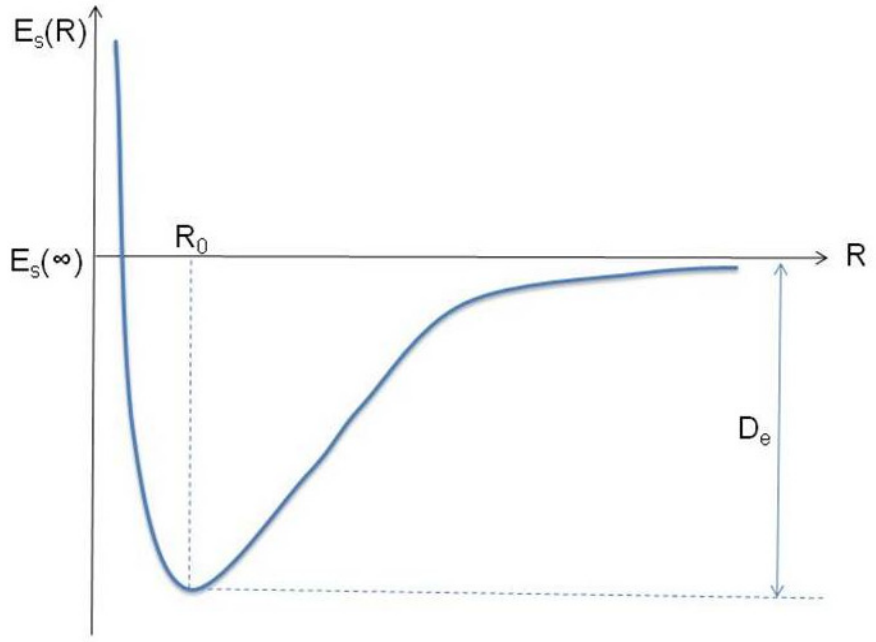

Born-Oppenheimer or *adiabatic* approximation introduced to equation **(3.2)** is equivalent to neglecting $\left|\nabla_R^2 \Phi_i\right|$ compared to $\left|\nabla_R^2 F_i\right|$ due to the fact that electronic function varies very slowly with respect to nuclear coordinates. As a result the set of coupled equations **(3.2)** reduces to the set of *uncoupled nuclear wave* equations [**45**]:

$$\left[-\frac{\hbar^2}{2\mu}\frac{1}{R^2}\frac{\partial}{\partial R}\left(R^2\frac{\partial}{\partial R}\right)+\frac{\left\langle \hat{\mathbf{N}}^2\right\rangle}{2\mu R^2}+E_s(R)-E\right]F_s(\mathbf{R})=0$$

$$s=1,2.... \qquad \textbf{(3.4)}$$

Each equation describes the vibrational and rotational motion of the molecule when the system is in a state s. For each s the total wave function is given by:

$$\Psi_s = F_s(\mathbf{R})\Phi_s(\mathbf{R};\mathbf{r_1},..\mathbf{r_N}) \qquad \textbf{(3.5)}$$

In **(3.4)** electronic energy $E_s(R)$ plays the role of a potential. A general form of Born-Oppenheimer potential for a bound state is shown in Fig. **3.1**. As $R\to 0$ potential energy is dominated by the Coulomb repulsion between nuclei. As $R\to\infty$ the potential energy asymptotically approaches the *dissociation limit*, which is the energy of two

isolated atomic fragments. The state represented by the potential in Fig. **3.1** is bound and therefore the potential has a minimum at R_0 around which the wave function can be confined.

3.1.1 Hydrogen molecular ion: electronic states.

The hydrogen molecular ion is the simplest of all molecular ions. It has two identical nuclei and one electron. The exact solution of the Schrödinger equation is possible for this ion and therefore it can be used as a model system to test and validate numerical methods before approaching more complicated molecules. One of the approximate methods of solving Schrödinger equation is LCAO – *linear combination of atomic orbitals* [**46**].

When the H_2^+ ion dissociates the only electron has to stay with either of the two protons A or B and for a system in the ground state we expect the solutions to be in the form of:

$$\Phi(\mathbf{R};\mathbf{r}) = \psi_{1s}(r_A) = \frac{1}{\sqrt{\pi}}\exp(-r) \qquad \textbf{(3.6)}$$

r_A is the distance between proton A and the electron and the $\mathbf{r}$ is the radius vector of the electron. H_2^+ is the homonuclear molecular ion, which has the midpoint between two identical nuclei as an additional center of symmetry. Consequently, the resulting spatial wave function can be symmetric or antisymmetric with respect to the reflection of the electron coordinates $\mathbf{r}\rightarrow\text{-}\mathbf{r}$. To verify that the solutions satisfy the symmetry criteria, the following linear combinations of the atomic orbitals can be used:

$$\Phi_g(\mathbf{R};\mathbf{r}) = \frac{1}{\sqrt{2}}\left[\psi_{1s}(r_A) + \psi_{1s}(r_B)\right] \qquad \textbf{(3.7a)}$$

$$\Phi_u(\mathbf{R};\mathbf{r}) = \frac{1}{\sqrt{2}}\left[\psi_{1s}(r_A) - \psi_{1s}(r_B)\right] \qquad \textbf{(3.7b)}$$

Φ_g is the symmetric (even) solution and Φ_u is the asymmetric (odd) solution: *gerade* Φ_g and *ungerade* Φ_u states respectively.

The expression for $E_g(R)$ and $E_u(R)$ – energies of gerade and ungerade states are [**45**]:

$$E_{g,u} = E_{1s} + \frac{1}{R}\frac{(1+R)\exp(-2R) \pm (1-2R^2/3)\exp(-R)}{1 \pm (1+R+R^2/3)\exp(-R)} \qquad \textbf{(3.8)}$$

$E_g(R)$ and $E_u(R)$ are plotted in Fig. **3.2**. The curve corresponding to plus sign in eq. **(3.8)** (E_+ or Φ_g) represents a bound state – attractive potential leading to the formation of a stable ion. It has a minimum at equilibrium internuclear distance R_0 = 2.49 a.u. corresponding to the molecular orbital eq. **(3.7a)** that is called *bonding* orbital.

Figure 3.2 Hydrogen molecular ion: electronic states

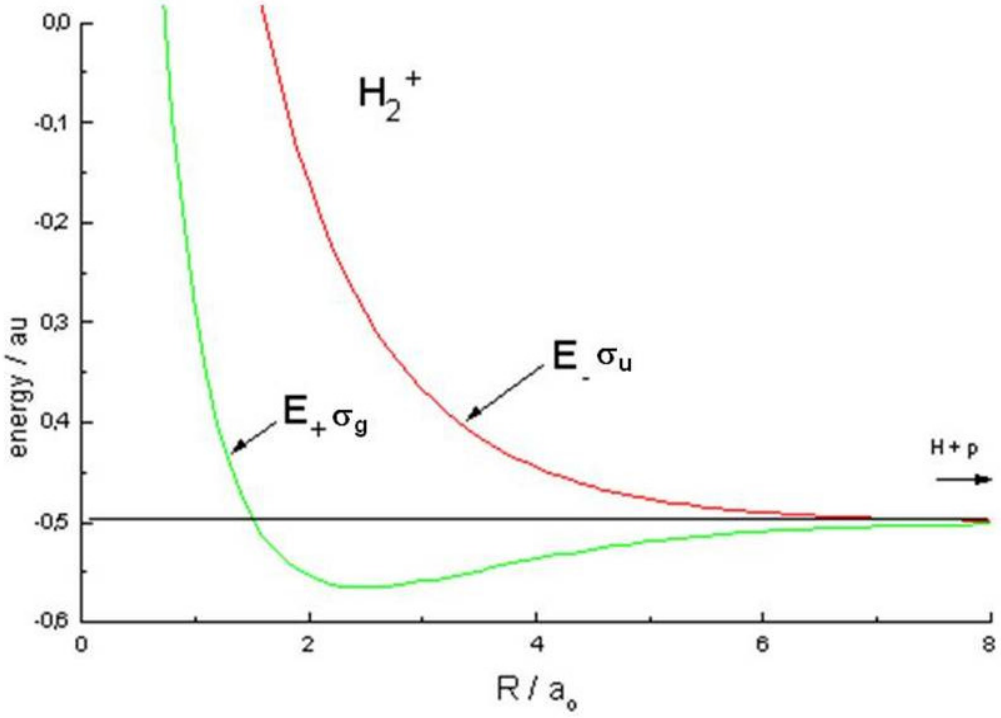

Ungerade state represented by the potential curve $E\_$ or Φ_u is a repulsive one. It has no minimum and the molecular ion in this state dissociates into a proton and neutral hydrogen ion in ground state. The corresponding molecular orbital eq. **(3.7b)** is called *antibonding* orbital.

The charge density for both states can be calculated as

$$\rho_{g,u} = -\left|\Phi_{g,u}\right|^2 \qquad \textbf{(3.9)}$$

For bonding orbital its value is greater than just the normalized sum of densities for isolated atoms brought together to a distance equal to the internuclear separation in H_2^+. This excessive negative charge is causing the binding and is the reason for the existence of the stable H_2^+ ion. To the contrary, for the antibonding orbital there is a point with zero charge density along the internuclear line in the deficiency of negative charge. This is qualitatively demonstrated in Fig. **3.3**, where orbital functions and their amplitude squares are plotted along the internuclear line.

Figure 3.3 (a) and (b): combinations of wave functions for two isolated H atoms plotted along internuclear line; (c) and (d): gerade and ungerade wave functions for the H_2^+ ion ; (e) and (f): charge densities of gerade and ungerade states for the H_2^+ ion. A and B are the positions of H nuclei

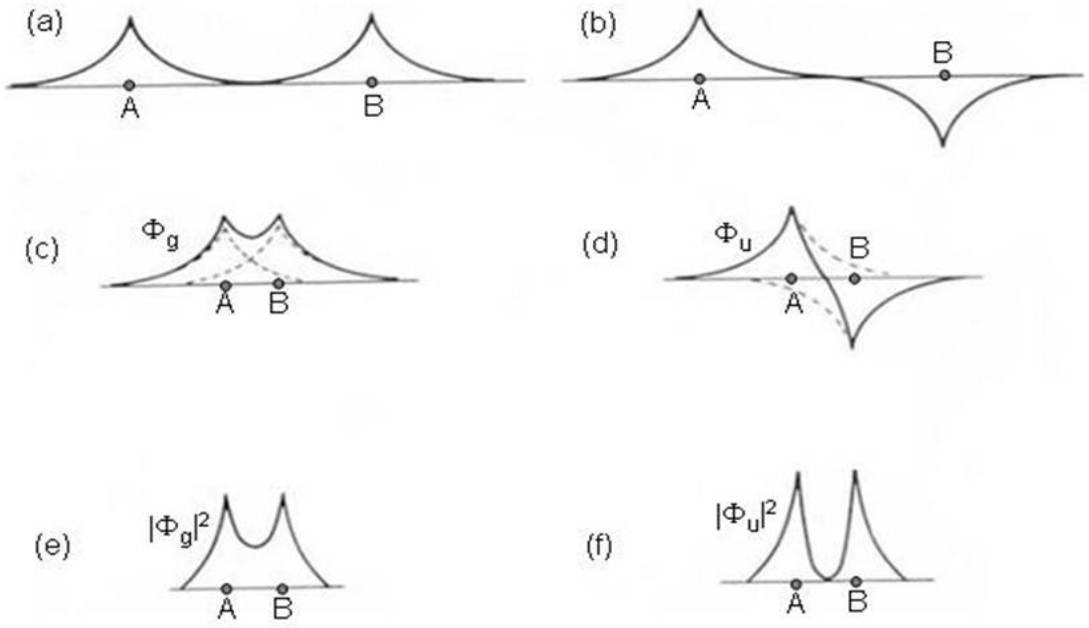

This observation can be generalized. To form a bound state in a molecule, the negative charge density between nuclei must be in excess compared to the charge distribution created by two isolated atoms. This charge density is determined by the overlap of wave functions centered on each nucleus; and the greatest contribution comes from outer shell (valence) electrons.

For heteronuclear diatomic molecule case there is no reflection symmetry over the midpoint of the internuclear line, and orbitals cannot be classified as gerade and ungerade anymore.

For the majority of the molecules the electronic structure is even more complicated for obvious reasons, like the growing number of nuclei with different electronic structure. Still, energy surfaces can be numerically calculated using several different techniques including the quantum chemistry LCAO method.

3.1.2 Diatomic molecule: vibrational and rotational structure

Now, we return to the eq. **(3.4)** which describes the vibrational and rotational nuclear motion of any diatomic molecule. Assume that the electrons are in the states with zero angular orbital momentum $\mathbf{L} = 0$. For a fixed electronic quantum number s $F_s(\mathbf{R})$ function can be written in a form of a product of the radial and angular functions. $F_s(\mathbf{R})$ must be an eigenfunction of $\mathbf{J}^2$ ($\mathbf{J}$ is the total orbital angular momentum of the molecule) and $\mathbf{J}_z$, (z is the chosen direction in space) with corresponding eigenvalues $J(J+1)\hbar^2$ and $M_J\hbar$. Spherical harmonics functions satisfy these requirements.

$$F_s(\mathbf{R}) = \frac{1}{R}\mathcal{F}^s_{v,J}(R)Y_{J;M_J}(\Theta,\Phi)\,. \qquad \textbf{(3.10)}$$

For the particular case of zero electron total angular orbital momentum the energy of the system cannot depend on M_J (energy levels with different M_J value have the same energy $(2J+1)$-fold degenerate), but $E(\mathbf{R})$ still depends on J. Substituting eq. **(3.10)** into eq. **(3.4)** we yield the radial equation [**45**]:

$$\left[-\frac{\hbar^2}{2\mu}\left(\frac{d^2}{dR^2}-\frac{J(J+1)}{R^2}\right)+E_s(R)-E_{s,\upsilon,J}\right]\mathcal{F}^s_{v,J}(R)=0 \qquad \textbf{(3.11)}$$

Additional quantum number ν is associated with vibrational motion and plays a role of a radial quantum number. For a given electronic state s the states with indexes ν and J are called *rovibrational states*. For a certain potential in form of $E_s(R)$ like for $1s\sigma_g$ bound state of H_2^+ ion shown in Fig. **3.2**, equation **(3.11)** can be solved numerically. Since *the motion in such a potential confined to a small region around the minimum energy*, it is

useful to expand $E_s(R)$ around the equilibrium point R_0 in a Taylor series to get a good idea of rotational and vibrational energy levels. The first derivative in R_0 is equal to zero and the terms of the order higher than 2 in $(R\text{-}R_0)$ can be neglected, thus $E_s(R)$ is approximated by the parabolic potential:

$$E_s(R) \cong E_s(R_0) + \frac{1}{2}k\left(R - R_0\right)^2,$$
$$k = \left.\frac{d^2 E_s}{dR^2}\right|_{R=R_0} \qquad \textbf{(3.12)}$$

The rotational energy can be approximated by the value at the equilibrium internuclear distance:

$$E_J = BJ(J+1), J = 1,2...$$
$$B = \frac{\hbar^2}{2\mu R_0^2} = \frac{\hbar^2}{2I_0} \qquad \textbf{(3.13)}$$

B is called *the rotational constant of the molecule*, and I_0 is the moment of inertia of the molecule with nuclei at distance R_0. From eq. **(3.11)** one can see that the total energy of the molecule is the sum of electronic energy at the equilibrium internuclear separation, rotational and vibrational energy:

$$E_{s,v,J} = E_s(R_0) + E_v + E_J \qquad \textbf{(3.14)}$$

E_v here are the eigenvalues of the equation describing the motion with simple harmonic potential $\frac{1}{2}k\left(R - R_0\right)^2$ where k is the force constant:

$$\left[-\frac{\hbar^2}{2\mu}\frac{d^2}{dR^2} + \frac{1}{2}k(R-R_0)^2 - E_v\right]\psi_v = 0 \qquad \textbf{(3.15)}$$

Those eigenvalues of eq.**(3.15)** are known to be [**45**]:

$$E_\upsilon = \hbar\omega_0(\upsilon + \frac{1}{2}), \upsilon = 0,1...$$
$$\omega_0 = \sqrt{k/\mu}. \quad \textbf{(3.16)}$$

The corresponding eigenfunctions ψ_v are the harmonic oscillator wave functions. The energies and function calculated with the parabolic approximation are close to real vibrational energies and functions *only for small* v when R is close to the equilibrium distance (Fig. **3.4**). With quantum number raising the vibrational levels are not evenly spaced anymore and become close to each other. The number of the levels is limited by the depth of the potential well.

Figure 3.4 Schematic drawing of energy levels diagram. Also shown the transition between states with and without change of electronic state E_s

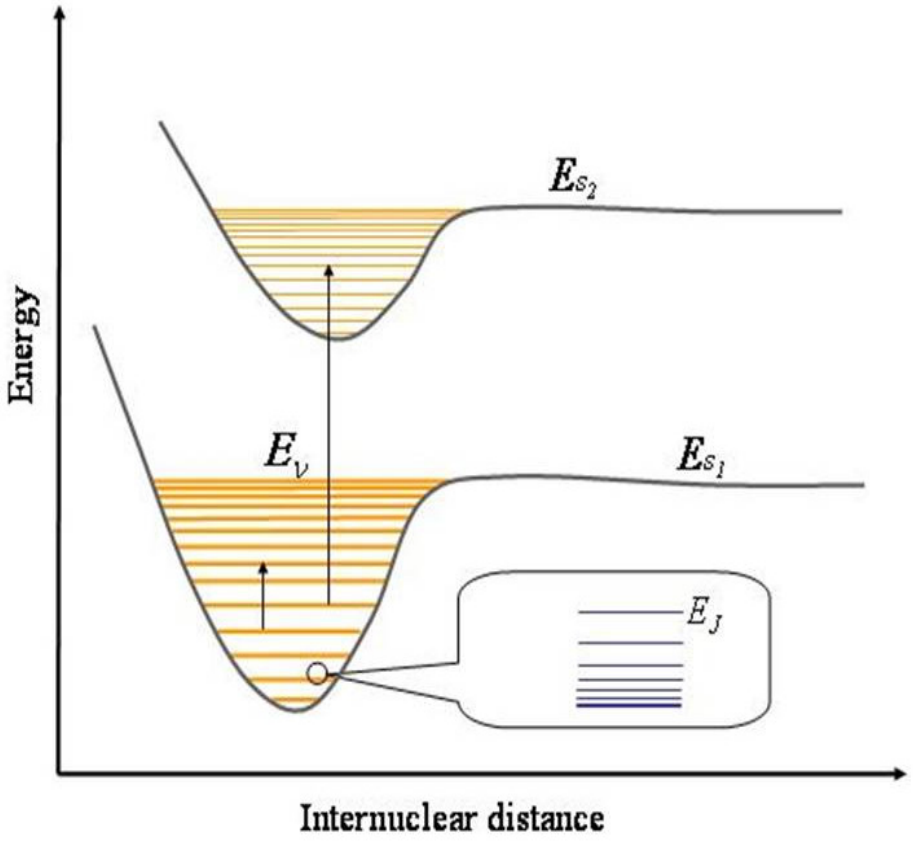

To discuss rotational energy levels of a diatomic molecule in general case, when electrons have non-zero total orbital angular momentum, we return again to the eq. **(3.4)**.

This time we consider that spins of electrons need not to be considered due to weak L-S coupling. In this case the total angular momentum of the molecule is **J** = **L**+**N**. Eq. **(3.4)** with substitution of the wave function in the form **(3.10)**, gives the radial equation for the nuclear wave function in general form [**45**]:

$$\left[-\frac{\hbar^2}{2\mu}\frac{d^2}{dR^2}+\frac{\left\langle \hat{\mathbf{N}}^2\right\rangle}{2\mu R^2}+E_s(R)-E\right]\mathcal{F}(R)=0 \tag{3.17}$$

With the approximation of weak L-S coupling and considering that $J_R = L_R$ (component of L in the direction, parallel to the internuclear line) the expectation value of $\mathbf{N}^2$:

$$<\hat{\mathbf{N}}^2>=<(\hat{\mathbf{J}}-\hat{\mathbf{L}})^2>=\hbar^2 J(J+1)-2\Lambda^2\hbar^2+<\hat{\mathbf{L}}^2> \tag{3.18}$$

Then the rotational energy at the equilibrium can be evaluated as:

$$E_J=\frac{1}{2\mu R_0^{\,2}}\left[J(J+1)\hbar^2-2\Lambda^2\hbar^2+<\hat{\mathbf{L}}^2>\right] \tag{3.19}$$

The last two terms do not depend on J and only characterize an electronic state, so that we can combine them with electronic energy term in the expression for the total energy:

$$E_{s,\upsilon,J}=\left(E_s(R_0)+\frac{1}{2\mu R_0^{\,2}}\left[-2\Lambda^2\hbar^2+<\hat{\mathbf{L}}^2>\right]\right)+E_\upsilon+BJ(J+1)=$$
$$=E_s'(R_0)+E_\upsilon+E_J \tag{3.20}$$

As a result the form for the rotation energy is the same that in case of **L** = 0 (Λ=0) (eq. **(3.13)**), but with the condition that

$$J\geq\Lambda \tag{3.21}$$

This condition arises from the fact that the magnitude of total orbital momentum must be greater or equal to any of its component.

According to eq. **(3.13)** the rotational energy of a diatomic molecule is a series of discrete rotational levels whose energies increase quadratically with increasing J. The energies of rotation (of the order of meV) are much smaller than vibration (of the order of eV) and thus rotational levels appear as a fine splitting of vibrational levels (Fig. **3.4**).

The evaluation of the rotational energy at the equilibrium point is equivalent to modeling a diatomic molecule as a classical rigid rotor with two point masses equal to masses of nuclei separated by a weightless rod of R_0 length [**47**]. But we understand that the bond in molecule is not rigid. In the same classic analogy it rather should be seen as a spring connecting two masses: the speed of rotation increases and nuclei are pulled away from the center by the centrifugal forces. The "spring" stretches, internuclear distance increases and, as a consequences, B decreases. With contribution of this effect, the rotational energy can be written as [**48**]:

$$E_J = BJ(J+1) - DJ^2(J+1)^2 \qquad \textbf{(3.22)}$$

where constant D is the centrifugal distortion constant. D depends on the stiffness of the bond and is always positive for diatomic molecules.

Separating vibrational and rotational degrees of freedom we should not forget that we use an approximation, which is valid to a certain extent. Both constants B and D are slightly dependent on the vibrational state of the molecule. The vibrational dependence of B is approximately given as [**48**]:

$$B_\upsilon = B_0 - \alpha(\upsilon + \frac{1}{2}) \qquad \textbf{(3.23)}$$

Here α is a vibration-rotation interaction constant and B_0 is a rotational constant of a hypothetic equilibrium state on the very bottom of the potential well. As a result, each vibrational level is characterized by its own rotational constant.

The transitions between energy levels are associated with emission or absorption of energy quanta equal to the energy difference between those levels. Each molecule is characterized by specific electronic, rotational and vibrational emission spectra, which are the sets of discrete lines due to a discrete nature of energy levels. Therefore these spectra are unique for a certain molecule. From classical electrodynamics it is known that a system can irradiate only if it is characterized by a non-zero permanent dipole moment $\boldsymbol{\mu_0}$. Also the transition amplitude between two states α and β is proportional to the dipole matrix element $\langle\psi_\alpha|\boldsymbol{\mu_0}|\psi_\beta\rangle$. Allowed transitions are defined by a non-vanishing dipole element. Therefore, they can be described by so-called *selection rules* involving only

quantum numbers of the initial and final states. Homonuclear diatomic molecules do not possess a permanent electric dipole moment due to their inversion symmetry. Rotational and vibrational motion preserves the symmetry of the molecule; and if the *electronic* state of the molecule does not change during the transition, then any rotational and vibrational transition is forbidden. If the diatomic molecule is heteronuclear or the electronic state changes, then the selection rules for transitions become [**47**]:

$$\begin{aligned} &\Delta J = \pm 1 \quad if \quad \Lambda = 0 \\ &\Delta J = 0, \pm 1 \quad if \quad \Lambda \neq 0 \\ &\Delta M_J = 0, \pm 1 \\ &\Delta \upsilon = \pm 1 \end{aligned} \tag{3.24}$$

The above section was dedicated to the description of stationary structure and energy spectra of a diatomic molecule. The goal of the next section is to discuss the phenomena and processes related to the interaction of molecules with strong laser fields.

3.2 Molecules in Strong Laser Field

Ionization takes place when an atom or molecule absorbs a number of photons with total energy greater than the ionization potential I_p for this atom (molecule), and the excess energy is carried away by the free electron. For the case when I_p is much greater than the photon energy, the ionization mechanism is conventionally classified into three types: multi-photon ionization, tunneling ionization and over-the-barrier ionization. To characterize these ionization mechanisms quantitatively, the *Keldysh parameter* is used (Keldysh 1965). This parameter is defined by the ratio of the electron binding energy (*ionization potential*) and the energy of the free electron oscillating with frequency ω of the laser electric field (*ponderomotive energy*) [**49**]:

$$\gamma = \sqrt{\frac{I_p}{2U_p}} \tag{3.25}$$

where U_p is the ponderomotive energy:

$$U_p = \left(\frac{F_0}{2\omega} \right)^2 \qquad \textbf{(2.26)}$$

F_0 is the amplitude of the laser field. According to the classification of Keldysh all three mechanisms are different regimes of nonlinear ionization and further treatment depends on how much time, T, it takes for the electron to overcome the ionization potential barrier (tunneling time) as compared to the laser period. The alternative definition of the Keldysh parameter is the ratio of the laser frequency and inverse of time T [**49**].

$$\gamma = \frac{\omega_{laser}}{\omega_T} \qquad \textbf{(2.27)}$$

Figure 3.5 Schematic drawing of three mechanisms of ionization for an atom: (a) field-free potential; (b) multiphoton ionization; (c) tunneling ionization; (d) over-the-barrier ionization

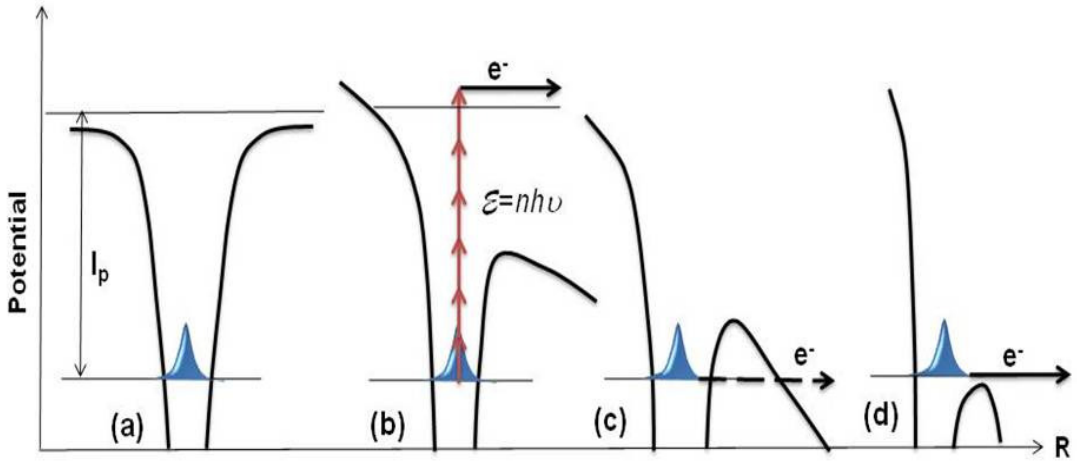

Considering both definitions of the Keldysh parameter, below I discuss the classification of the ionization regimes mentioned above:

1) The *multiphoton regime* corresponds to the condition **γ>>1** (Fig. **3.5(b)**). Energy of the electron in laser field is low compared to ionization potential. Experimental ionization rates are reproduced quite well by the lowest order perturbation theory via absorption of n photons. The ionization rate obeys the power law: $P_n = \sigma_n I^n$ [**50**] where I is intensity and σ is the n-photon ionization cross section. This formula is difficult to test experimentally, because of the spatial intensity distribution in the focal volume of the laser beam. At some threshold intensity (saturation intensity) the power law breaks down

and perturbation theory is no longer applicable because it is no longer possible to neglect the depletion of the initial state. The ionization rate is greatly enhanced if energy of n absorbed photons is equal to the ionization potential. It is also possible for the atom or molecule to absorb more photons than required for the ionization. Such a process is called *above threshold ionization* (ATI).

2) *Tunneling ionization (field ionization)* regime corresponds to γ**<1** (Fig. **3.5(c)**). This regime dominates at laser frequencies low enough that the electron has time to tunnel through the barrier during one laser cycle. Most infrared femtosecond laser experiments are performed in this regime. The laser period is greater than the tunneling (see eq. **(3.27)**) time and therefore the laser field can be treated classically. Each half-cycle of the field oscillations, the electron is pushed towards the barrier. Tunneling probability for the electron is determined by the width of the potential barrier and increases with laser filed intensity. The tunneling formula of Amosov, Delane and Krainov ADK is considered to be a good approximation for the ionization rate [**51**]:

$$P_{ADK} = \left(\frac{3e}{\pi}\right)^{3/2} \frac{Z^2}{3n^{*3}} \frac{2l+1}{2n^* - 1} \left(\frac{4eZ^3}{(2n^* - 1)n^{*3}F}\right)^{2n^* - 3/2} \exp\left(-\frac{2Z^3}{3n^{*3}F}\right) \qquad \textbf{(3.28)}$$

where $n^* = \sqrt{2I_p}$, I_p is the ionization potential, F is the amplitude of laser field, Z is the atomic/ionic charge, l is the orbital angular momentum quantum number and e=2.718… This formula gives values that are in a good agreement with experimental ionization rates for single ionization of atoms. It even works for *some* diatomic molecules as if they were atoms with the same ionization potentials as the molecules; but it fails to reproduce double ionization experiments [**52**-**54**].

3) *Over-the-barrier ionization* OBI process occurs at slightly higher intensities than tunneling, when the laser field strength is high enough to suppress the potential barrier of the atomic potential (Fig. **3.5(d)**) [**55**]. The situation can be treated classically. The condition for this regime can be extracted by equating the ionization potential to the relative maximum of the potential which is a superposition of the Coulomb potential and quasi-static laser field. The combined potential in atomic units:

$$V(R) = -\frac{Z}{R} - FR \qquad \textbf{(3.29)}$$

Barrier position R_b can be found from the condition of maximum of the function $dV/dR=0$ and then the height of the barrier $V(R_b)$ can be calculated. And the strength of the laser field required for barrier suppression to the level of the ionization potential is found to be [**56**]:

$$F_{OBI} = \frac{I_p^2}{4Z} \qquad \textbf{(3.30)}$$

At this point the inner potential barrier is suppressed to the extent that electron can escape classically from the potential well. However, estimating the ionization rates classically, one should realize that quantum effects like partial reflection of the wave packet and tunneling will still be contributing, unless the energy of the electron in the laser field is well above the ionization potential [**57**]. There is no discontinuity between the tunneling and the threshold of over-the-barrier regime. The ionization rate continues to increase smoothly and it comes close to unity for a single laser pulse cycle.

Though these regimes are characterized by certain parameter and conditions, it does not mean that it is easy to choose one ionization regime in an experiment. Under certain particular experimental conditions there is a minimum intensity for non-linear ionization processes to appear (appearance intensity). At some higher intensity the ionization rate will saturate. The saturation intensity and appearance intensity give upper and lower limits, which determine variation in Keldysh parameter, and these limits are not very far apart. [**21**] The choice of a certain regime is particularly complicated due to the *focal volume effect*. Laser intensity varies in focus. In principle, the target gas is supposed to overlap with the center of the focus. In practice, the central spot is very small and the target also overlaps with consecutive shells around the focus which are large in volume and lower in intensity. While the process under investigation is far from saturation, the volume effect does not play a significant role, because intense-laser phenomena are highly nonlinear, and then signal coming from the shell next to the center of focus drops down orders of magnitude. Close to saturation intensity the situation is different. For instance, if one studies the sequential processes like multiple ionization or

ionization and dissociation, the first step rate saturates at lower intensity than next one. It means that it is impossible to avoid the situation when only first process takes place in some focal shell around the central spot [**21**]. To reduce the volume effect in practice, one can increase the Raleigh range and make the interaction region smaller, so that it is inside the Raleigh range (see section **2.1**).

In general, the ionization in molecules is more complex than in atoms. Ionization potential becomes a function of internuclear separation. The potential barrier between nuclei can shift in laser field as well as the outer potential barrier that is demonstrated in Fig**. 3.6** adopted from [**58**].

Figure 3.6 Molecular potential wells showing the importance of (a) outer well; (b) inner well. The figure is from G. N. Gibson et al. Phys. Rev. Lett. 81, 2663 (1998) [58]

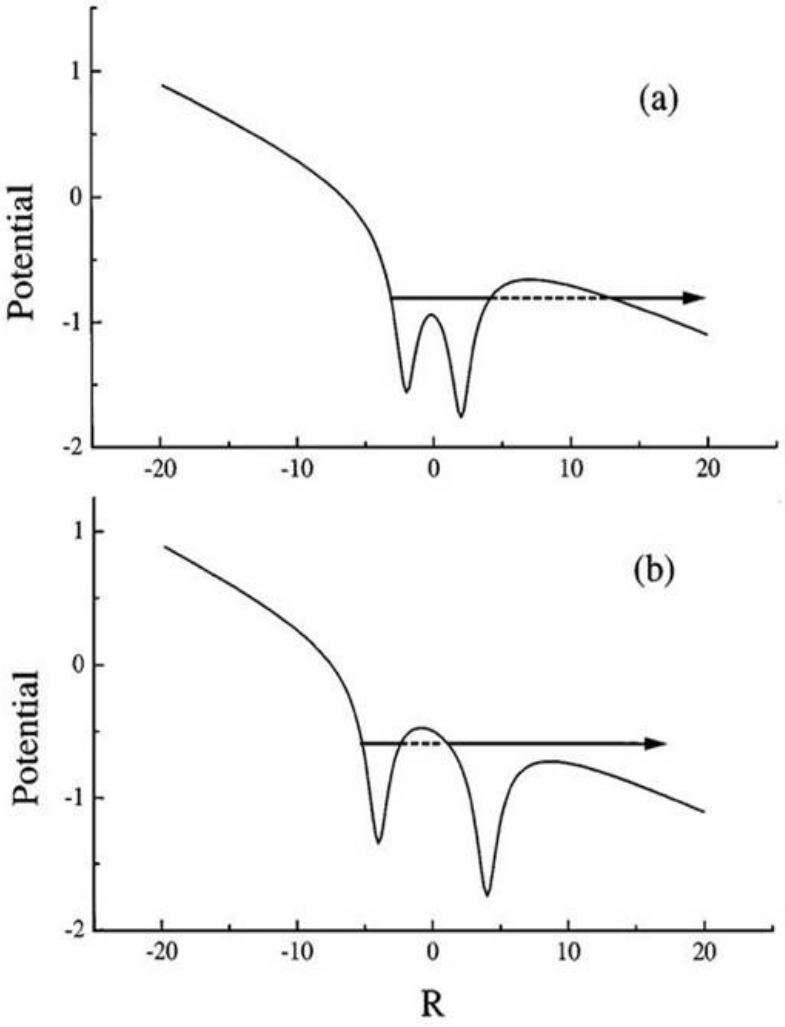

The ionization rate for small molecules can be approximated by eq. **(3.28)** if Z is treated as molecular (ionic) charge and, ionization potential I_p dependence on internuclear distance is taken into account. To apply eq. **(3.28)** in the case of diatomic molecules one can use an effective ionization potential $I_{p,eff}$ and an effective electric field F_{eff} instead of I_p and F. In the first order approximation of static field ionization, $I_{p,eff}$ and F_{eff} are expressed as [**59**]:

$$I_{p,eff} = I_p - \frac{eZ}{\left|R - x_0\right|} + \frac{eZx_0}{\left|R - x_0\right|^2} \qquad \textbf{(3.31)}$$

$$F_{eff} = F + \frac{Z}{\left|R - x_0\right|^2} \qquad \textbf{(3.32)}$$

Here $x_0=x_0(R,F)$ is the top of the inner potential barrier; $I_p=I_p(R)$ varies with internuclear separation and can be calculated as the energy gap between the ground electronic state and first excited state.

C. D. Lin's group in Kansas State University extended the ADK model and developed a molecular ADK (MO-ADK) theory based on symmetry properties of molecular orbitals [**60**]. This model is able to explain such a phenomenon as ionization suppression for certain molecules and predicted high harmonics cutoff extension for molecules with specific orbital symmetry like O_2. Ionization probabilities exhibit dependence on molecular alignment according to MO-ADK, which was also observed experimentally [**61**].

Ionization and *dissociation* of molecules in intense laser fields are two processes that accompany each other. The multielectron dissociative ionization of diatomic molecules is characterized by fragmentation of a molecule into two atomic ions with kinetic energy caused by ion mutual repulsion. The dominating force between charged particles is *Coulomb repulsion*; the process of molecular break-up is called *Coulomb explosion*. Measured energy of fragments contains information about internuclear distance at which ionization occurred. In several experiments, for instance with N_2 and I_2, it was observed that dissociation energy is a certain fraction of Coulomb energy, regardless of charged state and depending slightly on laser pulse length (for pulses >100

fs), though one would expect the energy to go down with pulse length increasing [**62**, **34**, **63**]. Also the experiments show that ionization rate is anomalously enhanced as internuclear separation reaches a certain range [**64**, **65**]. Experiments with hydrogen molecules showed that kinetic energy release of H^+ fragments is much lower than expected from Coulomb explosion in equilibrium geometry and also independent of pulse length for long pulses [**66**]. The explanation for the above observations is the existence of a phenomenon known as *charge-resonant enhanced ionization* (CREI). In the frame of the classical model this phenomenon is treated in the following way. In the case of a diatomic molecule explosion from equilibrium internuclear distance the Coulomb energy is given by:

$$CE = \frac{q_1 q_2}{R_e} \tag{3.33}$$

where q_1 and q_2 are charges of atomic fragments and R_e is the equilibrium internuclear distance for a neutral molecule. There are two possibilities suggested [**67**] for a reduction in Coulomb energy. One is electrostatic screening at each ionization state (effectively, reduction in q_1 and q_2) at R_e. Another explanation is that the molecular ion expands to some critical distance after first ionization at which it then subsequently ionizes. As long as the pulse is sufficiently long to let the molecule expand to R_c without ionizing it, the fragmentation takes place at the same internuclear distance and fragments end up with approximately the same kinetic energy release. Fig. **3.7** adopted from the paper [**68**] illustrates the process of molecular expansion to critical internuclear distance using the example of an I_2^+ molecular ion. The position of the electron energy level E_L in the double well potential can be approximated as:

$$E_L = \frac{\left(-E_1 - q_2/R_C\right) + \left(-E_2 - q_1/R_C\right)}{2} \tag{3.34}$$

In eq. **(3.34)** E_1 and E_2 are known ionization potentials of the atomic ions. They are lowered by q/R_c which is the Coulomb field of a neighboring atomic ion. Initially, when internuclear distance is small, the situation is similar to the previously discussed case of an atom with one potential well in the laser field. But as nuclei start moving apart, the

electron energy level rises (see eq. **(3.34)**) and the electric field becomes more effective at lowering the outer potential barrier. Finally, when the inner potential barrier U_1 touches the electron energy level E_L, internuclear separation reaches the critical value R_C. And, when the outer barrier is lowered by the laser field, the electron can escape from the potential well.

Figure 3.7 Model of the I_2^+ ion in a laser field: an outmost electron in a double well potential of two I^+ point-like charges and laser fields at three internuclear separations and different intensities in W/cm^2 indicated on each plot. The figure is from J. H. Posthumus et al. J. Phys. B 29, L525 (1996) [68]

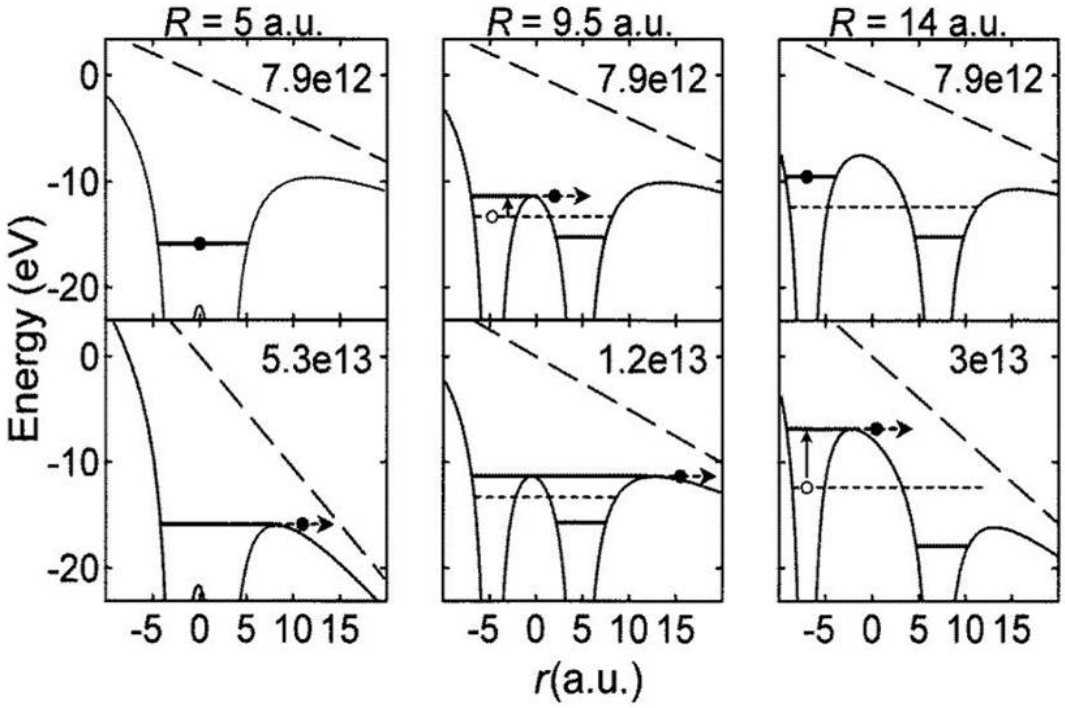

At larger internuclear distances the electron is localized in the left potential well (Fig. **3.7,** upper right panel) and the inner potential barrier is rising above the outer one, becoming an obstacle to ionization. The classical model of CREI was developed for multielectron diatomic molecules and multiple ionizations in [**69**]. As mentioned above, in experiments on fragmentation of some diatomic molecules like N_2 and I_2 it was observed that dissociation energy is a certain fraction of Coulomb explosion energy, regardless of charged state [**62, 34, 63**]. One explanation postulates that the nuclei freeze at R_c due to the existence of some bound state and consecutive ionizations occur at the same internuclear separation. Another explanation suggests that ionization rate at some

internuclear distance is enhanced and all ionization events happen while nuclei move through some region around R_c. The quantum-mechanical calculations, however, showed that the first situation can only exist for H_2^+ ion because its $1s\sigma_g$ state is bound and for other higher charge ions this mechanism does not work. Besides that, even for hydrogen ion the phenomenon of forming the bound state in the field (bond-hardening) happens only in certain intensity range (see section **3.3**). In Ref. [**69**] the authors found the range of the internuclear distances at which the ionization rate is greatly enhanced. In other words, ionization events happen simultaneously when the nuclei move through the critical separation, because around R_c the threshold for electron removal is reduced for all consecutive ionizations below the first ionization potential.

Figure 3.8 Illustration to a quantum-mechanical model of the charged-resonant enhanced ionization. The H_2^+ molecular potential in the laser field of $1x10^{14}$ W/cm^2 intensity shown for three fixed internuclear distances. The figure is from T. Zuo and A. D. Bandrauk. Phys. Rev. A 52, R2511 (1995) [14]

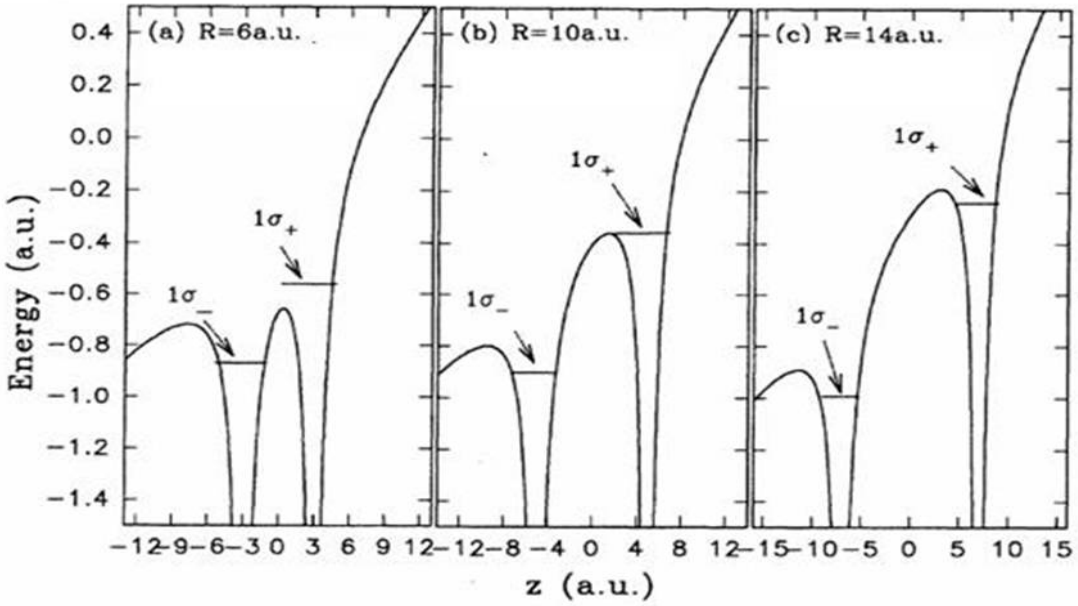

In the theoretical work of Zuo and Bandrauk [**14**] the ionization of the hydrogen molecular ion was studied as a function of internuclear distance by numerically solving the 3D time-dependent Schrödinger equation. The authors discovered an anomalously high ionization rate for large R for H_2^+ molecules oriented parallel to the linearly polarized laser field of $1x10^{14}$ W/cm^2 intensity and 1064 nm wavelength. The ionization

rate exceeded the rate for separated atoms by one order of magnitude. This phenomenon was attributed to the transitions between a pair of so-called *charge-resonant (CR) states*, which are $2p\sigma_u$ and $1s\sigma_g$ in the H_2^+ ion. Charge-resonant states are *strongly coupled* by the laser field at large internuclear distance due to their special properties: the dipole moment between the charge resonant states diverges linearly as $R/2$, energies are almost degenerate and the charge distribution is almost the same at large R. The existence of such CR states is the first condition for observation of CREI phenomena. The other condition is that the field-free molecular potential is altered by the instantaneous laser field in such a way that around some internuclear distance R_c the probability for the electron to tunnel through the inner and outer potential barriers increases significantly. This condition is achieved due to the combination of the following factors. Two autoionizing states $1\sigma^+$ and $1\sigma^-$ are the result of field mixing of H_2^+ gerade and ungerade states (Stark effect) (Fig. **3.8**). For the large internuclear distances these states are localized on each proton. As the gerade and ungerade become degenerate around R_c it makes the population on $1\sigma^+$ substantial. At the same time, at the critical internuclear distance the inner and outer potential barriers are both reduced by the external field thus, freeing the electron. In Fig. **3.7** adopted from [**14**] one can see the potential in the field and the field-induced levels for three internuclear distances. From their calculations the authors conclude that the highest ionization rate is measured at 10 au. At 6 au the ionization rate is lower because, though the $1\sigma^+$ is above the inner barrier, the outer barrier (most left in the picture) is broader and higher than at 10 au and reduces the ionization. At 14 au the separation between nuclei is large enough to reduce the situation to two isolated atoms and the ionization rate drops to the level of an atomic ionization. The calculated ionization rate spectrum is characterized by a peak at 7 au, which is lower than 10 au peak. This peak is attributed to the phenomenon called *laser-induced electron localization due to tunneling suppression*. At large internuclear distance tunneling between the wells in the molecular potential is suppressed. Population on the $1\sigma^+$ is prevented from flowing back to the lower $1\sigma^-$ level by the increased energy separation between the two levels due to the Stark shift effect, and trapped in the rising well for the

next half cycle of the oscillating field. As a result, the localized electron tunnels through the inner potential well. The authors in [**70**] conclude that for the H_2^+ ion for large to intermediate internuclear separations (5-12 au) the probability of ionization is anomalously enhanced and this phenomenon they call CREI and generalize it for higher charge states of diatomic molecules. The presence of charge resonant states is crucial for CREI to exist and the electron localization which breaks the inversion symmetry also plays an important role.

The classical and quantum mechanical models in [**69**, **14**] agree quantitatively and qualitatively.

3.2.1 Hydrogen molecule in laser field: bond softening and bond hardening.

As mentioned above, the simplest of all molecular systems are hydrogen and deuterium molecules and corresponding molecular ions. The following properties make them ideal models for studying laser-molecule interaction. True for both neutral molecule and ion, there is only one bound potential curve, which corresponds to the ground state, and the excited states are purely repulsive. For molecular ion, two lowest energy levels $1s\sigma_g$ and $2p\sigma_u$ are degenerate at large internuclear distance (see Fig**. 3.2**) and are strongly coupled in laser field. Another convenient characteristic of the hydrogen molecule is that ionization potential of H_2^+ is almost twice as large (~30 eV) compared to H_2 (~15 eV), that allows two-step treatment of ion formation and fragmentation. Hydrogen molecule and its ion demonstrate most of interesting strong field molecular physics observed also in more complex systems. Time-resolved imaging of vibrational wave packet motion and revivals, phenomena like CREI (section **3.2**), bond softening and bond hardening were first observed experimentally and studied theoretically in hydrogen and deuterium.

Bond softening (BS) and *bond hardening* (BH) are related to dissociation mechanisms of H_2^+. These phenomena are the result of inversion symmetry breaking of the system due to external field, modification of the energy surfaces due to the Stark effect, and mixing of the gerade and ungerade states. Laser field can weaken molecular

bond and induce dissociation through bond softening; or it can cause the opposite effect creating a bound state, so-called bond hardening (*vibrational trapping*) [**70**].

Figure 3.9 The Floquet picture for the H_2^+ ion. (a) Field dressed states. (b) The one-photon crossing is highly avoided and three-photon crossing is almost adiabatic as the gap is very narrow. The figure is from J. H. Posthumus. Rep. Prog. Phys. 67, 623 (2004) [21]

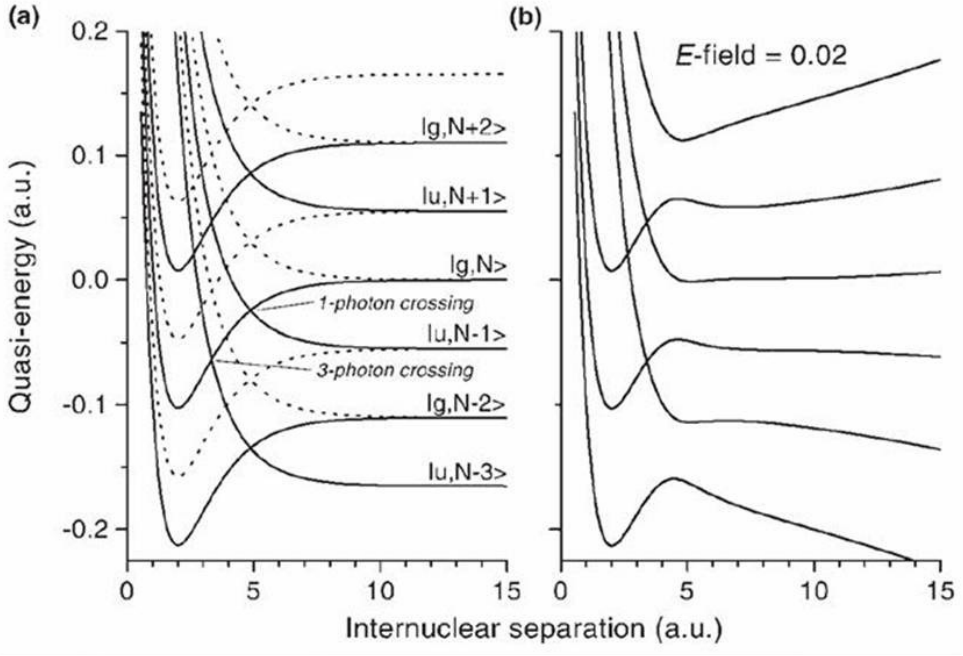

In the case of strong field and long wavelength, when the laser field is slow varying as compared to nuclear motion and number of photons is large, the *Floquet picture* is conventionally used for understanding molecule-field interaction [**71**]. The *Floquet theorem* states that solutions of the Schrödinger equation with time-periodic electric fields can be represented by a superposition of *Floquet states*. Such solutions are the common states of the molecule and laser field and called *field dressed states*. Each dressed state can be represented by a coherent superposition of the Floquet states. The Floquet states are of the same symmetry as the corresponding molecular field-free electronic state (gerade or ungerade) and separated by energy (dressed) equal to a number of absorbed or emitted photons, so that a *ladder* of these states is created around the field-free state (Fig. **3.9(a)**).

Interaction with the electric field is represented then by transition between the Floquet states. When the states are coupled by the field, it causes so-called *avoided crossings* of potential energy surfaces separated by an odd number of photons (selection

rule) (Fig. **3.9(b)**). Coupling depends on the molecular orientation and field strength. When the field is very weak then the potential curves are very close to the field-free (*diabatic*) ones and avoided crossings are not available. With the increasing intensity avoided crossings become available and the nuclear wave packet follows *adiabatic* curves.

In Fig. **3.10** we can see adiabatic and diabatic curves for H_2^+ ions with one- and three-photons crossings. The nuclear wave packet oscillates on the vibrational levels of the potential well of the diabatic bound state; at one-photon crossings it oscillates with the laser frequency and at three-photon crossings it oscillates 3 times faster. One- and three-photon avoided crossings become available in the increasing field. First, there is a one-photon crossing, which, according to [**70**], has no effect because the gap is above any of the vibrational levels in a potential well of σ_g. Then, at three-photon avoided crossing the wave packet initially arrives to the gap when it is very narrow, so that curves are close to diabatic. Therefore, there is high probability that the part of wave packet will cross the gap diabatically (Fig. **3.11(a)**) [**70**]. When wave packet returns back to the crossing later, the gap is already wide and the packet is trapped in a potential well of the adiabatic curve (Fig. **3.11(b)**). This is the *bond hardening phenomenon*. The rest of the wave packet continues to oscillate on the other side of the crossing. It returns to the gap during the next oscillation period, when it is wide enough to let wave packet escape down the adiabatic curve completing the *bond softening process* (Fig**. 3.11(c)**). While passing through the crossing, molecule emits one photon, and this process will correspond to the two-photon dissociation [**21**].

The bond-hardened states of course can be stable only in CW laser fields, and with pulsed laser they decay after a while. It is called *transient vibrational trapping*. As intensity decreases, the shape of the curves changes and the potential well bends upward. It finally releases the wave packet partially back to $1s\sigma_g$ and partially to one-photon dissociation limit. The faster intensity changes the stronger is the push and larger kinetic energy is (Fig. **3.11(c)**) [**70**].

Figure 3.10 Molecular potential curves of the H_2^+ ion dressed in 792 nm field. Showing the one- and three-photons avoided crossings and the gap width dependence on the field intensity. The figure is from L. J. Frasinski et al. Phys. Rev Lett. 83, 3625 (1999) [70]

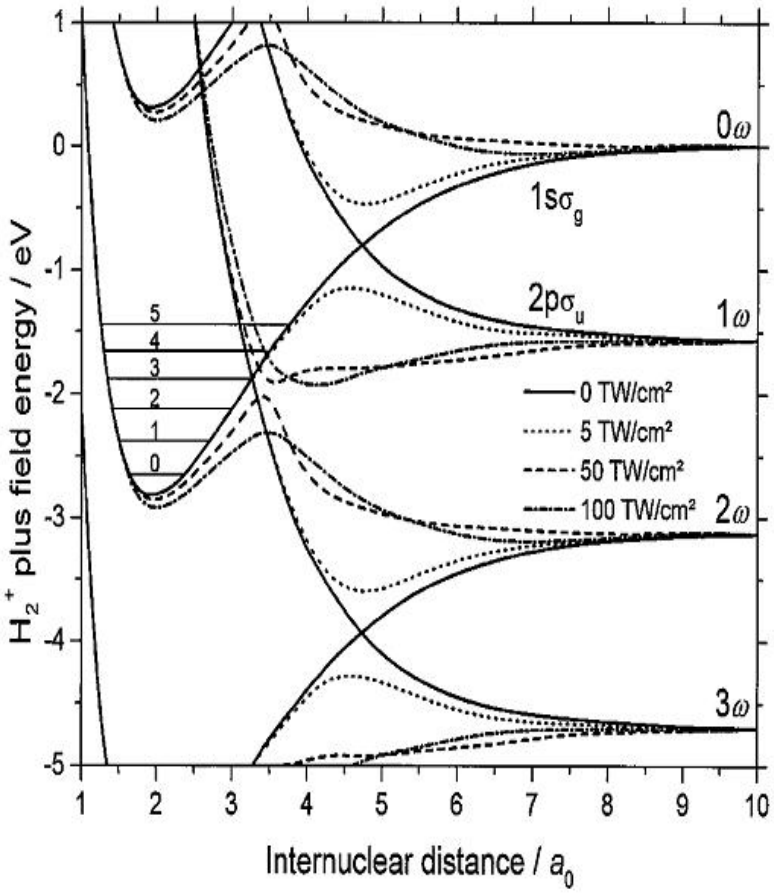

Bond hardening is observed over a very narrow range of intensities between 100 and 200 TW/cm^2 with near-IR laser pulses [**70**]. The lower intensity is the threshold for population trapping in the bond-hardened state. The upper limit is not so much related to the well becoming shallow and not holding any vibrational states, but rather to the point where the probability of ionization becomes much higher than the probability of trapping.

Figure 3.11 Schematic drawing of the bond-hardening dynamics. The three-photon crossing: (a) the gap is very narrow and the wave packet can pass it diabatically; (b) the gap is wide and the avoided crossing cannot be passes by the wave packet, it is trapped; (c) the wave packet is released. The figure is from L. J. Frasinski et al. Phys. Rev Lett. 83, 3625 (1999) [70]

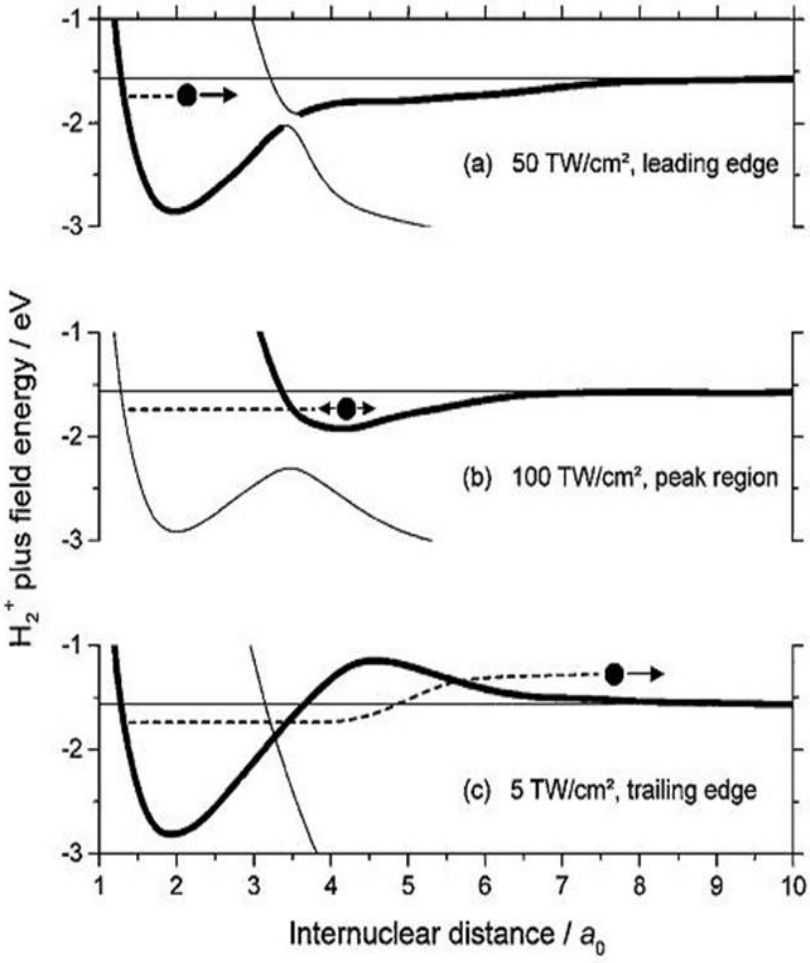

In recent work of Magrakveligze et al [**72**] quantum beat power spectra for H_2^+ and D_2^+ were simulated and analyzed in terms of field dressed states. The authors were interested in manifestations of BS and BH transient states and their dependence on laser pulse frequency, duration and intensity. Theoretical analysis revealed that pulses with a wavelength between 200 to 300 nm, peak intensity of about 10^{14} W/cm^2, and duration of less than 50 fs are well suited for the observation of transient vibrational trapping of the molecular motion in the potential well at one-photon crossings. For 1600 nm dissociation proceed through both one- and three-photon crossings and vibrational trapping is observed in the potential well at the three-photon crossing. As of today, there is no clear

experimental evidence of bond hardened states decay. Though, BS peak is clearly distinguished in TOF or kinetic energy release spectra along with the Coulomb explosion (CE) and the enhanced ionization (EI) peaks in experiments on D_2 and H_2 fragmentation, and using a wide range of experimental parameters (see Fig. **3.12** adopted from [**73**]).

Figure 3.12 D^+ kinetic energy spectra: intensity $5x10^{14}$ W/cm^2, linearly polarized pulse of two durations 8.6 fs and 40 fs. The figure is from F. Legare et al. Phys. Rev. Lett. 91, 093002 (2003) [73]

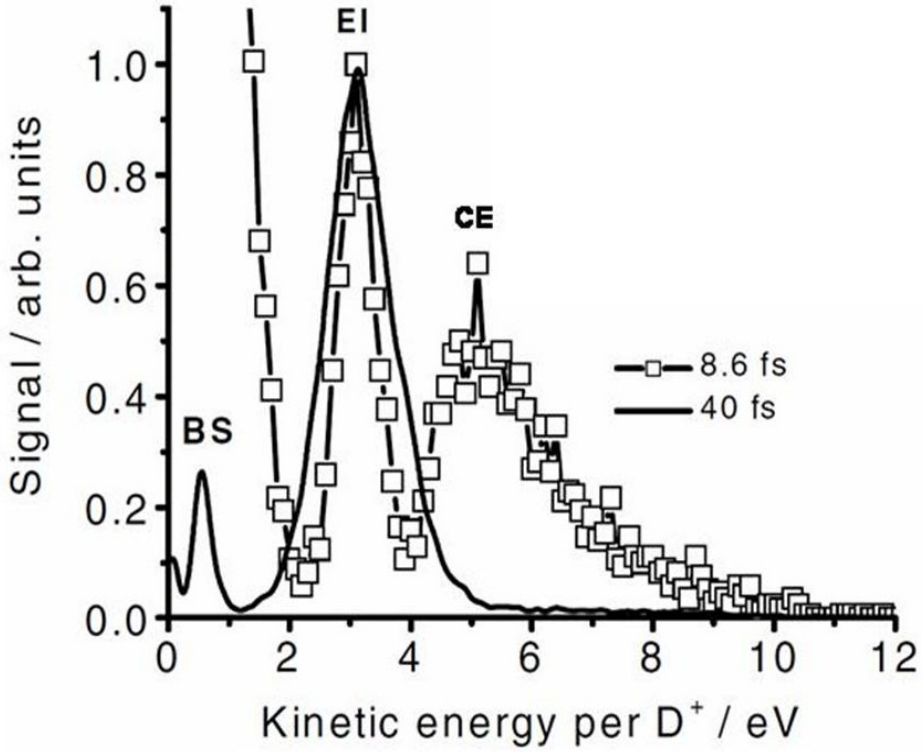

3.2.2 Rotation of diatomic molecules induced by laser field.

Molecular alignment is another effect of interaction with a strong laser field. It is related to *rotational Raman transitions* and requires an anisotropic polarizability in the molecule. When electromagnetic radiation falls on the molecule, the radiation can be scattered by it. When the scattered radiation is of a different frequency, the effect may be due to *Raman scattering* and can be used, for instance, for studying rotational levels structure of the homonuclear diatomic molecules in ground electronic state [**48**]. As mentioned in section **3.1.2** of this Chapter, for homonuclear diatomic molecules,

rotational transitions are forbidden if the electronic state does not change, because they have zero permanent dipole moment. But as a result of interaction with a strong laser field, the dipole can be induced due to the Stark effect (energy level splitting in an electric field) if polarizability of a molecule is anisotropic. When the system is initially in some state J and the energy of the incident monochromatic radiation does not correspond to the energy difference between the initial state and any other (rotational, vibrational, electronic) state, then the energy is not absorbed. The dipole is induced or else it can be said that the molecule is in the virtual state [**48**].

Looking at a diatomic molecule as the classical rigid rotor we write its dipole moment in a static field as

$$\overline{\mu} = \overline{\mu}_0 + \frac{1}{2}\boldsymbol{\alpha}\overline{E} \tag{3.35}$$

where $\overline{\mu}_0$ is the permanent dipole (which is zero for the homonuclear molecule) and $\boldsymbol{\alpha}$ is the anisotropic polarizability tensor. The second term is the dipole moment induced by the field. The higher order terms are neglected here. The anisotropic polarizability tensor has two principal components parallel $\alpha_{\|}$ and perpendicular $\alpha_{\perp}$ to the molecular axis of the diatomic molecule.

$$\frac{1}{2}\boldsymbol{\alpha}\overline{E} = \frac{1}{2}\left[\alpha_{\text{II}} E\cos\theta\hat{e}_{II} - \alpha_{\perp} E\sin\theta\hat{e}_{\perp}\right] \tag{3.36}$$

where θ is the angle between the molecular axis and the field direction in the body frame. The motion of the rigid rotor is governed by Newton's classical equation:

$$\overline{\mu}\times\overline{E}(t) = I\frac{d^2\theta}{dt^2} \tag{3.37}$$

where I is the moment of inertia of the diatomic molecule. Then in the field, the molecule experiences a torque:

$$\overline{\mu}\times\overline{E}(t) = \mu_0 E(t)\sin\theta - \frac{1}{4}\Delta\alpha E^2(t)\sin 2\theta \tag{3.38}$$

$\Delta\alpha = \left[\alpha_{\text{II}} - \alpha_{\perp}\right]$ is polarizability anisotropy.

In addition to the condition of having anisotropic polarizability for homonuclear diatomic molecules, the selection rules for rotational Raman transitions for all diatomic molecules are:

$$\Delta J = 0, \pm 2 \qquad \textbf{(3.39)}$$

Thus, all diatomic molecules independent of their symmetry show rotational Raman spectra.

In our experiment (Chapter **4**) the nuclear rotational dynamics of neutral hydrogen and deuterium and their molecular ions were studied. For the modeling of the field-free rotational wave packet evolution we used the quantum rotor model. The description of this model along with the details of the related numerical simulations can be found in the Appendix **C**.

CHAPTER 4 – Direct Coulomb explosion imaging of coherent nuclear dynamics induced by few-cycle laser pulses in light and heavy hydrogen

4.1 Introduction

A laser field couples with electronic motion and with vibrational and rotational nuclear motion. Time scales associated with each motion are significantly different as discussed in Chapter 3 of this thesis. Therefore, it is possible to focus on one kind of nuclear motion neglecting the others.

Available femtosecond lasers and the advantages of the pump-probe technique allow scientists to get better insight into the dynamics of nuclear motion during chemical reactions. Rotational and vibrational nuclear motions can be studied these days with high temporal and spatial resolution. The hydrogen and deuterium molecules and their molecular ions are popular targets for these kinds of studies, both experimental and theoretical. Even the simplest existing molecule, H_2^+, a seemingly uncomplicated system of two protons bound by a single electron, when put into a sufficiently strong oscillating electric field, presents researchers with an astonishing wealth of physical phenomena, such as bond softening [**12**], bond hardening [**12**, **74**], charge resonance enhanced ionization (CREI) [**14**, **75**], high-order harmonic generation (HHG) [**16**, **76**] and above threshold dissociation (ATD) [**15**] (for review see [**21**] and included references). Understanding the behavior of molecular hydrogen is an important first step towards larger more complex molecules. In particular, uncovering detailed ionization and dissociation mechanisms will contribute to disentangling the complex pathways involved in molecular Coulomb explosion – the technique carrying some promise for the dynamic imaging of molecular structure. Despite being the simplest neutral molecule, hydrogen in one sense is more challenging to study experimentally than larger molecules – its nuclei are the lightest and their motion is the fastest.

Figure 4.1 (a) D^+ kinetic energy spectrum as a function of the delay between pump and probe pulses; (b) The distribution of the D_2^+ wave packet probability density as a function of the internuclear distances and the delay. 1 – vibrations on $1s\sigma_g$ bound state; 2- the wave packet evolution on dissociative $2p\sigma_u$ curve; 3 – bond softening: $D_2^+ \rightarrow D^+ + D$. The figure is from Th. Ergler et al. Phys. Rev. Lett. 97, 193001 (2006) [77]

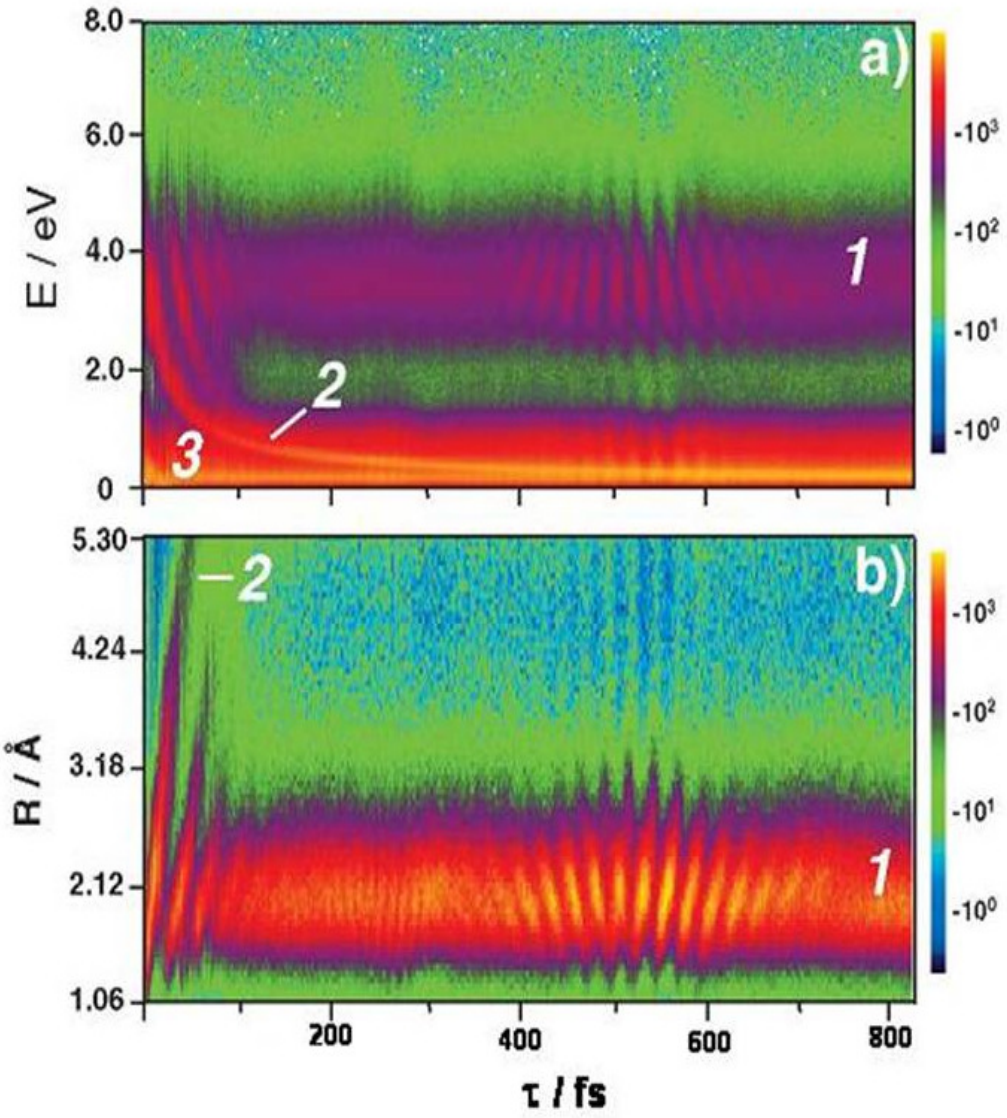

High-resolution real-time tracking of the nuclear wave packet motion on bound $1s\sigma_g$ and unbound $2p\sigma_u$ energy surfaces of H_2^+, D_2^+, and oscillation in the potential well of the ground state of a neutral D_2 molecule have been reported in several studies [**77-79**]. Kinetic energy of atomic fragments D^+ as a function of pump-probe delay spectra clearly demonstrate features reflecting the wave packet dynamics. First, a descending trace of the wave packet dissociating along the unbound $2p\sigma_u$ curve can be distinguished. Second,

the oscillation of the bound part of wave packet on the $1s\sigma_g$ potential surface is observed: the vibrational structure and its subsequent dephasing and rephrasing (half revival at ~250 fs and full revival at ~560 fs) are clearly seen in Fig. **4.1** adopted from the paper of Egler at al [**77**].

Numerical simulations of the wave packet motion on one-dimensional Born-Opennheimer potentials of the D_2^+ ion with the subsequent D^++D^+ Coulomb explosion showed a very good agreement between the experimental and calculated time-dependent kinetic energy release (KER) spectra. Fig. **4.2(a)** presents the KER versus pump-probe delay spectrum which reveals same features as the experimental spectrum on panel **(b)**. The vibrational dynamics of deuterium is very fast: as can be estimated from Fig. **4.2** the full oscillation period is about 20 fs.

Figure 4.2 Kinetic energy release for the $D_2^+ \rightarrow D^+ + D^+$ Coulomb explosion channel as a function of pump-probe delay. (a) model calculation; (b) Experiment: pump intensity 3×10^{14} W/cm^2; probe intensity 9×10^{14} W/cm^2; pulse duration is 10 fs. The figure is from A.S. Alnaser et al. Phys. Rev. A 72, 030702(R) (2005) [79]

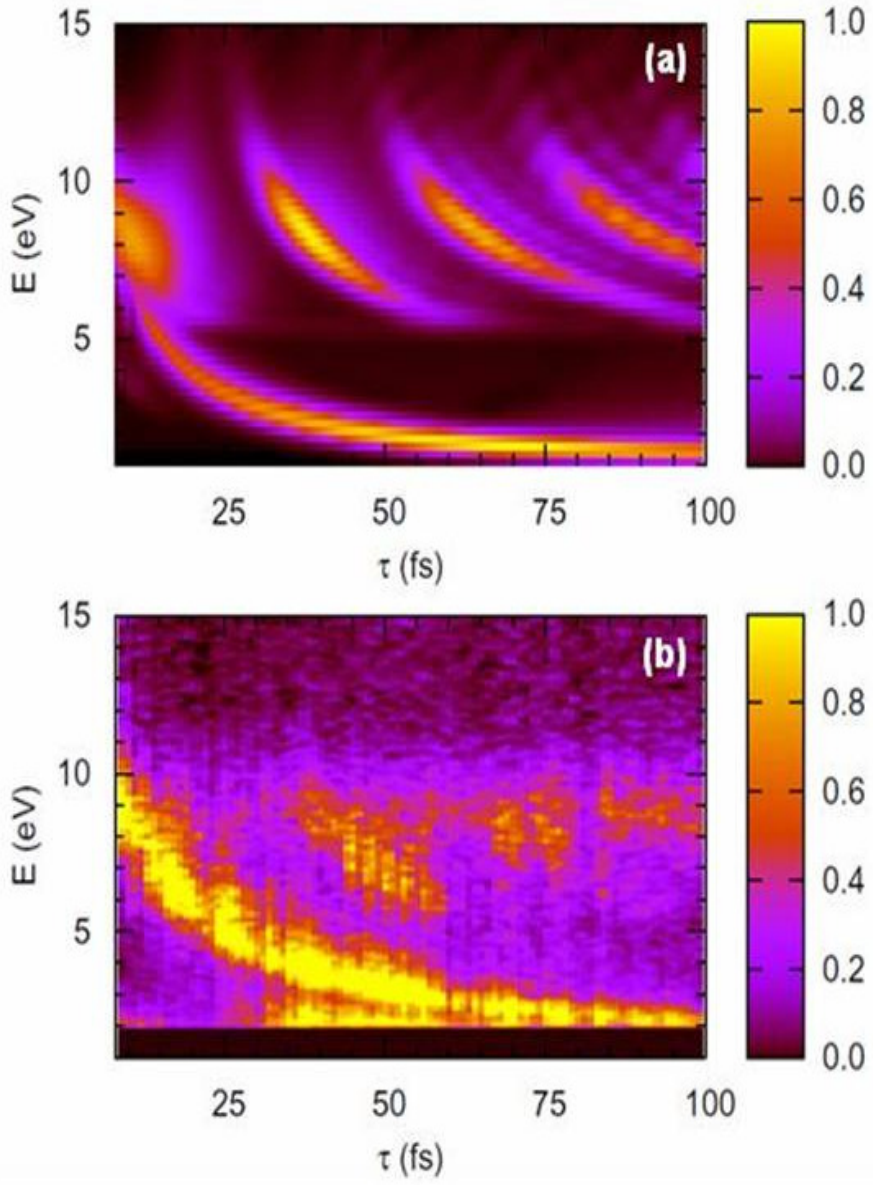

Coherent rotational wave packets are also being studied and successfully used as a tool for the molecular alignment experiments. Aligning molecules in a strong laser field has a significant potential for the application in different areas of light-matter interaction. For instance, it is employed for measuring an angular dependence of different molecular processes such as ionization [**80**] and high harmonics generation [**81**] and for a tomographic imaging of molecular orbitals [**82**].

If the laser field is applied adiabatically (pulse duration is much longer then the rotational period of a molecule), then the molecule aligns its axis parallel to the polarization direction and remains aligned for the duration of the pulse. But the presence of the strong aligning field can interfere with the measurements one wants to conduct. In contrast, when the pulse duration is much shorter than the rotation period, the pulse just gives molecule a "kick" in the direction of alignment. Resulting coherent rotational wave packet experiences periodic revivals resulting in so-called dynamic alignment. In this case rotation and alignment are field-free and the experimental measurements are unaffected by an external field. Above all, in short pulse experiments with linearly polarized pulses, like the ones we present in this study, molecular dissociation is rapid. It means that measured initial velocities of the break-up fragments are parallel to the molecular axis of the diatomic molecule. Therefore, in this kind of experiment we directly measure dynamics of the molecular orientation.

In classical visualization of rotation (see section **3.2.2**) we imagine an ensemble of randomly oriented diatomic molecules and an electric field applied along a chosen direction. The larger initial angle between the molecular and electric field axes θ is, the greater torque the molecule will experience (see section **3.3.1** for classical rigid rotor model). At some time following the pulse the faster rotating molecules will catch up with slower ones and the alignment will be achieved. As the molecules continue to rotate with different velocities the alignment will be destroyed. There is no classical analog to the periodic quantum revivals.

The quantum rigid rotor model describing field-free molecular rotation is discussed in detail in Appendix **B**. Briefly, from the quantum point of view, when the aligning pulse is short compared to the rotation period, a coherent superposition of rotational J states is created – rotational wave packet – that outlives the laser pulse and continues to evolve. The frequency components of the rotational wave packet are the beat frequencies between different pairs of rotational states. Due to the quantization of J-levels periodic field-free revivals occur. The greater number of J-levels is populated the longer the revival time is.

Figure 4.3 Imaging of the rotational wave packet for the N_2 molecule: pump-probe experiment with a linear pump, circular probe. The pulse duration for both pump and probe is 45 fs. Angle θ is the angle between the molecular axis and polarization plane of the probe pulse. (a) Rotational revivals for N_2 ($\langle\cos^2\theta\rangle$=0.5 corresponds to an isotropic distribution of molecular orientations) and the Fourier transform revealing populated J-states and beat frequencies. (b)-(d) Measured (dots) and calculated (solid lines) angular distributions measured at fixed moments depicted by arrows on $\langle\cos^2\theta\rangle$ distribution. The figure is from P. W. Dooley et al. Phys. Rev. A 68, 023406 (2003) [83]

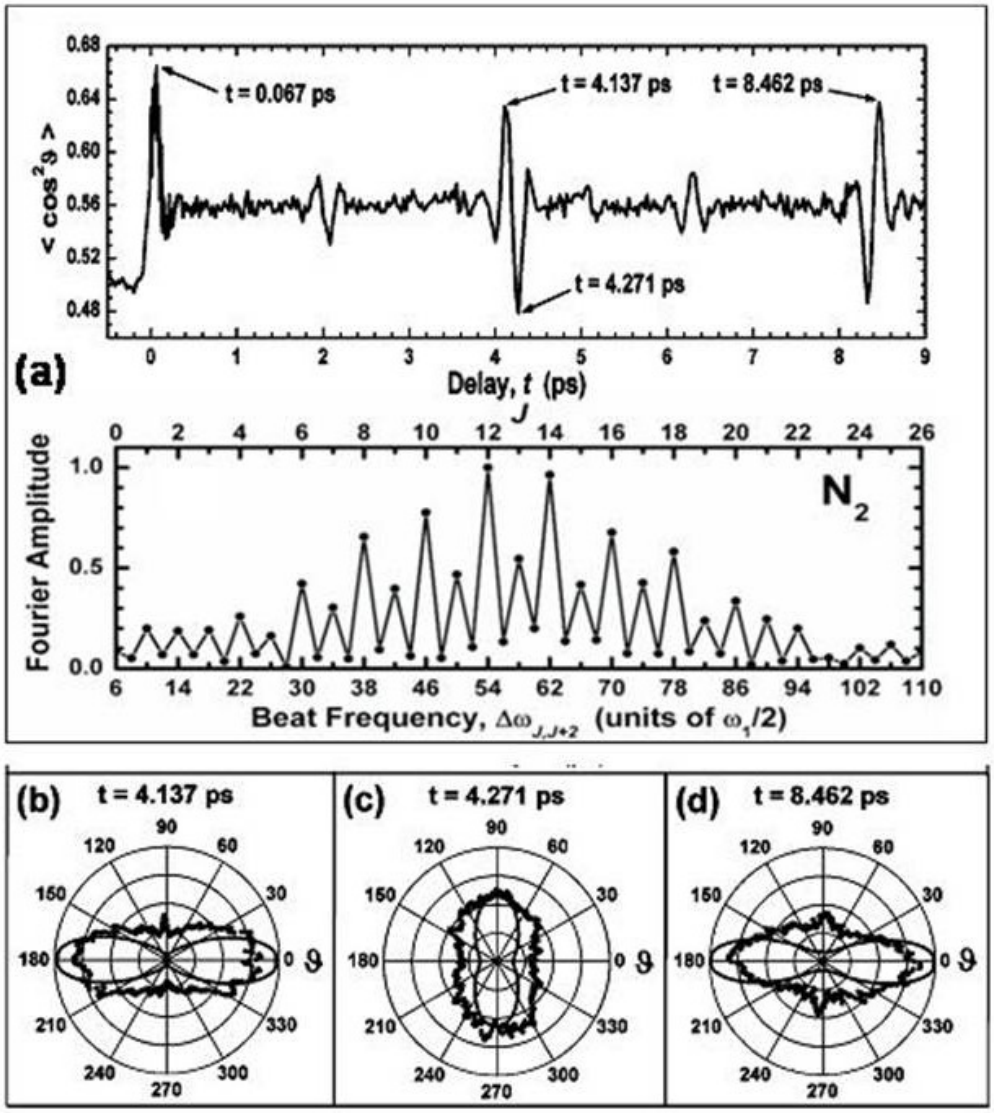

To extract qualitative information from measurements made in laboratory frame the complete angular distribution must be known. There are two traditional approaches to this problem [**83**]. (a) Measure the phases and amplitudes of all populated J-states. To do that we can measure the time-dependence of some parameter characterizing rotational motion and perform a Fourier transform. Then we can compare the experimental result

with some numeric simulation of the process with the same parameters as in the experiment. For instance, it is common to measure $<\cos^2\theta>$ as a degree of alignment, which has to be normalized to the background θ-distribution to correct for aligning effect of the exploding pulse. (b) Measure angular distribution at a particular time. The example of rotational revivals and angular distributions for N_2 molecule from [**83**] is presented in Fig. **4.3**.

With pulses around 50 fs long light molecules like N_2 and O_2 have been aligned [**83, 84**]. However, hydrogen and deuterium are much harder to align due to their low polarizability anisotropy and low rotational inertia. Energy separation between rotational levels is large: at the room temperature which corresponds to 25 meV only the first rotational state of hydrogen (15 meV) is populated - the second rotational state is 30 meV above the first one. With low polarizability anisotropy $\Delta\alpha$ a laser beam with peak intensity on the order of 10^{13} W/cm^2 produces a potential well as shallow as 3 meV [**86**]. Therefore, extracting parameters differential in respect to the molecular angle remains problematic for these lightest molecules. For instance, it remained unknown how different the ionization rates are for hydrogen molecules aligned parallel and perpendicular to the laser polarization. It was shown before that femtosecond pulses generate rotational wave packets in D_2 [**84**-**86**] and H_2 [**84**].

Here I present a study of nuclear dynamics induced in H_2 and D_2 by 8 fs 800 nm laser pulses. We probed fast nuclear motion by exploding the molecule with another more intense time-delayed few-cycle pulse and measuring the 3D momenta of the resulting fragments. We specifically focused on rotational motion of these molecules, having followed it for up to 10 ps in time delay. In this chapter I present the results in the following order. First, I show time-resolved kinetic energy release (KER) spectra and explain how we separate rotational dynamics in neutral molecules from that of molecular ions. Then, I focus on rotational motion of H_2, D_2, H_2^+ and D_2^+. I present and discuss measured time traces of $\langle\cos^2\theta\rangle$ - a parameter characterizing molecular alignment. Next, for neutral molecules I also show experimental angular distributions at different points in the evolution of coherent rotational wavepackets. Based on these distributions, and on measured time-dependent yields for single ionization channels of D_2, we put an upper limit on the strong-field ionization anisotropy of this molecule and conclude that its

ionization is nearly isotropic under conditions used in our experiment. The last subject in the discussion section is the rotational dynamics observed in molecules which have been ionized by the pump pulse. The chapter is concluded with the summary.

4.2 Results and discussion

Nuclear dynamics in H_2 and D_2 was initiated by an 8 fs pump pulse of peak intensity of 1.0×10^{14} W/cm^2. At this intensity only a small fraction of molecules within the interaction region is ionized at the peak of the pulse. In such molecules a coherent vibrational wavepacket is launched on the ground electronic state (σ_g) potential energy surface of the molecular ion. Consequently, at the tail of the pump pulse this wavepacket can be promoted to the lowest excited state (σ_u) which is repulsive, leading to dissociation of the molecule. However, the majority of the molecules remains neutral and experience only rotational excitation. The dynamics following the pump pulse is interrogated by a time-delayed probe pulse of the same duration but higher intensity (3×10^{14} W/cm^2). This intensity is sufficient to ionize most neutral molecules at least singly (dissociating some of them), to remove the remaining electron from molecular ions produced by the pump pulse, and to doubly ionize a significant fraction of neutrals. Doubly ionized molecules will undergo immediate Coulomb explosion, with the resulting kinetic energy release (KER) closely mapping the internuclear distance at which the last electron was removed. At the same time the direction of the fragments' momenta reflects the direction of internuclear axes at the same moment. Thus, time-dependent KER spectra image vibrational (and dissociative) motion of the molecule, while time-dependence of angular distributions reflects its rotational dynamics.

4.2.1 Coherent vibrational dynamics in D_2^+

Fig. **4.4** presents time-dependent KER spectra for D^+ (showing the sum energy for two fragments) in the time interval from -200 fs to 1200 fs. Most of the D^+ signal falls within the 9 – 15 eV energy band and does not exhibit any time dependence. That corresponds to sequential double ionization of neutral D_2 by a few-cycle pulse, when the enhanced ionization process (~ 5 eV energy) is suppressed. In addition one can see both

vibrating and dissociating wave packets launched by the pump in D_2^+. To better reveal that dynamics, the time-independent part can be easily subtracted from the KER spectra. In the initial matrix representing the full spectrum with both time-dependent and independent parts we choose a column vector corresponding to the area of the plot with a steady (clear of dynamical features) picture (at 800 fs delay). Cloning this vector we created a matrix of the time-independent background of the same dimensions as the initial one. The subtraction of the "background" matrix from the "full" matrix yields the "clean" spectrum shown in Fig. **4.4(b)**. The dissociating wavepacket results in a trace of monotonically decreasing kinetic energy which asymptotically approaches 1.2 eV – the ultimate energy of the dissociation fragments, as Coulomb repulsion adds nothing to this energy when the second ionization takes place at very large distances. The dissociation is mostly complete within 100 fs. The bound vibrational wavepacket undergoes a few quasi-periodic oscillations, before anharmonicity of the potential causes it to dephase. After about 600 fs the wavepacket experiences a revival, followed by another one 600 fs later, as was predicted theoretically [**87**] and was seen in previous experiments [**77**]. The spectra at negative delays represent the case of reverse order of pulses – when the more intense pulse serves as a pump. We did not follow it past 200 fs delays, but within that range the general features of the dynamics are similar to the weaker pump – stronger probe case, though the branching ratio between the bound and dissociating states is obviously changed in favor of dissociation.

Figure 4.4 Time-dependent kinetic energy release (KER) spectra for D_2. Pump pulse – 8 fs 1×10^{14} W/cm^2; probe pulse – 8 fs 3×10^{14} W/cm^2. Panel (a) shows full spectrum including the time-independent 9-16 eV band resulting from the probe exploding the neutral D_2 molecules. Panel (b) shows KER for the molecules ionized by the pump – time independent band is subtracted. (c) and (d) – same as (b) focusing on dynamics at short pump-probe delays and around the vibrational revival time. The figure is from I. A. Bocharova et al. Phys. Rev. A 77, 053407 (2008)

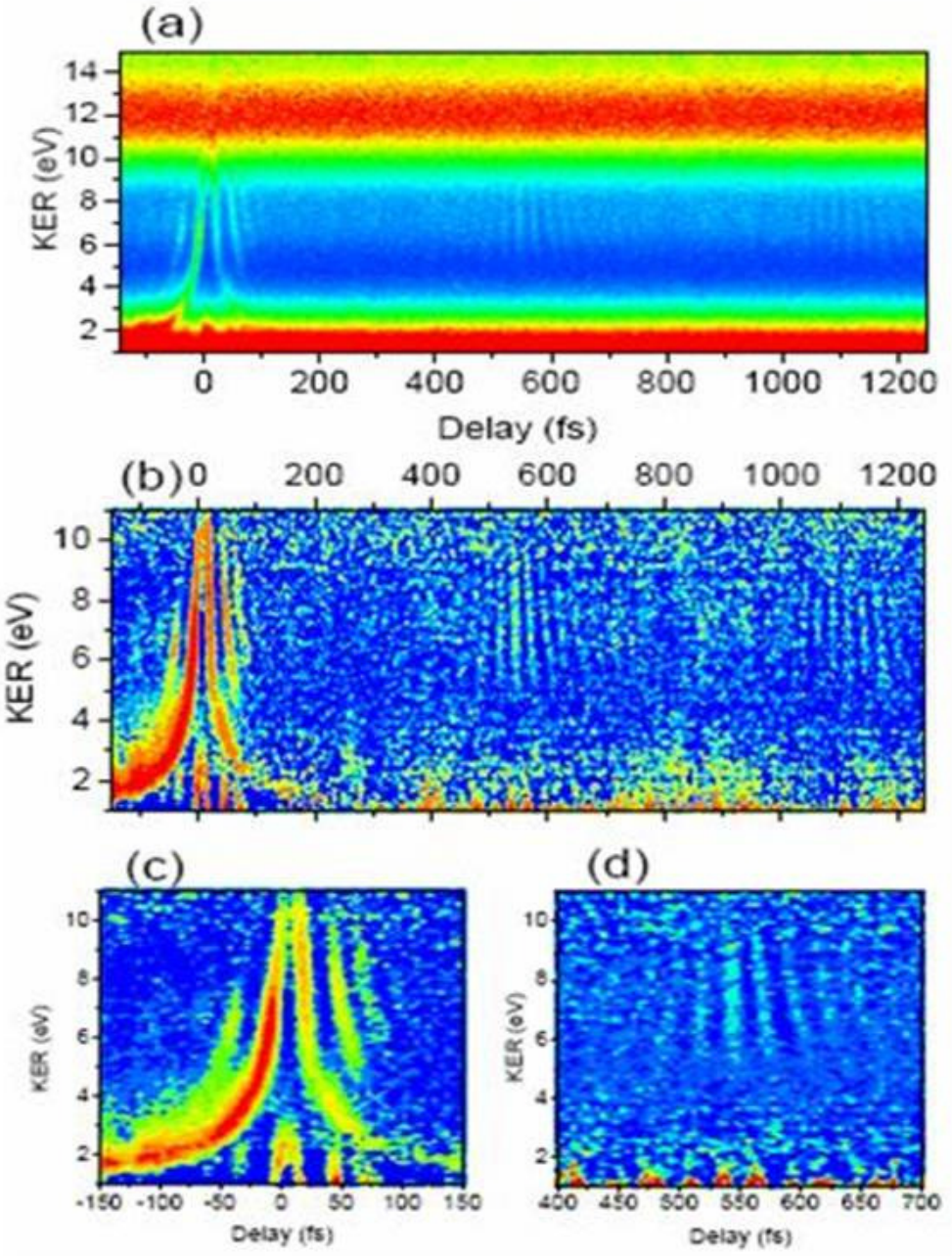

4.2.2 Coherent rotational dynamics in neutral molecules

To image the rotational motion we measured time-dependent angular distributions of fragments. In the first approximation angular distributions can be characterized by a single parameter - $\langle\cos^2\theta\rangle$ - average squared cosine of the angle θ between the molecular axes and a preferred direction (in our case the polarization direction of the pump pulse). To separate rotational dynamics of neutral molecules from that of molecular ions we put a gate on kinetic energy of the fragments: 9 – 15 eV fragments are dominated by exploding neutrals, while 5 – 9 eV fragments come mostly from the ions which are typically ionized the second time at larger internuclear distances. Even for short 8 fs linearly polarized probe pulses the Coulomb explosion process itself is not isotropic: when applied to an initially isotropic ensemble of molecules it produces a fragment angular distribution biased towards the laser polarization direction. This bias is caused by a combination of factors: a possible angular dependence of both ionization steps and also of the intermediate nuclear dynamics (so-called geometric alignment); rotation of molecular axis towards the polarization direction during the pulse before the explosion (dynamic alignment); and limited validity of the axial recoil approximation for fast rotating molecules (post-ionization alignment [**88**]). The relative importance of those factors for hydrogen Coulomb explosion is still being debated. In our analysis we accounted for this bias by normalizing the measured angular distributions to those obtained with probe pulses alone, so that after the normalization an isotropic ensemble of molecules would yield an isotropic distribution of fragments with $\langle\cos^2\theta\rangle = 1/3$.

Figure 4.5 Rotational dynamics of neutral H_2 and D_2: (a) and (b) – measured (symbols and dotted line) and calculated (solid line) time traces of $\langle\cos^2\theta\rangle$ (see text for details) for H_2 and D_2; (c) and (d) – Fourier spectra of measured (with symbols) and calculated (inverted scale) time traces of $\langle\cos^2\theta\rangle$ for H_2 and D_2. Each line corresponds to a (J, J+2) energy difference as indicated. Arrows represent the spectral bandwidth of an 8 fs laser pulse. Simulations used 10 fs 1×10^{14} W/cm^2 pulses. Initial rotational temperature was taken to be 250 K for D_2 and 295 K for H_2. The figure is from I. A. Bocharova et al. Phys. Rev. A 77, 053407 (2008)

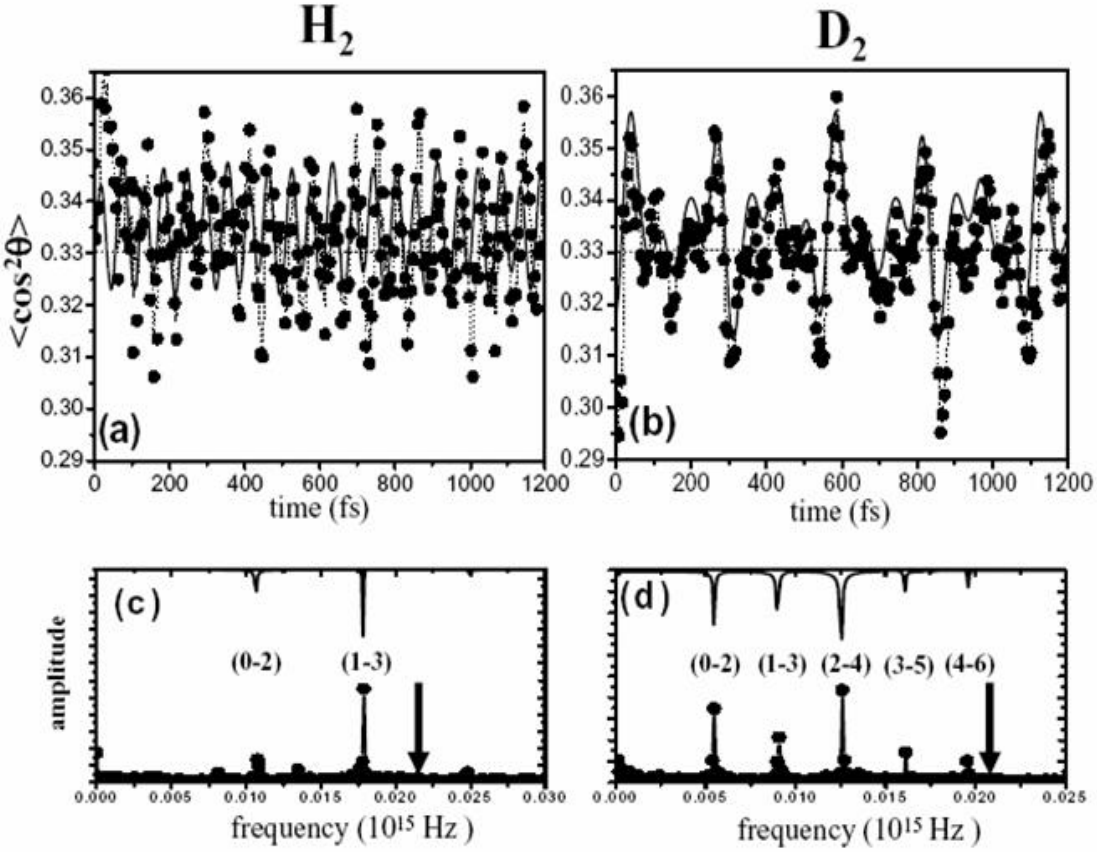

The time dependence of $\langle\cos^2\theta\rangle$ for normalized angular distributions of neutral D_2 and H_2, isolated by limiting the KER to 9-15 eV, is shown in Fig. **4.5**. The trace is typical of coherent rotational wavepackets with characteristic periodic revivals and alternating states of alignment and anti-alignment. For D_2 the full rotational period is 558 fs, while for H_2 it is half that (279 fs). The figure presents only the 0 – 1200 fs delay-time range to emphasize the main features of the dynamics. This pattern repeats itself periodically up to 10 ps of delay without any signs of decoherence. These coherent rotational wavepackets can be interpreted as very fast classical rotations of the molecular axes: it takes only 30 fs for H_2 and 40 fs for D_2 to rotate by 90° (from alignment to anti-alignment). Although the range of change for $\langle\cos^2\theta\rangle$ is almost the same (0.30 – 0.36) for light and heavy

molecules, for D_2 the revivals look more like those seen in heavier molecules (O_2 and N_2 – [**84**]), while for H_2 they more resemble a beating pattern. The Fourier transform of the two time traces emphasizes the difference. Each narrow line in the Fourier spectrum corresponds to an energy difference between a pair of rotational states with rotational quantum numbers J and J+2. For H_2 the spectrum is dominated by just two lines – (0-2) and (1-3). Each of them is associated with a particular nuclear spin isomer of light hydrogen: ortho-H_2 is allowed only odd J states, para-H_2 only even J states.

Nucleus of an H-atom consists of a single proton. It is characterized by spin ½. In H_2 molecule spins of the protons couple with a resultant spin *I* of the molecule 1 (parallel proton spins) or 0 (antiparallel proton spins). For the first spin-state of H_2 the statistical weight *(2I+1)* is 3 (projections of the spin are -1, 0 and 1): those are the triplet symmetric states; for the second one the weight is 1: that is the antisymmetric singlet state. The odd J-states are antisymmetric and even J-states are symmetric with respect to the nuclei interchange. The total wave function of hydrogen must be antisymmetric, and the electron ground state is symmetric. J-states now must be coupled with spin-functions of specific symmetry to maintain required overall symmetry. Therefore even J-states must have spin 0 (ortho-hydrogen) and odd J-states must have spin 1 (para-hydrogen). The statistical weight defines that odd states occur three times as frequently as the even in light hydrogen. For deuterium the difference is that the nucleus of D-atom consists of a proton and neutron and its spin is 1 and the total wave function is symmetric with respect to the nuclei interchange. Therefore, the D_2 nucleus has a resultant spin 2, 1 (symmetric spin-states) or 0 (antisymmetric spin-state) with statistical weight 5, 3 and 1 correspondingly. Even Js are symmetric states must have spin either 0 or 2 and odd Js are antisymmetric states must have spin 1. It means that the ratio of occurrence of ortho- and para-deuterium is 3:(1+5):3 = 1:2, so that even Js appear twice as often as odd states.

The statistical ortho-para ratio (3:1 for H_2 and 1:2 for D_2) is reflected in the relative heights of the two lines in the beat frequency spectra. Obviously, in each H_2 spin form the rotational wavepackets consist of just the 2 lowest rotational states beating with each other. In contrast, the D_2 Fourier spectra contain more lines: three for ortho-D_2 (0-2, 2-4 and 4-6) and two for para-D_2 (1-3 and 3-5) resulting in better defined wavepackets and revivals.

The difference between the light and heavy molecules is easy to understand in terms of energy separation between the adjacent J and J+2 rotational levels. The energy separation is twice as large for H_2, making rotational excitation through a sequential non-resonance stimulated Raman process more difficult. For both H_2 and D_2 the rotational level spacing is much larger than for any other molecule, making them particularly hard to align. For a stimulated Raman transition between two levels to occur efficiently their energy difference must not exceed the bandwidth of the laser pulse, which must contain both up and down transition frequencies. The bandwidth of an 8 fs pulse is given by the uncertainty principle as $\Delta\nu \cdot (8\text{ fs}) \geq (2\pi)^{-1}$ as $\Delta\nu = 0.02\times10^{15}$ Hz, which corresponds to the cutoff frequency in the Fourier spectra for both H_2 and D_2. It appears that, quite counterintuitively, even shorter pulses (or non-transform-limited pulses with a broader bandwidth) are needed to better align hydrogen.

We simulated rotational dynamics of neutral H_2 and D_2 molecules by solving the time-dependent Schrödinger equation for a rigid rotor coupled to the field by anisotropic polarizability (see Appendix **C** for details). The calculated $\langle\cos^2\theta\rangle$ traces and Fourier spectra are in excellent agreement with our experimental results, when we use a Gaussian pulse of 10 fs (intensity FWHM) duration and 1×10^{14} W/cm^2 peak intensity. However, to reproduce our experimental results well we had to take the initial rotational temperature of D_2 to be 250 K or higher. That is more than twice as hot as the measured translational temperature of our D_2 jet (110 K) and only slightly cooler than the room temperature. We conclude that our weakly supersonic molecular jet does not efficiently cool rotational motion of D_2, "freezing" it in a non-Boltzmann distribution with high effective temperature. The large rotational energy level spacing is also responsible for that. We used Boltzmann distribution of initial rotational states in our calculations.

The experimental angular distributions measured for neutral D_2 molecules at the times of maximum alignment and anti-alignment are shown in Fig. **4.6**. They can be well approximated by the formula

$$\Pi(\theta) = \frac{3}{4\pi(1+2\varepsilon)}(\cos^2\theta + \varepsilon\sin^2\theta) \qquad \textbf{(4.1)}$$

where $\Pi(\theta)$ is the probability (per unit solid angle) that the molecular axis makes angle θ with laser polarization, parameter ε describes the ratio of the probabilities for a molecule to be perpendicular and parallel to the laser polarization, and the normalization factor is selected so that $2\pi\int_0^{\pi}\Pi(\theta)\sin\theta d\theta = 1$. For angular distribution **(4.1)**

$$\left\langle \cos^2\theta \right\rangle = \frac{2\varepsilon + 3}{5(2\varepsilon + 1)}. \qquad \textbf{(4.2)}$$

The value of ε corresponding to alignment (anti-alignment) is 0.75 (1.5) meaning that the ratio of probabilities changes by a factor of two as the wavepackets evolve.

4.2.3 Angular dependence of ionization for neutral D_2

It is interesting to use anisotropic angular distributions in order to estimate anisotropy of strong-field ionization rates for D_2. It has been predicted theoretically [**60**] and demonstrated experimentally [**83**, **89**, **90**] that for most linear molecules ionization rates (probabilities) strongly depend on molecular orientation in respect to the laser electric field vector, with this angular dependence reflecting the symmetry of the corresponding molecular orbital. For instance, N_2 is more likely to ionize when it is parallel to the electric field, while for O_2 the ionization probability is the largest for about 45° angle. It is important to know this ionization anisotropy in order to calculate total ionization rates for isotropic molecular gases, to fully understand strong-field experiments performed on pre-aligned molecules and to judge the validity of various theoretical models. It is of particular interest for D_2, as this molecule exhibits significant suppression of ionization rates in comparison to Ar (which has similar ionization potential). Various theories disagree on this issue, with MO-ADK predicting almost no anisotropy [**60**] and other theories finding significant angular dependence [**91**]. To shed some light on this issue we followed time-dependent yields for different ionization channels of rotating D_2 molecules. Fig. **4.7** presents the measured yields for D_2^+ and $D^+ + D$ channels, as well as their correlation with values of $\langle\cos^2\theta\rangle$.

Figure 4.6 Experimental angular distributions measured for D_2 at the times of maximum alignment (hollow circles) and anti-alignment (filled circles). Normalized relative yields (per unit solid angle) for $D^+ + D^+$ channels (9 eV< KER < 18 eV) are shown as functions of cosθ and θ, where θ is the angle between molecular axis (momentum vector of D^+) and polarization direction of the aligning pulse. To improve statistics, momentum angles for uncorrelated D^+ ions with energies 4.5 – 9 eV were measured. Only D^+ ions initially flying away from the detector were considered in order to exclude overlapping backwards H^+ signal from background H_2. The resulting distributions were symmetrically reflected into the other hemisphere. Solid lines show fits with the function $(\cos^2\theta + \varepsilon\sin^2\theta)$: ε = 0.75 for aligned and ε = 1.5 for anti-aligned distributions. The figure is from I. A. Bocharova et al. Phys. Rev. A 77, 053407 (2008)

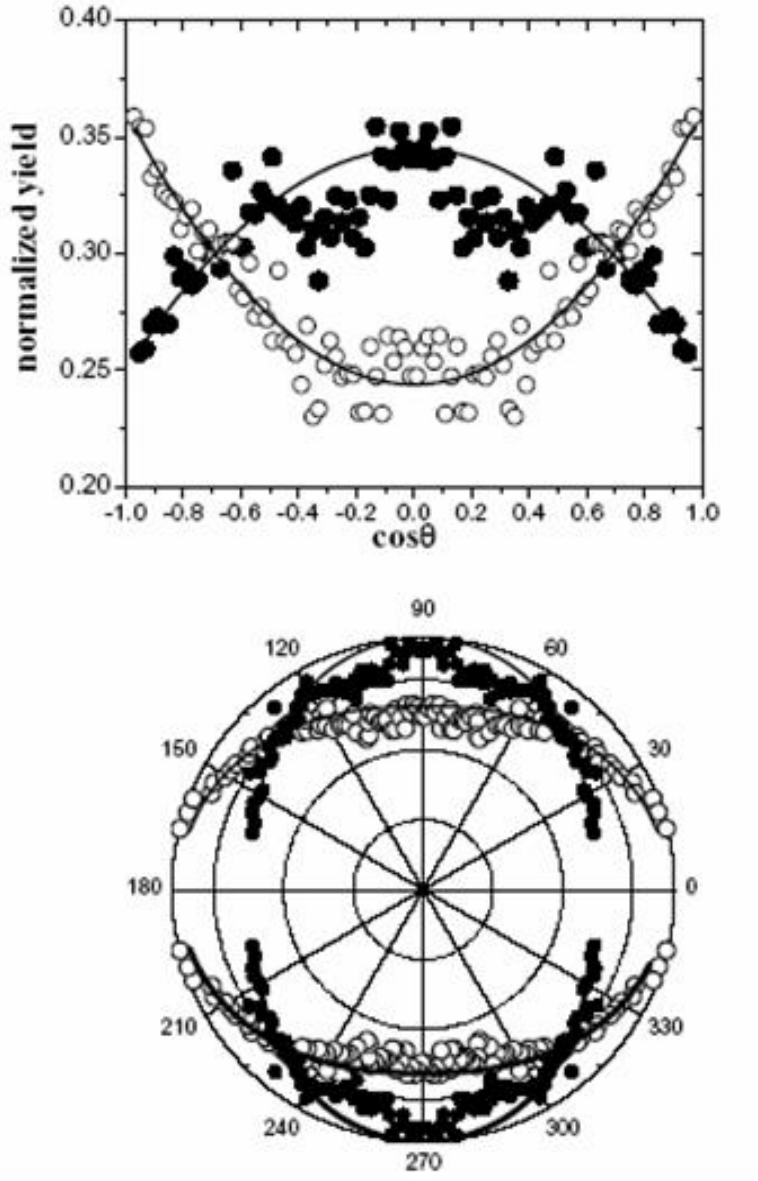

Figure 4.7 Time-dependent yields for single ionization channels of rotating neutral D_2: (a) – alignment parameter $<\cos^2\theta>$; (b) - yield for the bond softening ($D^+ + D$) channel; (c) - yield for the molecular ion (D_2^+); (d) - total yield for both single ionization channels; (e), (f) and (g) – correlation graphs between $<\cos^2\theta>$ and time-dependent yields for ($D^+ + D$), D_2^+ and total single ionization of D_2 respectively. The figure is from I. A. Bocharova et al. Phys. Rev. A 77, 053407 (2008)

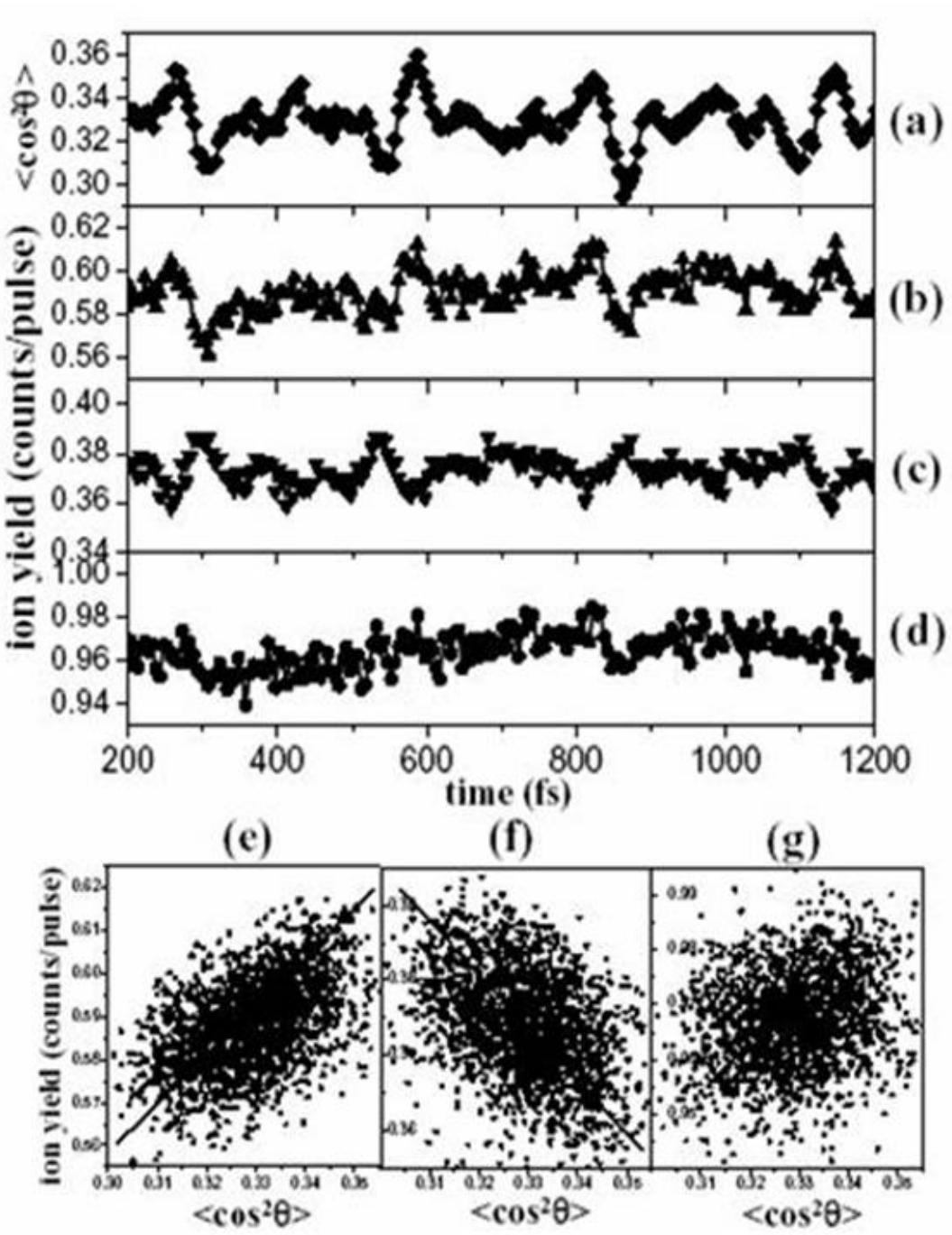

The yield of the Coulomb explosion ($D^+ + D^+$) channel (not shown) did not exhibit any correlation with $\langle\cos^2\theta\rangle$, while the two single ionization channels do correlate with molecular alignment. The yield of an intact molecular ion correlates negatively – less D_2^+ is produced when neutral molecules are aligned along the laser electric field. At the same time the ($D^+ + D$) channel correlates positively – more low energy (0 to 2 eV) deuterons are produced when molecules are aligned. Together these two channels represent single ionization of D_2 by the probe pulse. Some molecular ions remain bound, while others are dissociated by the same pulse through laser-induced bond softening. The bond softening process is known to be very strongly anisotropic – the required field coupling of σ_g and σ_u electronic states is the strongest for molecules aligned along the field. Therefore it is not surprising that at times of maximum alignment more molecular ions are lost to bond softening than for anti-aligned distributions. On balance, variations of the two single ionization channels almost cancel each other out, with a very small positive correlation (yield variation ≤ 1.5%) remaining for total singly ionized D_2 yield.

Based on these results and experimental angular distributions we can put an upper limit on the ionization anisotropy of D_2. To do this we assume that the anisotropic ionization probability is represented by $P(\theta) \sim \cos^2\theta + e \cdot \sin^2\theta$, where θ is the angle between the molecular axis and the laser electric field vector and parameter e represents the ratio of probabilities for molecules aligned perpendicular and along the field. The total ionization signal can be found as

$$S \sim \int_0^{\pi} P(\theta)\Pi(\theta)\sin\theta d\theta \qquad \textbf{(4.3)}$$

where $\Pi(\theta)$ is the angular distribution of molecular axes, which is assumed to be axially symmetric around the polarization (alignment) direction. We also assume that the probe pulse itself does not affect angular distributions much, which seems reasonable with 8 fs pulse duration being less than 40 fs taken by molecules to rotate by 90°. For angular distributions of molecular axes given by **(4.1)** the total ionization signal depends on both anisotropies (ε of the angular distribution and e of the ionization probability) as

$$S(\varepsilon, e) \sim \frac{3 + 2e + 2\varepsilon + 8e\varepsilon}{5(1 + 2\varepsilon)}. \qquad \textbf{(4.4)}$$

Using this formula we can put a lower limit of 0.8 on the value of ***e*** consistent with our data, meaning that with our experimental conditions D_2 molecules aligned along the laser electric field have at the most 1.25 higher probability to be ionized than those aligned perpendicular to the field. Thus, strong field ionization of D_2 appears to be nearly isotropic. However we must note that in our experiments the probe pulse peak intensity (3×10^{14} W/cm^2) was fairly close to saturation intensity and the anisotropy may be much higher for weaker pulses.

4.2.4 Rotation of molecular ions

We also followed rotational dynamics of molecules which are ionized by the pump pulse.

In experimental and theoretical studies of molecular fragmentation it is common to neglect rotational motion and fix the molecular axis along the laser polarization direction. This approximation is based on the observation that molecular dissociation and ionization are very alignment dependent processes. Therefore, in theoretical calculations on phenomena which occur in H_2^+ ion in response to a laser pulse molecule is assumed to be vibrating along fixed direction. Analyzing data collected in experiment it is also often assumed that the angular distribution of fragment measured on the detector is the same as at the moment of molecular break up. Indeed, for pulses much longer than rotational period of H_2^+ ($\approx$ 556 fs) in calculations which included rotation it was shown that the angular distribution of dissociation fragments is very tightly focused along polarization direction. [**66**]. Nowadays, a few femtosecond pulses are used to study the dynamics of such a small molecules, but the same axial recoil approximation is used. It is important to study the rotational dynamics of hydrogen molecular ion to understand the significance of the effect.

Theoretically, the rotation of the hydrogen ion during the process of dissociation initiated by laser pulses was studied in [**92, 93**]. This study was done in relation with the importance of rotation for predicting the dynamics of angular distribution of atomic fragments and therefore the validity of axial approximation. The study was performed for

several pulse lengths between 5 and 135 fs for intensities of the order of 10^{13} W/cm^2 (non-ionizing pulse). The importance of rotation was estimated by calculating the maximum number of rotational J-states populated by pulse for each vibrational state in H_2^+ bound state. It was shown that axial approximation holds best for pulses not shorter than 135 fs: there is a significant alignment during the pulse but very insignificant field-free rotation after the pulse is gone. Calculations of dissociation fragments angular distribution with or without rotation included give little to no difference. To the contrary, with pulses as short as what we use in our experiments (~10 fs) the calculated average square cosine shows relative post-pulse changes of about 10% (and even higher for shorter pulses). The rotational revivals of hydrogen ions have been never observed in experiment, to our knowledge. In our study we attempted to observe the characteristic features of the rotational dynamics of D_2^+ and H_2^+ ions. In the reference [**92**], though, authors also note that effect of rotation and alignment depends strongly on initial population distribution of vibrational and rotational states. Therefore, the direct comparison between our experimental results and the calculations performed on H_2^+ ion is impossible. The calculations were performed starting with the ion in its ground electronic state, incoherently populated vibration states and Boltzmann distribution of population on rotational states. In our experiments H_2^+ ion is produced by ionization of a neutral molecule, and in the laser pulse the states of H_2^+ are coherently populated which also likely gives more weight to the higher J-states.

The molecules which are ionized by the pump pulse in our experiment are characterized by lower KER since the second ionization by the probe typically happens at larger internuclear distances. We plotted $\langle\cos^2\theta\rangle$ for H^+ and D^+ fragments with KER between 5 eV and 9 eV (Fig. **4.8**). Unlike the rotational wavepackets in neutral molecules, the rotational dynamics in molecular ions does not exhibit periodic coherent behavior. There is a prompt alignment immediately after the pulse, much stronger than in the neutrals, which very quickly dephases and never revives within our 10000 fs experimental time-scale. The maximum degree of alignment is reached 18 fs after the peak of the pump pulse for H_2^+ and 35 fs after the pulse for D_2^+. These times are relevant for understanding the dynamics of Coulomb explosion of hydrogen by femtosecond laser pulses, in particular the issue of dynamic versus geometric alignment of molecules during

the pulse. Our data indicate that H_2^+ can be aligned in just 18 fs, while it takes twice as long to align the heavier D_2^+. Therefore, for pulses of about 15 fs duration and more for H_2 and 30 fs and more for D_2 alignment during the pulse will contribute significantly to the overall dynamics of the molecule-field interactions. The absence of prominent rotational revivals in the ions is due to the broad distribution of vibrational states resulting from strong field ionization of neutral molecules. An exact form of that vibrational distribution is a matter of great interest in its own right, with the scarce experimental data [**94**] indicating that it is a strongly non-Frank-Condon one. Each of the vibrational states forming the wavepacket has a different rotational constant (and time) and in its pure form would revive at a different time. Instead of a rigid rotor (as in the case of a neutral molecule) we have a rotor with time-dependent fast-varying rotational constant, resulting in quasi-chaotic rotational motion. Due to that coupling of vibrations and rotations, the vibrational frequency differences seen in time-dependent KER spectra [**95**] also appear in Fourier transforms of time-dependent $\langle\cos^2\theta\rangle$ traces for D_2^+. It is interesting to note that if instead of a coherent vibrational wavepacket one looked at an incoherent superposition of vibrational states (as in ions coming, for instance, from an ion source) one would expect to see coherent rotational motion again, with revivals at regular intervals determined by a rotational constant describing the averaged time-independent distribution of internuclear distances for those ions.

Figure 4.8 Rotational dynamics of D_2^+ and H_2^+ ions produced by the pump: time traces for $\langle\cos^2\theta\rangle$ measured using fragments with 4 eV < KER < 9 eV. Insets represent the full experimental delay time range of 0 to 10000 fs. The figure is from I. A. Bocharova et al. Phys. Rev. A 77, 053407 (2008)

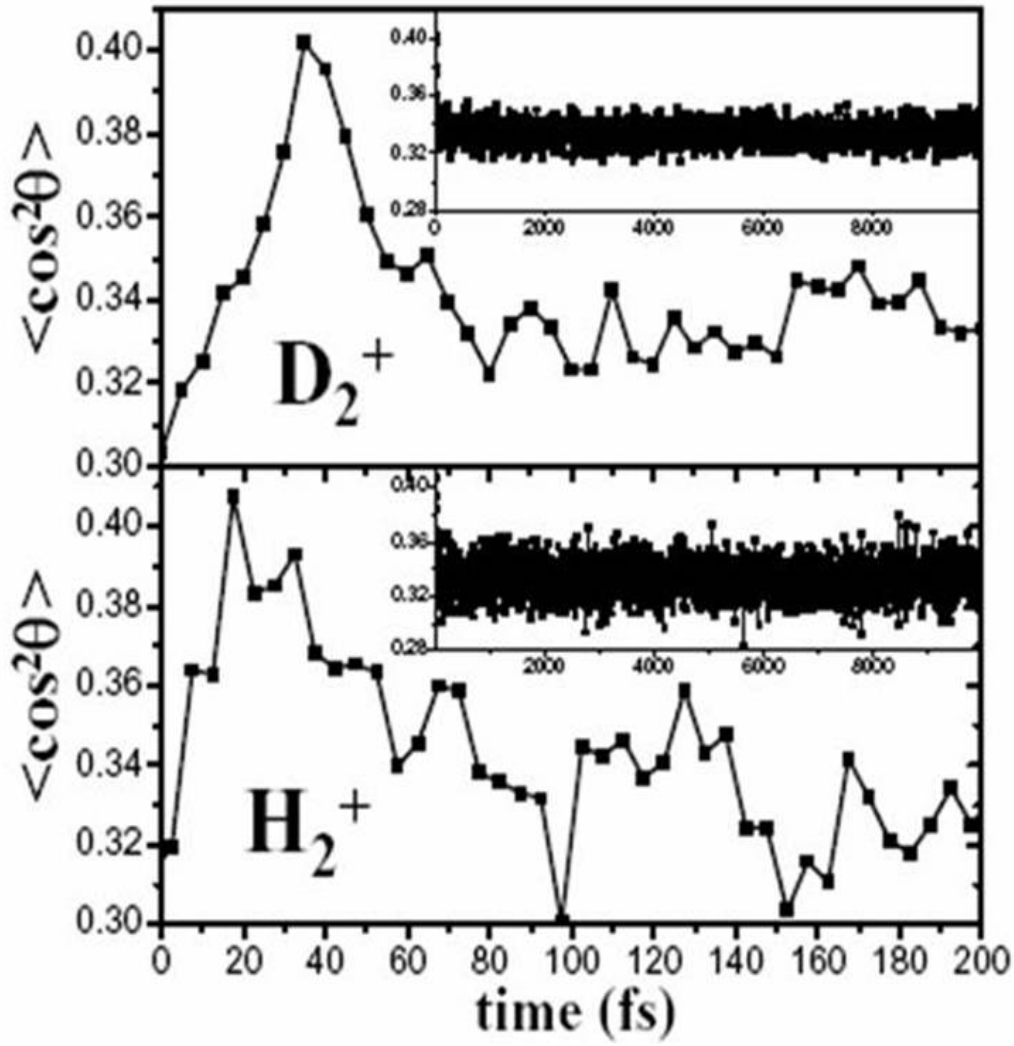

4.3 Summary

In summary, we reported a direct time-resolved Coulomb explosion imaging experiment following coherent nuclear dynamics induced by a few-cycle near-IR laser pulse in D_2 and H_2. In neutral molecules the rotational dynamics is that of a rigid rotor coupled to the electric field by its anisotropic polarizability. As in larger diatomics, periodic rotational revivals corresponding to partial alignment of molecular axes are seen in both light and heavy hydrogen. However, the degree of alignment is quite low for both ($\langle\cos^2\theta\rangle \approx 0.36$) due to large energy spacing between the rotational levels of the two molecules. This large rotational level spacing is also the reason for inefficient rotational cooling of D_2 in a supersonic jet. We found that the effective rotational temperature in our jet is 250 K, while the translational temperature was 110 K. We do not believe, however, that high initial rotational temperature was the main reason for poor alignment. Much more importantly, even few-cycle pulses do not have sufficient spectral bandwidth to excite the high rotational states needed to produce well localized wavepackets in both H_2 and D_2. At the most, states with J = 3 in H_2 and J = 6 in D_2 can be efficiently excited by a non-resonant stimulated Raman process using 8 fs pulses. That puts a natural limit on the degree of field-free alignment achievable in molecular hydrogen with short single-color pulses and calls for development of other more efficient methods in order to experimentally study its angle-differential properties. One possible solution may involve using two-color aligning pulses (for instance ω+2ω) with a much broader combined spectrum. Despite the relatively poor alignment we were able to put an upper limit of 1.25 on the ratio of ionization probabilities for D_2 molecules aligned along and perpendicular to the laser electric field. Strong-field ionization of D_2 appears to be nearly isotropic in agreement with predictions of the Molecular ADK theory.

In molecular ions we observed coupled rovibrational dynamics. Only vibrational revivals were seen in D_2^+. Within the 10 ps experimental time-scale, rotational motion of D_2^+ and H_2^+ did not exhibit any coherence beyond the initial prompt alignment immediately after the pulse. That alignment occurred very fast (18 fs in H_2^+ and 35 fs in D_2^+) and was much better defined than in neutral molecules. The absence of revivals is not at all surprising, since different vibrational states forming the coherent wavepacket

have very different and incommensurate rotational times. To fully understand nuclear wavepacket dynamics in hydrogen molecular ions one must treat the coupled vibrational and rotational degrees of freedom simultaneously, particularly with both motions taking place on a very similar time-scale. Properly taking rotations into account may resolve the remaining discrepancies between the experimental results and one-dimensional vibrations-only model calculations [**95**].

CHAPTER 5 – Inelastic rescattering processes in D_2 molecules measured with few-cycle laser pulses

5.1 Introduction

Behavior of experimental atomic double ionization yields as a function of laser field intensity fails to follow rates predicted by tunneling theory as intensity drops to some threshold limit. The logarithmic scale plots of the ion signal as a function of intensity are characterized by a distinctive feature, so-called "knee"-structure, showing 4-6 orders yield enhancement comparing to the sequential tunneling calculations results for all rare-gas atoms and some molecules (Fig. **5.1**) [**5, 52, 54**]. This phenomenon was attributed to non-sequential processes. In other words, each ionization step cannot be treated independently. The increase in double ionization rate was termed non-sequential double ionization (NSDI) and several possible mechanisms of NSDI were suggested and discussed [**5, 6, 96, 97**].

Figure 5.1 Ion yield as a function of intensity of 800 nm linearly polarized light for (a) Ne single and double ionization (the figure is from S. Larochelle et al. J. Phys. B 31, 1201 (1998) [52]); (b) Ar single ionization and N_2 molecular rates for single, double ionization and two fragmentation channels (the figure is from S. L. Chin et al. J. Phys. B 25, L249 (1992) [54]). Solid lines are indicating calculations performed assuming sequential processes

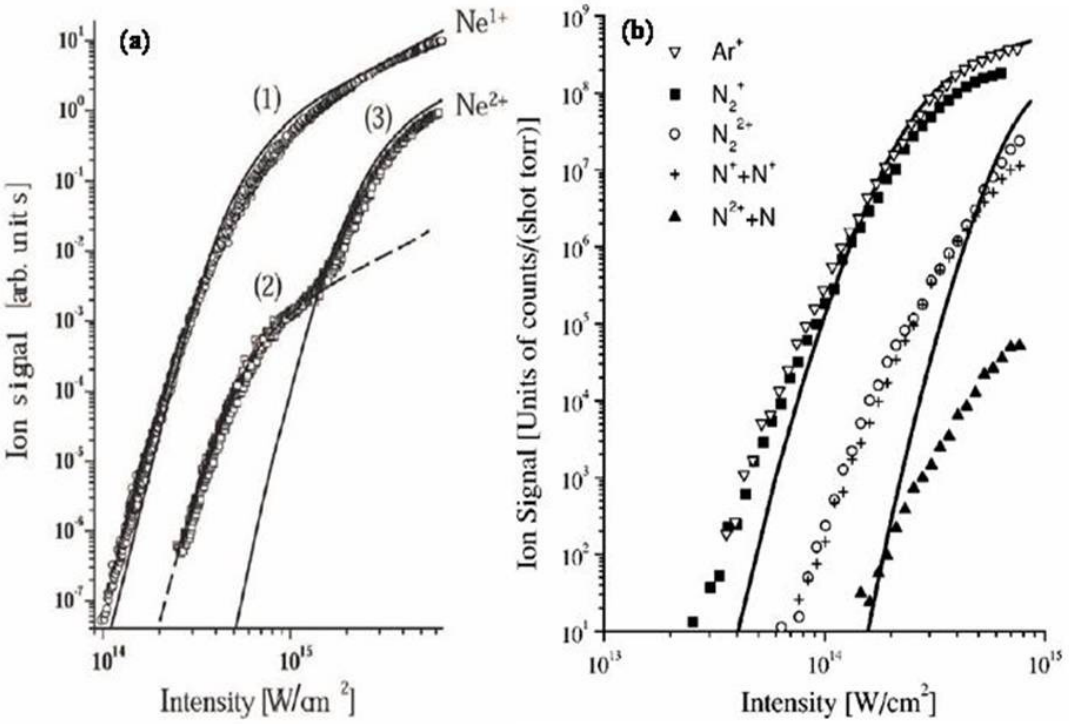

Among all suggested mechanisms recollision was supported by later experiments and proven to be able to explain the enhanced double ionization yield. Strong dependence of the double ionization rate on ellipticity of laser light became one of the key observations [**5**, **54**, **97**]. For circularly polarized light recollision ionization rate is completely suppressed because the electron misses the ion core (see Fig. **5.2**). There was also observed strong ellipticity dependence of such recollision-related phenomena as high harmonic generation [**98**] and above-threshold ionization [**99**]. Three-step laser-induced electron rescattering model proposed by Corkum [**100**] and Schafer et al [**101**] well accounted for all the above phenomena [**100**]. According to that model, electron is first ejected from the atom/molecule with near zero kinetic energy by tunneling through the barrier formed by the ion core and reduced by the oscillating laser field (step 1). Then the electron quivers in laser field and eventually is driven away with velocity dependent on the phase of the field at which it was liberated. Some of the electrons will return to the

ion core by the linearly polarized laser field (step 2) and finally recollide with the parent ion (step 3) (Fig. **5.3**).

Figure 5.2 Demonstration of the effect of elliptically and circularly polarized light on the recollision process. (a) Slight ellipticity makes free electron shift laterally on the way back, so that it will probably miss the ion core. (b) In circularly polarized field an electron is taken away from the ion core and don't have a chance to recollide.

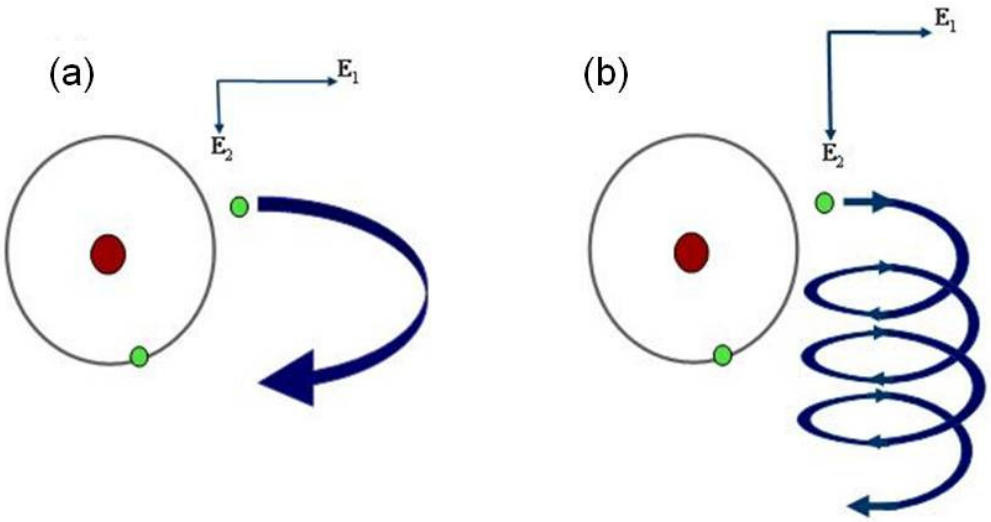

Figure 5.3 Schematic presentation of the three-step model: (a) and (b) an electron escapes from the potential well; (c) it is driven back to the ion core; (d) the electron recollides with the ion core. The figure is from P. Corkum and F. Krause. Nature Phys. 6, 323 (2007) [102]

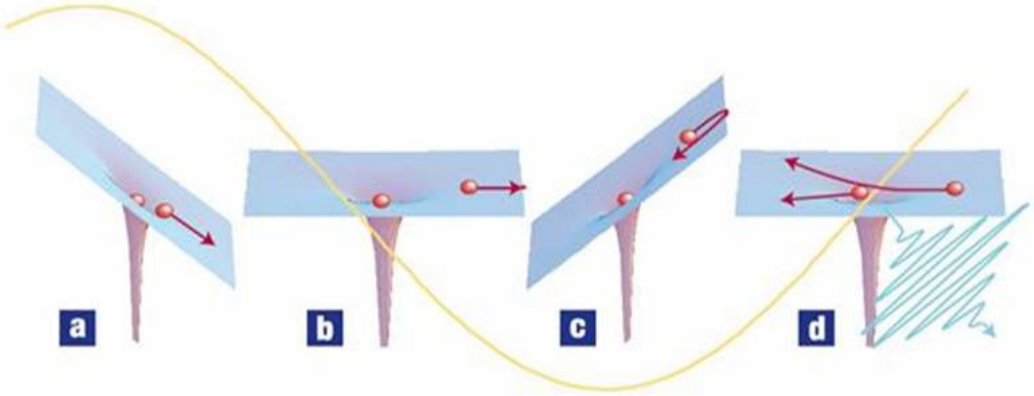

The recollision may result in recombination, which is responsible for high harmonics generation, or in elastic or inelastic rescattering depending on energy of the returning electron. In an inelastic process, the rescattering electron can either ionize the parent ion directly, by knocking out the second electron (direct NSDI), or it may

electronically excite the ion, which then can be subsequently ionized by the laser field (RESI - Recollision Excitation with Subsequent field Ionization [**18**]). Those rescattering processes have been observed for noble gas atoms by investigating double ionization with recoil-ion momentum imaging [**18, 103**-**105**]. After the rescattering process, doubly or singly ionized ions can also gain momentum from the field. The final momentum is determined by the phase of the field at which the ionizations took place. Singly charged ion is produced at the peak of the laser field with highest probability. Therefore, its longitudinal momentum distribution has a peak at zero momentum. For doubly charged ions momentum distributions look different for RESI and direct double ionization processes. For RESI the returning electron only excites the ion and the second electron is removed later by the laser electric field close to its peak. As a result the momentum distribution peaks at zero for doubly charged ions resulting from this process. But for the direct NSDI process the second ionization is caused by the first electron returning with energy high enough to knock out the second electron. The return of energetic electrons is more likely to happen at zero of electric field causing the ion gain momentum in longitudinal direction and resulting in a double peak distribution with a dip at zero momentum. The direct NSDI process is characterized by a minimum at zero in the longitudinal momentum distribution of the doubly charged ion, in contrast to a peak at zero, which is obtained for RESI.

When the laser peak intensity is sufficiently low, the excited electronic states of the parent ion populated by recollision may survive without ionizing further. It is very challenging to detect those excited electronic states in atoms. However, in diatomic molecules, the excited electronic states of the singly charged molecular ion are often dissociative, resulting in one atomic ion fragment that can be easily detected, thus offering the possibility of studying the recollision-induced electronic excitation without subsequent field ionization.

5.2 Experimental setup

The experiments were performed at the Advanced Laser Light Source (ALLS) research facility located in Varennes, Quebec, Canada in collaboration with the group of Prof. F. Legaré. The techniques we used were very similar to those used in JRM Laboratory at Kansas State University. They are described in Chapter **2**. I will discuss the specifics of experimental setup here. The few-cycle laser pulses were generated using the standard approach based on spectral broadening in a hollow core fiber and dispersion compensation using chirped mirrors. 35 fs laser pulses of 0.2 mJ energy at 5 kHz repetition rate (Dragon laser system, KMLabs, Boulder, USA) were coupled into a hollow core fiber filled with argon at 1 atm. The resulting few-cycle pulses had maximum energy of 150 μJ. Dispersion compensation was achieved using chirped mirrors (Femtolasers). Using an interferometric autocorrelator, the pulse duration was characterized to be 6.5 fs. Linear polarization was fixed after the capillary using two germanium plates. In combination with a half-wave plate located before the fiber, the energy could be precisely controlled. The pulses were focused by a parabolic mirror (f = 10 cm) onto a supersonic jet of D_2 molecules inside a uniform-electric-field ion imaging spectrometer.

5.3 Results and discussion

In this study we report our observations of NSDI and Recollison Excitation without subsequent field ionization (RE, $D_2^{+*} \rightarrow D^+ + D$) in D_2. By using few-cycle laser pulses, the rescattering processes can be highlighted by suppressing completely the sequential double ionization process. Here we demonstrate that NSDI of D_2 at 800 nm wavelength is mainly due to the recollision excitation of D_2^+ followed by field ionization (RESI) on sub-cycle time scale. At low intensity (1×10^{14} W/cm^2), the D^+ kinetic energy spectrum contains only the RE channel and numerical simulations confirmed the contribution of two dissociative excited electronic states ($^2\Sigma_u^+$ and $^2\Pi_u$) (Fig. **5.4**) to the RE process in agreement with theoretical predictions [**19**, **106**].

Figure 5.4 Electronic states of the D_2^+ ion.

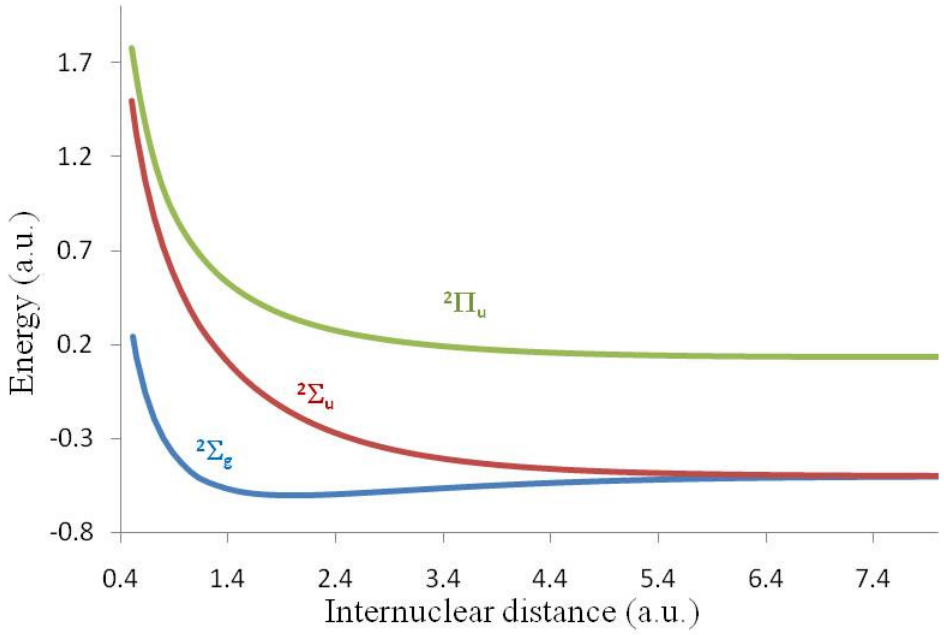

Figure 5.5 Illustration to the experimental technique utilizing the molecular clock: (a) the quantum mechanical perspective of recollision: a wave function is split by ionization, a part of it stays in the potential well, the other part is gone and then brought back to probe the vibrational wave packet; (b) an optical interferometer analogy. The figure is from J. Levesque, P. B. Corkum. Can. J. Phys. 84, 1 (2006) [107]

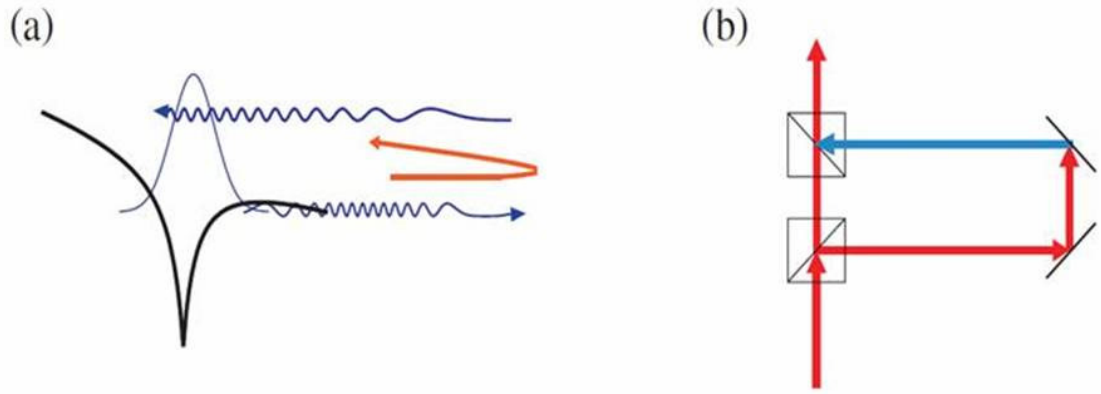

The physical concept behind this experiment is the use of the molecular clock as introduced by Niikura and co-workers [**108**]. This technique is analogous to well-known pump-probe measurements. Tunnel ionization of H_2, or D_2, starts the clock by launching two correlated wave packets: an electron one in the continuum and a vibrational one on the ground electronic state of D_2^+ ($^2\Sigma_g^+$). When the electron returns to the parent molecular ion, recollision probes the vibrational wave packet and stops the molecular clock. Fig. **5.5** shows the electron wave packet splitting and probing of the bound part by

the returning electron wave (panel **(a)**) and also demonstrates the analogy with an optical interferometer (panel **(b)**). We focus on inelastic rescattering which may induce either (i) electronic excitation leading to the dissociation of $D_2^{+*} \rightarrow D^+ + D$, or (ii) recollision excitation of D_2^+ plus subsequent field ionization (RESI) to produce D_2^{++}, or (iii) direct double ionization (direct NSDI) also producing D_2^{++}. The last two processes thus both result in Coulomb explosion ($D_2^{++} \rightarrow D^+ + D^+$) with two ions whose momentum sum is close to zero. By looking at all D^+ ions (non-correlated spectra) and also at only ion pairs ($D^+ + D^+$) with zero momentum sum (correlated spectra), we can separate these contributions and determine at any intensity and ellipticity the relative proportions of dissociation from Coulombic D_2^{++} or from D_2^{+*} dissociative excited electronic states.

Because there are multiple pathways leading to the same final D^+ kinetic energy with multi-cycle laser pulses, the molecular clock is very difficult to read precisely. For instance, it remains a matter of debate whether the first [**108**] or the third return [**19**, **106**] is the most dominant. In addition, with multi-cycle laser pulses, sequential double ionization due to charge resonance enhanced ionization (CREI, [**14, 76**]) dominates the D^+ kinetic energy spectra in the range between 2 and 5 eV, where fragments produced via RE should also appear. We show here that by using few-cycle laser pulses of sufficiently low intensity, these problems can be overcome. Such short pulses (sub-7 fs) efficiently suppress CREI by not giving the molecule enough time to stretch to the critical distance [**73**]. Then, for intensities below 2×10^{14} W/cm^2, sequential double ionization is effectively turned off and the inelastic rescattering processes become dominant. Finally, using such very short pulses ensures that this recollision is dominated by a single electron return [**109**]. In this way, the different inelastic rescattering processes can be clearly distinguished and investigated as a function of laser intensity and ellipticity.

Figure 5.6 Kinetic energy spectra for uncorrelated (solid line) and correlated (circles) D^+ fragments measured with circularly (top) and linearly (bottom) polarized 6.5 fs laser pulses of peak intensity 4×10^{14} W/cm^2. Bond softening (BS) and sequential double ionization (SI) peaks are indicated. The spectra are normalized such that the high energy peak has a value of 1

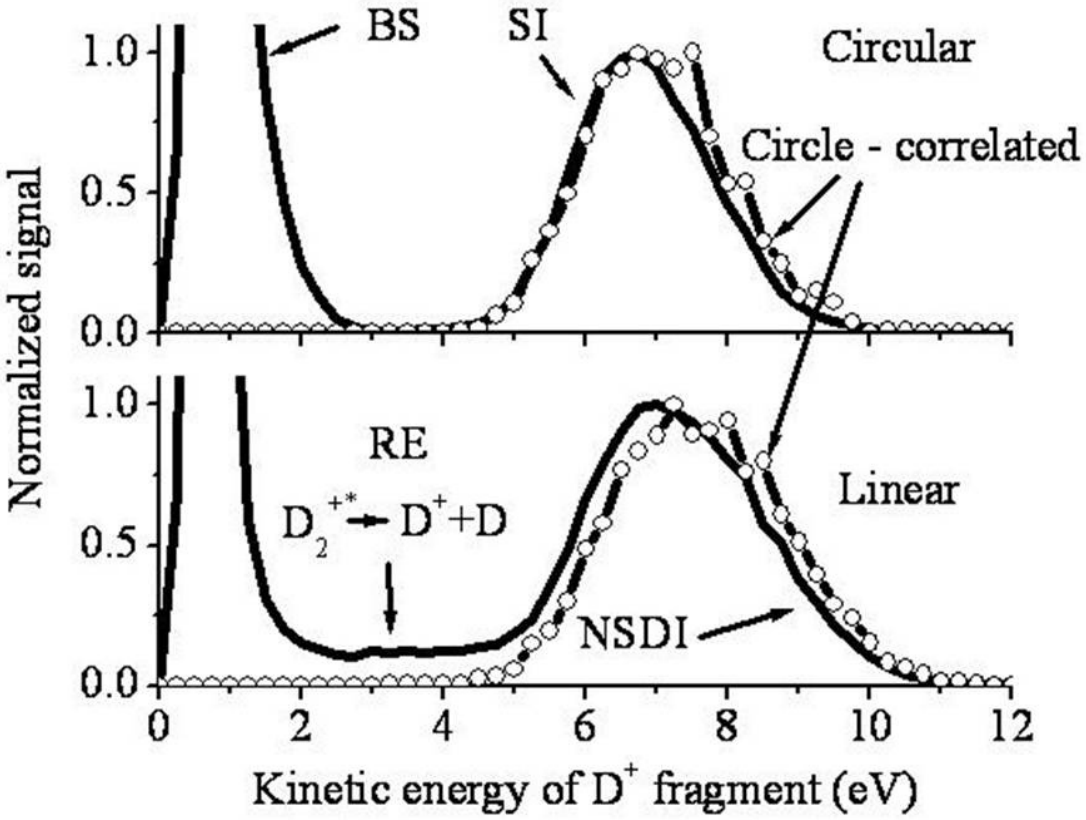

Fig. **5.6** presents the D^+ kinetic energy spectra obtained for circularly and linearly polarized sub-7 fs laser pulses with an intensity of 4×10^{14} W/cm^2. For circular polarization, the recollision processes are completely suppressed [**100**]. The kinetic energy spectrum consists of two peaks: (i) bond softening (BS) below 2 eV [**110**], and (ii) a peak at 6.5 eV. Under zero sum momentum condition, only the high energy peak remains, confirming that those fragments are produced by sequential double ionization: $D_2^{++} \rightarrow D^+ + D^+$ [**73**]. Comparison of this spectrum with the one obtained with linear polarization, when recollision can occur, reveals two important differences: (i) at high kinetic energy (E > 8eV), the spectra are broader for linear polarization implying significant contribution to high-energy D^+ fragments produced by recollision, and (ii) uncorrelated D^+ fragments with kinetic energies between 2.5 and 4.5 eV are seen for

linear (but not for circular) polarization. This allows us to infer that those fragments are from D_2^+ excited electronic states populated during recollision, which dissociate into D_2^{+*} → $D^+ + D$.

Figure 5.7 Kinetic energy spectra for non-correlated (solid line) and correlated (circles) D^+ fragments measured with linearly polarized 6.5 fs laser pulses at intensities where sequential double ionization is suppressed. The spectra are normalized such that the high energy peak has a value of 1

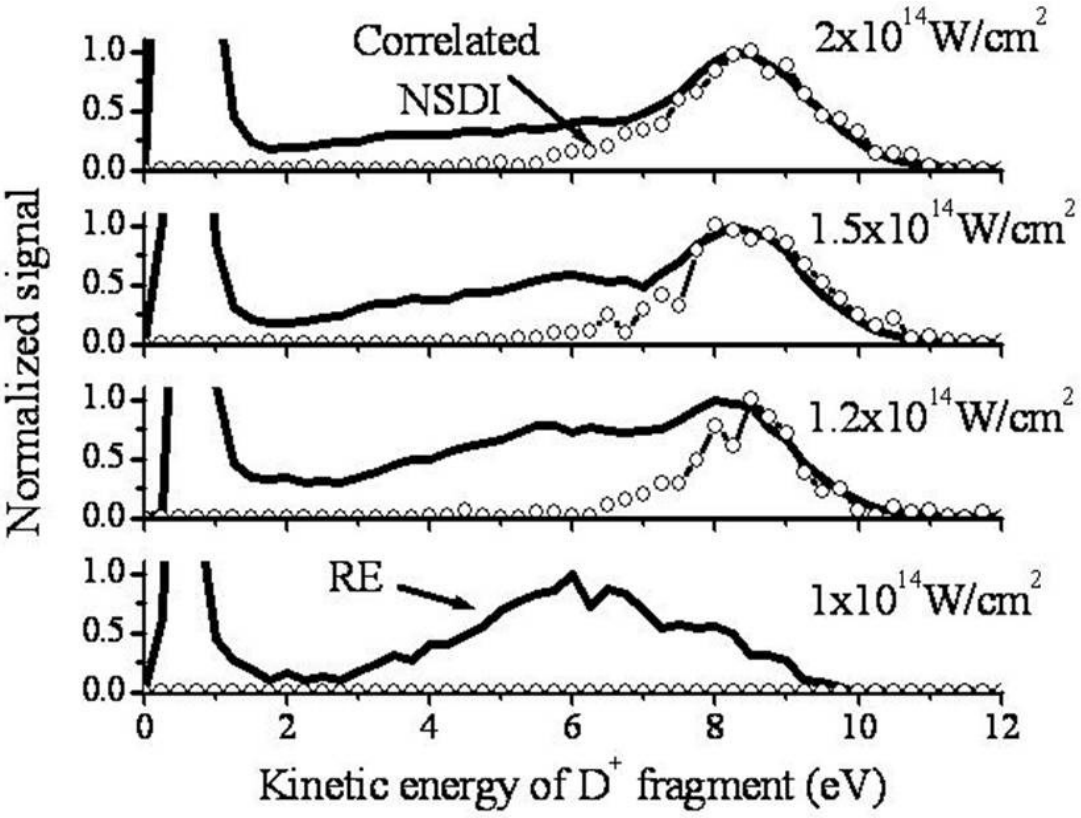

Next, by using laser intensity values below 2×10^{14} W/cm^2, when field ionization of the ground state D_2^+ becomes suppressed as the intensity is reduced, we show that the fragments with kinetic energy larger than 8 eV are produced by NSDI and the ones with energies between 2.5 and 4.5 eV come from the dissociation of D_2^+ electronically excited by recollision (D_2^{+*} → $D^+ + D$). Fig. **5.7** presents the D^+ kinetic energy spectra obtained for linear polarization and intensities from 2×10^{14} W/cm^2 down to half that value. Comparison of these spectra with the ones in Fig. **5.6** and with each other reveals striking differences for D^+ fragments with kinetic energies higher than 2 eV. The bond softening

(BS) peak below 2 eV is seen for all intensities. Beside BS, at 1.0×10^{14} W/cm^2, the non-correlated spectrum contains only one broad peak centered at about 6 eV, while the correlated signal is absent (implying a complete absence of the D_2^{++} channel). A second peak at about 8 eV appears as intensity is increased and becomes predominant at 2.0×10^{14} W/cm^2. In the correlated spectra, only the high kinetic energy peak remains, confirming that those fragments are produced by double ionization.

Figure 5.8 Ellipticity dependence of the number of high kinetic energy D^+ fragments (E > 2eV) for 2×10^{14} W/cm^2 (square) and 1.5×10^{14} W/cm^2 (circle)

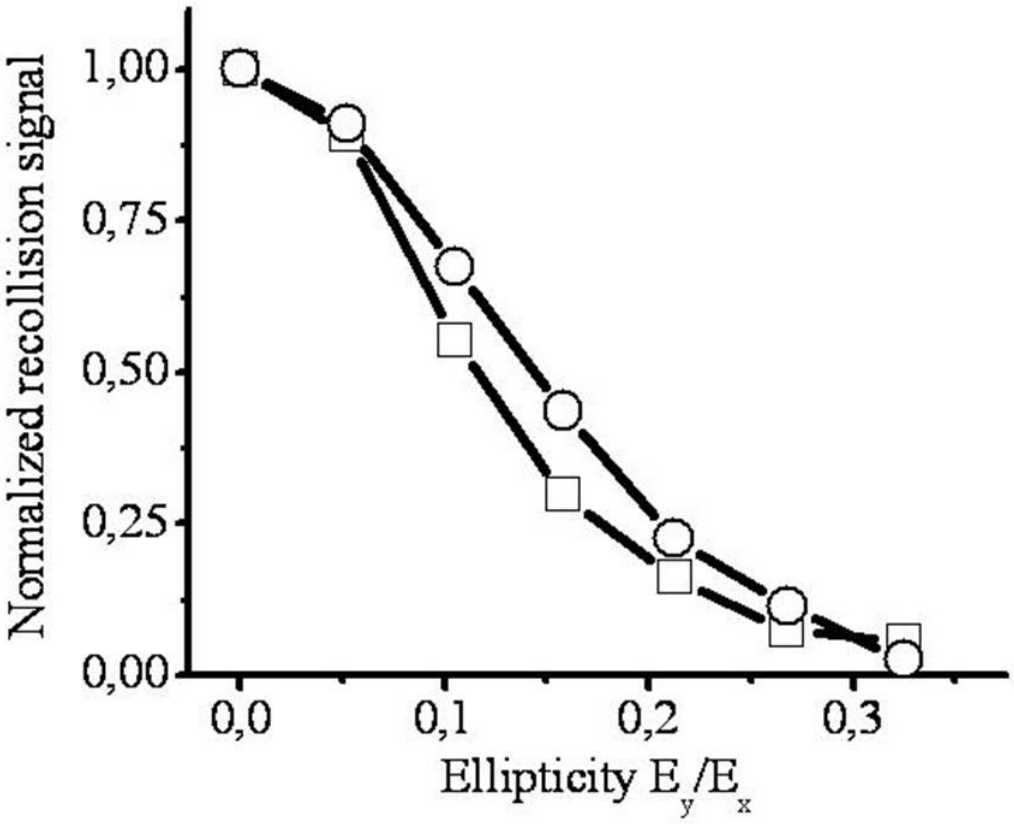

To confirm the physical origin of those D^+ fragments with kinetic energies larger than 2 eV, we have measured their yield as a function of laser ellipticity for two intensities. Fig. **5.8** shows the ellipticity dependence at 2×10^{14} W/cm^2 (squares) and 1.5×10^{14} W/cm^2 (circles) peak intensities, and the yield for both is seen to drop rapidly as the ellipticity increases, confirming that those D^+ fragments are mainly produced by laser-induced electron recollision (the recollision probability is known to decrease rapidly with ellipticity). Therefore, we can conclude that the uncorrelated fragments ($D_2^{+*} \rightarrow D^+$

+ D) with more than 2 eV of kinetic energy indeed result from RE (recollision induced electronic excitation without subsequent field ionization), while the high kinetic energy correlated fragments ($D_2^{++} \rightarrow D^+ + D^+$) are produced through NSDI.

Figure 5.9 Kinetic energy spectra for non-correlated D^+ fragments as a function of laser ellipticity for 2×10^{14} W/cm^2 and 1.5×10^{14} W/cm^2. At 2×10^{14} W/cm^2 with E_y/E_x=0.32, the dashed curve is the spectrum obtained with circular polarization at 4×10^{14} W/cm^2 (see Fig. 5.6). At 1.5×10^{14} W/cm^2 with E_y/E_x=0.27, the dashed curve is the spectrum obtained with linear polarization at 1×10^{14} W/cm^2 (see Fig. 5.7)

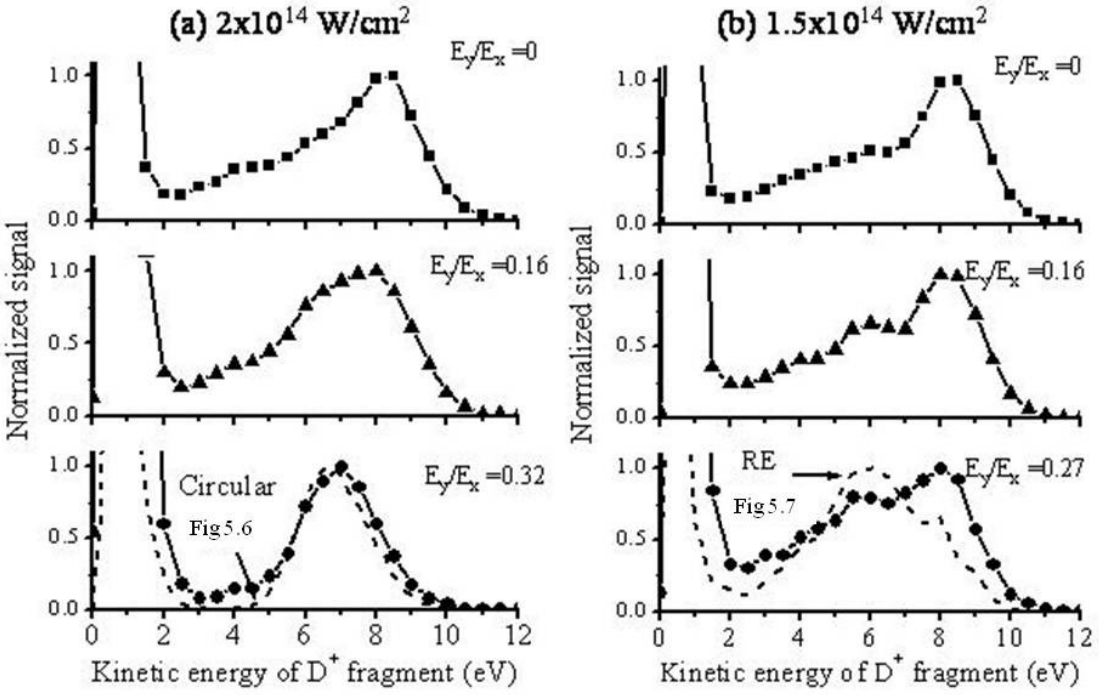

At 2×10^{14} W/cm^2, the total yield remains non-zero even at relatively high ellipticity (> 0.3). This is explained by the kinetic energy spectra presented in Fig. **5.9(a)**. At 2×10^{14} W/cm^2, as the ellipticity increased, the yield decreases by a factor of 20 and the D^+ kinetic energy spectra become very similar to the ones measured at 4×10^{14} W/cm^2 with circular polarization (see Fig. **5.9(a)**, left panel, E_y/E_x=0.32). With circular polarization, the high kinetic energy fragments can only be produced via sequential double ionization. That confirms that at 2×10^{14} W/cm^2 few-cycle pulses with high ellipticity, the observed ion yields arise from sequential double ionization. However, for linear polarization the probability of this process is much lower than that of inelastic rescattering. This is in stark contrast with the results obtained with multi-cycle laser pulses: due to CREI, the probability of sequential double ionization is always at least 10

times larger than the one for recollision processes [**108**]. This means that using few-cycle laser pulses, the yields ratio of the rescattering processes and sequential double ionization can be carefully measured.

Fig. **5.9** also presents the kinetic energy spectra as a function of ellipticity for a fixed intensity of 1.5×10^{14} W/cm^2 (Fig. **5.9(b)**). Comparison of spectra in Figs. **5.9(a)** and **(b)** reveals significant differences between 1.5 and 2×10^{14} W/cm^2. At 1.5×10^{14} W/cm^2, even at large ellipticity ($\varepsilon = 0.27$), there is no indication of the contribution of sequential double ionization. At large ellipticity, the spectrum is dominated by RE with a small contribution of NSDI. In fact, we observed that the yield for the high kinetic energy fragments (> 8 eV), produced via NSDI ($D_2^+ \rightarrow D^+ + D^+$), decreases more rapidly with ellipticity than that of the low energy fragments (2 eV – 8 eV), produced via RE ($D_2^{+*} \rightarrow D^+ + D$). At large ellipticity values, the kinetic energy spectrum is dominated by RE, like in Fig. **5.7** for intensities below 1.2×10^{14} W/cm^2. For comparison, we included in Fig. **5.9(b)** the D^+ spectrum from Fig .**5.7** obtained with linear polarization at 1×10^{14} W/cm^2 (dashed curve).

To understand those experimental observations, we calculated the D^+ recollision spectra assuming the same model as used by Niikura and coworkers [**108**]. Calculations were performed by Prof. F. Legaré. Briefly, during the first ionization step, the vibrational wave function of D_2 is projected onto the ground electronic state of D_2^+ ($X^2\Sigma_g^+$). The radial distortion due to the dependence of the ionization rate on internuclear distance is taken into account. The resulting vibrational wave packet is propagated by numerical solution of the time-dependent Schrödinger equation. Then, for every 0.05 fs of delay after first ionization, we have calculated the kinetic energy spectra assuming (1) direct double ionization, (2) RE to $^2\Sigma_u^+$ and (3) RE to $^2\Pi_u$ (Fig. **5.4**). For RE, we have limited our calculation to those two excited electronic states based on theoretical predictions from Tong et *al.* [**19**, **106**]. Finally, the calculated D^+ spectra for those three final states are summed using the temporal structure of the first return for 800 nm laser wavelength [**108**].

In Fig. **5.10**, we compare **(a)** the calculated D^+ kinetic energy spectrum for direct double ionization with the experimental correlated spectrum shown in Fig. **5.7** (we

compare with 1.5×10^{14} W/cm^2), and **(b)** the calculated RE spectra ($^2\Sigma_u^+$ and $^2\Pi_u$) with the experimental one measured at 1×10^{14} W/cm^2 (also Fig. **5.7**).

Figure 5.10 (a) The correlated spectrum at 1.5×10^{14} W/cm^2 (squares) and the result of numerical simulations assuming a single recollision with $D_2^{++} \rightarrow D^+ + D^+$ as the final state (solid line). (b)The uncorrelated spectrum at 1.0×10^{14} W/cm^2 (squares) and the RE spectrum calculated with 75% contribution of the $^2\Sigma_u$ state and 25% of $^2\Pi_u$ (solid line). Individual contributions of those two states are also shown (dashed lines)

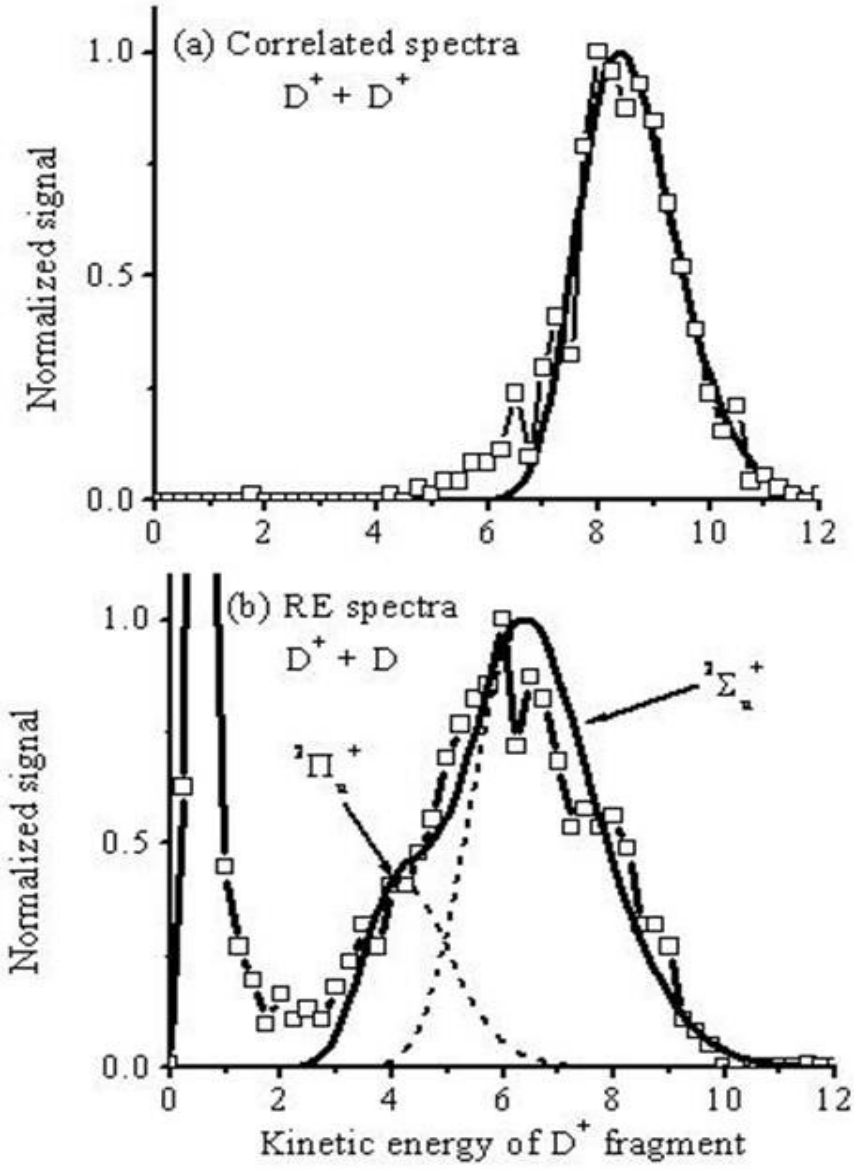

Comparison (a) of Fig. **5.10** at 1.5×10^{14} W/cm^2 with experiment confirms that the recollision dynamics is dominated by a single return and seems to suggest that double ionization occurs through direct NSDI. However, the recolliding electron returns with

maximum kinetic energy (3.17Up) 1.8 fs after first ionization. During this time, the vibrational wave packet moves on the ground electronic state of D_2^+ $^2\Sigma_g^+$ and reaches an average bond distance of ~0.9 Å. To induce direct NSDI at this distance, the kinetic energy of the recolliding electron has to be larger than 32 eV. However, at 1.5×10^{14} W/cm^2, 3.17Up ≈ 28 eV, which is not sufficient for direct double ionization. This suggests that NSDI actually occurs through RESI. As mentioned before, the first step of RESI is the electronic excitation of the parent ion via recollision. In this process, the recollision of the energetic electron (~3.17 Up) with the parent ion occurs near the zero of electric field, and the subsequent field ionization takes place within the next half optical cycle. With increasing ellipticity at fixed intensity (Fig. **5.8**) or decreasing intensity for linear polarization (Fig. **5.7**), the strength of the electric field within the next half cycle decreases and the probability for subsequent field ionization decreases as well, explaining the evolution of the spectra shown in Fig. **5.7** and Fig. **5.10(b)**. Intensity and ellipticity measurements provide the same conclusion about the origin of NSDI and confirm RESI mechanism.

Comparison **(b)** of Fig. **5.10** at the lower intensity of 1.0×10^{14} W/cm^2 (so that second ionization is completely suppressed and only RE is left) suggests that the RE spectra can be largely explained by RE to the states $^2\Sigma_u^+$ and $^2\Pi_u$, the first state being the source of the high energy RE fragments and the second state yielding the low energy part of the spectrum. The $^2\Sigma_u^+$ state contributes the most to the RE spectrum as one should expect from field free inelastic scattering cross-section [**111**].

5.4 Summary

In conclusion, we have successfully identified different inelastic rescattering processes (RE and NSDI) induced in D_2 by few-cycle laser pulses. For the first time, we showed that sequential double ionization can be completely suppressed by using few-cycle pulses and careful selection of the laser field strength, allowing the isolation of the inelastic rescattering processes. Our measurements reveal that the relative yields of RE and NSDI depend on both intensity and ellipticity of few-cycle laser pulses. From that yield dependence on the peak electric field, we determined that NSDI in D_2 occurs via the

RESI mechanism. Also, we have isolated the RE spectra from NSDI. The RE spectra have been well explained by the contribution of two electronic states ($^2\Sigma_u^+$ and $^2\Pi_u$). Using COLTRIMS (COLd Target Recoil Ion. Momentum Spectroscopy) [**112**], it should be possible to confirm definitively the contribution of those electronic states by correlating the kinetic energy of the D^+ fragments with the photoelectron spectra. All these results show how few-cycle laser pulses can be used to great advantage to perform electron collision spectroscopy. This experimental approach can be also applied to studying inelastic rescattering processes in other diatomic molecules which have singly charged dissociating electronic states.

CHAPTER 6 – Nuclear wave packet dynamics of N_2, O_2 and CO molecules following their interaction with intense few-cycle laser pulse

6.1 Introduction

The interaction of intense near IR few-cycle laser pulses with atoms and molecules has become a topic of great interest and is being intensively studied nowadays. Studies of N_2, O_2 and CO molecular structure and dynamics during chemical transformations are of particular importance. Nitrogen and oxygen are components of the Earth's atmosphere and participate in many chemical reactions in our environment. Carbon monoxide is also very common on our planet. It plays a major role in modern technology, in industrial processes like iron melting [**113**], and also is very toxic: CO poisoning is a common type of fatal poisoning all over the world [**114**].

Compared to atoms, diatomic molecules like oxygen, nitrogen and carbon monoxide have additional degrees of freedom that make their dynamics in a laser field much more complicated. Alignment, symmetric and asymmetric charge break-up, enhanced ionization at the critical internuclear distance and a variety of dissociation pathways, associated with different electronic states of parent molecular ions come into play.

Often all of the above mentioned phenomena are studied in oxygen, nitrogen and carbon monoxide molecules in a comparative manner [**90, 97, 115**]. All three of them are diatomic molecule gases; the elements N and O are next to each other in the periodic table, but N_2 and O_2 have very different symmetries of the outer shells, which causes strong differences in processes such as ionization, excitation and dissociation in the laser field. CO has the same molecular mass as N_2 and they both have the same electronic structure of the outer shell. They also have similar physical properties such as boiling and melting points, etc. On the other hand, CO is a heteronuclear molecule; compared to N_2 and O_2 its symmetry about internuclear line midpoint is broken which adds characteristic features to nuclear dynamics.

Many recent studies on both N_2 and O_2 were dedicated to the study of field induced alignment [**116**, **117**], angular dependence of the ionization rate [**118**, **119**] and symmetric and asymmetric molecular fragmentation with a single laser pulse [**120**, **121**]. These experiments were traditionally conducted by measuring the time-of-flight and/or kinetic energy release (KER) of the atomic fragments assuming that this energy originated from Coulomb repulsion of the nuclei. The studies showed that the internuclear distance at the moment of separation was about the same, regardless of the charge state or even the molecule, and was approximately equal to 2-3R_e (R_e is the equilibrium bond length of a neutral molecule in its ground electronic zero vibrational state). The experimental KER of the fragments was found to be low compared to the Coulomb kinetic energy for laser pulses of 15 fs and longer for nitrogen, oxygen and carbon monoxide [**42**, **119**]. These observations are consistent with the theory of the ionization rate dependence on the internuclear distance and enhanced ionization at a critical internuclear separation [**75**]. The traditional approach with a single long pulse does not give an answer to the question of how the process of molecular expansion occurs, and contains no information on ionization and dissociation pathways. This is a question of observing the dynamics of internuclear motion on a femtosecond timescale. Understanding the mechanisms of enhanced ionization, symmetric and asymmetric dissociation and excitation of molecular and atomic ions – all kinds of nuclear and electronic motion – is only possible by probing the change in the molecular structure as a function of time using ultra short pulses.

In our experiments we measured the kinetic energy release of charge symmetric and asymmetric Coulomb breakup of diatomic molecules as a function of time delay between the pump and probe pulses. The schematic drawing of mapping the molecular structure dynamics by measuring the kinetic energy release of the explosion fragments is shown in Fig. **6.1**. The first step is to promote a molecule AB with a laser pulse (pump) from its stationary ground state to an unknown non-stationary state of the AB^{p+} ion on which dynamics is to be observed. Then we use the second laser pulse (probe) to further ionize the molecule, thus projecting the nuclear wave packet onto a known Coulomb repulsive state. If the probe pulse comes with zero delay with respect to the pump then the situation is equivalent to having just one strong pulse that explodes the neutral

molecule at the equilibrium internuclear distance with maximum Coulomb energy. When the probe comes with some delay Δt it allows for the wave packet evolution on the intermediate electronic state/states. Internuclear distance changes during this evolution. For a purely dissociative state of the molecular ion, the internuclear distance grows larger with increasing delay and the Coulomb explosion energy decreases. At the same time the molecule acquires some kinetic energy being accelerated on the AB^{p+} potential. The kinetic energy release is the total energy of the break-up fragments including the Coulomb energy and kinetic energy acquired by the molecular ion in the intermediate state:

$$KER\,(R,\Delta t) = KE(R,\Delta t) + CE\,(R,\Delta t) \qquad \textbf{(6.1)}$$

Thus, measuring KER as a function of delay is equivalent to measuring the state of the molecule at certain internuclear distances. At long internuclear distances dissociative states can be approximated by Coulomb potentials and approach an asymptotic limit. At this limit the molecule completely dissociates. Therefore, at long delays the probe pulse ionizes two independent atomic ions. The energy of the collected fragments does not depend on the delay anymore, and its value is determined only by the initial internuclear separation and the dissociation limit energy of the molecular ion in this state.

Figure 6.1 Schematic presentation of mapping molecular dynamics by measuring the kinetic energy release as a function of the delay between pump and probe

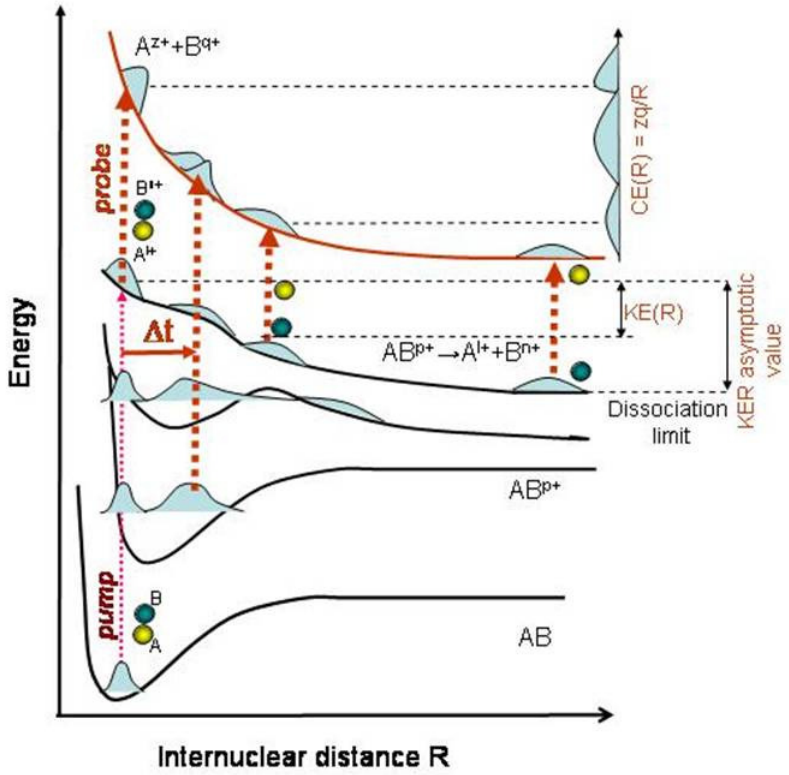

The pulses we used were shorter than 10 fs. This guaranteed that geometry changes during the interaction with a pulse were minimal. Using the Coulomb explosion and the pump-probe technique in our studies, we were able to map complete the nuclear dynamics in nitrogen, oxygen and carbon monoxide following their interaction with an intense few-cycle laser pulse. In the second part of this report we describe simple classical and quantum models, which present a general way to simulate the dynamics of nuclear wave packets, and to identify parent molecular ions and electronic states contributing to the processes under investigation.

6.2 Nitrogen molecule N_2

6.2.1 Experimental results and discussion

The time-dependent KER spectra for four breakup channels, N^++N^+ (1,1), N^{2+}+N^+ (2,1), N^{2+}+N^{2+} (2,2) and N^{3+}+N^{2+} (3,2), are presented in Fig. **6.2**. Zero on the delay axis of these plots means that the pump and probe pulses come at the same time. Negative

delays mean that the pump pulse comes after probe; in other words the pulses switch their places and if they were of the same peak intensity the picture would be symmetric about the zero delay. These spectra reveal several time dependent features that reflect the behavior of parts of the nuclear wave packet, its motion on dissociative and quasi-bound electronic potentials of several intermediate molecular ions. The descending traces start at about 25 eV for the (2,1) channel; 45 eV for (2,2); 65 eV for (3,2), and smoothly go down to be separated into two distinct traces at larger delays. Each of those reaches a certain asymptotic energy, correspond to molecular dissociation of the intermediate molecular ions. We will be calling them "dissociative part of the wave packet". For the (1,1) channel there is also a very faint low energy dissociative trace that starts to be visible below 5 eV after 40 fs of delay. It corresponds to the dissociation of excited states of the singly charged molecular ion – N_2^{+*}. At the higher energies there is another feature that characterizes the part of the nuclear wave packet which remains and does not dissociate on our timescale. For all channels except (1,1) we observe time dependent behavior within that region. The high energy part of the (1,1) spectrum represents mostly N^+ fragments that are produced by the probe pulse only from those neutral molecules not affected by pump, and thus exhibits no time dependence.

The experimental spectra for the symmetric (2,2) break-up channel (N^{2+}+N^{2+}) are rich in dynamics and statistics. From this point on, we will focus on this particular channel to develop our discussion on symmetric fragmentation. KER versus pump-probe delay for the (2,2) channel is shown in Fig. **6.3**. Each of the dissociative traces indicates the final break-up of the N_2 molecule into the same N^{2+}+N^{2+} fragments but via different intermediate charged states N_2^{q+}. These intermediate states can be identified using our simulations (see sections **6.2.2**, **6.2.3**) and each of them may also include several different electronic states.

Figure 6.2 Time-dependent kinetic energy release (KER) spectra (integrated over the solid 4π angle) for N_2 for (a) N^++N^+; (b) N^{2+}+N^+; (c) N^{2+}+N^{2+} and (d) N^{3+}+N^{2+} breakup channels. Pump pulse width - 8fs, intensity - 8×10^{14} W/cm^2; probe pulse width - 8fs, intensity - 17×10^{14} W/cm^2

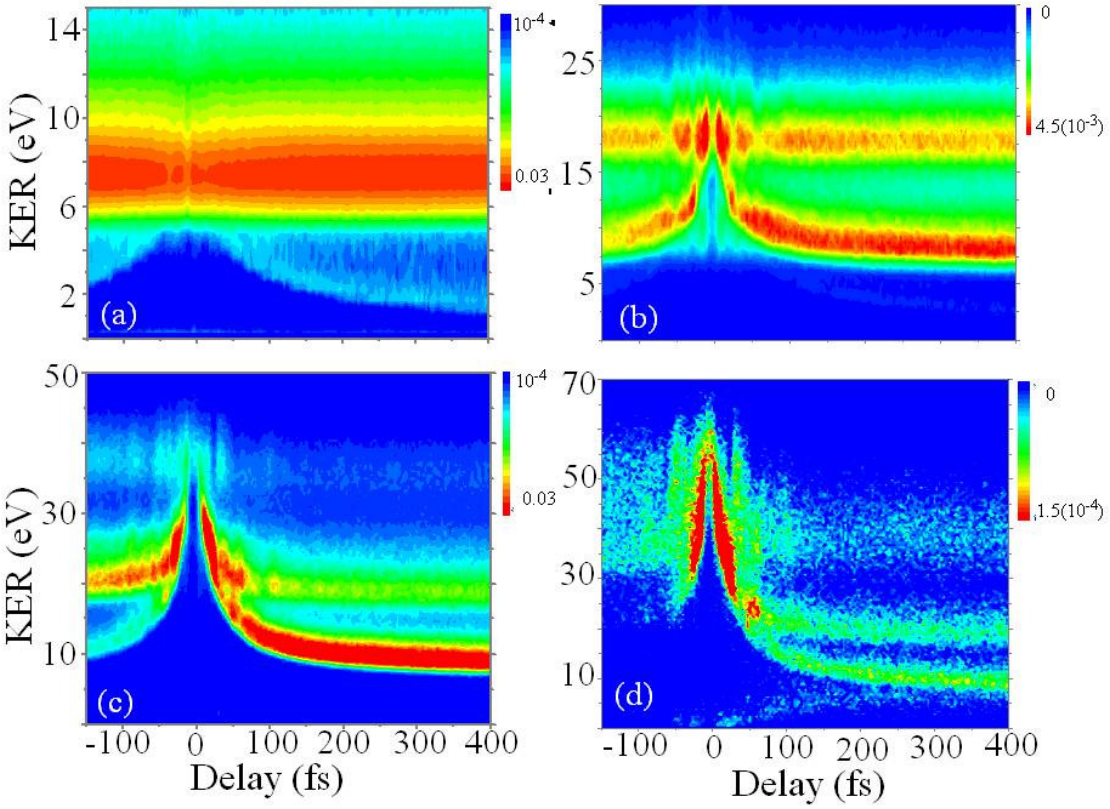

Looking at energy features below 30 eV, we notice that after about 350 fs the dynamics is essentially over, and the KER spectra remain static. It means that after that time the second pulse probes well separated in space atomic fragments of the molecule. These fragments are moving independently with the constant energy. The additional Coulomb energy due to their further ionization by the probe is small. Shape, width, intensity and energy asymptote of each dissociative feature suggest that it contains all the information about electronic states contributing to the process of dissociation. At long delays dissociative traces reach their KER limits and these broadened curves are centered at about 3 eV (Fig**. 6.3(a)**), 9 eV and 18 eV (Fig**. 6.3**), respectively. This final KER value, by the energy conservation law, is the difference between the maximum potential energy of the wave packet and the dissociation limit on a certain electronic state. These three curves correspond to the three intermediate charge states – N_2^+, N_2^{2+} and N_2^{3+} respectively.

Figure 6.3 Time-dependent kinetic energy release (KER) spectra (integrated over the solid 4π angle) for N_2 for $N^{2+}+N^{2+}$ breakup channel. Pump pulse width - 8fs, intensity - 8×10^{14} W/cm^2; probe pulse width - 8fs, intensity - 17×10^{14} W/cm^2. (a) Full spectrum with intermediate charge states indicated. (b) Same spectrum zoomed on the short delays part

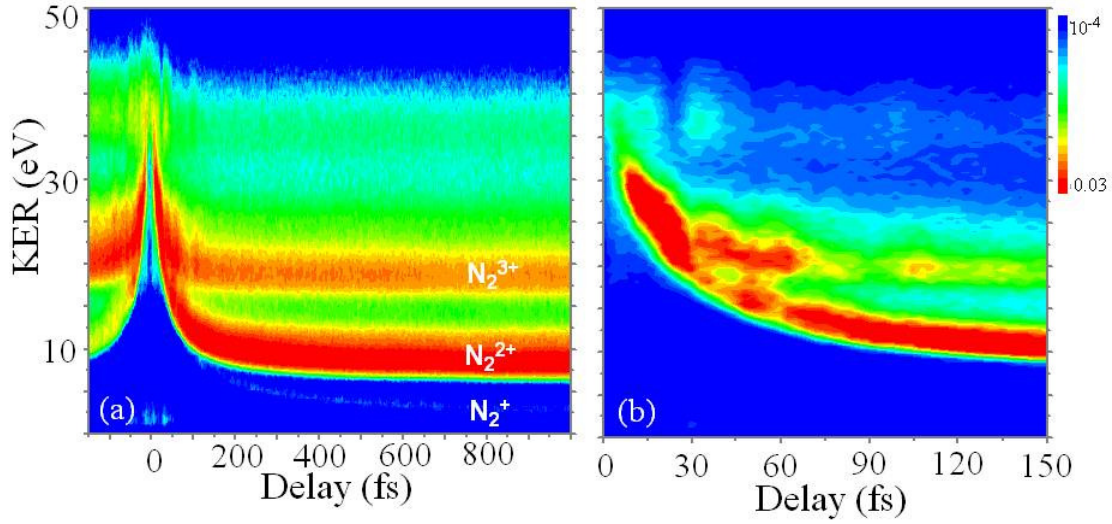

Figure 6.4 Time-dependent kinetic energy release (KER) spectra (integrated over the solid 4π angle) for N_2 for the $N^{2+}+N^{2+}$ breakup channel. (a) Pump pulse width - 8fs, intensity - 20×10^{14} W/cm^2; probe pulse width - 8fs, intensity - 16×10^{14} W/cm^2. (b) Pump pulse width - 8fs, intensity - 16×10^{14} W/cm^2; probe pulse width - 8fs, intensity - 12×10^{14} W/cm^2

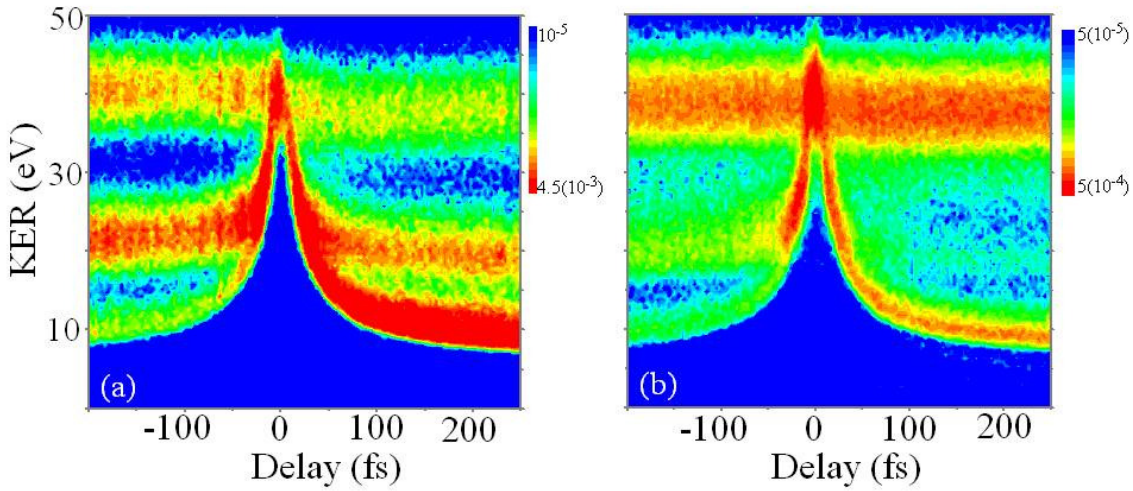

For the energies above 30 eV there is a bound part of the spectrum. At shorter delays we can distinguish a structure inside that band. We associate that structure with wave packet oscillating in potential wells of bound or quasi bound electronic states of singly or doubly charged molecular ions.

If we look at negative delays in Fig. **6.3** we can see that the plot is not exactly symmetric relative to zero delay. The only parameter that is changed is the ratio of the

pump and probe intensities. It affects the ionization probabilities for both ionization steps and relative populations of the intermediate states.

Fig. **6.4** presents two more sets of data for the same (2,2) channel, which have different intensities of the pump and probe pulses. The same general features are present, but those features can have different intensities, widths or slightly shifted energies depending on the peak intensities of the pump and probe pulses. Not all of the dissociative traces are present in different sets of data. Such differences are to be expected, considering that population, and consequently the contributions of different intermediate charge states and electronic states, depend on laser pulse intensity. A pump pulse will remove one, two, or three electrons from the neutral molecule and populate electronic levels with different probabilities depending on the peak intensity.

Figure 6.5 Time-dependent kinetic energy release (KER) spectra (integrated over the solid 4π angle) for N_2 for the N^{3+}+N^+ breakup channel. Pump pulse width - 8fs, intensity - 8×10^{14} W/cm^2; probe pulse width - 8fs, intensity - 17×10^{14} W/cm^2

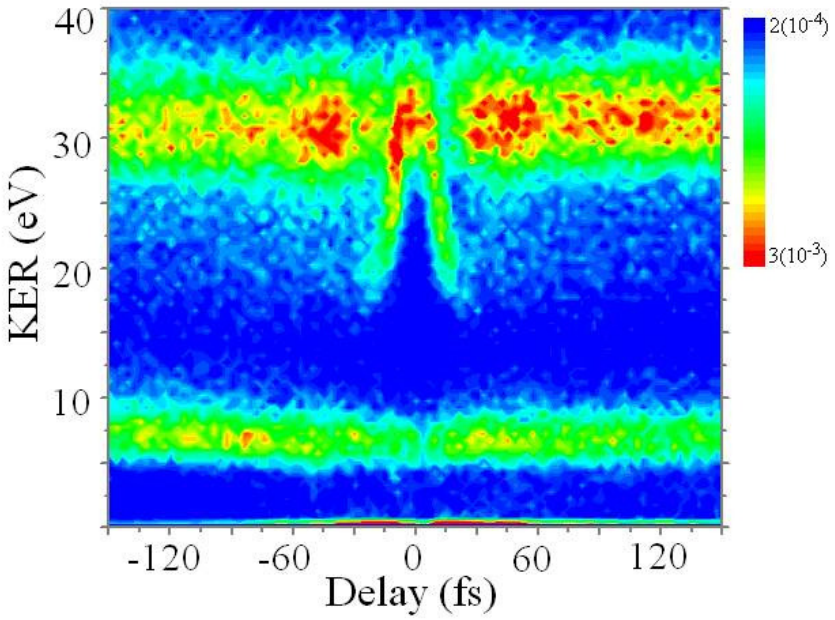

Asymmetric break up was also observed in our experiments, particularly the channel (3,1), which we will discuss in detail (see Fig. **6.5**). The striking feature of this plot is the dissociative trace which starts at zero delay at about 38 eV and disappears at about 20 fs delay at KER of 16 eV. The phenomenon of charge asymmetric dissociation and its mechanism, the conditions under which it occurs, and its competition with

symmetric breakup were discussed earlier in single pulse studies with different wavelength and pulses longer than 30 fs. McKenna et al [**122**] did not observe (3,1) channel with 800 nm 55 fs pulses though they did register atomic ions up to N^{3+}. They refer to the classical appearance intensity curves [**68**] to show that the (2,2) channel is energetically favorable compared to (3,1) at this pulse length. The other study [**121**] with 33 fs 800 nm pulses up to $1.5*10^{15}$ Wcm^{-2} observed (2,2) and (3,1) channels and discussed possible mechanisms of symmetric and asymmetric dissociation. Their conclusion agrees with what we directly see in our spectra: the (3,1) channel is created only at small internuclear separations.

Figure 6.6 Symmetric (2,2) vs asymmetric (3,1) channel production: competing mechanisms. Comparison between long 600 fs and short 33 fs pulse of the same peak intensity.Solid line is 600 fs laser pulse; dotted line is 33 fs laser pulse. Triangles and squares indicate steps of certain dissociation paths. The figure is from J. P. Nibarger et al. Phys. Rev. A 63, 053406 (2001) [121]

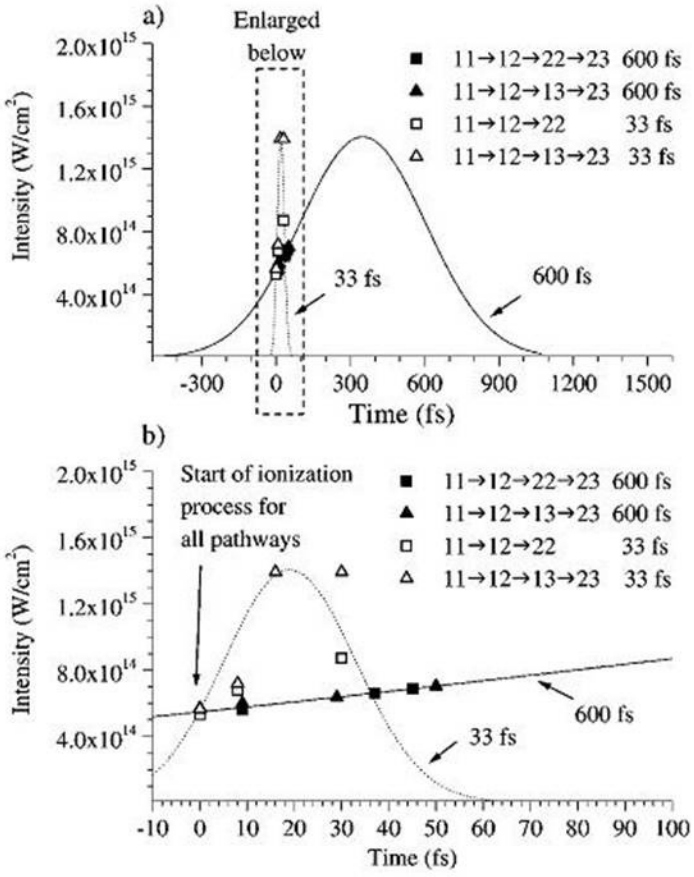

The authors discussed two competing ionization mechanisms: ionization dominated by intensity rise or by the enhanced ionization at the critical distance. The idea in [**121**] is that while the intensity on the rising edge of the pulse increases, electrons are being removed and the (3,1) channel appears at some point. But for the (2,2) channel to be produced the rising intensity itself is not sufficient. The governing mechanism for this case is enhanced ionization: internuclear separation has to reach a critical value for that to happen. After that point the symmetric (2,2) channel becomes energetically more favorable. It means that if the intensity does not get high enough to produce (3,1) fragments before the critical distance is reached, then it will never appear, and the (2,2) channel dominates. Fig. **6.6**, adopted from reference [**121**], demonstrates that for the case of 600 fs and 33 fs pulse of the same peak intensity. The ionization starts on the rising edge of the pulse, and N_2^{2+} (1,1) is produced first. As we can see, even the peak intensity of the 33 fs pulse is not sufficient to produce the (2,2) channel. However, it appears later on the falling edge of the short pulse. That can only be explained by the fact that the critical distance is reached by that moment, and the intensity does not play significant role in appearance of the (2,2) channel. On the other hand, looking at the 600 fs pulse, we can see, that the (2,2) channel is produced long before the intensity gets to its maximum value. It appears though, at the same moment as with the short pulse, when the internuclear separation reaches the same critical value. Therefore, with the long pulse the (3,1) channel doesn't have a chance to appear.

In our experiment we employed two pulses. As long as they come one after another with a short delay, the molecules do not have time to expand to the critical distance and we see them dissociating into the (3,1) channel with the probe pulse. But as soon as the delay gets longer than 20 fs the molecule expands to the critical separation before the probe pulse comes and with enhanced ionization the (3,1) channel disappears. The enhanced ionization phenomenon is closely related to the electron localization process [**14**]. In dissociating N_2^{3+} state the nuclei are moving apart until an electron finally localizes at one of the nuclei (N^{2+}+N^{+}). At this point the probe pulse will most likely remove the electron from N+ producing the (2,2) channel. On the other hand, we observe the (2,2) channel for all delays, not only starting with 20 fs. Before the localization takes place at the critical internuclear distance, it cannot be distinguished

from which nuclei the electron is removed. As a result, the probe pulse with enough intensity can produce both the (2,2) and (3,1) channels.

As for another asymmetric channel, (3,2) (Fig. **6.2(d)**), even though the statistics are not very high, one can see that it exists for all delays in our experiment. The competitor for this channel would be the (4,1) fragmentation of N_2^{5+} ion. However, in our experiment we did not observe this channel. The N^{4+} ion has such a high ionization potential that with the pump and probe intensities we had it was impossible to produce it.

To uncover the details of the dynamics of the molecular structure following its interaction with the laser field, we have to learn how to read the information recorded in experimental spectra. Fig. **6.7** shows the multitude of potential curves for the nitrogen molecule and its molecular ions [**123**-**126**]. The next step in our study is to answer the question of whether we can distinguish which of these states contribute to the molecular dynamics.

Figure 6.7 Several low lying potential curves for the N_2 molecule and N_2^+, N_2^{2+}, N_2^{3+} molecular ions.

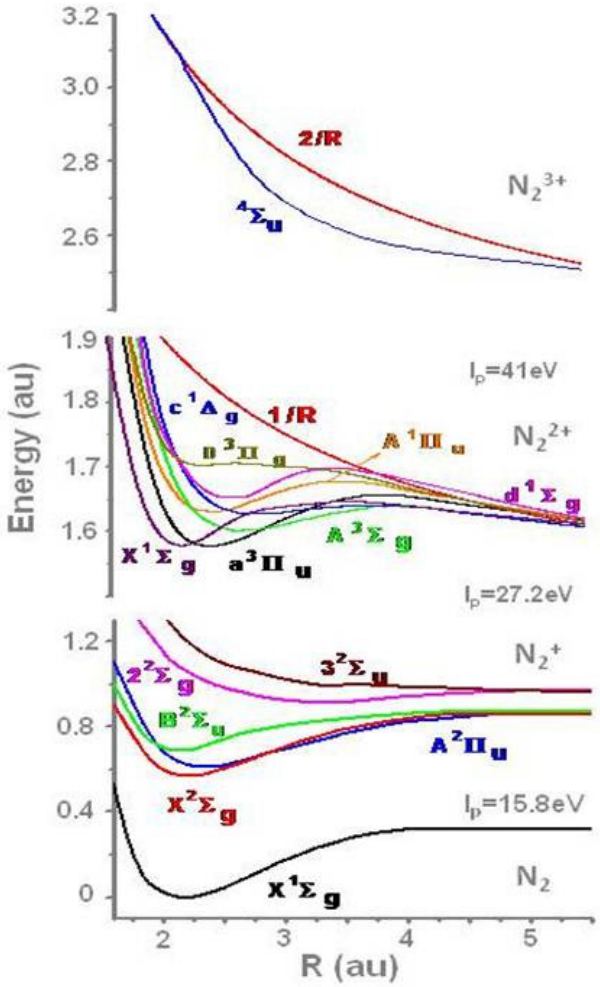

6.2.2 Classical model: results and discussion

Our classical model of a diatomic molecule dissociation following its interaction with near IR short laser pulse is based on the classical equations of motion. We simply assume that one or several electrons are removed by a laser pulse from a neutral molecule in its ground state (at the equilibrium internuclear distance of 2.2 au). Then, in a classical picture, the "particle", with mass equal to the reduced mass of the nuclei starts moving with zero initial momentum in the field created by a potential of the molecular ion. This potential can be purely repulsive possess a single minimum, or be more complicated in behavior, as we can see by looking at the potential curves in Fig. **6.8**. We want to describe the subsequent evolution of the "particle" in each of these potentials and the consecutive Coulomb explosion by the delayed probe pulse. Ultimately, we obtain a kinetic energy release for the explosion fragments as a function of time delay, in order to compare it to our experimental spectra. In the experiment a probe pulse comes with various delays and breaks the molecular ion in two atomic fragments. Thus, to map time evolution of energy at each time step we have to add the Coulomb energy of the fragments interaction to the kinetic energy of the "particle" in the ion potential.

To find out which of the many dissociation pathways is operational at our experimental conditions we have to make an educated guess and try out a number of different potential curves as intermediate states in the dissociation process. In this case the potential curves have to be known. In the calculations we used potential curves for N_2, N_2^+, N_2^{2+}, N_2^{3+} as a function of internuclear distance (Fig. **6.7**). By looking at dissociating limits, shapes and slopes of the potential curves and comparing them to the behavior of experimental KER as a function of time, we selected several of them as trial curves for our calculations. The details of the calculations are given in the Appendix **D**.

In the experiment our pump and probe pulses are short but not infinitely short. Therefore, several ionizations taking place during one pulse follow one another with some short time delay, which is a fraction of the pulse duration. If we assume that all these electrons are not removed simultaneously, then the wave packet goes up to one or two more intermediate states before the Coulomb explosion. The time between these ionization steps allows for a slight change in internuclear distance, which reduces the

final Coulomb energy and the KER. That is reflected in the fact that the experimental KER is always lower than the model with instantaneous ionization would predict. This effect can be roughly accounted for in our calculations, if we add one more intermediate state and let the classical "particle" move in some average 2/R Coulomb potential (roughly approximating the N_2^{3+} potential) for a short time, which we introduce as a parameter. Varying this parameter we can match the calculated energy at zero delay with the experimental value. We reach the best agreement with the experiment when this parameter is equal to 5 fs which is about two thirds of the pulse FWHM.

The results of the calculations and a schematic drawing of the wave packet motion on potential curves are presented in Fig. **6.8**. Plotting the calculated curves on top of the experimental spectra, we can immediately see that even this simple model gives us very good insight into the fragmentation process. We identify the intermediate charged states by matching asymptotic energies at long delays, and we can also compare the shape and curvature of each curve at short delays to decide which individual electronic states of each ion may be involved. The dissociation trace, which corresponds to the N_2^{2+} parent ion, is broad so that several electronic states of the ion can fit inside this feature. The density of states is high as can be seen in Fig. **6.8** and many states can be populated simultaneously. The analysis is less obvious with the oscillating (bound) part of the spectra. The structure that we see at short delays cannot be exactly matched with classical oscillations in potential wells. But not being able to find out the frequencies, we still can rule out those states that give energies too high or too low in comparison to the experimental values.

Figure 6.8 Classical model results. (a) Schematic presentation of the wave packet motion on potential curves. (b) Classically calculated time dependant KER traces put on top of experimental spectrum. Each line corresponds to a certain intermediate electronic state of a molecular ion

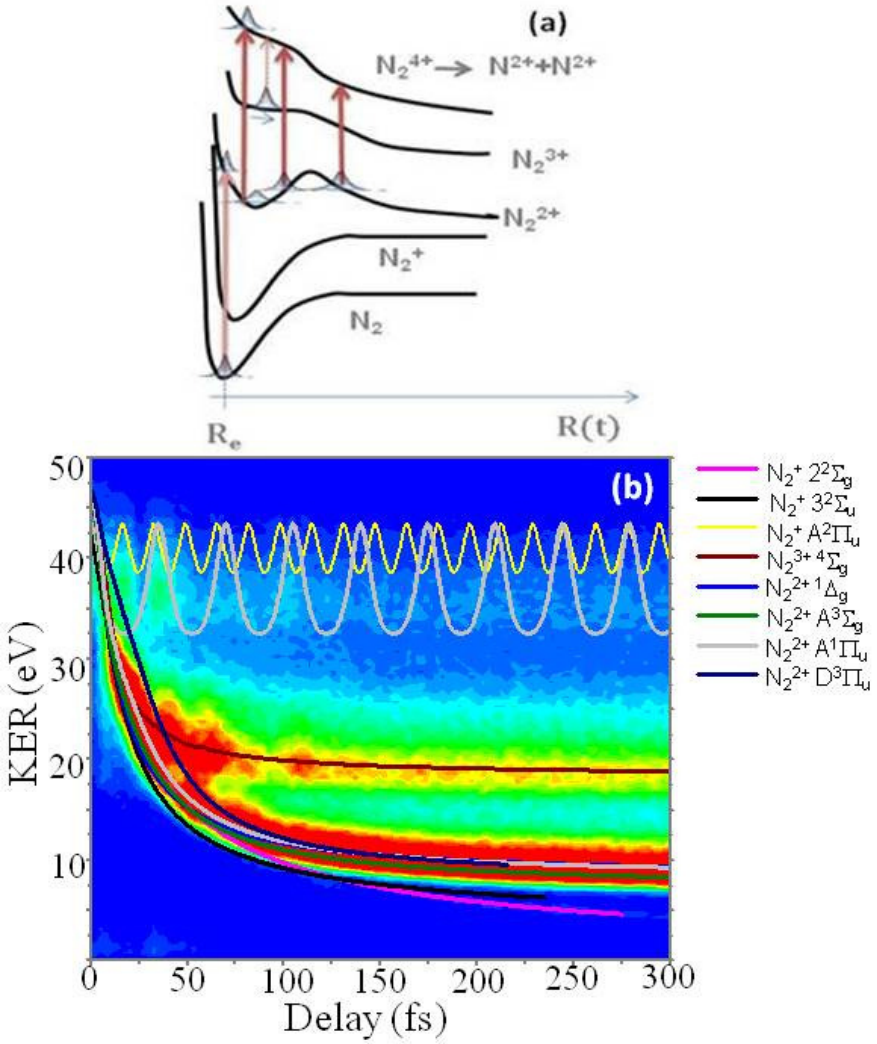

6.2.3 Quantum model: results and discussion

The next step in modeling nuclear dynamic is to take into account quantum effects. From the quantum mechanical point of view the solution of our problem can be found by solving the time-dependent Schrödinger equation with a certain potential. It accounts for such effects as tunneling through a barrier; initial width and shape and spread of a wave packet during its time propagation [**127**]. Details of the calculation are presented in Appendix **E**.

The calculated spectra for the (2,2) channel together with the experimental spectra are shown on Figures **6.9, 6.10, 6.11** and **6.12**. Panels **(b)**, **(c)** and **(d)** of **Fig. 6.9** show calculated spectra for wave packet evolution on three different electronic states: $A^3\Sigma_g$, $d^1\Sigma_g$ and $c^1\Delta_g$. At the starting point of the evolution a wave function is centered at 2.2 au (Franck-Condon transition from N_2 $X^1\Sigma_g$). For the $A^3\Sigma_g$ and $d^1\Sigma_g$ the largest part of the wave packet goes over the potential barrier and dissociates, but a small part is left in a shallow potential well and keeps oscillating. We also observe weak dissociation traces going down to the same asymptotic energy after each oscillation, indicating tunneling through the potential barrier. The $c^1\Delta_g$ state seems to not have any vibration states but has a very shallow depth, which forces a part of the wave packet to bounce once and then to completely dissociate. Asymptotic energies for all these states converge to the experimental value**.**

Figure 6.9 Simulated time dependant KER spectra for various possible dissociation pathways (a) experimental spectrum for comparison; (b) $N_2 \rightarrow N_2^{2+}(A^3\Sigma_g) \rightarrow N_2^{4+} \rightarrow N^{2+}+N^{2+}$; (c) $N_2 \rightarrow N_2^{2+}(d^1\Sigma_g) \rightarrow N_2^{4+} \rightarrow N^{2+}+N^{2+}$; (d) $N_2 \rightarrow N_2^{2+}(c^1\Delta_g) \rightarrow N_2^{4+} \rightarrow N^{2+}+N^{2+}$

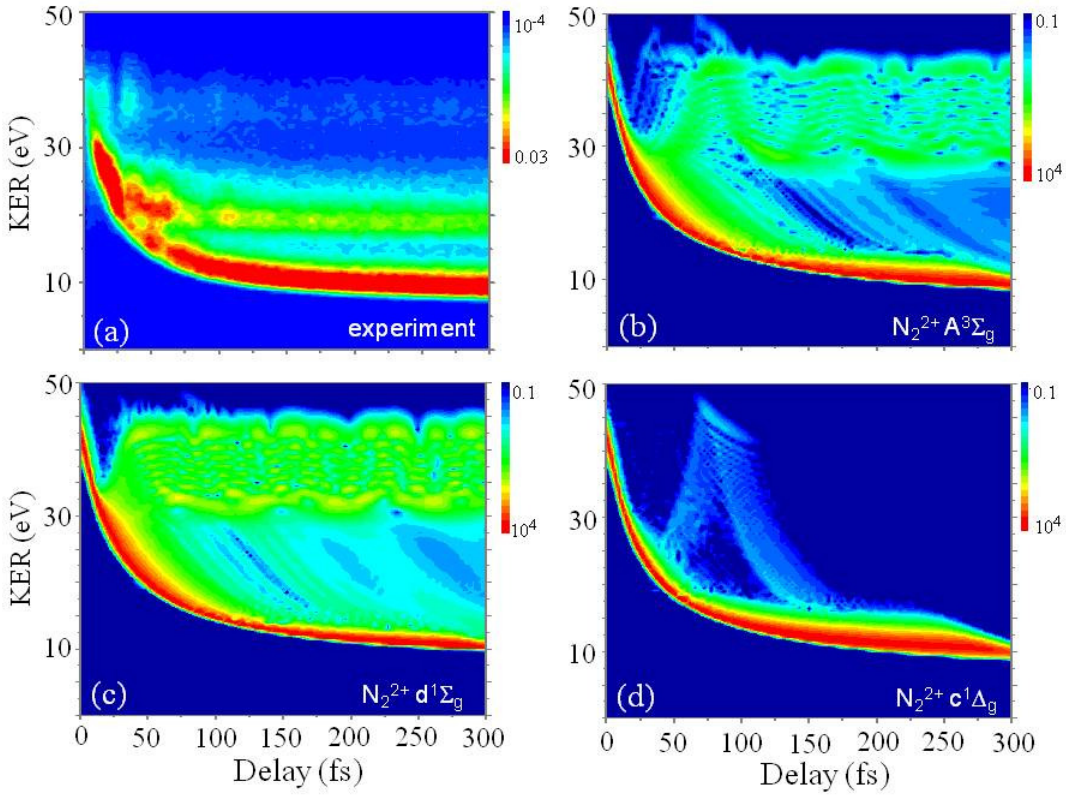

Figure 6.10 Simulated time-dependant KER spectra for various possible dissociation pathways (a) experimental spectrum for comparison; (b) $N_2 \rightarrow N_2^{2+}(a^3\Pi_u) \rightarrow N_2^{4+} \rightarrow N^{2+}+N^{2+}$; (c) $N_2 \rightarrow N_2^{2+}(A^1\Pi_u) \rightarrow N_2^{4+} \rightarrow N^{2+}+N^{2+}$; (d) $N_2 \rightarrow N_2^{2+}(D^3\Pi_g) \rightarrow N_2^{4+} \rightarrow N^{2+}+N^{2+}$

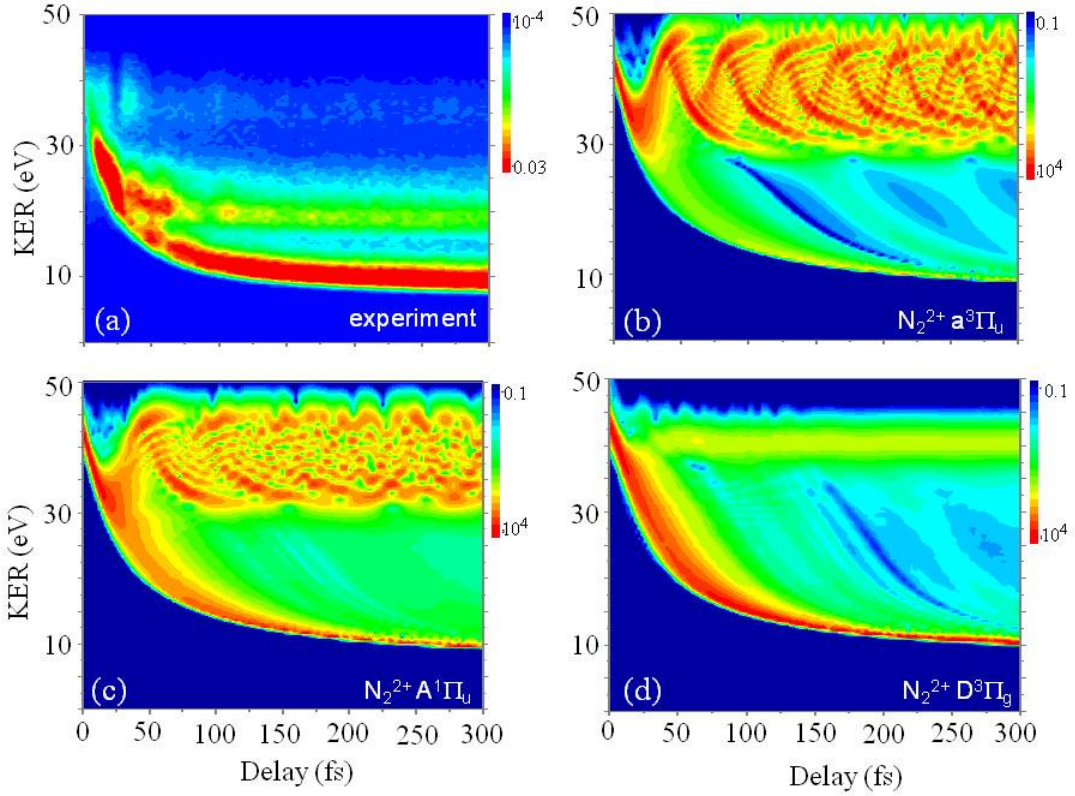

Figure 6.11 (a) Experimental spectrum; (b) simulated time dependant KER spectra for $N_2 \rightarrow N_2^+(^2\Sigma_g^+) \rightarrow N_2^{4+} \rightarrow N^{2+}+N^{2+}$ dissociation pathway

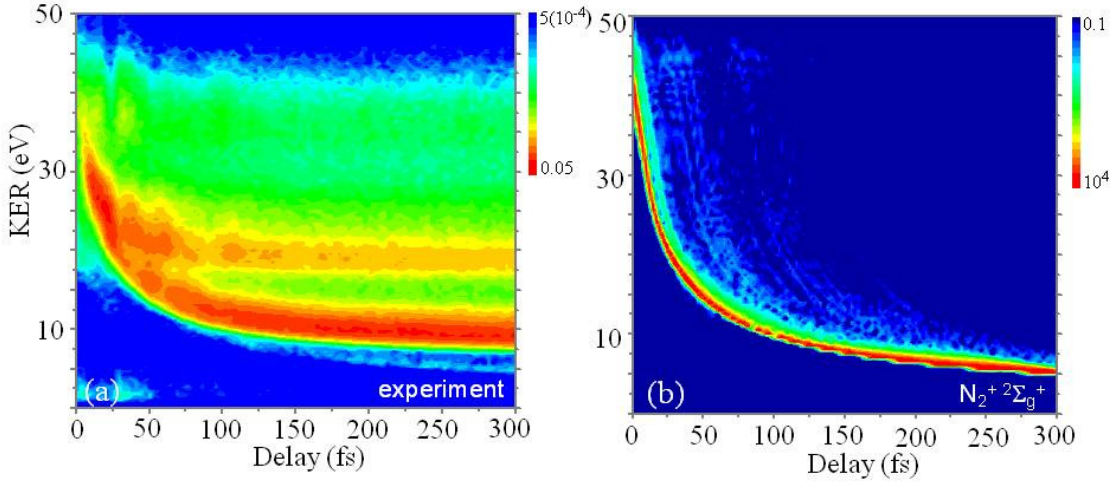

Figure 6.12 (a) Experimental spectrum; (b) simulated time dependant KER spectra for $N_2 \rightarrow N_2^{3+}(^4\Sigma_g) \rightarrow N_2^{4+} \rightarrow N^{2+}+N^{2+}$ dissociation pathway

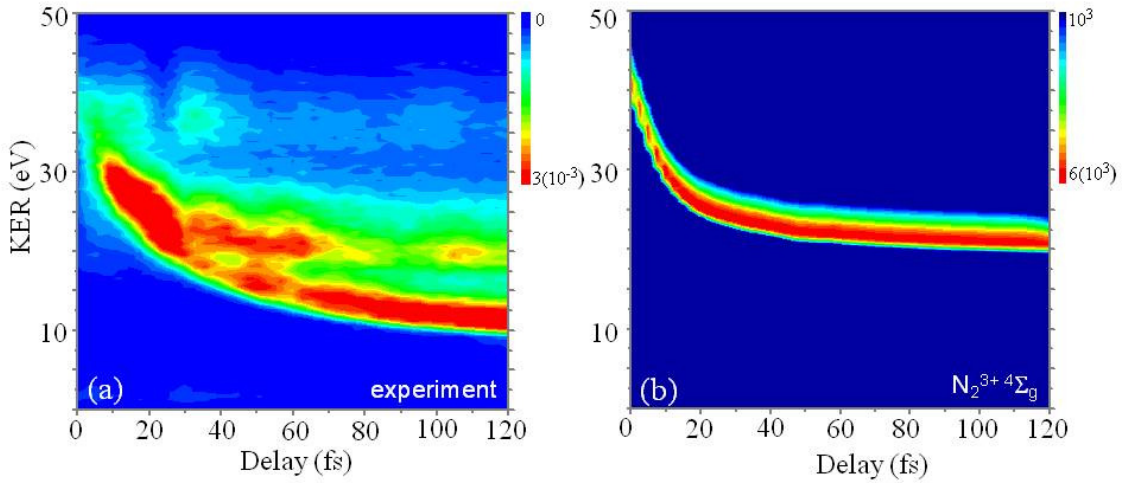

There are three more spectra for the N_2^{2+} states shown in Fig. **6.10**: $a^3\Pi_u$, $A^1\Pi_u$ and $D^3\Pi_g$. The $a^3\Pi_u$ and $A^1\Pi_u$ states both have prominent bound parts with large amplitude and high energies compared to the experimental spectra. The $D^3\Pi_g$ state has a flat part to it and some fraction of the wave packet slows down significantly at the energy of about 42 eV, which looks very different from what we see in the experiment.

Fig. **6.11** presents an excellent agreement between the calculated spectrum for the wave packet evolution on the $^2\Sigma_g^+$ unbound state of N_2^+ and a faint dissociative trace on the experimental plot. Dissociative states of the N_2^+ ion are highly excited states [**124**] which can be populated with low probability at our experimental conditions. The low energy states are bound. Taking any of them as a trial potential in either classical or quantum model will result in pure oscillatory spectra with energies much higher than those measured in our experiments.

Fig. **6.12** reveals the origin of the dissociative feature with high asymptotic energy. A wave packet launched on the unbound non-Coulombic $^4\Sigma_g$ state of the N_2^{3+} ion follows the same path on KER spectrum as the experimental trace. Among the electronic states of the N_2^{4+} ion with the lowest dissociation limit, $^4\Sigma_g$ was picked as the most diverging from the Coulomb 4/R potential according to [**126**]. All non-Coulombic states of N_2^{4+} calculated in [**126**] are unbound and very close to each other in energies and shapes. Judging from the width and intensity of the corresponding trace on Fig. **6.12 (a)**,

the intensity of the pump pulse is sufficient to populate all the states that converge to the lowest dissociation limit.

6.2.4 Summary

The nuclear dynamics in molecular nitrogen following its interaction with laser field has been investigated by measuring the kinetic energy release of Coulomb explosion fragments as a function of time. For the first time pulses as short as 8 fs were used for pump-probe experiments on N_2 to thoroughly scan over a large range of delays to observe the bound and dissociative motion of nitrogen molecular ions in real time. We studied Coulomb charge symmetric and asymmetric break-up channels up to N^{3+}+N^{2+}. We demonstrated specific details of dynamics for the asymmetric N^{3+}+N^{+} channel and supported the idea of two competing ionization mechanism first suggested in [**121**].

With simple classical and quantum models we have extracted information about intermediate electronic states contributing to the molecular dynamics and fragmentation process.

Our future plans include using the velocity mapping imaging (VMI) technique to acquire enough statistics to analyze the bound part of the nuclear wave packet more thoroughly. We further intend to use Fourier analysis to extract information about vibrational [**128**] and rotational [**72**] beat frequencies and bound and quasi bound states of nitrogen molecular ions contributing to the nuclear dynamics; and to use angular information from the VMI data to distinguish parallel and perpendicular transitions between electronic states**.**

6.3 Oxygen molecule O_2

6.3.1 Experimental results and discussion

KER spectra for four break-up channels O^{+}+O^{+}, O^{2+}+O^{+}, O^{2+}+O^{2+} and O^{3+}+O^{+} are shown on Fig. **6.13**. The main features of these spectra, which are similar to those seen in hydrogen and nitrogen, are discussed in section **6.2.1** in context of N_2 experiments. For the (1,1) channel there is a dissociative trace that starts to be visible below 6 eV and after 40 fs of delay and goes down to below 3 eV at 200 fs. The high-energy part of the (1,1)

spectrum represents mostly O^+ fragments that are produced by the probe pulse only from those neutral molecules that were not affected by the pump. For the (2,1) and (2,2) channels we observe time dependent behavior inside the high-energy region. To put our discussion into context, we compare O_2 spectra with the corresponding spectra for N_2. In addition to the common features in both molecules, like dissociation traces which start at zero delay, one can see that for oxygen parts of the wave packet start their trips down in energy later in time, after being bound in some potential well. More specifically, we compare the (2,2) channels for nitrogen and oxygen (Fig. **6.13(c)**). Unlike in nitrogen, in O_2 the population is distributed more evenly between dissociative and bound states. An immediate guess that one can make is that bound or quasi-bound intermediate states of the parent ions are energetically more accessible and easier populated for oxygen than for nitrogen at our experimental conditions. Two dissociative traces are also almost equally intense and come very close to each other in energy (around 7 eV and 11 eV at 200fs). Those dissociative traces that start at later delays come to merge with the 11 eV trace, suggesting that electronic states of the same parent O_2^{q+} ion are populated and cause this type of dynamics. For nitrogen, to the contrary, the bound part of the spectrum is very weak in comparison to the dissociative part and it is also more narrow in energy range; the dissociation trace starts at zero delay and any leaking out of the wave packet oscillating in potential well is negligibly small, so that it cannot be clearly distinguished in the experimental plots. It can be suggested at this point that bound or quasi-bound intermediate electronic states are hard to access in our experimental conditions and their potential wells are deeper in nitrogen than in oxygen.

Similar to N_2, KER spectra for O_2 are taken starting from negative delays. The asymmetry of the spectra about zero carries information about different pump and probe intensity values, and the influence of those differences on the population distribution of the intermediate states.

The asymmetric (3,1) break-up channel, O^{3+}+O^+, was also observed in our experiment (see Fig. **6.13(d)**). The same phenomenon is observed for oxygen that we noted for the nitrogen asymmetric break-up: bright dissociation trace that appears at 0 delay at around 40 eV goes down to about 18 eV and then disappears completely at the same delay of 20 fs. This observation adds up to the conclusion that this phenomenon of

charge asymmetric break up is not specific to nitrogen molecule, but it is rather common for homonuclear diatomics.

The next step is to apply our classical and quantum models to extract the information about parent ions and electronic states contributing to dynamics we observe in the oxygen experiment.

Figure 6.13 Time-dependent kinetic energy release (KER) spectra (integrated over the solid 4π angle) for O_2 for (a) O^++O^+; (b) O^{2+}+O^+; (c) O^{2+}+O^{2+} and (d) O^{3+}+O^+ breakup channels. Pump pulse width - 8fs, intensity - 7×10^{14} W/cm^2; probe pulse width - 8fs, intensity - 11×10^{14} W/cm^2

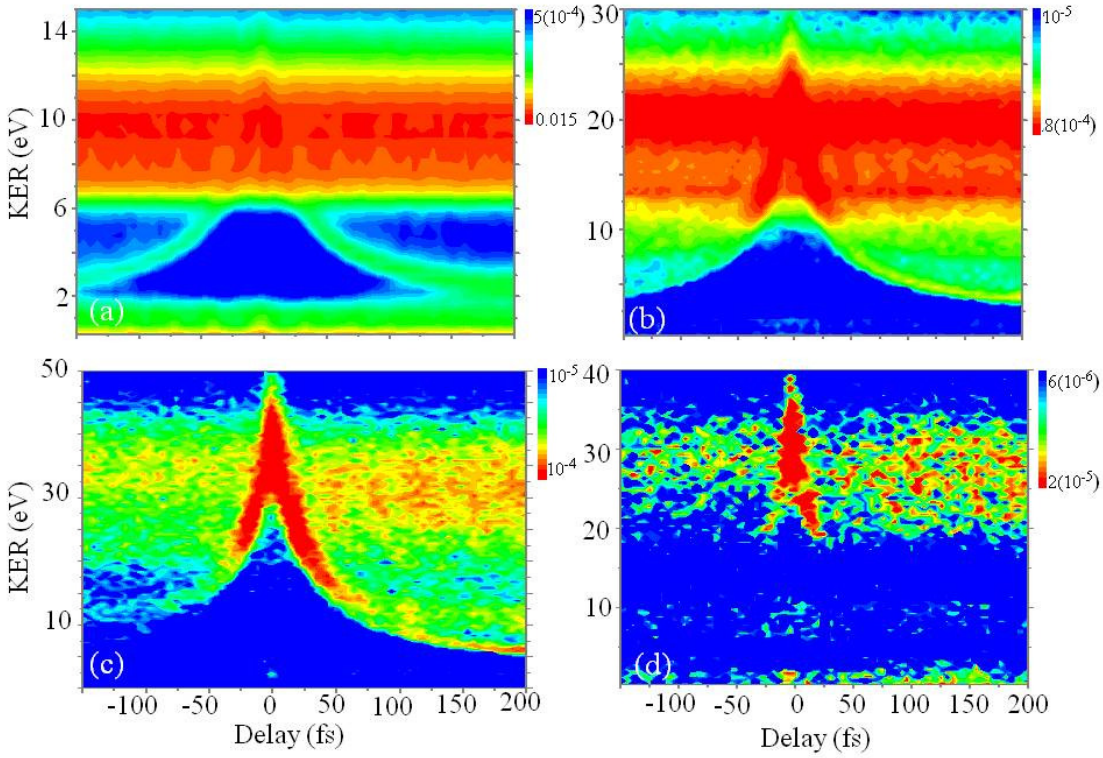

6.3.2 Classical model: results and discussion

The description of classical model and detailed calculations are provided in section **6.2.2** and Appendix **D**. Trial potential curves for oxygen are presented in Fig. **6.14**.

The results of the calculations and a schematic drawing of the wave packet motion on potential curves are presented in Fig. **6.15**. The potential curves for the neutral molecule and molecular ions were found in references [**129-133**]. As it is the case with the

nitrogen molecule we plot the classically calculated traces on top of the experimental spectra for the O^{2+}+O^{2+} channel. As seen in the Fig. **6.15**, the upper dissociation trace which comes to the energy of about 11 eV after 200 fs can be assigned to some electronic states of the doubly charged molecular ion. The lower trace appears to characterize dissociation via population of excited states of the singly charged molecular ion. It is impossible to model quantum effects of the motion of wave packet, like leaking from potential well, in the frame of a classical model. We will discuss quantum simulations in the next section. Nonetheless, we tried to model the oscillatory part classically, like we did for N_2 molecule. Though, it did not allow us to assign a particular state, it did allow us to exclude those states which are not in the correct energy range.

Figure 6.14 Several low lying potential curves for the O_2 molecule and O_2^+, O_2^{2+}, O_2^{3+} molecular ions.

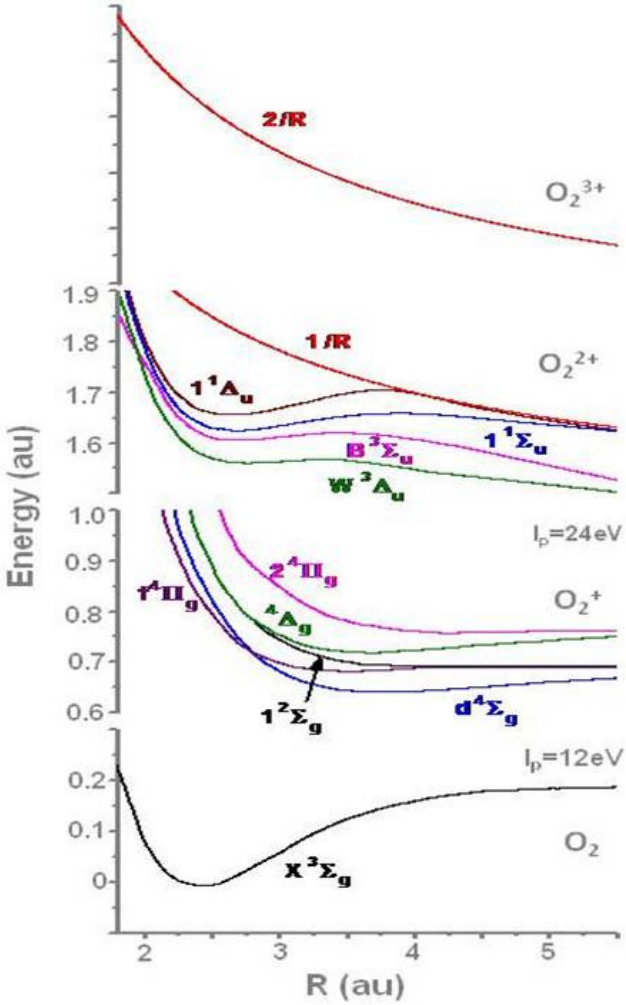

Figure 6.15 (a) Schematic presentation of wave packet motion on potential curves of the O^+ and O^{2+} ions. (b) Classically calculated time dependant KER traces put on top of the experimental spectrum. Each line corresponds to a certain intermediate electronic state of a molecular ion

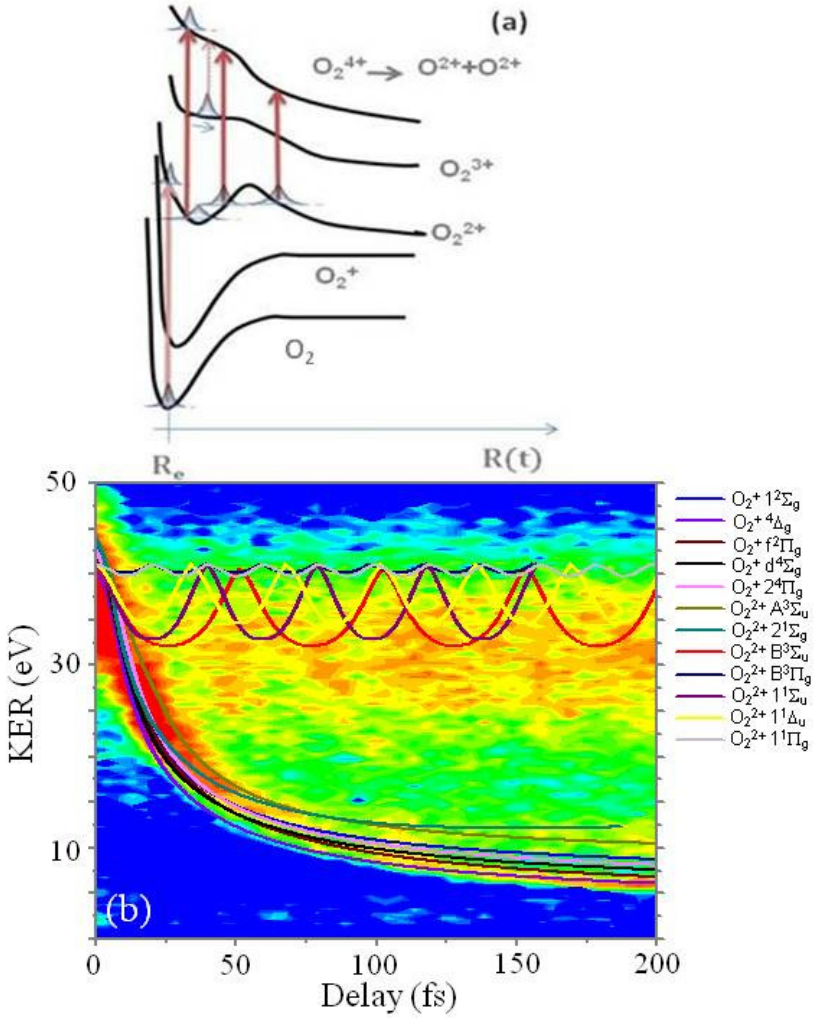

6.3.3 Quantum model: results and discussion

Here I discuss the results of quantum modeling of nuclear wave packet dynamics for oxygen. Details of calculations are presented in Appendix **E**.

The calculated spectra for the (2,2) channel and the experimental spectra are shown in Figures **6.16** and **6.17**. Panels **(b)**, **(c)**, **(d)**, **(e)** and **(f)** of Fig. **6.16** show the spectra for wave packet evolving on five different electronic states of the O_2^+ ion: $2^4\Pi_g$, $1^2\Sigma_g$, $d_4\Sigma_g$, $f^4\Pi_g$ and $^4\Delta_g$ correspondingly. At the starting point of the evolution a wave

function is centered at 2.4 au (Franck-Condon transition from O_2 $X^3\Sigma_g$). All of these states are exhibiting very similar behavior. They are all dissociative with very shallow potential wells which contain a few vibrational states [**132**]. Therefore, most of the wave packet dissociates immediately with about the same asymptotic kinetic energy release of 5-7 eV, which is observed in our experiments. A small part of the wave packet (orders of magnitude smaller: see the color scheme to Fig. **6.16**) stays bound for a while but leaks out after a few oscillations and dissociates to the same KER. There are four more spectra for nuclear wave packet propagation on $1^1\Delta_u$, $B^3\Sigma_u$, $W^3\Sigma_u$ and $1^1\Sigma_u$ states of O_2^{2+} ion (see Fig. **6.17**). All four of them are characterized by potential wells deep enough to keep significant part of the wave function bound and oscillating with the amplitudes and in energy range comparable to the experimental values. These states dissociate to the same KER of about 11 eV that agrees very well with the corresponding features in the experimental spectra.

Figure 6.16 Simulated time dependant KER spectra for various possible dissociation pathways (a) experimental spectrum for comparison; (b) $O_2 \rightarrow O_2^+(2^4\Pi_g) \rightarrow O_2^{4+} \rightarrow O^{2+}+O^{2+}$; (c) $O_2 \rightarrow O_2^+(1^2\Sigma_g) \rightarrow O_2^{4+} \rightarrow O^{2+}+O^{2+}$; (d) $O_2 \rightarrow O_2^+(d^4\Sigma_g) \rightarrow O_2^{4+} \rightarrow O^{2+}+O^{2+}$; (e) $O_2 \rightarrow O_2^+(f^4\Pi_g) \rightarrow O_2^{4+} \rightarrow O^{2+}+O^{2+}$; (f) $O_2 \rightarrow O_2^+(^4\Delta_g) \rightarrow O_2^{4+} \rightarrow O^{2+}+O^{2+}$

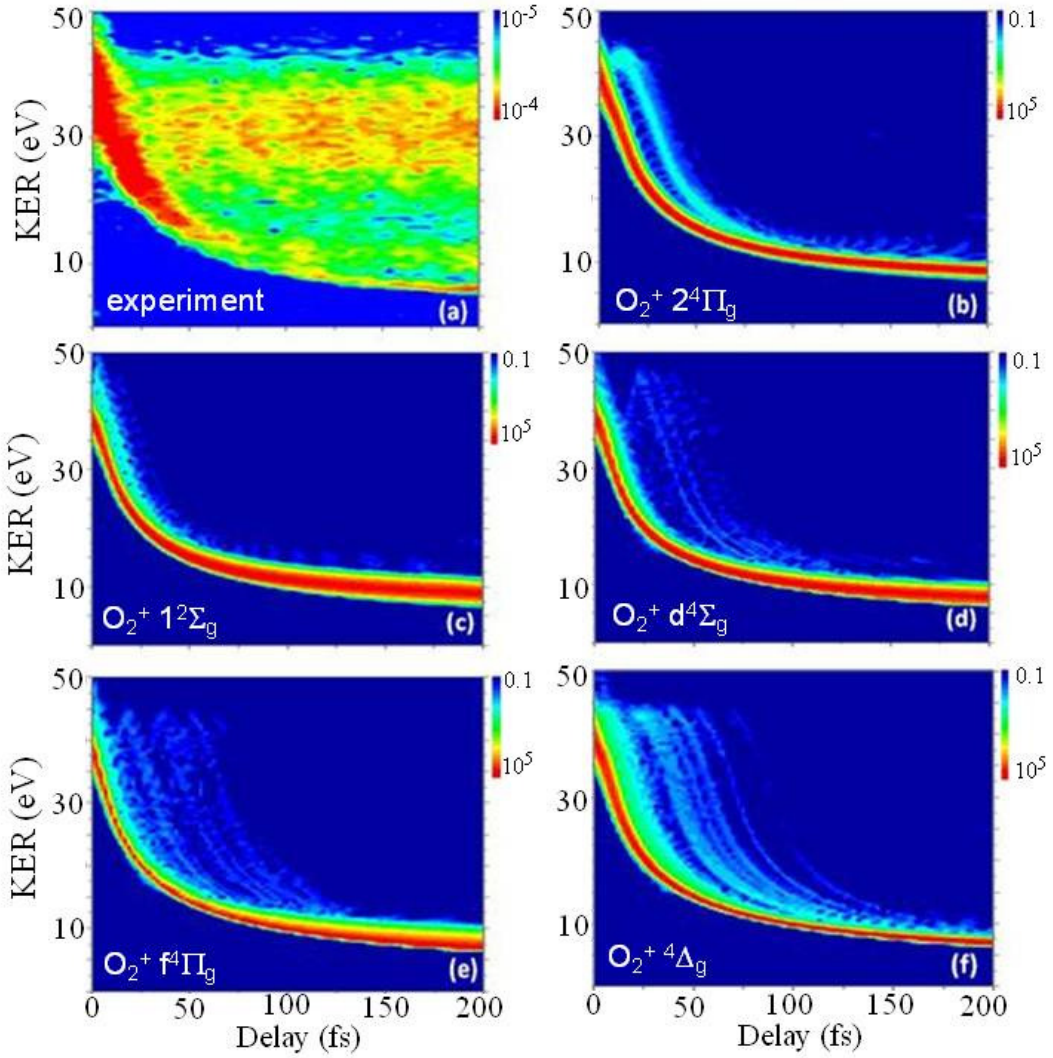

Figure 6.17 Simulated time dependant KER spectra for various possible dissociation pathways (a) experimental spectrum for comparison; (b) $O_2 \rightarrow O_2^{2+}(1^1\Delta_u) \rightarrow O_2^{4+} \rightarrow O^{2+}+O^{2+}$; (c) $O_2 \rightarrow O_2^{2+}(B^3\Sigma_u) \rightarrow O_2^{4+} \rightarrow O^{2+}+O^{2+}$; (d) $O_2 \rightarrow O_2^{2+}(W^3\Sigma_u) \rightarrow O_2^{4+} \rightarrow O^{2+}+O^{2+}$; (e) $O_2 \rightarrow O_2^{2+}(1^1\Sigma_u) \rightarrow O_2^{4+} \rightarrow O^{2+}+O^{2+}$

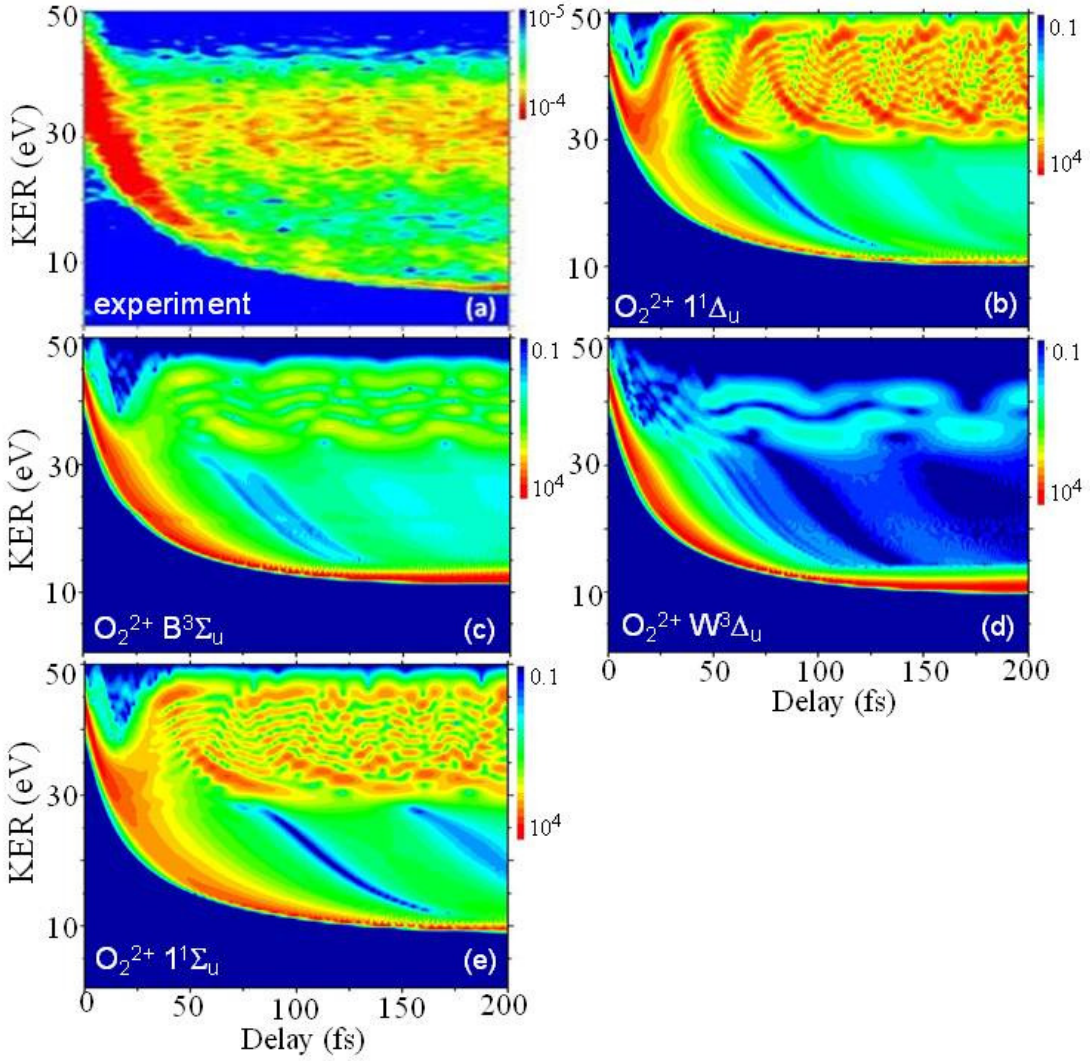

6.3.4 Summary

Here we studied nuclear wave packet dynamics for the O_2 molecule initiated by the interaction with intense few-cycle near-IR laser pulses. We followed the same procedure as we did before with the nitrogen molecule and applied a classical and a quantum model to interpret the experimental spectra of time-dependent kinetic energy release for symmetric $O^{2+}+O^{2+}$ break up. As it was done with the nitrogen molecule we were able to assign each feature of the experimental spectrum to an intermediate

molecular ion responsible for the observed dynamics. Unlike in nitrogen, where most of the dynamics takes place on electronic states of molecular di-cation N_2^{2+}, we found that mostly dissociative states of singly charged molecular ion and quasi-bound states of doubly charged ion participate in the nuclear dynamics of oxygen at our experimental conditions.

6.4 Carbon monoxide molecule CO

6.4.1 Experimental results and discussion

KER spectra for four break-up channels C^++O^+, C^{2+}+O^+, C^++O^{2+} and C^{2+}+O^{2+} are shown in Fig. **6.18**. The main features of these spectra are common for all diatomic molecules studied and described previously [see section **6.2.1**]. For the (1,1) channel (Fig. **6.18 (a)**) there is no visible kinetic energy variation with time. Both (2,1) and (1,2) channels (Fig. **6.18 (b)**, **(c)**) reveal features that are familiar from previous experiments with homonuclear diatomic molecules D_2, N_2, O_2. However, C^{2+}+O^+ channel is more abundant than C^++O^{2+} because it is easier to make C^{2+} than O^{2+} due to its lower ionization potential. The C^{2+}+O^{2+} fragmentation channel (Fig. **6.18 (d)**) also demonstrates time-dependent kinetic energy release; and one can distinguish dissociation traces going down to low energy but most of the statistics are concentrated in the region between 22 and 30 eV and along dissociative traces up to 30 fs delay. Similar to N_2 and O_2, KER spectra for CO are taken starting from negative delays and show some asymmetry due to the effect of the changing intensity ratio of pump and probe. To interpret the experimental results we applied our quantum model to simulate KER time-dependent spectra for CO, a heteronuclear diatomic molecule.

Figure 6.18 Experimental kinetic energy release vs delay between pump and probe spectra for break up channels (a) CO → C^{+}+O^{+}; (b) CO → C^{2+}+O^{+}; (c) CO → C^{+}+O^{2+}; (d) (b) CO → C^{2+}+O^{2+}. Pump intensity - 9*10^{14} W/cm^{2}; probe intensity - 14*10^{14} W/cm^{2}; pulse width - 8 fs

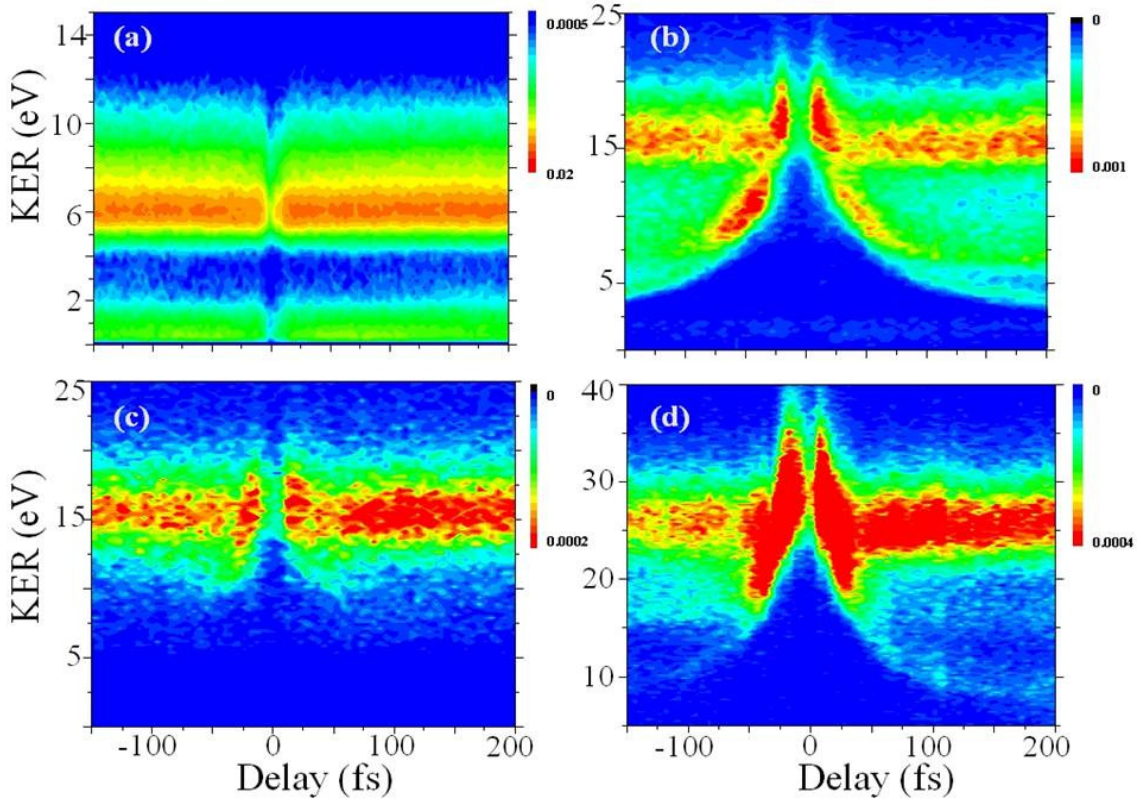

6.4.2 Quantum model: results and discussion

For calculation of kinetic energy release as a function of time for CO we used the same model that was described for the nitrogen and oxygen molecules before. The best statistics we acquired in our experiment for the CO → C^{2+}+O^{+} (2,1) channel, thus, we simulated the break up on CO^{3+} curve approximated by corresponding Coulomb potential via the CO^{+} and CO^{2+} intermediate states. The trial potential curves are presented in Fig. **6.19**. The potential curves for the neutral molecule and molecular ions were found in references [**134**-**137**].

The calculated spectra for the (2,1) channel together with the experimental spectra are shown on Figures **6.20**, **6.21**, **6.22, 6.23** and **6.24**. Panels **(b)**, **(c)** and **(d)** of Fig. **6.20** show the spectra for wave packets evolving on the $E^{2}\Pi$, $D^{2}\Pi$ and $F^{2}\Pi$ electronic states of

the CO^+ molecular ion. The initial wave packet is a projection of the CO ground state wave function; it is centered at 2.1 au (Franck-Condon transition from CO $X^1\Sigma^+$). These three states are all purely dissociative, but come to different asymptotic values of energy. The trace on panel **(c)**, corresponding to the $D^2\Pi$ state, goes down to approximately 7 eV at 200 fs delay and follows one of the dissociative traces in the experimental spectra, while the other two seem to have higher asymptotic energies.

Figure 6.19 Selected potential curves for the CO molecule, CO^+ and CO^{2+} ions

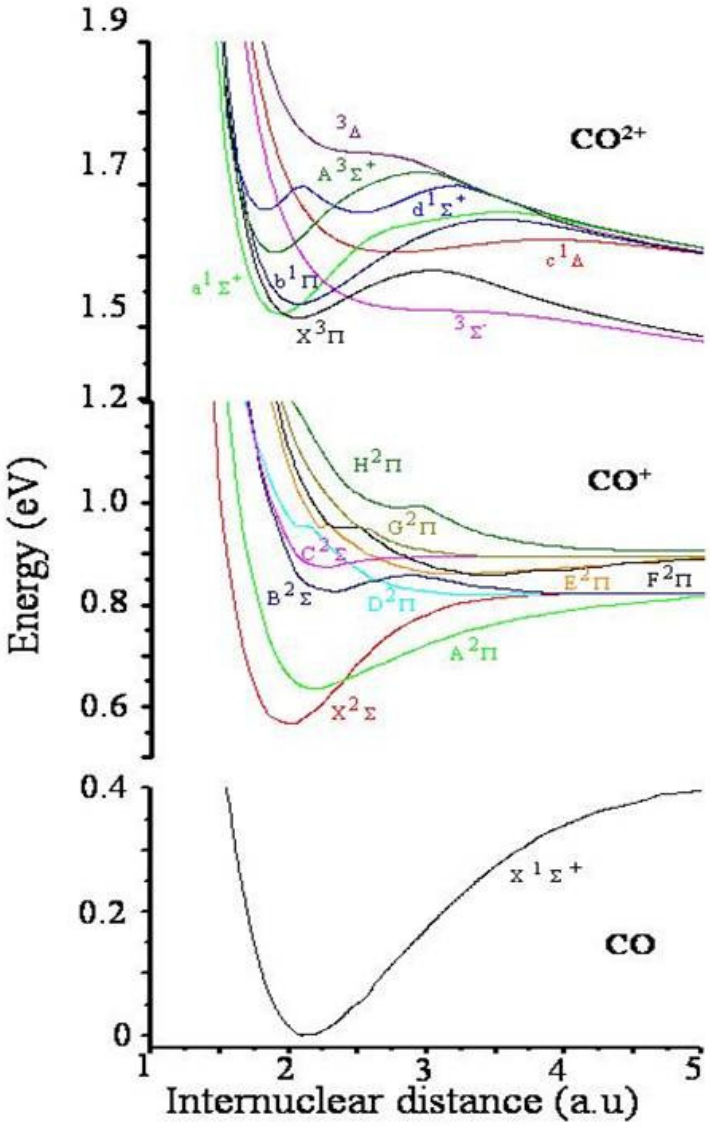

States $A^2\Pi$ and $C^2\Sigma$, corresponding to spectra **(b)** and **(c)** on Fig. **6.21,** cause dissociation of the wave packet to the energy slightly below 5 eV at 200 fs, like we see on **(a)** spectrum, and keep a part of the wave packet bouncing in a well. The oscillating

part though does not quite fit any feature that we see in the experiment. In Fig. **6.22,** neither of the states produces features with energies that correspond to the experimental values. The pure bound state $X^2\Sigma$ produces oscillations in the energy range significantly higher than what we observed. Spectrum **(c)** in Fig. **6.23** models the wave packet behavior on the potential curve of the $b^1\Pi$ electronic state of CO^{2+} and reveals oscillating and dissociating features closely resembling those in the experimental spectrum **(a)**. Though we are not able to distinguish clearly a structure inside the region between 13 and 18 eV in the experimental plot, we see that in the simulated spectra the bound part falls within the same energy range. Dissociation on the $c^1\Delta$ potential produces KER vs time spectrum which fits the experimental feature with 7 eV asymptote. The other calculated spectra in Figures **6.23** and **6.24** simulating the wave packet evolution on the CO^{2+} potential curves do not show a good match to any of the experimental features.

6.4.3 Summary

To summarize, looking at the experimental KER plots as a function of delay between pump and probe pulse and comparing them to the spectra, simulating the evolution of the wave packet on potential curves of an intermediate molecular ion, we can identify specific features and characterize them as a result of certain dynamics and dissociation pathways. The CO molecule is heteronuclear; it is not symmetric about the midpoint between nuclei, which makes its dynamics richer and more complex, on one hand. On the other hand, the introduced asymmetry makes pathways more distinguishable from each other and it is easier to single out an electronic state associated with a certain feature on the experimental spectrum than it was for the N_2 or O_2 molecules.

Figure 6.20 Kinetic energy release as a function of time spectra for CO → C^{2+}+O^{+} fragmentation channel (a) experimental; and simulated through different pathways: (b) CO → $CO^{+}(E^{2}\Pi)$ → CO^{3+} → C^{2+}+O^{+}, (c) CO → $CO^{+}(D^{2}\Pi)$ → CO^{3+} → C^{2+}+O^{+}, (d) CO → $CO^{+}(F^{2}\Pi)$ → CO^{3+} → C^{2+}+O^{+}

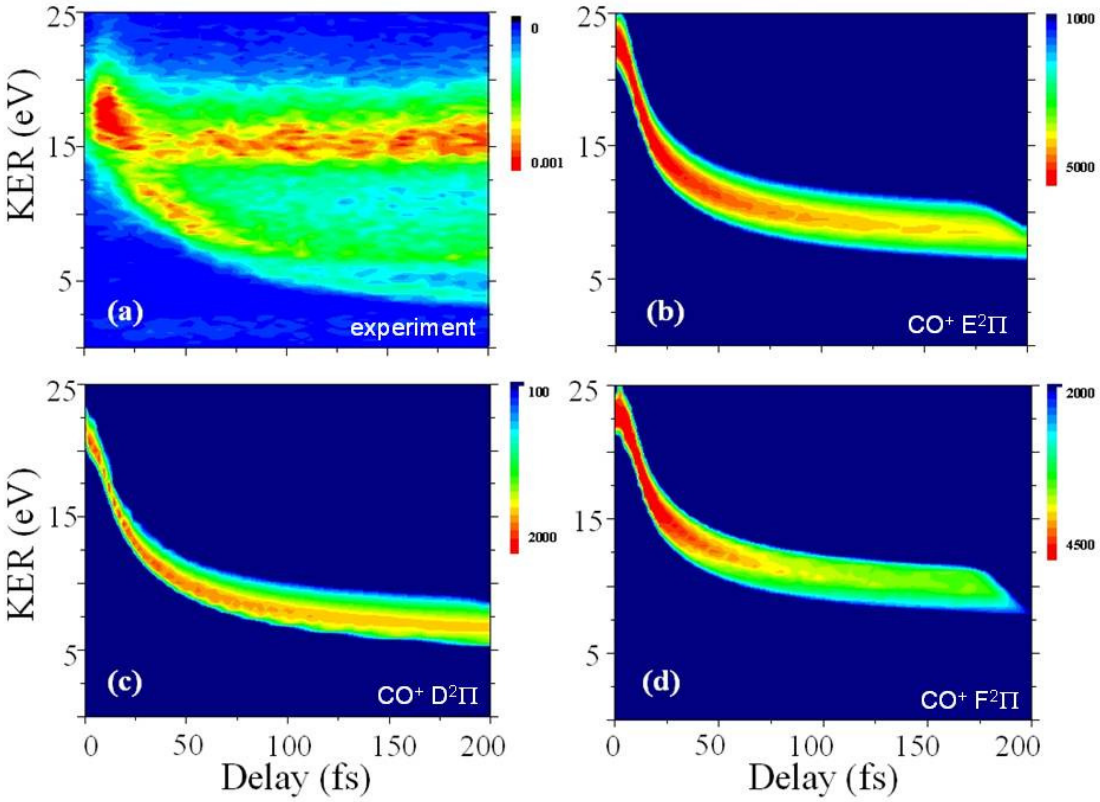

Figure 6.21 Kinetic energy release as a function of time spectra for CO → C^{2+}+O^{+} fragmentation channel (a) experimental; and simulated through different pathways: (b) CO → $CO^{+}(A^{2}\Pi)$ →CO^{3+} → C^{2+}+O^{+}, (c) CO → $CO^{+}(C^{2}\Sigma)$ → CO^{3+} → C^{2+}+O^{+}, (d) CO → $CO^{+}(B^{2}\Sigma)$ → CO^{3+} → C^{2+}+O^{+}

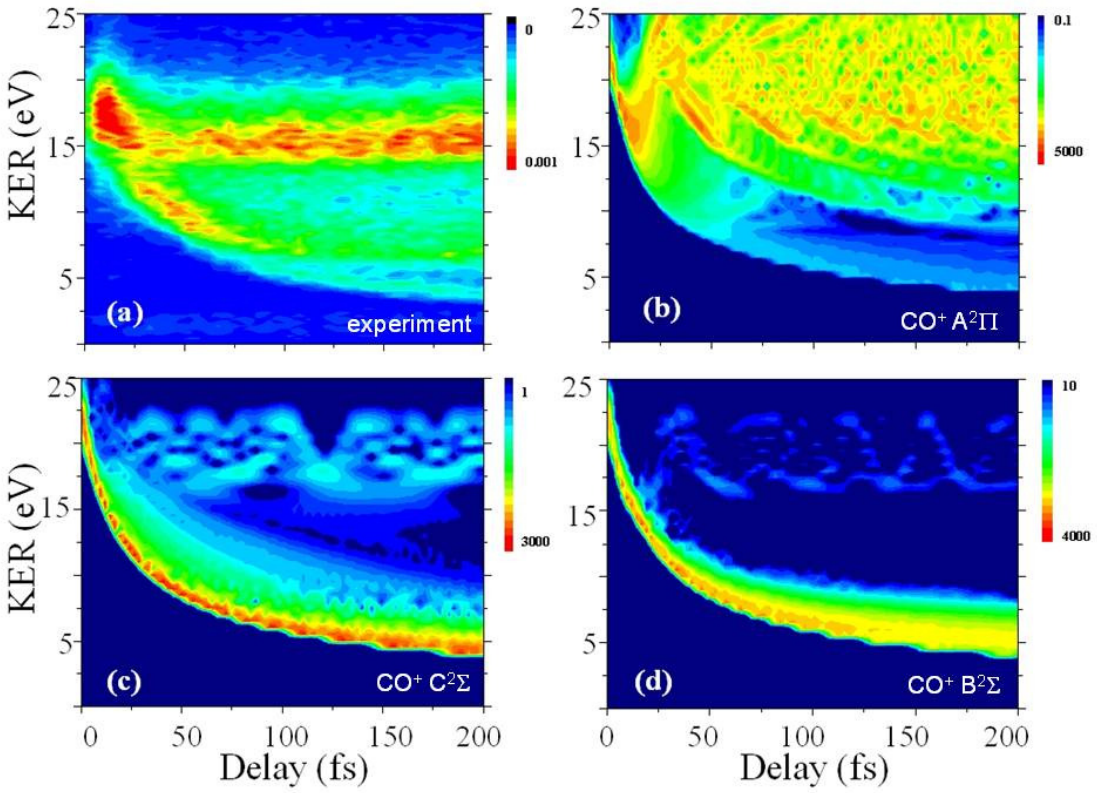

Figure 6.22 Kinetic energy release as a function of time spectra for CO → C^{2+}+O^{+} fragmentation channel (a) experimental; and simulated through different pathways: (b) CO → $CO^{+}(G^{2}\Pi)$ → CO^{3+} → C^{2+}+O^{+}, (c) CO → $CO^{+}(X^{2}\Sigma)$ → CO^{3+} → C^{2+}+O^{+}, (d) CO → $CO^{+}(H^{2}\Pi)$→ CO^{3+} → C^{2+}+O^{+}

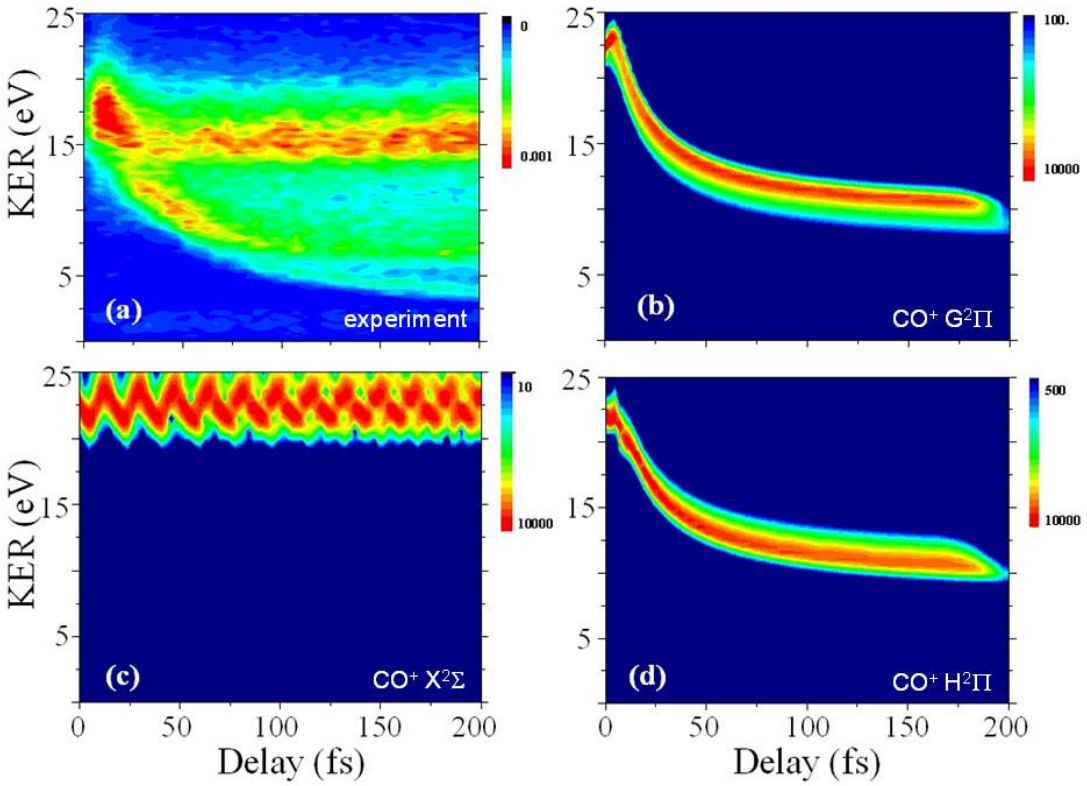

Figure 6.23 Kinetic energy release as a function of time spectra for CO → C^{2+}+O^{+} fragmentation channel (a) experimental; and simulated through different pathways: (b) CO → CO^{2+} ($^{3}\Sigma^{-}$)→ CO^{3+} → C^{2+}+O^{+}, (c) CO → CO^{2+} ($b^{1}\Pi$)→ CO^{3+} → C^{2+}+O^{+}, (d) CO → CO^{2+} ($c^{1}\Delta$)→ CO^{3+} → C^{2+}+O^{+}

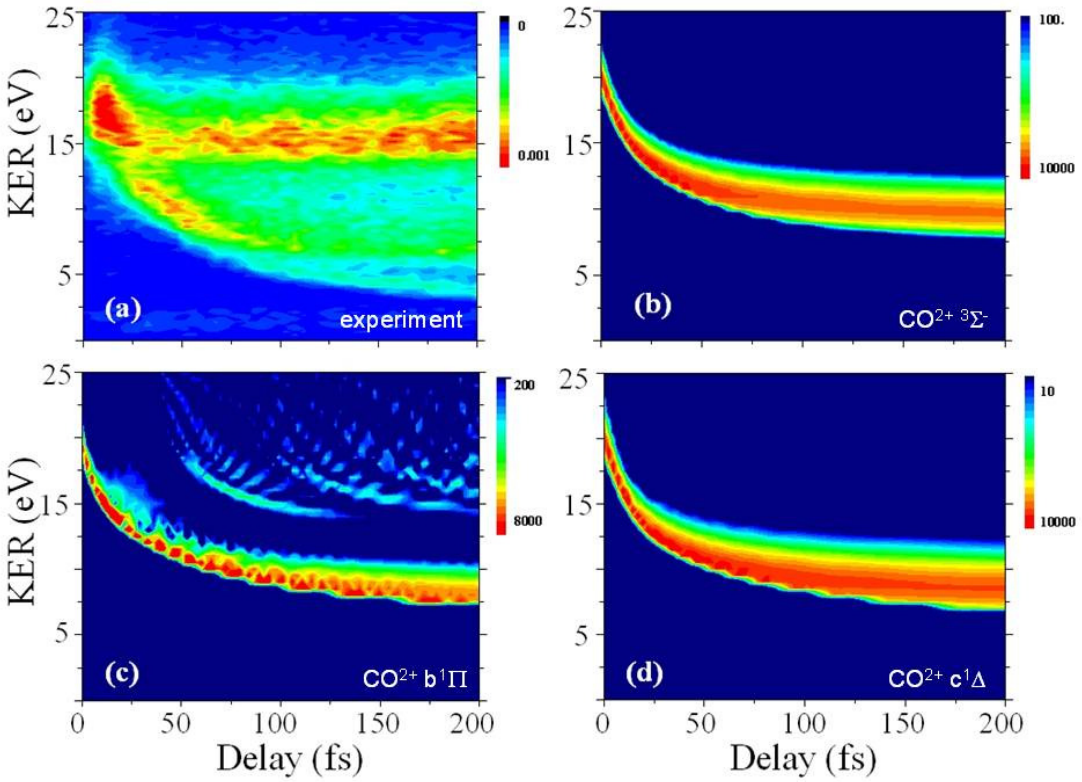

Figure 6.24 Kinetic energy release as a function of time spectra for CO → C^{2+}+O^{+} fragmentation channel (a) experimental; and simulated through different pathways: (b) CO → CO^{2+} ($A^3\Sigma^+$)→ CO^{3+} → C^{2+}+O^{+}, (c) CO → CO^{2+} ($^3\Delta$)→ CO^{3+} → C^{2+}+O^{+}, (d) CO → CO^{2+} ($d^1\Sigma^+$)→ CO^{3+} → C^{2+}+O^{+}

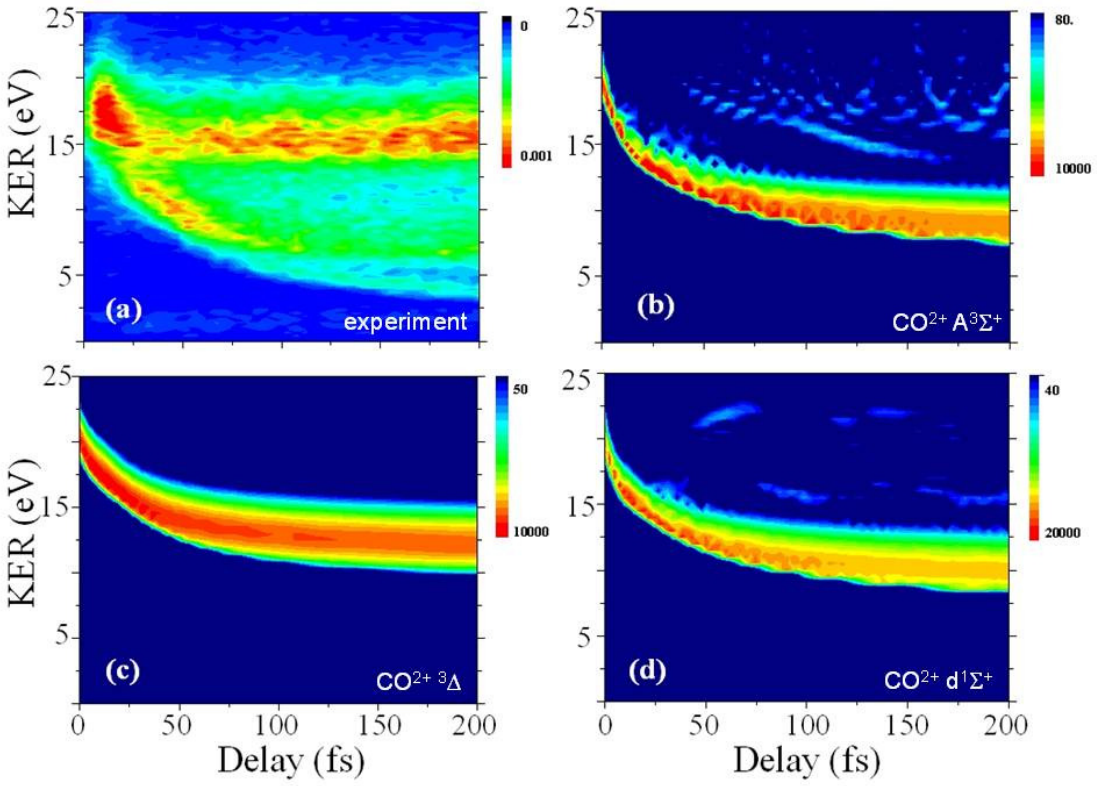

CHAPTER 7 – Effects of laser pulse duration and intensity on Coulomb explosion of CO_2: signatures of charge-resonant enhanced ionization

7.1 Introduction

In the previous chapters of this dissertation we showed that an ultrafast molecular dynamics can be studied using femtosecond laser pulses in combination with the Coulomb Explosion Imaging (CEI). The processes of molecular ionization, excitation to different electronic states of molecular ions and dissociation are initiated in a target molecule with the laser pulse, and products of reaction between the molecule and light are collected and analyzed.

CEI is an experimental technique that allows reconstruction of the molecular geometry and orientation at the moment of the explosion by measuring full 3D momenta of its break-up fragments. It is assumed that the fragment ions interact via pure Coulomb potential. To follow structural transformations of a small molecule in time we have to use pulses, which are shorter than a characteristic time of the nuclear dynamics for a particular molecule. In several experimental studies of diatomic molecules like N_2 and I_2 with pulses of 50 fs to 2 ps, the energies of emerging charged fragments were measured to be significantly lower than corresponding Coulomb explosion energies expected from the equilibrium geometry of a neutral molecule [**67, 138**]. These kinetic energies were found to be a certain fraction of the Coulomb energy independent of the charged state of a parent molecular ion [**67**]. A simple explanation suggests that the molecular ion relaxes to a critical value of internuclear distance, where it quickly ionizes to different charged states. This phenomenon is called charge-resonant enhanced ionization (CREI). A model was created for diatomic [**14, 69**] and extended to triatomic molecules [**139**, **140**] which reproduced and predicted experimental results very well for the diatomic ones [**36**]**.** The model predicts strong enhancement of the ionization rate at the critical internuclear distance. The molecular ionization is qualitatively different from the atomic ionization. Unlike in an atom, in a molecule an electron experiences multi-well ionic potentials and it can be localized at one of the nuclei and then escape via tunneling through the inner

barrier into the continuum. Intuitively, it should not be different for molecules consisting of any number of atoms. However, there is still no direct experimental evidence of the CREI-like phenomenon in triatomic molecules. In previous studies, it was established that for the CO_2 molecule, similar to diatomics, fragmentation in experiments with pulses of 50-150 fs duration yields the experimental kinetic energy releases which are considerably lower than the expected Coulomb energies [**141**, **142**]. This result can be attributed either to the screening effect caused by an electronic rearrangement around nuclei (they repel each other with lower effective charge) or to the enhanced ionization. In the work of K. Zao et al [**140**] the authors relate the two mechanisms through the charge defect parameter which depends on the charge state and the ratio between the critical distance and the equilibrium bond length. They claim that the screening model can account for the severe bending of the geometry by taking into account the time it takes for an electron to return to the ion core in the rescattering process. Both the critical distance model and screening mechanism give explosion energies close to the experimental values. On the other hand, as the bond angle decreases a discrepancy in behavior of the two models appears: the charge defect is supposed to decrease and the critical distance is independent of the angle. Bending of the molecular geometry during a fragmentation process was studied theoretically and experimentally [**143**, **144**]. Hishikawa et al [**143**] measured the bending amplitude as a function of a charged state of CO_2^{z+}. They found that higher charge states lead to smaller bending amplitudes, which was explained by the fact that ionization is more efficient for a linear configuration. However, they reported bending amplitudes as highs as ~40^0 for the CO_2^{z+} states ($3 \leq z \leq 6$) (compared to 12.5^0 amplitude for the CO_2 ground state). The theoretical work by Kono et al [**144**] supports the experimental evidence of a bond stretching in CO_2^{2+} being accompanied by the large amplitude bending of about 40^0, which they claim to be responsible for the measured structures of the CO_2^{3+} molecular ion. In the work of Brichta et al [**145**], 50 fs pulses and a full momentum imaging technique were employed to explore a multichannel fragmentation of CO_2 charged states up to CO_2^{6+} and the molecular geometry before the explosion was reconstructed. The authors claim that their experimental data on the C-O bond length dependence on fragmentation channel qualitatively agree with the enhanced ionization model. They suggest that judging from

their results on bending of the molecular skeleton, the molecule spends longer time in the states of the doubly and singly charged ion than in the higher charge states. The bending angle distribution they measured did not agree quantitatively with that reported in [**143**, **144**], which the authors attribute to the imperfection of the techniques that were used before. Nevertheless, the previous studies with pulses longer than 50 fs suggest that electronic states of CO_2^{2+} are responsible for the geometry bending measured for higher charged states and that the enhanced ionization takes place at some critical distance 2-3 R_e (equilibrium C-O bond for the CO_2 neutral molecule) due to the dynamics on the CO_2^{2+} potential energy surfaces.

In this study, we obtained an experimental evidence of the charge-resonant enhanced ionization by measuring characteristic observables for Coulomb break-up channels of molecular ions up to CO_2^{6+} initiated by pulses in a wide range of durations (from 7 to 200 fs). From our data we extracted a value of the critical C-O bond length as 2.2 Angstrom and calculated the molecular geometries. We also claim that the charge state responsible for the dynamics followed by CREI is the molecular tri-cation CO_2^{3+}. A quantum mechanical calculation suggests that among the electronic states of CO_2^{3+} there are gerade and ungerade ones, which can be coupled with one 800 nm photon, when the C-O internuclear distance reaches 2.2 A. This allows us to propose an analogy with the well-studied CREI phenomena in the H_2^+ molecular ion.

7.2 Experimental setup

The experiments were performed at the Advanced Laser Light Source (ALLS) located at INRS-EMT in Varennes, Quebec in collaboration with experimental groups of Prof. Francois Legare (INRS-EMT) and Prof. Joseph Sanderson (University of Waterloo). The techniques and setup we used there are very similar to those employed for the experiments at JRM Laboratory at Kansas State University. Briefly, few-cycle laser pulses were generated using the standard approach based on the spectral broadening in a hollow core fiber and the dispersion compensation using chirped mirrors. We pumped the hollow core fiber with 35 fs laser pulses of 0.3 mJ energy at 5 kHz repetition rate (Dragon laser system, KMLabs, Boulder, USA). The resulting few-cycle pulses had

the maximum energy of 150 μJ. The dispersion compensation was achieved using commercially available chirped mirrors together with a pair of fused silica wedges (Femtolasers, Vienna, Austria). Using an interferometric autocorrelator, the pulse duration was measured to be 6.5 fs. Linear polarization is fixed after the capillary using two germanium plates at the Brewster angle. In combination with a half wave plate positioned before the hollow core fiber, the energy per pulse can be precisely controlled. The few-cycle laser pulses were focused by a parabolic mirror (f = 10 cm) on a well-collimated supersonic jet of target molecules inside a uniform-electric-field ion imaging spectrometer. The resulting atomic fragments are detected and their full 3D momenta are determined using a time- and position-sensitive delay-line anode detector at the end of the spectrometer (RoentDek Handels GmbH). The direction of the supersonic jet, the laser beam propagation axis, and the time-of-flight axis of the spectrometer are orthogonal to each other. To achieve longer pulse durations (35, 55, 100 and 200 fs) we avoided the spectral broadening in the fiber by pumping it to the atmospheric air pressure and used an acousto-optic programmable dispersive filter (DAZZLER) on the entrance to the amplifier of the laser system to apply necessary amount of GVD (group velocity dispersion).

7.3 Results and discussion

In the experiment we analyze atomic fragments in the triple coincidence: (O^{k+} C^{q+} O^{l+}) ions are identified as resulting from the Coulomb explosion of a single molecular ion if their total momentum is close to zero ($< 5\times10^{-23}$ kg×m/s).

All momenta and energies can be calculated from the classical equations of motion. In our study we concentrate mostly on CO_2^{3+} and CO_2^{6+} molecular ions and resulting symmetric channels O^++C^++O^+ (111) and O^{2+}+C^{2+}+O^{2+} (222).

Figure 7.1 Mass spectra for the CO_2 Coulomb explosion fragments: (a) pulse length - 200 fs, intensity $2*10^{14}$ W/cm^2; (b) pulse length - 7 fs, intensity $20*10^{14}$ W/cm^2; Ratio of the C^+ to C^{2+} peak areas is about 1.9 for both (a) and (b)

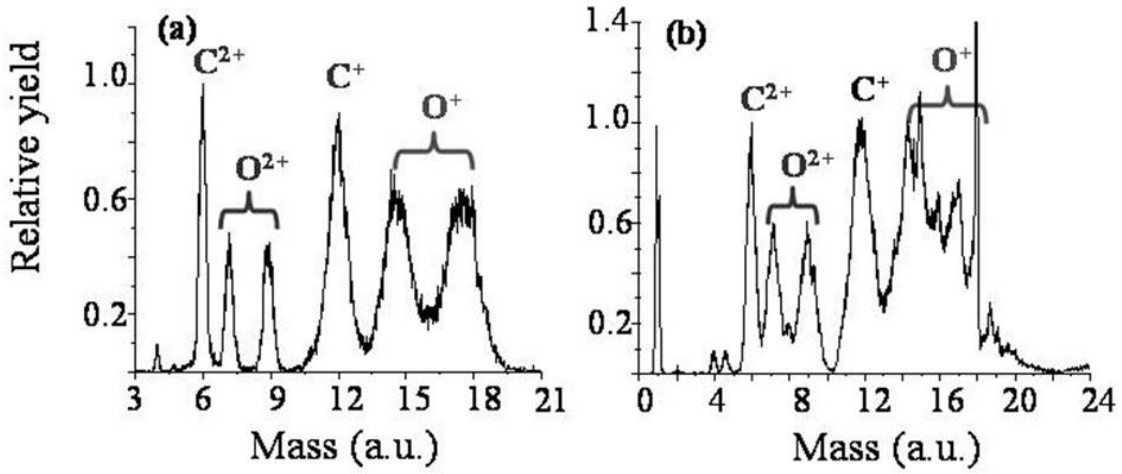

In Fig. **7.1** mass spectra produced from calibration of time-of-flight spectra are presented. The peaks indicating charged states of C and O atoms are labeled. The ion yield is normalized to the height of the C^{2+} peak. Panel (a) corresponds to the 200 fs pulse duration and panel (b) corresponds to the 7 fs pulse. For the two spectra the ratio of areas under the C^{2+} and C^+ peaks is the same, but to produce that high doubly charged ion yield with the 7 fs pulse we had to increase the intensity ten-fold in comparison to 200 fs. It means that the long pulse even of low intensity can easily produce doubly charged atomic fragments. This fact is the first experimental hint of the enhanced ionization in carbon dioxide: the molecular ion dissociating by a long pulse has enough time to extend the C-O bond length to the critical value where it easily ionizes to higher charged states. Contrary to that, with the shortest pulse the molecule Coulomb explodes before C-O reached the critical length and high intensity is needed to produce CO_2^{6+} within the 7 fs pulse duration.

Figure 7.2 Angular distribution dN/dθ for O^{2+} fragments of CO_2 Coulomb explosion for 3 different pulse durations: filled circles (green curve) – 200 fs; hollow circles (red) – 35 fs and hollow triangles (black) – 7fs

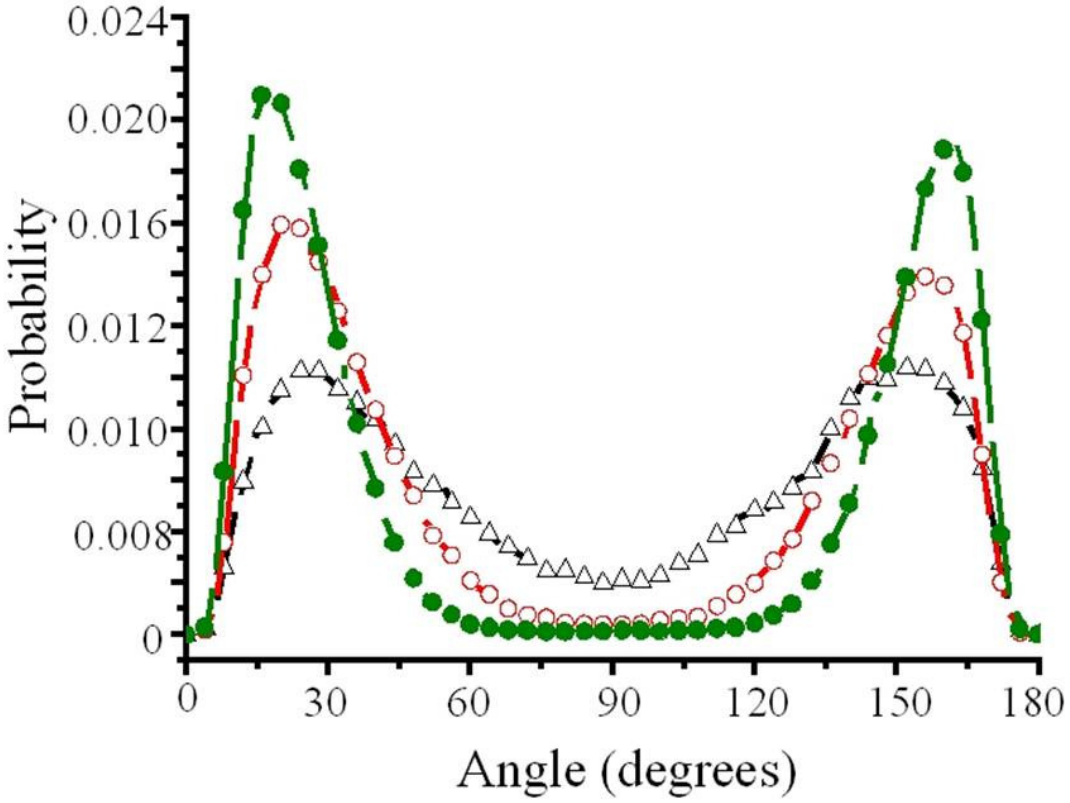

Fig. **7.2** shows the angular distribution of uncorrelated O^{2+} fragments for three different pulse lengths of 7, 35 and 200 fs. Measured is the probability dN/dθ for the O^{2+} fragments as a function of θ angle between the polarization direction (time-of-flight axis) and velocity vector of the ions. For the 200 fs pulse the probability is characterized by two sharp peaks at 15^0 and 165^0 and near zero probability for the direction perpendicular to the molecular axis. A molecule with its axis aligned parallel to the laser polarization has a significantly higher probability to explode than a molecule with any other orientation [**36**]. For the 7 fs pulse duration the peaks are at about 30^0 and 150^0 and not as sharp; the probability smoothly decreases and it is distinctly non-zero even at 90^0. These observations support the idea of the CREI-like phenomenon. It is known that linear molecules are often easier ionized when they are oriented along the field polarization axis, because the dipole created by the field is larger in this case than for any other direction, and an electron is easier localized on one of the nuclei. In other words, the

coupling of two charge-resonant states to the field is strongest along its polarization direction; the field acts over a longer distance, and therefore, the enhanced ionization which happens at a particular combination of the electric field and internuclear separation (critical values) is strongly peaked along the polarization direction [**146**]. In Fig. **7.2** we see that the angular distribution for the 200 fs pulse is very directional: molecules mostly dissociate parallel to the field. But for the 7 fs pulse the fragments are more uniformly distributed over all angles, meaning that the molecules exploded by the laser pulse can have different orientations in respect to the laser field.

Figure 7.3 Total kinetic energy distribution for (a) $CO_2^{3+} \rightarrow O^+ + C^+ + O^+$; (b) $CO_2^{6+} \rightarrow O^{2+} + C^{2+} + O^{2+}$ Coulomb explosion channels. Each curve corresponds to a certain pulse length: filled circles (black curve) – 7 fs; hollow circles (red) – 35 fs; filled triangles (green) – 55 fs; hollow triangles (blue) – 100 fs; hollow squares (magenta) – 200fs

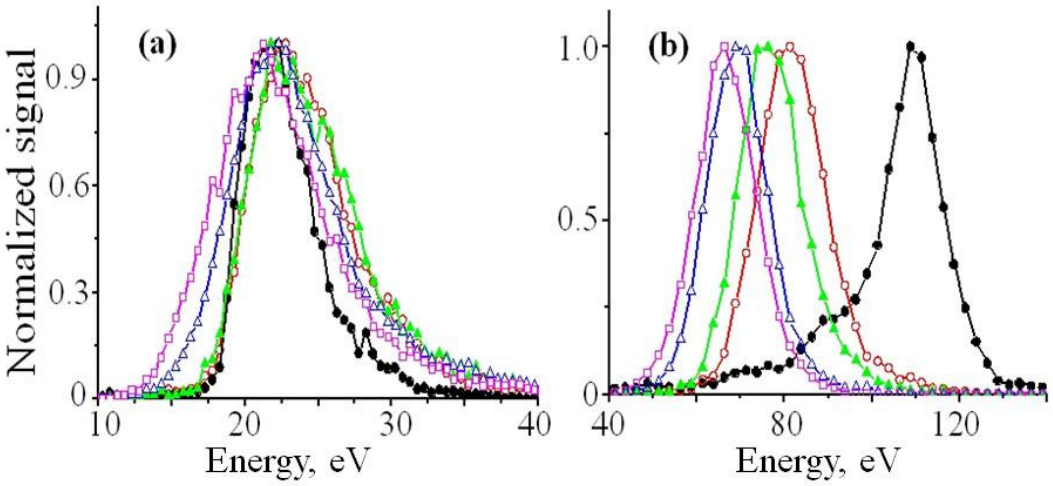

Fig. **7.3** presents the total kinetic energy measured for the (111) (Fig. **7.3** (a)) and (222) (Fig. **7.3** (b)) channels for five pulse durations. The KER of $CO_2^{3+} \rightarrow O^+ + C^+ + O^+$ fragmentation is about 23 eV independent of the pulse duration. The three electrons are removed sequentially by the pulse independent of its duration; therefore the break-up happens at about the same internuclear C-O separation for all pulse lengths. The Coulomb explosion energy (CE) of the CO_2 equilibrium structure calculated for the (111) channel is 31 eV [**142**], which is about 8 eV higher than the measured value. The reduction in energy can be explained by two following factors. Firstly, the electrons are not removed instantaneously and the molecule has time to stretch a little between ionization events. The second reason is related to the ionization rate dependence on an

internuclear distance. Even in an instantaneous transition of a wave packet to the higher state its depletion is R-dependent, and after the transition the initial shape of the wave packet is distorted [**78**]. Such wave packet distortion towards larger internuclear separations following three consecutive tunnel ionizations will result in longer average bond lengths and lower KER. For the channel $CO_2^{6+} \rightarrow O^{2+}+C^{2+}+O^{2+}$ in Fig. 7.3(b) we observe a striking feature: for the 7 fs pulse duration the fragment ions are the most energetic with a maximum at 111 eV which is very close to the Coulomb explosion energy expected from the equilibrium geometry of 124 eV (90%). However, for the next closest pulse duration of 35 fs the KER is only around 80 eV (65% of CE) and the KER is shifted to even smaller energies for every other pulse length with very close values (64-65 eV) for 100 and 200 fs. From this plot it is evident that for pulses longer than 7 fs the fragmentation mechanism is different than for the shortest pulse. The total energy peaks are very close to each other for 35 to 200 fs and far from the Coulomb energy value. It means that the ionization of CO_2^{3+} to CO_2^{6+} and subsequent break-up into the (222) channel occur in a narrow range of C-O bond lengths. This bond distance corresponds to the critical internuclear distance, and is independent of the pulse duration.

Figure 7.4 Kinetic energy release to the Coulomb energy ratio as a function of the pulse duration for channel (111) – red line with filled triangles; (222) – dark blue line with filled circles; (112) – purple line filled squares; (212) cyan line hollow squares and (122) – blue line with hollow triangles

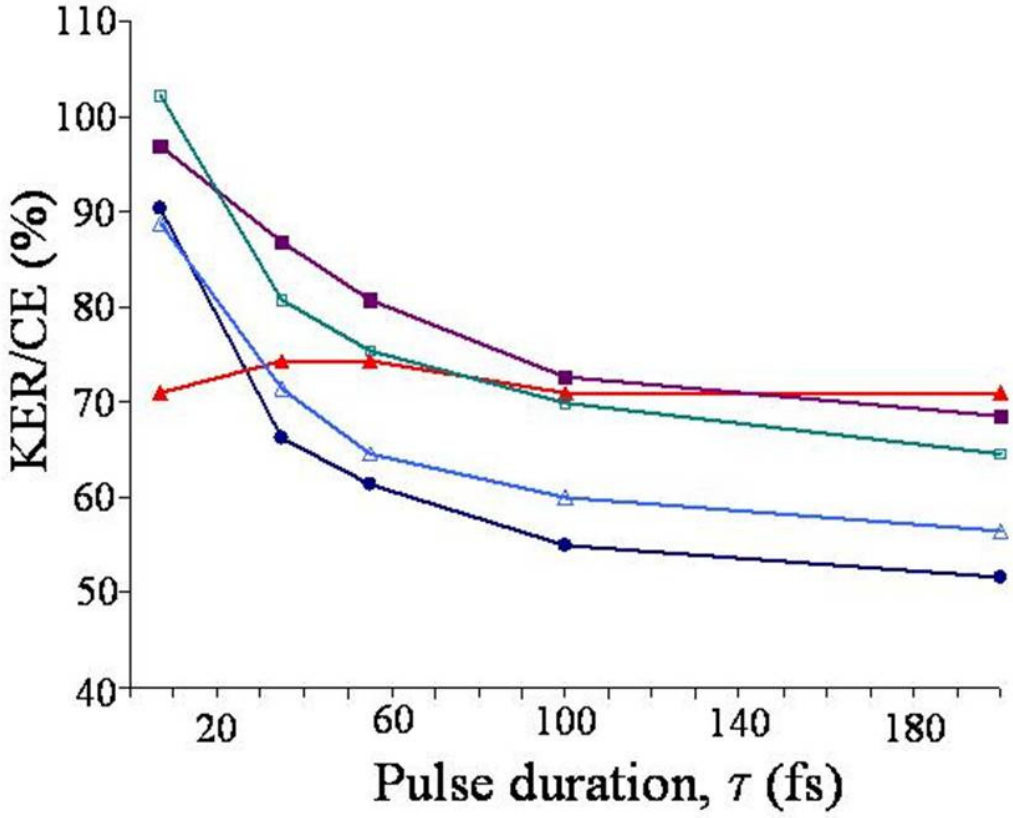

We also analyzed the data on channels $CO_2^{4+} \rightarrow O^+ + C^+ + O^{2+}$ (112), $CO_2^{5+} \rightarrow O^{2+} + C^+ + O^{2+}$ (212) and $CO_2^{5+} \rightarrow O^+ + C^{2+} + O^{2+}$ (122). Though the statistics is not as good as for the (111) and (222) channels, it allowed us to determine the dependence of the ratio between KER and the Coulomb energy (CE) on the pulse duration for each channel (see Fig. **7.4**). One can observe the same tendency of very slow increase of the ratio (k=KER/CE) as the pulse duration decreases from 200 to 100 fs; then it increases more significantly as the pulse shortens to 35 fs, and finally there is a jump up to almost 100 % for the 7 fs pulse for all the channels except (111). This behavior of the ratio also supports the idea of the dominance of the enhanced ionization mechanism, which can be turned off only with very short pulses. The fact that the (111) channel exhibits a different behavior and the corresponding curve is flat with the energy ratio slightly above 70 %, indicates a different mechanism. The (111) channel is the product of dissociation of the CO_2^{3+} state whereas all the other channels are produced from higher charged states.

Independent of the pulse duration, the molecular tri-cation dissociates with the same energy, corresponding to the dissociation limit of the contributing electronic states, bringing us to the conclusion that there is no critical bond length for ionization of the CO_2^+ and CO_2^{2+} molecular ions.

The experimental data bring us to the conclusion that molecular dynamics on the CO_2^{3+} potential energy surfaces is responsible for the phenomenon analogous to the well-known CREI observed and described for the hydrogen molecule [**14**].

7.4 Geometry reconstruction

It is possible to reconstruct a molecular geometry from our momentum triple coincidence data. The calculations were performed by our collaborator J. P. Brichta (University of Waterloo, Canada). A simplex algorithm was used to reconstruct molecular geometries at the moment before the explosion. Positively charged ions of the appropriate mass and charge (C^{k+} and O^{m+}) are placed at rest at guess positions and interact via repulsive Coulomb potential. Following the time integration of the classical equations of motion, the calculated asymptotic momenta are compared to the experimental momenta, and, based on the degree of agreement; the guess geometry is adjusted accordingly. An early version of this algorithm was used in the work on CO_2 [**145**] with 50 fs laser pulses. Recently, this algorithm has been refined and presented in detail in reference [**147**].

The results of calculations are presented in Fig. **7.5**. Each panel of the figure corresponds to a certain pulse duration. Distance in angstroms is on X and Y axes; the center of mass of the carbon and one of the oxygen nuclei is put at (X;Y) = (0;0) and the other oxygen is placed on the Y = 0 line. The distribution of all possible locations of C and O nuclei is indicated by hollow circles around most probable positions connected with solid lines. The solid curve on each panel is showing the distribution for a horizontal coordinate of the second O nucleus. For the 100 fs pulse duration the C-O bond length reaches 2.2 A and stays the same for 200 fs, whereas for 7 fs it is only 1.2 A which is very close to the equilibrium value of 1.15 A. One can see that with a long pulse the C-O

bond stretches to twice the equilibrium length before the Coulomb explosion due to the dynamics on the CO_2^{3+} potential energy surfaces.

Figure 7.5 Calculated CO_2 structures at the moment of the $CO_2^{6+} \rightarrow O^{2+}+C^{2+}+O^{2+}$ Coulomb explosion. Each panel corresponds to a certain pulse length: (a) 7 fs; (b) 35 fs; (c) 55 fs; (d) 100 fs; (f) 200fs. Center-of-mass between C and left O nuclei is fixed at (0;0); probability distributions of C and O positions are represented by hollow squares and circles around most probable positions connected with lines. Second O nucleus is placed on the (R;0) line; probability distribution of its horizontal coordinate is shown in black curve with filled area under it

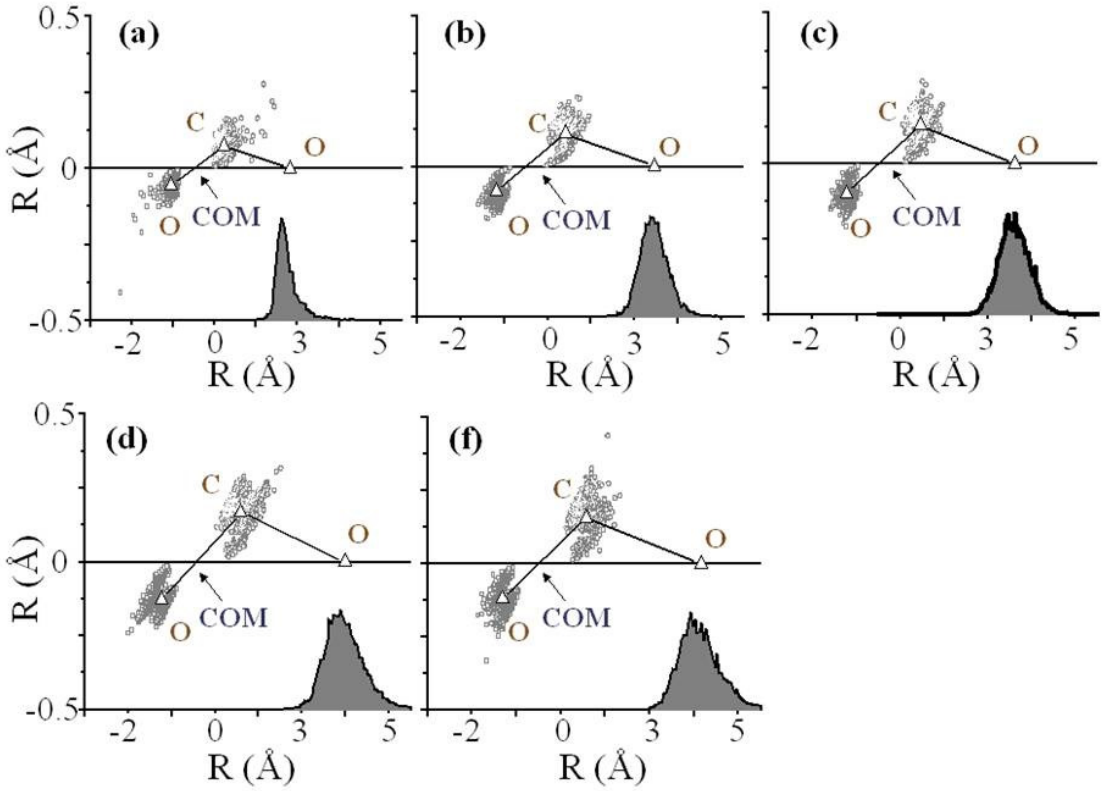

The analysis of channels (222) and (111) in the CO_2 break-up points to the conclusion that the CO_2^{3+} molecular ion is an intermediate state which undergoes a CREI-like process at the 2.2 A critical C-O distance. To investigate the details of this dynamics several low-lying 1D Born-Oppenheimer potentials for the carbon dioxide tri-cation were calculated by our collaborators from Prof. Andre Bandrauk's group (Universite de Sherbrooke) using linear combinations of atomic orbitals. Fig. **7.6** presents the two lowest 1D potentials for CO_2^{3+} (left panel) together with H_2^+ gerade and ungerade potentials (right panel). When the molecule is in its equilibrium geometry and the C-O

bond length is about 1.15 A, about 16 eV of energy (which is more than 10 photons of 800 nm laser pulse) is needed to couple the bonding $5\sigma_g$ and anti-bonding $4\sigma_u$ orbitals. With an increase of the C-O length, the energy gap is narrowing down until it reduces to about 1.5 eV (1 photon) at the 2.2 A internuclear distance. The shapes of molecular orbitals at the equilibrium and the critical internuclear distances are also shown in Fig.**7.6**; their overlap defines the probability of the electronic transition. This picture is similar to the dynamics on hydrogen molecular ion gerade and ungerade curves: CREI is observed at the critical internuclear distance of about 2.6 A, where the energy difference between the two potentials is about 1.5 eV.

Figure 7.6 Gerade and ungerade states for (a) H_2^+ ion; (b) CO_2^{3+}. For the tri-cation of carbon monoxide shapes of molecular orbitals at the C-O equilibrium and critical bond length are shown

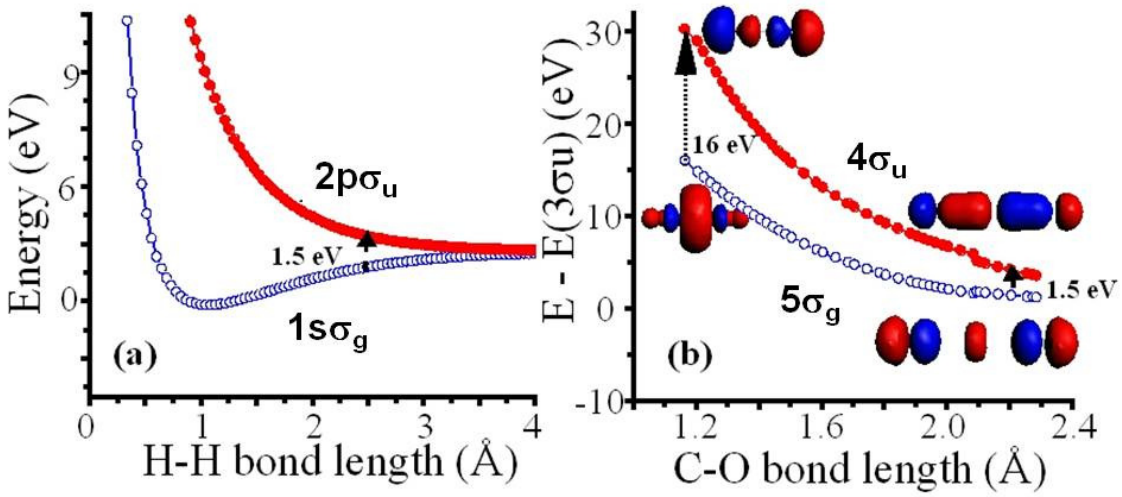

7.5 Summary

To summarize, we studied the effect of pulse duration and intensity on the three-particle fragmentation of the CO_2 molecule. Particularly, we focused on the $CO_2^{3+} \rightarrow O^+ + C^+ + O^+$ and $CO_2^{6+} \rightarrow O^{2+} + C^{2+} + O^{2+}$ break-up channels. The measurements of mass spectra, kinetic energy and angular distribution of fragments showed a signature of a CREI-like phenomenon at the 2.2 A C-O bond length. This enhanced ionization is the dominant multiple ionization mechanism responsible for production of CO_2^{n+} ions with $n > 3$ for long pulses ($\geq$ 100 fs). The dissociation of the molecular tri-cation CO_2^{3+} does not exhibit any CREI-like dependence of KER on a pulse duration, thus indicating that the

tri-cation is, in fact, the intermediate state experiencing CREI. This conclusion is supported by a quantum chemical calculation of energies for the gerade and ungerade states of CO_2^{3+}. The molecular structure before the $O^{2+}+C^{2+}+O^{2+}$ Coulomb explosion was also reconstructed with sub-0.3 A spatial resolution for five different pulse lengths in the range from 7 to 200 fs using the experimental momenta measured for triple-coincidence events. The reconstructed geometries were found to support the idea that the shortest pulse of 7 fs explodes the molecule from near equilibrium geometry. The CO_2^{3+} lowest gerade and ungerade potential curves are shown to exhibit R-dependent behavior similar to H_2^+ molecular ion states, which cause the enhanced ionization through the charge resonant transition ($\sigma_g \rightarrow \sigma_u$) in the laser field.

References

[1] International trends in applied optics. Edited by A. H. Guenther. SPIE 2002.

[2] M. V. Ammosov , N. B. Delone, V. P. Krainov. Tunnel ionization of complex atoms and of atomic ions in an alternating electromagnetic field. Zh. Eksp. Teor. Fiz., 91, 2008 (1986) [Sov. Phys. JETP **64**, 1435 (1986)].

[3] D. N. Fittinghoff, P. R. Bolton, B. Chang and K. C. Kulander. Polarization dependence of tunneling ionization of helium and neon by 120-fs pilses at 614 nm. Phys. Rev. A, **49**, 2174 International (1994).

[4] A.S. Alnaser, T. Osipov, E. P. Benis, A. Wech, B. Shan, C. L. Cocke, X. M. Tong, and C. D. Lin. Rescattering Double Ionization of D2 and H2 by Intense Laser Pulses. Phys. Rev. Lett., **91**, 163002 (2003)

[5] D. N. Fittinghoff, P. R. Bolton, B. Chang, and K. C. Kulander. Observation of nonsequential double ionization of helium with optical tunneling. Phys. Rev. Lett., **69**, 2642 (1992)

[6] B. Walker, B. Sheehy, L. F. DiMauro, P. Agostini, K. J. Schafer, and K. C. Kulander. Precision Measurement of Strong Field Double Ionization of Helium. Phys. Rev. Lett., **73**, 1227 (1994).

[7] M. Awashti and A. Saenz. Internuclear-distance dependence of ionization of H_2 in strong laser field. J. Phys. B, **39**, S389 (2006).]

[8] M. Plummer, J. F. McCann. Orientation dependence of field ionization of the hydrogen molecular ion. J. Phys. B, **30**, L401 (1997)

[9] A.S. Alnaser, S. Voss, X.-M. Tong, C. M. Maharjan, P. Ranitovic, B. Ulrich, T. Osipov, B. Shan, Z. Chang, and C. L. Cocke. Effects of molecular structure on ion disintegration patterns in ionization of O2 and N2 by short laser pulses. Phys. Rev. Lett., **93**, 113003 (2004)

[10] F. Légaré, K. F. Lee, I. V. Litvinyuk, P. W. Dooley, S. S. Wesolowski, P. R. Bunker, P. Dombi, F. Krausz, A. D. Bandrauk, D. M. Villeneuve, and P. B. Corkum. Laser Coulomb-explosion imaging of small molecules. Phys. Rev. A **71**, 013415 (2005).

[11] J Ullrich, R Moshammer, R Dörner, O Jagutzki, V Mergel, H Schmidt-Böcking and L Spielberger. Recoil-ion momentum spectroscopy. J. Phys. B **30**, 2917 (1997)

[12] P. H. Bucksbaum, A. Zavriyev, H. G. Muller, and D. W. Schumacher. Softening of the H_2^+ molecular bond in intense laser fields. Phys. Rev. Lett. **64**, 1883 (1990)

[13] L. J. Frasinski, E. J. Divall, A. J. Langley, J. H. Posthumus, J. Plumridge, P. F. Taday, and K. Codling. Manipulation of bond hardening in H_2^+ by chirping of intense femtosecond laser pulses. Phys. Rev. Lett. **83**, 3625 (1999)

[14] T. Zuo and A. D. Bandrauk. Charge-resonance-enhanced ionization of diatomic molecular ions by intense lasers. Phys. Rev. A **52**, R2511 (1995)

[15] A.Zavriyev, P. H. Bucksbaum, H. G. Muller, and D. W. Schumacher. Ionization and dissociation of H2 in intense laser fields at 1.064 μm, 532 nm, and 355 nm. Phys. Rev. A. **42**, 5500 (1990)

[16] Y. Liang, S. Augst, S. L. Chin, Y. Beaudoin, and M. Chaker. High harmonic generation in atomic and diatomic molecular gases using intense picosecond laser pulses-a comparison. J. Phys. B **27**, 5119 (1994)

[17] F. Légaré, K. F. Lee, A. D. Bandrauk, D. M. Villeneuve, and P. B. Corkum. Laser Coulomb explosion imaging for probing ultrafast molecular dynamics. J. Phys. B **39**, S503 (2006).

[18] Th. Weber, M. Weckenbrock, A. Staudte, L. Spielberger, O. Jagutzki, V. Mergel, F. Afaneh, G. Urbasch, M. Vollmer, H. Giessen, and R. Dörner. Recoil-Ion Momentum Distributions for Single and Double Ionization of Helium in Strong Laser Fields. Phys. Rev. Lett. **84**, 443 (2000).

[19] X.M. Tong, Z.X. Zhao, and C.D. Lin, Phys. Probing molecular dynamics at attosecond resolution with femtosecond laser pulses. Phys. Rev. Lett. **91**, 233203 (2003).

[20] O. Svelto. Principles of lasers. 3rd edition. Polytechnic Institute of Milan and NRC Milan, Italy. Chapter 4 and 5 (1990).

[21] J. H. Posthumus. The dynamics of small molecules in intense laser fields. Rep. Prog. Phys. **67**, 623 (2004).

[22] http://jrm.phys.ksu.edu/lasers.html

[23] http://www.mellesgriot.com

[24] A.F. Siegman. Lasers. University Science Book. Chapter 16. (1986).

[25] D. Kane and R. Trebino. Characterization of Arbitrary Femtosecond Pulses Using Frequency-Resolved Optical Gating. IEEE J. Quantum Electron. **29**, 571 (1993).

[26] C. Dong, P. So, T. French, E. Gratton. Fluorescence lifetime imaging by asynchronous pump-probe microscopy. Biophys. J. **69**, 2234 (2009).

[27] J. A. Mondal, S. Verma, H. N. Ghosh, D. K. Palit. Relaxation dynamics in the excited states of a ketocyanine dye probed by femtosecond transient absorption spectroscopy. J. Chem Sci. **120**, 45 (2008).

[28] D. M. Neumark. Time-resolved photoelectron spectroscopy of molecules and clusters. Ann. Rev. Phys. Chem. **52**, 255 (2001).

[29] S. Nie, X.Wang, J. Li, R. Clinite, J. Cao. Femtosecond electron diffraction: Direct probe of ultrafast structural dynamics in metal films. Microsc. Res. Tech. **72**, 131 (2009).

[30] Z. Vager, R. Naaman, E. P. Kanter. Coulomb Explosion Imaging of small molecules. Science **244**, 426 (1989).

[31] D. Mathur. Multiply charged molecules. Phys.Rep. **225**, 193 (1993).

[32] F. Légaré, K. F. Lee, I. V. Litvinyuk, A. D. Bandrauk, D. M. Villeneuve, and P. B. Corkum. Imaging the time-dependent structure of a molecule as it undergoes dynamics. Phys. Rev A **72**, 052717 (2005).

[33] W. T. Hill, III, J. Zhu, D. L. Hatten, Y. Cui, J. Goldhar, and S. Yang. Role of non-Coulombic potential curves in intense-field dissociative ionization of diatomic molecules. Phys. Rev. Lett. **69**, 2646 (1992).

[34] C. P. Safvan and D. Mathur. Dissociation of highly charged N_2^{q+} ($q \geq 2$) ions via non-Coulombic potential energy curves J. Phys. B **27**, 4073 (1994).

[35] A.Bandrauk, D. G. Musaev, and K. Morokuma. Electronic states of the triply charged molecular ion N23+ and laser-induced Coulomb explosion. Phys. Rev. A **59**, 4309 (1999).

[36] Ch. Ellert, H. Stapelfeldt, E. Constant, H. Sakai, J. Wright, D. M. Rayner, and P. B. Corkum. Observing molecular dynamics with timed Coulomb explosion imaging. Phil. Trans. A **356**, 329 (1998)

[37] F. Légaré, K. F. Lee, A. D. Bandrauk, D. M. Villeneuve, and P. B. Corkum. Laser Coulomb explosion imaging for probing ultrafast molecular dynamics. J. Phys. B **39**, S503 (2006).

[38] R. Döerner, V. Mergel, O. Jagutzki, L. Spielberger, J. Ullrich, R. Moshammer, H. Schmidt-Böcking. Cold Target recoil Ion Momentum Spectroscopy: a „Momentum microscope“ to view atomic collision dynamics. Phys. Rep. **330**, 95 (2000).

[39] J. Ullrich, H. Schmidt-Böcking. Time-of-Flight Spectrometer for the Determination of Microradian Projectile Scattering Angles in Atomic Collisions. Phys. Lett. A **125**, 193 (1987).

[40] S. Zhang, X. Ma, H. Liu, B. Li, and X. Zhu. Properties and applications of cold supersonic gas jet. Sci. In China G **49**, 709 (2006).

[41] A.S. Alnaser, X. M. Tong, T. Osipov, S. Voss, C. M. Maharjan, B. Shan, Z. Chang, and C. L. Cocke. Laser-peak-intensity calibration using recoil-ion momentum imaging. Phys. Rev. A **70**, 023413 (2004).

[42] S. Voss, A. S. Alnaser, X.-M. Tong, C. Maharjan, P. Ranitovic, B. Ulrich, B. Shan, Z. Chang, C. D. Lin, and C. L. Cocke. High resolution kinetic energy release spectra and angular distributions from double ionization of nitrogen and oxygen by short laser pulse. J. Phys. B **37**, 4239 (2004).

[43] T. Osipov. Experimental study of photoelectron diffraction from two-center molecules by means of the COLTRIMS technique. PhD Dissertation. Kansas State University (2003).

[44] M. Born and R. Oppenheimer. On the quantum theory of the molecules. Ann. Physik **84**, 457 (1927) (Translated by S M Blinder).

[45] B. H. Bransden and C. J. Joachain. Physics of atoms and molecules. 2nd edition. Pearson Education (2003). Chapters 9 and 10.

[46] J. D. Roberts. Notes on Molecular Orbital Calculations. W. A. Benjamin, Menlo Park, CA (1962)

[47] G. Herzberg. Molecular spectra and molecular structure. I. Spectra of diatomic molecules. 2nd edition. Krieger Publishing Company, Malabar, FL (1950). Chapters 3 and 4.

[48] J. M. Hollas. Modern spectroscopy. 2nd edition. J. Willey and sons, Chichester, W. Sussex, England (1992). Chapter 1.

[49] J. F. McCann and J. H. Posthumus. Molecular dynamics in intense laser field. Phil. Trans. R. Soc. Lond. A **357**, 1309 (1999).

[50] F. Fabre, G. Petite, P. Agostini and M. Clement. Multiphoton above-threshold ionisation of xenon at 0.53 and 1.06 μm. J. Phys. B. **15**, 1353 (1982) .

[51] M. V. Ammosov, N. B. Delone, V. P. Krainov. Tunnel ionization of complex atoms and of atomic ions in an alternating electromagnetic field. Zh. Eksp. Teor. Fiz., 91, 2008 (1986) [Sov. Phys. JETP **64**, 1435 (1986)].

[52] S. Larochelle, A. Talebpour, and S.L. Chin. Non-sequential multiple ionization of rare gas atoms in a Ti:Sapphire laser field. J. Phys. B **31**, 1201 (1998).

[53] S.L. Chin, Y. Liang, J. E. Decker, F. A. Ilkov, M. V. Ammosov. Tunnel ionization of diatomic molecules by an intense CO_2 laser. J. Phys. B **25**, L249 (1992).

[54] C. Guo, M. Li, J. P. Nibarger, and G. N. Gibson. Nonsequential double ionization of molecular fragments. Phys. Rev. A **61**, 033413 (2000).

[55] K. Yamanouchi, S. L. Chin, P. Agostini, G. Ferrante. Progress in ultrafast intense laser science. Springer (2007) Volume 2, Chapter 3.

[56] S. Augst, D. D. Meyerhofer, D. Strickland, and S. L. Chint. Laser ionization of noble gases by Coulomb-barrier suppression. J. Opt Soc. Am. B **8**, 858 (1991).

[57] J. Görlinger, L. Plagne, H.-J. Kull. Above-barrier ionization and quantum interference in strong fields. Applied Phys. B **71**, 331 (2000).

[58] G.N. Gibson, G. Dunne, and K.J. Bergquist. Tunneling ionization rates from arbitrary potential wells. Phys. Rev. Lett. **81**, 2663 (1998).

[59] P. Dietrich, M.Y. Ivanov, F.A. Ilkov, and P.B. Corkum. Two-Electron Dissociative Ionization of H_2 and D_2 in Infrared Laser FieldsPhys. Rev. Lett. **77**, 4150 (1996).

[60] X. M. Tong, Z. X. Zhao, and C. D. Lin. Theory of molecular tunneling ionization. Phys. Rev. A **66**, 033402 (2002).

[61] I.V. Litvinyuk, K. F. Lee, P. W. Dooley, D. M. Rayner, D. M. Villeneuve, and P. B. Corkum. Alignment-dependent strong field ionization of molecules. Phys. Rev. Lett. **90**, 233003 (2003)

[62] D. T. Strickland, Y. Beaudoin, P. Dietrich, and P. B. Corkum. Optical studies of internally confined molecular iodine ions. Phys. Rev. Lett. **68**, 2755 (1992).

[63] L. J. Frasinski, P. A. Hatherly, K. Codling, M. Larsson, A. Persson, C-G. Wahlstrom. Multielectron dissociative ionization of CO_2 in intense laser fields. J. Phys.B **27**, L109 (1994).

[64] D. Normand and M. Schmidt. Multiple ionization of atomic and molecular iodine in strong laser fields. Phys. Rev A **53**, R1958 (1996).

[65] E. Constant, H. Stapelfeldt, and P. B. Corkum. Observation of Enhanced Ionization of Molecular Ions in Intense Laser Fields. Phys. Rev. Lett. **76**, 4140 (1996).

[66] A.Giustu-Suzor, F. H. Mies, L. F. DiMauro, E. Charron, and B. Yang. Dynamics of H_2^+ in intense laser fields. J. Phys. B **28**, 309 (1995).

[67] J. H. Posthumus, L. J. Frasinski, A. J. Giles, and K. Codling. Dissociative ionization of molecules in intense laser fields: a method of predicting ion kinetic energies and appearance intensities. J. Phys. B **28**, L349 (1995).

[68] J. H. Posthumus, A. J. Giles, M. R. Thompson, W. Shaikh, A. J. Langley, L. J. Frasinski, and K. Codling. The dissociation dynamics of diatomic molecules in intense laser fields. J. Phys. B **29**, L525 (1996).

[69] D. M. Villeneuve, M. Yu. Ivanov, and P. B. Corkum. Enhanced ionization of diatomic molecules in strong laser fields: A classical model. Phys Rev A **54**, 736 (1996).

[70] L. J. Frasinski, J. H. Posthumus, J. Plumridge, and K. Codling, P. F. Taday and A. J. Langley. Manipulation of Bond Hardening in H2+ by Chirping of Intense Femtosecond Laser Pulses, Phys. Rev Lett. **83**, 3625 (1999).

[71] H. Niikura, V. R. Bhardwaj, F. Legare, I. V. Litvinyuk, P. W. Dooley, D. M. Rayner, M. Yu. Ivanov, P. B. Corkum and D. M. Villeneuve. Ionization of small molecules. Strong field laser physics. Edited by T. Brabec. Spinger Science and Buisseness Media. (2008).

[72] M.Magrakvelidze, F. He, Th. Niederhausen, I.V. Litvinyuk, and U. Thumm. Quantum-beat imaging of the nuclear dynamics in D_2^+: dependence of bond softening and bond hardening on laser intensity, wavelength and pulse duration. Phys. Rev. A **79**, 0334010 (2009).

[73] F. Legare, I. V. Litvinyuk, P. W. Dooley, F. Quere, A. D. Bandrauk, D. M. Villeneuve, and P. B. Corkum. Time-resolved double ionization with few cycle laser pulses. Phys. Rev. Lett. **91**, 093002 (2003).

[74] A.D. Bandrauk and M.L. Sink. Photodissociation in intense laser field: predissociation analogy. J. Chem. Phys. **74,** 1110 (1981).

[75] T. Seideman, M.Y. Ivanov, and P.B. Corkum. Role of Electron Localization in Intense-Field Molecular IonizationPhys. Rev. Lett. **75**, 2819 (1995).

[76] S. Baker, J.S. Robinson, C.A. Haworth, H. Teng, R.A. Smith, C.C. Chiril, M. Lein, J.W.G. Tisch, and J.P. Marangos. Probing Proton Dynamics in Molecules on an Attosecond Time Scale. Science **312**, 424 (2006).

[77] Th. Ergler, B. Feuerstein, A. Rudenko, K. Zrost, C. D. Schroter, R. Moshammer, and J. Ullrich. Spatiotemporal Imaging of Ultrafast Molecular Motion: Collapse and Revival of the D_2^+ Nuclear wave packet. Phys. Rev. Lett. **97**, 193001 (2006).

[78] Th. Ergler, B. Feuerstein, A. Rudenko, K. Zrost, C. D. Schroter, R. Moshammer, and J. Ullrich. Quantum-Phase Resolved Mapping of Ground-State Vibrational D_2 Wave Packets via Selective Depletion in Intense Laser Pulses. Phys. Rev. Lett. **97**, 103004 (2006)

[79] A.S. Alnaser, B. Ulrich, X. M. Tong, I. V. Litvinyuk, C. M. Maharjan, P. Ranitovic, T. Osipov, R. Ali, S. Ghimire, Z. Chang, C. D. Lin, and C. L. Cocke. Simultaneous real-time tracking of wave-packet evolving on two different potential curves in H_2^+ and D_2^+, Phys. Rev. A **72**, 030702(R) (2005).

[80] A.Jarón-Becker, A. Becker, and F. H. M. Faisal. Dependence of Strong-field Photoelectron Angular Distributions on Molecular Orientation. J. Phys. B **36**, L375 (2003).

[81] N. Hay, R. Velotta, M. Lein, R. de Nalda, E. Heesel, M. Castillejo, and J. P. Marangos. High-order Harmonic Generation in Laser-aligned Molecules. Phys. Rev. A **65**, 053805 (2002)

[82] J. Itatani, J. Levesque, D. Zeidler, H. Niikura, H. Pépin, J. C. Kieffer, P. B. Corkum, D. M. Villeneuve. Tomographic Imaging of Of Molecular Orbitals. Nature **432**, 867 (2004).

[83] P. W. Dooley, I. V. Litvinyuk, Kevin F. Lee, D. M. Rayner, M. Spanner, D. M. Villeneuve, and P. B. Corkum. Direct Imaging of Rotational Wave-Packet Dynamics of Diatomic Molecules. Phys. Rev. A **68**, 023406 (2003).

[84] Y.-H. Chen, S. Varma, A. York, and H. M. Milchberg. Single-shot, space- and time-resolved measurement of rotational wavepacket revivals in H_2, D_2, N_2, O_2, and N_2O. Opt. Exp. **15**, 11341 (2007).

[85] Kevin F. Lee, F. Legare, D. M. Villeneuve, and P. B. Corkum. Measured field-free alignment of deuterium by few-cycle pulses. J. Phys. B **39**, 4081 (2006).

[86] W.A. Bryan, E.M.L. English, J. McKenna, J. Wood, C.R. Calvert, I.C.E. Turcu, R. Torres, J.L. Collier, I.D. Williams, and W.R. Newell. Mapping the evolution of optically generated rotational wave packets in a room-temperature ensemble of D_2. Phys. Rev. A **76**, 023414 (2007).

[87] B. Feuerstein and U. Thumm. Mapping of coherent and decohering nuclear wave-packet dynamics in D_2^+ with ultrashort laser pulses. Phys. Rev. A **67**, 063408 (2003).

[88] X.M. Tong, Z.X. Zhao, A.S. Alnaser, S. Voss, C.L. Cocke and C.D. Lin. Post ionization alignment of the fragmentation of molecules in an ultrashort intense laser field. J. Phys. B **38**, 333 (2005).

[89] D. Pavicic, K.F. Lee, D.M. Rayner, P.B. Corkum, and D.M. Villeneuve. Direct Measurement of the Angular Dependence of Ionization for N_2, O_2, and CO_2 in Intense Laser Fields. Phys. Rev. Lett. **98**, 243001 (2007).

[90] A.S. Alnaser, C.M. Maharjan, X.M. Tong, B. Ulrich, P. Ranitovic, B. Shan, Z. Chang, C.D. Lin, C.L. Cocke, and I.V. Litvinyuk. Effects of orbital symmetries in dissociative ionization of molecules by few-cycle laser pulses. Phys. Rev. A **71**, 031403(R) (2005).

[91] A.Apalategui and A. Saenz. Multiphoton ionization of the hydrogen molecule H_2. J. Phys. B **35**, 1909 (2002).

[92] F. Anis and B. D. Esry. Role of nuclear rotation in dissociation of H_2^+ in a short laser pulse. Phys. Rev. A. **77**, 033416 (2008).

[93] F. Anis T. Cackowski and B. D. Esry. Rotational dynamics of dissociating H_2^+ in a short intense laser pulse. J. Phys. B **42**, 091001 (2009).

[94] X. Urbain, B. Fabre, E.M. Staicu-Casagrande, N. de Ruette, V.M. Andrianarijaona, J. Jureta, J.H. Posthumus, A. Saenz, E. Baldit, and C. Cornaggia. Intense-Laser-Field

Ionization of Molecular Hydrogen in the Tunneling Regime and Its Effect on the Vibrational Excitation of H_2^+. Phys. Rev. Lett. **92**, 163004 (2004).

[95] Feuerstein, Th. Ergler, A. Rudenko, K. Zrost, C.D. Schroter, R. Moshammer, J. Ullrich, T. Niederhausen and U. Thumm. Complete Characterization of Molecular Dynamics in Ultrashort Laser Fields. Phys. Rev. Lett. **99**, 153002 (2007).

[96] R. Dörner, Th. Weber, M. Weckenbrock, A. Staudte, M. Hattass, R. Moshammer, J. Ulrich, and H. Shmidt-Böcking. Multiple ionization in strong laser fields. Adv. At. Mol. Phys. **75**, 3122 (2002).

[97] B. Walker, E. Mevel, B. Yang, P. Breger, J-P. Chamberet, A. Antonetti, L. F. DiMauro, and P. Agostini. Double ionization in the perturbative and tunneling regimes. Phys. Rev. A **48**, R894 (1993).

[98] K.S. Budil, P. Salières, M.D. Perry, and A. L'Huillier. Influence of ellipticity on harmonic generation. Phys. Rev. A **48**, R3437 (1993).

[99] G.G. Paulus, F. Grasbon, A. Dreischuh, H. Walther, R. Kopold, and W. Becker. Above-Threshold Ionization by an Elliptically Polarized Field: Interplay between Electronic Quantum Trajectories. Phys. Rev. Lett. **84**, 3791 (2000).

[100] P.B. Corkum, Plasma perspective on strong-field multiphoton ionization. Phys. Rev. Lett. **71,** 1993 (1994)

[101] K.J. Schafer, B. Young, L. F. DiMauro, and K. C. Kulander. Above threshold ionization beyond the high harmonic cutoff. Phys. Rev. Lett. **70**, 1599 (1993).

[102] P. Corkum and F. Krause. Attosecond Science. Nature Phys. **6**, 323 (2007).

[103] A. Rudenko, K. Zrost, B. Feuerstein, V. L. B. de Jesus, C. D. Schrőter, R. Moshammer, and J. Ullrich. Correlated Multielectron Dynamics in Ultrafast Laser Pulse Interactions with Atoms. Phys.Rev. Lett. **93**, 253001 (2004).

[104] V. L. B. de Jesus, B. Feuerstein, K. Zrost, D. Fischer, A. Rudenko, F. Afaneh, C.D. Schröter, R. Moshammer, and J. Ullrich. Atomic structure dependence of nonsequential double ionization of He, Ne and Ar in strong laser pulses. J. Phys. B: At. Mol. Opt. Phys. **37**, L161 (2004).

[105] A.S. Alnaser, D. Comtois, A. T. Hasan, D. M. Villeneuve, J-C. Kieffer, and I. V. Litvinyuk. Strong-field non-sequential double ionization: wavelength dependence of ion momentum distributions for neon and argon. J. Phys. B: At. Mol. Opt. Phys. **41**, 031001 (2008).

[106] X.M. Tong, Z.X. Zhao, and C.D. Lin. Correlation dynamics between electrons and ions in the fragmentation of D_2 molecules by short laser pulses. Phys. Rev. A **68**, 043412 (2003).

[107] J. Levesque, P. B. Corkum. Attosecond science and technology. Can. J. Phys. **84**, 1 (2006).

[108] H. Niikura, F. Légaré, R. Hasbani, A.D. Bandrauk, M.Y. Ivanov, D.M. Villeneuve, and P.B. Corkum. Sub-laser-cycle electron pulses for probing molecular dynamics. Nature **417**, 917 (2002).

[109] A.S. Alnaser, X. M. Tong, T. Osipov, S. Voss, C. M. Maharjan, P. Ranitovic, B. Ulrich, B. Shan, Z. Chang, C. D. Lin, and C. L. Cocke. Routes to Control of H_2 Coulomb Explosion in Few-Cycle Laser Pulses. Phys. Rev. Lett. **93**, 183202 (2004).

[110] A.Zavriyev, P. H. Bucksbaum, J. Squier, and F. Saline. Light-induced vibrational structure in H_2^+ and D_2^+ in intense laser fields. Phys. Rev. Lett. **70**, 1077 (1993).

[111] J.M. Peek. Inelastic scattering of electrons by the hydrogen molecular ion. Phys. Rev. **134**, A877 (1964).

[112] R. Dörner, V. Mergel, O. Jagutzki, L. Spielberger, J. Ulrich, R. Moshammer, and H. Schmidt-Böcking. Cold target recoil ion momentum spectroscopy: a 'momentum microscope' to view atomic collision dynamics. Phys. Rep. **330**, 95 (2000).

[113] C. Elschenbroich, A. Salzer. Organometallics : A Concise Introduction. 2nd Edition, Wiley-VCH: Weinheim (2006).

[114] S. T. Omaye. Metabolic modulation of carbon monoxide toxicity. Toxicology.**180,** 139 (2002).

[115] Th. Weber, O. Jagutzki, M. Hattass, A. Staudte, A. Nauert, L. Schmidt, M. H. Prior, A. L. Landers, A. Bräuning-Demian, H. Bräuning, C. L. Cocke, T. Osipov, I. Ali, R. Díez Muiño, D. Rolles, F. J. García de Abajo, C. S. Fadley, M. A. Van Hove, A. Cassimi, H. Schmidt-Böcking and R. Dörner. K-shell photoionization of CO and N_2 : is there a link between the photoelectron angular distribution and the molecular decay dynamics? J. Phys. B **34**, 3669 (2001).

[116] K. Miyazaki, T. Shimizu and D. Normand. Femtosecond-laser-induced alignment in Coulomb explosion of N_2. J. Phys. B **37**, 753 (2004).

[117] J. Muth-Böhm, A. Becker, and F. H. M. Faisal. Suppressed molecular ionization for a class of diatomics in intense femtosecond laser fields. Phys. Rev. Lett. **85**, 2280 (2000).

[118] D. Pinkham and R. R. Jones. Intense laser ionization of transiently aligned CO. Phys. Rev. A **72**, 023418 (2005).

[119] H. Ren, R. Ma, J. Chen, X. Li, H. Yang and Q. Gong. Field Ionization and Coulomb Explosion of CO in an intense femtosecond laser field. J. Phys. B **36**, 2179 (2003).

[120] C. Guo, M. Li, and G. N. Gibson. Charge asymmetric dissociation induced by sequential and nonsequential strong field ionization. Phys. Rev. Lett. **82**, 2492 (1999).

[121] J. P. Nibarger, S. V. Menon, and G. N. Gibson. Comprehensive analysis of strong-field ionization and dissociation of diatomic nitrogen. Phys. Rev. A **63**, 053406 (2001).

[122] J. McKenna, M. Suresh, B. Srigengan, and I.D. Williams; W.A. Bryan, E.M.L. English, S. L. Stebbings, and W.R. Newell; I.C.E. Turcu, J. M. Smith, E. J. Divall, C. J. Hooker, A. J. Langley, and J.L. Collier. Ultrafast ionization study of N_2 in intense linearly and circularly polarized laser fields. Phys. Rev. A **73**, 043401 (2006).

[123] E. Thulstrup and A. Andersen. Configuration interaction studies of bound, low-lying states of N_2^-, N_2, N_2^+ and N_2^{2+}. J. Phys. B **8**, 965 (1975).

[124] T. Aoto and K. Ito; Y. Hikosaka; A. Shibasaki, R. Hirayama, N. Yamamono, and E. Miyoshi. Ineer-valence states of N_2^+ and the dissociation dynamics studied by threshold

photoelectron spectroscopy and configuration interaction calculation. J. Chem. Phys. **124**, 234306 (2006).

[125] M. Lundqvist, D. Edvardsson, P. Baltzer, and B. Wannberg. Doppler-free kinetic energy release spectrum on N_2^{2+}. J. Phys. B **29**, 1489 (1996).

[126] A. Bandrauk, D. G. Musaev, and K. Morokuma. Electronic states of the triply charged molecular ion N_2^{3+} and laser-induced Coulomb explosion. Phys. Rev. A **59**, 4309 (1999).

[127] T. Niederhausen and Uwe Thumm. Controlled vibrational quenching of nuclear wave packets in D_2^+. Phys. Rev. A **77**, 013407 (2008).

[128] U. Thumm, T. Niederhausen, B. Feuerstein. Time-series analysis of vibrational nuclear wave-packet dynamics in D_2^+. Phys. Rev. A **77**, 063401 (2008).

[129] N. H. F. Beebe, E. W. Thultsrup, and A. Andersen. Configuration interaction calculations of low-lying electronic states of O_2, O_2^+, and O_2^{2+}. J. Chem Phys. **64** 2080 (1976).

[130] M. Lindqvist, D. Edvardsson, P. Baltzer, M. Larson, and B. Wannberg. Observation of predissociation and tunneling process in O_2^{2+}: a study using Doppler free kinetic energy release spectroscopy and *ab initio* CI calculations. J. Phys. B **29**, 499 (1996).

[131] D. Edvardsson, S. Lunell, F. Rakowitz, C. M. Marian, L. Karlsson. Calculation of predissociation rates in O_2^{2+} by *ab initio* MRD-CI method. Chem. Phys. 2**29**, 203 (1998).

[132] A. Mitrushenkov, P. Palmieri, G. Chambaud, P. Rosmus. Spin-orbit induced predissociation of the $B^2\Sigma_g^-$ and $2^2\Sigma_g^+$ states of the O_2^+ ion. Chem. Phys. Lett. **378**, 463 (2003).

[133] A. A. Wills, A. A. Cafolla and J. Comer. The production of autoionizing states of atomic oxygen by the photodissociation of O_2. J. Phys. B **24**, 3989 (1991).

[134] W. Coughran, J. Rose, T.-I. Shibuya, and V. McKoy. Equations-of-motion method: potential energy curves for N_2, CO, and C_2H_4. J. Chem. Phys. **58**, 2699 (1973).

[135] W. Li, S. A. Lahankar, C. Huang, P. S. Shternin, O. S. Vasyutinskii, and A. G. Suits. Multiphoton processes of CO at 230 nm. Phys. Chem. Chem. Phys. **8**, 2950 (2006).

[136] P. Lablanque; J. Delwiche and M.-J. Hubin-Franskin; I. Nenner, and P. Morin; K. Ito; J. H. D. Eland; J.-M. Robbe and G. Gandara; J. Fournier and P. G. Fournier. Experimental and theoretical investigation of the spectroscopy and dynamics of multiply charged CO cations. Phys. Rev. A **40**, 5673 (1989).

[137] T. Šedicová, P. R. Žďánská, and V. Špirko. Computed lifetimes of metastable states of CO^{2+}. J. Chem. Phys. **124**, 214303 (2006).

[138] D. Normand, C. Cornaggia, J. Lavancier, J. Morellec, and H. X. Liu. Multielectron dissociative ionization of O_2 in an intense picosecond laser field. Phys. Rev A, **44**, 475 (1991)

[139] T. Zuo and A. D. Bandrauk. Phase control of molecular ionization: H_2^+ and H_3^{2+} in intense two-color laser fields. Phys. Rev A **54**, 3254 (1996).

[140] K. Zao, G. Zhang, and W. T. Hill III. Strong-field dissociative ionization of a linear triatomic molecule: Relationship between Coulomb-explosion energies and bond angle. Phys. Rev A, **68**, 063408 (2003).

[141] C. Cornaggia, M. Shmidt and D. Normand. Coulomb explosion of CO_2 in an intense femtosecond laser field. J. Phys. B, **27**, L123 (1994).

[142] W. A. Bryan, J. H. Sanderson, A. El-Zein, W. R. Newell, P. F. Taday, and A. J. Langley. Laser-induced Coulomb explosion, geometry modification and reorientation of carbon dioxide. J. Phys. B, **33**, 745 (2000).

[143] A. Hishikawa, A. Iwamae, and K. Yamanouchi. Ultrafast deformation of the geometrical structure of CO_2 induced in intense laser fields. Phys. Rev. Lett., **83**, 1127 (1999).

[144] H. Kono, S. Koseki, M. Shiota, and Y. Fujimura. A theoretical study of electronic dynamics and deformation of CO_2 in intense laser. J. Phys. Chem. A, **105**, 5627 (2001).

[145] J.P. Brichta, S. J. Walker, R. Helsten and J. H. Sanderson. Ultrafast imaging of multielectronic dissociative ionization of CO_2 in an intense laser field. J. Phys. B, **40**, 117 (2007).

[146] L.J. Frasinski, J. Plumridge, J. H. Posthumus, and K. Codling. Counterintuitive Alignment of H_2^+ in Intense Femtosecond Laser Fields. Phys. Rev. Lett., **86**, 2544 (2001).

[147] J.P. Brichta, A. N. Seaman, and J. H. Sanderson. Ultrafast imaging of polyatomic molecules with simplex algorithm. Comp. Phys. Commun. **180**, 197 (2009).

[148] S. Chelkowski, P. B. Corkum, and A. D. Bandrauk. Femtosecond Coulomb explosion imaging of vibrational wave function. Phys. Rev. Lett. **82**, 3416 (1999).

[149] T. Niederhausen. Quantum Dynamics in Laser-Assisted Collisions, Laser-Molecule Interactions, and Particle-Surface Scattering. PhD dissertation. Kansas State University (2007).

Appendix A - **Temperature of the molecular jet**

The resolution of the measured momentum and translational temperature of the gas jet are related through the Maxwell-Boltzmann distribution. It describes the probability of particle momentum (magnitude or direction) being measured around a certain value as a function of temperature in gases. Distribution for the z-component of momentum p_z can be written down as:

$$f(p_z) = \sqrt{\frac{M}{2\pi K_B T}} \exp\left[-\frac{p_z^2}{2MK_B T} \right] \qquad \textbf{(A.1)}$$

where M is the mass of a particle K_B is the Boltzmann constant and T is the temperature.

For the temperature measurement we used our standard setup (Fig. **2.1**) with the laser beam going to the chamber instead of being split in the interferometer. We performed the measurements of the longitudinal momentum distribution (along jet direction) of the D_2^+ and H_2^+ ions. A polarization of the beam was made horizontal (along the spectrometer axis). The extracting voltage was as low as 3 V/cm. The data were taken for three different backing pressures of each gas.

In Fig. **A.1** there are sets of data for deuterium and hydrogen for a single gas backing pressure. Each momentum distribution is characterized by two peaks. The broad peak is due to hydrogen and deuterium molecules from the "hot" background in the COLTRIMS chamber. Origin (OriginLab software) fitting tool was used to fit normal distribution function to both peaks with:

$$Y = Y_0 + Y_{\max} \exp\left[-\frac{(p_y - p_{y0})^2}{2\Delta^2} \right] \qquad \textbf{(A.2)}$$

Fitting parameter Δ is related to FWHM Δp

$$2\Delta = \Delta p / \sqrt{\ln(4)} \qquad \textbf{(A.3)}$$

Extracting Δ for each peak and comparing it to the corresponding part of the equ. **(1)** one can find the temperature of the jet at the given pressure. The background peak width and temperature, obviously, do not depend on the backing pressure.

Figure A.1 Experimental transversal momentum distribution (black curve with squares) and fitted normal distribution (red and blue curves) for (a) D_2^+ ions, backing pressure is 12 psi and (b) H_2^+ ions backing pressure is 10 psi. Blue line fits the peak corresponding to ions coming from the jet and red line is the one for D_2^+ and H_2^+ from the chamber background

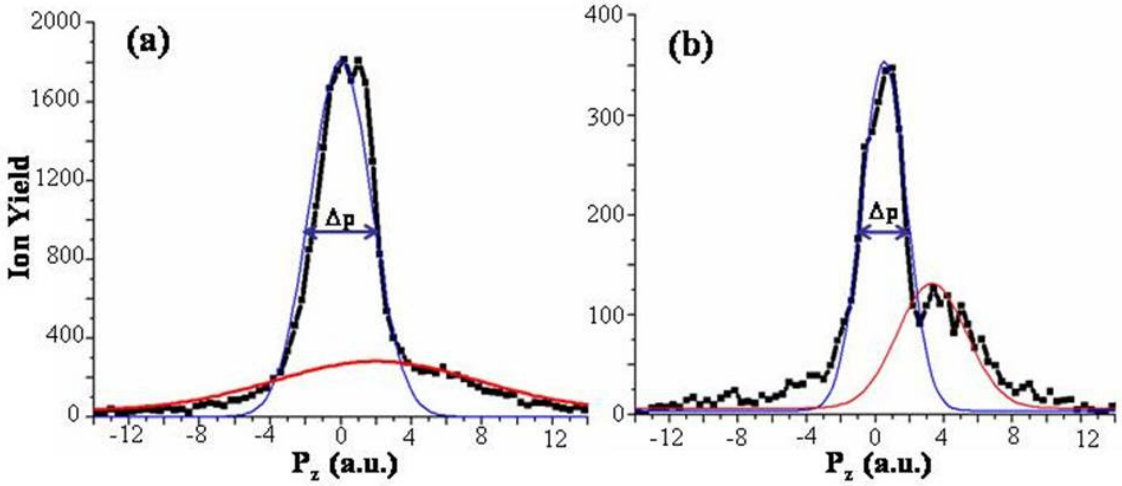

$$\Delta^2 = MK_B T \qquad \textbf{(A.4a)}$$

$$T = \frac{\Delta p^2}{4\ln(4) MK_B} \qquad \textbf{(A.4b)}$$

When put on the same plot, the three measurements give a linear dependence of the jet temperature on backing gas pressure as can be seen in Fig. **A.2**. Linear fit was performed in the Origin (OriginLab).

From the background peak fit we extract the temperature of the hydrogen and deuterium molecules in background. As it was expected, the temperature of the background was close to the room temperature (~300 K) and did not depend on the backing pressure.

Figure A.2 Experimental data (black curve with squares) and linear fit (blue line) for jet temperature dependence on backing pressure for (a) deuterium and (b) hydrogen.

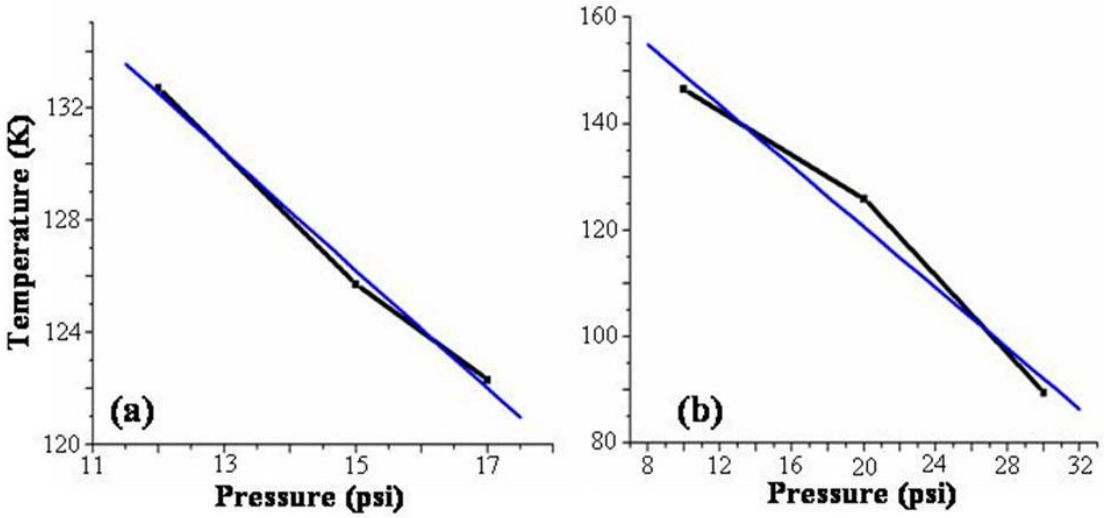

Appendix B - **Data analysis subroutine**

Figure B.1 Analysis subroutine: page 1

```
c-----------------------------------------------------------------------
      subroutine analyse(tdc,cnt,counts,adc,nadc,scl,nscl,param,oldrec)

c
c-----------------------------------------------------------------------
      implicit none
      integer*4 cnt(32), adc(*),scl(*),nscl,nrec, nel, energy, counts(*)
      integer*4 mu1, mu2, qu1, qu2
      integer ln, rn, tn, bn, cpn, nadc, param, parama
      integer p, b, k, m, l,j
      real tdc(32,16),flux, redm
      real m1, m2, q1, q2
      real s1, E1, z, s2, E2, E, s, q
      real a1, a2, t1, t2
      real tofall, tofall1, tofall2, xr3, yr3, xr4,yr4, rtof1old
      real xr1, xr_0, yr_20, xr_20, yr1, yr_0
      real rtof1, rtof2, xr2, yr2, gxr, gyr
      real xr1old,xr2old,yr1old,yr2old
      real xrsum, yrsum, xrsd, yrsd
      real totalr,totalrran1,tsumx, tsumy
      real et1, et2
      real pxr(4), pyr(4), pzr(4), ppr, pr, prrx, prry, prrz, prrz2, prd
      real prs,prrs, tsum, prd2, prdif, pz, px, py
      real pzran1,pxran1,pyran1,pzran2,pxran2,pyran2
      real prsran1,prsran2,prsran
      real pxrold(4), pyrold(4), pzrold(4) ,totalrold,tofalold
      real rec(3,16),el(3,16),oldrec(3,16), te_0
      real omega, c
      real onex(16),twox(16),oney(16),twoy(16),cp(16),ec,xcm,ycm

      integer left, right, up, down, mcp, i
      real pau, PI, me, mu
      real nx, ny, nz
      parameter (PI=3.14159265359)
      parameter (mu=1.661E-27)
      parameter (me=9.1094E-31)



      data omega/0.2250896/
      data pau/1.993E-24/     !a.u. of momentum
      data ec/1.602E-19/









      data te_0/-13./    ! offset in time signal defined by length of
c                         cables carring signals from detector to
c                         electronics

```

Figure B.2 Analysis subroutine: page 2

```
      data xrsum/-110./   ! time sums
      data xrsd/6./
      data yrsum/-105./
      data yrsd/4./

      data gxr/1.064/   ! position signals conversion constants
      data gyr/1.064/

      do i=1, cnt(9)
      call hf1(-109,tdc(9,i),1.)
      enddo

c-----------------------------------------------------------------------
      left=5
      right=7
      down=6
      up=8
      mcp=9
c -----------------------------------------------------------------------


      param=param+(1.+(-0.5*Rand()))

      call hf1(-3,(-param/1000.),1.) ! number of laser pulses is plotted
c                                      as a function of delay

c  Time and position signals read by the detectors
c-----------------------------------------------------------------------
      ln = cnt(left)
      do i=1,cnt(left)
          onex(i)=tdc(left,i)+.5*rndm()
      enddo
      rn = cnt(right)
      do i=1,cnt(right)
          twox(i)=tdc(right,i)+.5*rndm()
      enddo
      bn = cnt(down)
      do i=1,cnt(down)
          oney(i)=tdc(down,i)+.5*rndm()
      enddo
      tn = cnt(up)
      do i=1,cnt(up)
          twoy(i)=tdc(up,i)+.5*rndm()
      enddo
      cpn = cnt(mcp)
      do i=1,cnt(mcp)
          cp(i)=tdc(mcp,i)+.5*rndm()
      enddo
c-----------------------------------------------------------------------
      nrec=4.  ! maximum number of recoils out of all recorded by TDC
c               that are analysed
```

Figure B.3 Analysis subroutine: page 3

```
104         call resort(nrec,cp,cpn,onex,ln,twox,rn, ! resort subroutin is
105     c                                             sorting collected
106     *            oney,bn,twoy,tn,                ! signals to attribute
107     c                                             them to one recoil
108     *            xrsum,yrsum,xrsd,yrsd,          ! and characterize each
109     c                                             of them
110     *            rec)                            ! with 4 position and 1
111     c                                             time signals
112
113        if(nrec.lt.2)return      ! if number of recoils that left after
114     c                            resort is less then 2 then the event
115     c                              is not analysed further
116
117         do k=1,nrec
118          tofall = tdc(11,1)-rec(1,k)+te_0  ! time of flight for the event
119          tofalold = tdc(11,1)-oldrec(1,k)+te_0    ! tof for previous event
120          call hf1(553,tofall,1.) ! TOF histogram
121         enddo
122
123
124     C-------------------------------------------------------------------------
125         tsumx=2*tdc(9,1)-tdc(5,1)-tdc(7,1) !time sums check
126         tsumy=2*tdc(9,1)-tdc(6,1)-tdc(8,1)
127
128         call hf1(-110,tsumx,1.)
129         call hf1(-111,tsumy,1.)
130         call hf1(-1,tdc(11,1),1.)  !photodiod signal check
131
132
133            do m=1,nrec
134            do l=1,nrec
135             rtof1=tdc(11,1)-rec(1,m)+te_0   ! TOF for 1st recoil from pair
136             rtof2=tdc(11,1)-rec(1,l)+te_0   ! TOF for 2nd recoil from pair
137             rtof1old=tdc(11,1)-oldrec(1,m)+te_0 ! TOF for one recoil from
138     c                                             previous event
139             call hf2 (600,rtof1,rtof2,1.)   ! PIPICO spectrum plot
140
141     c       PIPICO ramdom coincidences subtruction
142             call hf2 (601,rtof1,rtof2,1.)
143             call hf2 (601,rtof1,rtof1old,-1.)
144
145           enddo
146           enddo
147
148           if(abs(rtof1-3270).lt.250.)then
149     *     (rtof1-2600.).lt.60.and.(rtof1-2600.).gt.0.)then! gate on TOF of
150     c                                                      a specific ion
151     c Analysis of each pair of ions from the event
152     c-------------------------------------------------------------------------
153           do m=1,nrec-1
154           do l=1+m,nrec
155              rtof1=tdc(11,1)-rec(1,m)+te_0
```

Figure B.4 Analysis subroutine: page 4

```
156             rtof2=tdc(11,1)-rec(1,l)+te_0
157            rtof1old=tdc(11,1)-oldrec(1,m)+te_0
158
159         xr1 = gxr*rec(2,m)  ! image of an ion on delay-line detector
160         yr1 = gyr*rec(3,m)
161
162         xr2 = gxr*rec(2,l)
163         yr2 = gyr*rec(3,l)
164
165         xr1old = gxr*oldrec(2,m) ! image of an ion from previous event
166         yr1old = gyr*oldrec(3,m)
167
168         xr2old = gxr*oldrec(2,l)
169         yr2old = gyr*oldrec(3,l)
170
171
172         call hf2(511,xr1,yr1,1.) !plot image histogram
173
174         xr_0=-1.1    !center of image on the detector for an ion
175          yr_0=0.
176
177          xr_20=-1.1
178          yr_20=0.
179
180         q1=qu1*ec
181         q2=qu2*ec
182         m1=mu1*1.661E-27
183         m2=mu2*1.661E-27
184
185         s=0.056              ! ion travel distance in spectrometer (meters)
186
187          E=2570.             ! electric field across spectrometer (V/m)
188
189          q1=2*ec             ! 1st recoil ion charge
190          q2=1*ec             ! 2st recoil ion charge
191          m1=14.              ! 1st recoil ion mass
192          m2=14.              ! 1st recoil ion mass
193
194c        Calculating momenta of each recoil in pair, their kinetic energy;
195c         kinetic energy and momentum in center-of-mass system
196c-----------------------------------------------------------------------
197         pzr(1)=(1.E9*m1*mu*s/(rtof1) -
198     *           1.E-9*E*q1*(rtof1)/2.)/pau
199         pyr(1)=(5.E5*m1*mu*(yr1-yr_0)/(rtof1))/pau
200         pxr(1)=(5.E5*m1*mu*(xr1-xr_0)/(rtof1))/pau
201
202         pzrold(1)=(1.E9*m1*mu*s/(rtof1old) -       ! momenta for recoil
203c                                                  ion from previous event
204     *           1.E-9*E*q1*(rtof1old)/2.)/pau
205         pyrold(1)=(5.E5*m1*mu*(yr1old-yr_0)/(rtof1old))/pau
206         pxrold(1)=(5.E5*m1*mu*(xr1old-xr_0)/(rtof1old))/pau
207
```

Figure B.5 Analysis subroutine: page 5

```
208         et1= 27.2*((pxr(1))**2+(pyr(1))**2+
209      *                (pzr(1))**2)/(2.*m1*1836.)
210
211
212         pzr(2)=(1.E9*m2*mu*s/(rtof2) -
213      *          1.E-9*E*q2*(rtof2)/2.)/pau
214         pyr(2)=(5.E5*m2*mu*(yr2-yr_20)/(rtof2))/pau
215         pxr(2)=(5.E5*m2*mu*(xr2-xr_20)/(rtof2))/pau
216
217         et2= 27.2*((pxr(2))**2+
218      *                (pyr(2))**2+
219      *                (pzr(2))**2)/(2.*m1*1836.)
220
221        sum_et=et1+et2
222        call hf2(910,(-param/1000.),et1,1.) ! plot kinetic energy of an ion
223 c                                          as a function of delay
224
225         prrx = pxr(1)-pxr(2)
226         prry = pyr(1)-pyr(2)
227         prrz = pzr(1)-pzr(2)
228
229         pz = pzr(1)+pzr(2)
230         px = pxr(1)+pxr(2)
231         py = pyr(1)+pyr(2)
232
233         pxran1 = pxrold(2)+pxr(1)
234         pyran1 = pyrold(2)+pyr(1)
235         pzran1 = pzrold(2)+pzr(1)
236
237         prs = sqrt((px)**2+(py)**2+(pz)**2) ! total momentum for a pair of
238 c                                           ions
239
240         prsran1=sqrt((pxran1)**2+(pyran1)**2+(pzran1)**2) ! momentum sum
241 c                                      for two ions from different events
242
243          totalr=27.2*((pxr(1)-pxr(2))**2+(pyr(1)-pyr(2))**2+
244      *                (pzr(1)-pzr(2))**2)/(56.*1836.)  ! KER of COM
245          totalrran1=27.2*((pxr(1)-pxrold(2))**2+(pyr(1)-pyrold(2))**2+
246      *                (pzr(1)-pzrold(2))**2)/(56.*1836.)! same as above
247 c                                   but two ions come from different events
248 c-----------------------------------------
249
250          call hf1(-16,pz,1.)
251          call hf1(-17,px,1.)
252          call hf1(-18,py,1.)
253          call hf1(-11,prs,1.)
254
255         call hf2(809,prs,totalr,1.) ! E vs P diagram
256
257 c       E vs P: ramdom coincidences subtruction
258         call hf2(810,prs,totalr,1.)
259         call hf2(810,prsran1,totalrran1,-1.)
```

Figure B.6 Analysis subroutine: page 6

```
c-------------------------------------------------
c
        if (prs.lt.15.and.totalr.lt.50.)then  ! gate on E vs P on real
c                                              coincidences
        call hf2(930,(-param/1000.),totalr,1.) ! KER vs delay plot
c
c        KER vs delay randoms subtruction
         call hf2(932,(-param/1000.),totalr,1.)
         call hf2(932,(-param/1000.),totalrran1,-1.)
c-------------------------------------------------------------
       endif
       endif
       endif
       enddo
       enddo

c   Write all time and coordinate signals to an array to use for randoms
c   subtraction for next event
c-------------------------------------------------------------------------

       do i=1,3
       do j=1,nrec
         oldrec(i,j)=rec(i,j)
        enddo
        enddo
      end

C Present all the histograms in format of hbook file for ploting in Paw++
C-------------------------------------------------------------------------
        subroutine booking(histfile)
C-------------------------------------------------------------------------

        parameter (nwpawc=4000000)
        common /pawc/ hmemor(nwpawc)
        common /quest/iquest(100)
        character*80 histfile
        real PI
        parameter (PI=3.14159265359)

        call hlimit(nwpawc)
c       print *,'Subroutine: booking...'
        call htitle(' offline analyse')
        iquest(10)=65000                        !record length of hbook file
        call hropen(1,'als98',histfile,'NQ',2048,istat)
        if (istat .ne. 0) then
           stop 'Error in opening hbook file'
        endif
c-------------------------------------------------------------------------

        call hbook1(-3,'delay',400,-200.,1000.,0.)
        call hbook1(553,'ngtofall',4000,0.,4000.,0.)
        call hbook2(510,'xy r1',400,-100.,100.,400,-100.,100.,0.)
```

Figure B.7 Analysis subroutine: page 7

```
311         call hbook2(600,'pipico',300,600.,3600.,300,600.,3600.,0.)
312         call hbook2(601,'pipico',300,600.,3600.,300,600.,3600.,0.)
313         call hbook2(810,'E_p',100,0.,100.,600,0.,120.,0.)
314         call hbook2(809,'E_p',100,0.,100.,600,0.,120.,0.)
315         call hbook2(930,'KER vs Delay',400,-200.,1000.,160,0.,80.,0.)
316         call hbook2(932,'KER vs Delay',400,-200.,1000.,160,0.,80.,0.)
317         call hbook2(910,'KERng vs Delay',400,-200.,1000.,120,0.,60.,0.)
318         call hbook1(-16,'pz',200,-50.,50.,0.)
319         call hbook1(-17,'px',800,-200.,200.,0.)
320         call hbook1(-18,'py',800,-200.,200.,0.)
321         call hbook1(-11,'prs',400,0.,200.,0.)
322         call hbook1(-1,'tdc10',36000,0.,36000.,0.)
323         call hbook1(-109,'rawtof',32000,0.,32000.,0.)
324         call hbook1(-110,'sumx',200,-200.,200.,0.)
325         call hbook1(-111,'sumy',200,-200.,200.,0.)
326
327       end
```

Appendix C - **Numerical simulations of the field-free rotational wave packet dynamics**

The calculations are similar to those described in the Ref. [**83**]. First, we numerically solve the time-dependent Schrödinger equation which describes the interaction of a neutral molecule in the ground vibrational state with a laser pulse through the non-resonant ac Stark shift:

$$i\dot{\psi}(\vartheta,t) = [B\mathbf{J}^2 - U(t)\cos^2\vartheta]\psi(\vartheta,t) \qquad \textbf{(C.1)}$$

where θ is the angle between the laser field polarization direction and the molecular axis, **J** is the angular momentum operator, B is the rotational constant of the molecule and U(t) is the effective time-dependent interaction potential:

$$U(t) = -\frac{1}{4}(\alpha_\perp + \Delta\alpha\cos^2\vartheta)E^2(t) \qquad \textbf{(C.2)}$$

$$E^2(t) = E_0^2 Exp[-4Ln(2)\frac{(t-t')^2}{\tau^2}] \qquad \textbf{(C.2a)}$$

where $\Delta\alpha$ and $\alpha_\perp$ are the polarizability anisotropy and the polarizability component perpendicular to the molecular axis, and E(t) is the electric field strength which is taken in the shape of a Gaussian pulse envelope of duration τ. We used the same pulse peak intensity and duration which were estimated for the actual pulse in our experiments.

Numerical integration of the TDSE by the finite differences method is done in the basis of rotational eigenstates of the rigid rotor $|\, J, M \,\rangle$ over the time interval of 10τ centered on the peak of the pulse. Starting with a pure single rotational state the integration yields populations and phases of all rotational states involved in the resulting coherent superposition

$$\psi_0 = \sum_J a_J \left| J, M \right\rangle \qquad \textbf{(C.3)}$$

where a_J are the complex amplitudes for each rotational state. This wavepacket is then subjected to field-free evolution:

$$\psi(t) = \sum_J a_J e^{-i(E_J/\hbar)t} \left| J, M \right\rangle \qquad \textbf{(C.4)}$$

$$E_J = BJ(J+1) - D[J(J+1)]^2 \qquad \textbf{(C.4a)}$$

where E_J are the energies of a rotor including the centrifugal distortion term. To compare the simulation to our experimental data we extracted the same observable that we measured - $\langle\cos^2\theta\rangle$ the average cosine squared of the angle between the molecular axis and the polarization direction of the pulse:

$$\left\langle \cos^2 \vartheta \right\rangle = \left\langle \psi(t) \left| \cos^2 \vartheta \right| \psi(t) \right\rangle =$$

$$\sum (\left|a_J\right|^2 C_{J,J,M} + \left|a_J\right|\left|a_{J+2}\right| \cos(\Delta\omega_{J,J+2} t + \varphi_{J,J+2}) C_{J,J+2,M}) \qquad \textbf{(C.5)}$$

$$C_{J,J,M} = \left\langle J, M \left| \cos^2 \vartheta \right| J, M \right\rangle \qquad \textbf{(C.5a)}$$

$$C_{J,J+2,M} = \left\langle J, M \left| \cos^2 \vartheta \right| J+2, M \right\rangle \qquad \textbf{(C.5b)}$$

where $\phi_{J,J+2}$ is the phase difference between the *J* and *J+2* states at the start of the evolution, and $\Delta\omega_{J,J+2}$ are the frequency differences between rotational states characterized by rotational quantum numbers *J* and *J+2*.

To account for a finite initial rotational temperature of the target we summed the results obtained for different initial rotational states weighted by the Boltzmann population of each state for a given rotational temperature:

$$\left\langle \cos^2 \vartheta \right\rangle_T = \sum_J \frac{\exp[-\frac{E_J}{kT}]}{Q} \sum_M < \cos^2 \vartheta >_{J,M} \qquad \textbf{(C.6)}$$

where Q is the partition function. The thermal averaging is done separately for each spin form (ortho and para) of H_2 and D_2, with each form being allowed only even or odd values of *J*. Thus for H_2 (nuclear spin - ½) ortho form (total spin - 1) can be only in *J = 1,3,5,..* and para (total spin – 0) in *J = 0, 2, 4,..*, with ortho to para ratio of 3:1. For D_2 (nuclear spin – 1) ortho form (total spin – 0 or 2) can be in even *J* states, while para (total spin – 1) only in odd *J* states, with ortho to para ratio of 2:1. Contributions from ortho

and para spin forms were added together with proper weights for H_2 and D_2, to produce the calculated traces of $\langle \cos^2\theta \rangle$.

Appendix D - **Molecular fragmentation: classical model**

Using one electronic state of a molecular ion at a time, we start a wave packet on a potential curve at an internuclear distance R_e=*2.2* au which is the equilibrium position for the neutral nitrogen molecule. In this case we have an accelerated motion in the known potential *V(R)* with known initial conditions (*R(t = 0) = R_e, v(t = 0) = 0*). It is possible to calculate the time and kinetic energy corresponding to each wave packet position. For that we use classical dynamics equations for the acceleration **(D.1)**, position **(D.3)**, time **(D.4)** and the energy conservation law **(D.5)**.

$$a = -\frac{1}{\mu}\frac{dV(R)}{dR}, \qquad \textbf{(D.1)}$$

$\mu = \frac{m}{2}$ is the reduced mass for a homonuclear diatomic molecule

For very small step ΔR we use the trapezoid rule:

$$a\left(\frac{\Delta R}{2}\right) \approx -\frac{1}{\mu}\frac{\Delta V(R)}{\Delta R}, \qquad \textbf{(D.2)}$$

$$\Delta R = v_0 t + \frac{a t^2}{2} \qquad \textbf{(D.3)}$$

$$t = \frac{-v_0 + \sqrt{v_0^2 + 2a\Delta R}}{a}, \qquad \textbf{(D.4)}$$

$$KE(t) = \Delta V(R(t)). \qquad \textbf{(D.5)}$$

To calculate the kinetic energy release we add the Coulomb explosion energy for ion fragments at internuclear distance *R*.

$$CE(R(t)) = \frac{q_1 q_2}{R(t)}, \qquad \textbf{(D.6)}$$

$$KER(t) = KE(t) + CE(t). \qquad \textbf{(D.7)}$$

To compare results to the experiment one needs to plot the calculated curves on top of the experimental KER spectra.

Appendix E - **Molecular fragmentation: quantum model**

From the quantum mechanical point of view, we solve a problem of the wave packet propagation on one-dimensional Born-Oppenheimer potential curves. This time the propagation was performed by solving the time-dependent Schrodinger equation on a numerical grid using the Crank-Nicholson scheme.

In atomic units TDSE for a nuclear wave function has a form

$$i\frac{\partial}{\partial t}\Psi(R,t) = \hat{H}\Psi(R,t), \qquad \textbf{(E.1)}$$

where $\hat{H} = \hat{T} + \hat{V}(R,t)$, *V(R)* is the time independent Born-Oppenheimer potential, $\hat{T}$ is the kinetic energy operator

$$\hat{T} = -\frac{1}{2\mu}\frac{\partial^2}{\partial R^2}, \qquad \textbf{(E.2)}$$

μ - is a reduced mass of the two nuclei.

Equation **(E.1)** can be integrated to find *Ψ(R,t)*:

$$\Psi(R,t) = \hat{\tau}\exp\left(-i\int_{t_0}^{t}\hat{H}dt'\right)\Psi(R,t_0), \qquad \textbf{(E.3)}$$

$\hat{\tau}$ is the time-ordering operator.

As the potential in our case is time-independent, this integration comes to a simple form:

$$\Psi(R,t) = \exp\left(-i\hat{H}t\right)\Psi(R,t_0), \qquad \textbf{(E.4)}$$

$\exp\left(-i\hat{H}t\right)$ is called the time evolution operator. *Ψ(R,t₀)* is the initial wave packet which we choose to be the wave function of the neutral molecule ground state.

To calculate *Ψ(R,t)* for a small time step later *Ψ(R,t+Δt)* one can make use of the Cayley scheme which is the method of discretization in time. For a small time step *Δt*:

$$\Psi(R,t_0+\Delta t) = \exp\left(-i\hat{H}\Delta t\right)\Psi(R,t_0), \qquad \textbf{(E.5)}$$

$$\exp\left(i\hat{H}\,\frac{\Delta t}{2}\right)\Psi(R,t_0+\Delta t)=\exp\left(-i\hat{H}\,\frac{\Delta t}{2}\right)\Psi(R,t_0)\,, \qquad \textbf{(E.6)}$$

and using Taylor expansion around Δt

$$\left(\mathbf{I}+i\hat{H}\,\frac{\Delta t}{2}\right)\Psi(R,t_0+\Delta t)=\left(\mathbf{I}-i\hat{H}\,\frac{\Delta t}{2}\right)\Psi(R,t_0)\,, \qquad \textbf{(E.7)}$$

$$\Psi(R,t_0+\Delta t)=\frac{\left(\mathbf{I}-i\hat{H}\,\frac{\Delta t}{2}\right)}{\left(\mathbf{I}+i\hat{H}\,\frac{\Delta t}{2}\right)}\Psi(R,t_0)\,. \qquad \textbf{(E.8)}$$

The finite differencing in space coordinate can be combined with the Cayley scheme to solve equation **(E.1)** for the one-dimensional case iteratively.

For free propagation the Hamiltonian has a form:

$$\hat{H}=\hat{T}=-\frac{1}{2\mu}\frac{\partial^2}{\partial R^2}\,. \qquad \textbf{(E.9)}$$

The numerical second derivative in the kinetic energy operator can be expressed, using a three-point formula (Abramowitz), in a form:

$$\Psi''(R)=\frac{\Psi(R-\Delta R)-2\Psi(R)+\Psi(R+\Delta R)}{\Delta R^2}+\vartheta(\Delta R^4)\,. \qquad \textbf{(E.10)}$$

And the discretized kinetic energy operator has a form of a tridiagonal matrix:

$$(T_R)_{ij}=-\frac{1}{2\mu\Delta R^2}(\delta_{i,j-1}-2\delta_{i,j}+\delta_{i,j+1})\,. \qquad \textbf{(E.11)}$$

For the case of one dimensional system only the diagonal potential term is added to the tridiagonal kinetic energy matrix

$$\hat{H}=(\hat{T}_R)_{ij}+V\delta_{ij}\,. \qquad \textbf{(E.12)}$$

The combination of the Cayley scheme for discretization in time (equ. **(E.8)**) and finite differencing method for spatial derivative (equ. **(E.10)**) is known as the Crank-Nicholson propagation and used for solving TDSE for the nuclear wave packet propagation on one of the potential curves of a molecular ion.

In our simple QM model a laser pulse is short and does not couple the potential curves. After removal of one or two electrons from the neutral molecule N_2 at time $t_0 = 0$ the ground state wave packet undergoes a Franck-Condon transition on one of the curves of the N_2^+ or N_2^{2+} molecular ion. There field free time propagation starts. After some delay, the probe pulse removes more electrons to Coulomb explode the ion into N^{2+}+N^{2+}. To take into account the fact that these electrons are not removed instantaneously by the laser pulse of a certain width, we let the wave packet evolve on an intermediate N_2^{3+} state. The time of propagation on that state is a parameter in our model which we vary to match the calculated KER with the experimental value.

To calculate KER as a function of time we project $\Psi(R,t)$ onto the Coulomb radial (l=0) wave function $\Phi_c(E,R)$. KER then is given by Franck-Condon factor [**148**]:

$$KER(t) = \left| \int_0^\infty \Phi_C^*(E,R)\Psi(R,t)dR \right|^2 . \qquad \textbf{(E.13)}$$

To perform the described calculations we adopted the FORTRAN code from the dissertation of Th. Niederhausen [**149**].